UV Studies of Star Formation in Different Extragalactic Environments

A thesis

submitted for the degree of

Doctor of Philosophy

in

The Department of Physics,

Pondicherry University,

Puducherry - 605 014, India



by

Amrutha S

Indian Institute of Astrophysics,

Bangalore - 560 034, India



January 2026

UV Studies of Star Formation in Different Extragalactic Environments

Amrutha S

Indian Institute of Astrophysics



Indian Institute of Astrophysics

Bangalore - 560 034, India

Title of the thesis	:	**UV Studies of Star Formation in Different Extragalactic Environments**
Name of the author	:	**Amrutha S**
Address	:	Indian Institute of Astrophysics II Block, Koramangala Bangalore - 560 034, India
Email	:	amrutha.s@iiap.res.in
Name of the supervisor	:	**Prof. Pravabati Chingangbam**
Address	:	Indian Institute of Astrophysics II Block, Koramangala Bangalore - 560 034, India
Email	:	prava@iiap.res.in
Name of the co-supervisor	:	**Prof. Mousumi Das**
Address	:	Indian Institute of Astrophysics II Block, Koramangala Bangalore - 560 034, India
Email	:	mousumi@iiap.res.in

Declaration of Authorship

I hereby declare that the matter contained in this thesis is the result of the investigations carried out by me at the Indian Institute of Astrophysics, Bangalore, under the supervision of Prof. Pravabati Chingangbam and Prof. Mousumi Das. This work has not been submitted for the award of any other degree, diploma, associateship, fellowship, etc., of any other university or institute.

Signed: 

Date: 20/08/2026

Certificate

This is to certify that the thesis entitled **'UV Studies of Star Formation in Different Extragalactic Environments'** submitted to Pondicherry University by Ms. Amrutha S for the award of the degree of Doctor of Philosophy is based on the results of the investigations carried out by her under my supervision and guidance, at the Indian Institute of Astrophysics. This thesis has not been submitted for the award of any other degree, diploma, associateship, fellowship, etc., of any other university or institute.

Signed: Bomshati CL

Date: 20/08/2026

List of Publications

1. **S. Amrutha**; Mousumi Das; Jyoti Yadav, 2024, "A comparative study of star-forming dwarf galaxies using the UVIT", *Monthly Notices of the Royal Astronomical Society*, 530, 2, 2199–2231. *

2. **S. Amrutha**; Mousumi Das, 2025, "A Pilot Method to Determine the High Mass End of the Stellar Initial Mass Function in Galaxies Using UVIT, Hα-MUSE Observations and Applied to NGC 628", *The Astrophysical Journal*, 987, 11 †

3. **S Amrutha**; Dimitra Rigopoulou; Mousumi Das; Jyoti Yadav, 2026, "Spatial correlations of PAH, UV, and Hα emission and IMF–PAH variations in the star-forming complexes of NGC 628", *Monthly Notices of the Royal Astronomical Society*, 551, 1, 1410. ‡

4. Athokpam Langlen Chanu; **S Amrutha**; Pravabati Chingangbam; Changbom Park; 2026, "Morphological Complexity of NGC 628—A Multiwavelength Multiscale Analysis Using the Ordinal Pattern Framework", *The Astrophysical Journal*, 1003, 50. §

5. **S Amrutha**; Mousumi Das; Daniel Vaz; Jarle Brinchmann, 2026, "Ultraviolet Properties of the Ultra-Faint Dwarf Galaxy Leo T: Insights from UVIT Observations", *Astronomy and Astrophysics, under revision.* ¶

6. Rakshit Chauhan; S Subramanian; Deepak A. Kudari; **S Amrutha**; Mousumi Das, 2025, "Dwarf-dwarf interactions and their influence on star formation: Insights from post-merger galaxies", *Astronomy and Astrophysics*,702, A222.

7. Jyoti Yadav; Mousumi Das; **S Amrutha**; Dimitra Rigopoulou, 2026, "Star formation beyond the optical disk: The low-density outskirts of NGC 2090", *Astronomy and Astrophysics*, 709 A172.

---

*presented in Chapter 6
†presented in Chapter 3
‡presented in Chapter 4
§presented in Chapter 5
¶presented in Chapter 7

Presentations

1. Presented online talk titled "**Probing Star Formation and the High Mass Stellar IMF with UVIT** " at the conference *Instrumentation and Scientific Frontiers in Ultraviolet Astronomy*, Marseille, France.

2. Presented a short talk titled "**Constraining the High-Mass Stellar IMF in Galaxies: A Pilot Method Using UVIT and Hα–MUSE Observations Applied to NGC 628** " at the conference *Star Formation in Different Environments 2025*, ICISE, Quy Nhon, Vietnam.

3. Presented a poster titled "**Understanding stellar initial mass function in the different regions of NGC 628 using MUSE and UVIT observations**" in *National conference Astronomical Society of India (ASI) 2025*, NIT Rourkela, India.

4. Presented a talk titled "**A pilot study of High mass end Initial Mass Function of NGC 628 using UV and Hα emission** " at the conference *The Network for UltraViolet Astrophysics (NUVA) (e-meeting), 2024.*

5. Presented a poster titled "**A Comparative UVIT analysis of Star Forming Dwarf Galaxy types**" in *Small Galaxies, Cosmic Questions - II 2024*, Durham University, UK.

6. Presented a poster titled "**An Hα and UVIT study of the star-forming complexes in the inner disk of NGC 628**" in *National conference Astronomical Society of India (ASI) 2024*, IISc Bengaluru, India.

7. Presented a talk titled "**Comparing Properties of Star-Forming Dwarf Galaxy Types using UVIT Data**" at the conference *The Network for UltraViolet Astrophysics (NUVA) (e-meeting), 2023.*

8. Presented a poster titled "**A comparative UV study of Star-Forming Dwarf Galaxy types using UVIT**" at *Indo-French CEFIPRA Astronomy meeting-III on SKA and multi-wavelength synergies 2023*, IIA Bangalore, India.

9. Presented a talk titled "**A comparative UV study of Star-Forming Dwarf Galaxy types using UVIT**" in *National conference Astronomical Society of India (ASI) 2023*, IIT Indore, India.

10. Presented a poster titled "**A UV study of Star Forming Dwarf Galaxies using UVIT observations**" at *Two-day conference to celebrate seven years of AstroSat*, , ISRO, Bangalore, India.

Acknowledgements

I extend my heartfelt thanks to my "Super"visors, Prof. Mousumi Das and Prof. Pravabati Chingangbam, for their constant support, encouragement, and guidance. Both of them have been incredibly cool, approachable, and supportive throughout my research journey. Prof. Mousumi has always encouraged me to think independently and explore projects with just the right amount of guidance. Their combined mentorship has helped me grow as a researcher, both in working independently and in collaborating effectively with others.

I thank my collaborators, Prof. Dimitra Rigopoulou, Dr. Langlen Chanu, Dr. Daniel Vaz, Prof. Jarle Brinchmann and Dr. Jyoti Yadav for their insightful discussions and valuable inputs. I also appreciate the support of Dr. Smitha Subramanian, Dr. Ravi Joshi, Rakshit, Prajna, and Vikranth for their confidence in me and for providing opportunities to collaborate. I am grateful to the members of my Doctoral Committee, Dr. Sudhanshu Barway and Prof. Alok Sharan, for their helpful feedback and constructive suggestions.

I would like to thank the Director and the Dean of the Faculty of Sciences, IIA, as well as all the academic and administrative staff for providing a research-friendly environment. I am especially grateful to the staff of the Board of Graduate Studies (BGS)—Shankar Sir, Vijaylakshmi, and Sandhya for their timely assistance with administrative processes. I also thank the Data Centre staff for their technical support with computer- and internet-related matters. I appreciate the IIA library team for helping me access the necessary books essential for my research. I am grateful to the University of Pondicherry administration for their ongoing support.

I express my sincere gratitude to the instructors of the PhD coursework. The remarkable dedication with which they taught during the COVID pandemic played an important role in helping me choose my PhD research topic and carry out my

studies effectively. I would also like to thank the entire extragalactic group for arranging timely talks and discussions.

Bhaskara has become a second home to me, where I have spent most of my PhD life. I am grateful to the Bhaskara supervisors for their care and attention, and to all the cooks and cleaning staff for providing delicious food and ensuring a comfortable, hassle-free stay.

I would like to thank my batchmates, Soumya, Sipra, Neeraj, Judhajeet, Payel, Anisha, and Amlan—and my other close friends, including Dhanush, Parvathy, Manju, and many more juniors, seniors, and friends at IIA for making this PhD journey truly memorable. I will surely miss the treks, yoga, birthday parties, and festival celebrations, where we all came together despite our busy schedules, and also cherish the time we spent together over food and small walks every day.

I would also like to remember all the teachers and friends I have had throughout my life. Many relatives and cousins have encouraged me and expressed pride in the path I chose. Their guidance, support, and even criticism have shaped me into the person I am today, and for that, I am truly grateful.

Finally, my deepest gratitude goes to my entire family for their unwavering support throughout my pursuit of a PhD. Despite social pressures, they always encouraged me to excel and trusted me wholeheartedly. I cannot thank enough the divine love and strength that have guided me at every step. This acknowledgement is surely not enough to express all the love and support I have received throughout this wonderful journey.

Amrutha

Data and software usage

We have utilised data from ground and space-based telescopes for the study presented in this thesis. I would like to express my sincere gratitude to the members and affiliates of the facility for providing this dataset.

We have obtained Far-Ultraviolet (FUV) and Near-Ultraviolet (NUV) archival data, as well as our own observational data, from the Ultra-Violet Imaging Telescope onboard the ASTROSAT mission of the Indian Space Research Organisation (ISRO). We have also used FUV and NUV archival data from Galaxy Evolution Explorer.

We used archival optical data from the Multi-Unit Spectroscopic Explorer (MUSE) on the Very Large Telescope, which provides high-resolution three-dimensional spectroscopic data cubes.

For our Infrared (IR) data, we utilised the Multiband Imaging Photometer for Spitzer (MIPS) and the Infrared Array Camera (IRAC), both of which are components of the Spitzer Space Telescope operated by the Jet Propulsion Laboratory at the California Institute of Technology under a contract with NASA. Additionally, we incorporated high-resolution archival data from the Mid-IR instrument and a Near-IR camera of the NASA/ESA/CSA James Webb Space Telescope. The data were downloaded from the Mikulski Archive for Space Telescopes at the Space Telescope Science Institute. The molecular data used in this study were obtained from the Atacama Large Millimeter Array.

This work made use of different softwares, such as `astropy` (Astropy Collaboration et al. 2013, 2018), Source Extractor (Bertin & Arnouts 1996) TOPCAT (Taylor 2005), `IRAF` (Tody 1993), `matplotlib` (Hunter 2007), `Photutils` (Bradley et al. 2022), `numpy` (Harris et al. 2020).

Dedicated to
my family

for their love and support.

Abstract

Star formation is crucial for galaxy evolution and can be driven by both internal processes and external interactions with neighboring galaxies. By studying the properties of star formation, we can infer the potential causes behind it. This complex process also depends on the surrounding environment, which influences the physical properties of both the stellar and gaseous components that support star formation. Therefore, it is essential to understand how the environment impacts star formation and how this process, in turn, affects the environment.

Within galaxies, star-forming environments can vary from their nuclei to their outer disks. It also varies over different galaxy types, from dwarfs to massive spirals. Analyzing these variations offers insights into both local and global star formation processes.

Our thesis focuses on UV studies of star formation in various extragalactic environments and its impact on the interstellar medium (ISM) and structural complexity of a galaxy. We primarily utilize observations from the Ultra-Violet Imaging Telescope (UVIT), along with multiwavelength data, for a comprehensive analysis. Using UVIT and other high-resolution observations, we conducted a spatially resolved study. We detected star-forming complexes (SFCs) ranging from a few parsecs to hundreds of parsecs in size. Our studies include a nearby massive galaxy (NGC 628), a sample of 16 star-forming dwarf galaxies (SFDGs), and an ultra-faint dwarf galaxy (UFDG; Leo T).

In our study, we estimated an approximate high-mass Initial Mass Function (IMF) for the SFCs across NGC 628 using Hα and UV emissions. Our results indicate that the IMF derived from B-type stars is steeper and more reliable. We observed little variation in the high-mass IMF between arms and spurs within NGC 628. Additionally, we analyzed the properties of polyaromatic hydrocarbons (PAHs), noting an increase in small

PAH molecules as SFCs become top-heavy and blue. We also examined emissions in bubble and superbubble regions, highlighted in James Webb Space Telescope (JWST) images.

To quantify the morphological complexity, we conducted a multiwavelength multiscale analysis of NGC 628, employing statistical measures such as permutation entropy, disequilibrium, and statistical complexity. This analysis yielded a characteristic smoothing scale of about 196 parsecs, which marks a transition from star formation-driven scales to those influenced by galaxy dynamics.

Dwarf galaxies have completely different star-forming environments; they are characterized by low mass, small size, and a metal-poor composition, and are very different compared to the massive galaxy discussed above. We studied SFDGs and one UFDG using UVIT observations. We classified the SFDGs in our sample into dwarf spirals, irregulars, and blue compact dwarfs (BCDs), and found that their properties, including star formation rate and SFC sizes, depend on morphology. We also examined the FUV emission in Leo T, a UFDG, to gain insight into star formation in extreme environments. By comparing FUV SFCs with high-resolution optical data, we also identified UV-emitting stars.

Thus, this thesis provides a comprehensive study of star formation across diverse environments within galaxies and over different galaxy types, utilizing our own UV observations and multiwavelength archival data.

Contents

Abstract **i**

List of Figures **ix**

List of Tables **xvii**

Abbreviations **xix**

1 Introduction **1**
1.1 Galaxies . . . 1
1.1.1 Galaxy formation theories . . . 3
1.1.2 Classification of galaxies . . . 5
1.1.3 Dwarf galaxy . . . 9
1.1.4 Galaxy and ISM Composition . . . 13
1.1.5 Multiwavelength view of Galaxies . . . 15
1.2 Star formation . . . 16
1.3 Initial Mass Function . . . 20
1.4 Star formation in nearby galaxies . . . 22
1.5 Star formation rate tracers . . . 25
1.6 Motivation and goals of the thesis . . . 26
1.7 Overview of the thesis . . . 28

2 Data and Methodologies **31**
2.1 Ultraviolet . . . 31
2.1.1 UltraViolet Imaging Telescope (UVIT) . . . 31
2.1.2 Galaxy Evolution Explorer (GALEX) . . . 34
2.2 Optical . . . 34
2.2.1 Multi-Unit Spectroscopic Explorer (MUSE) . . . 34
2.2.2 Hubble Space Telescope (HST) . . . 35
2.3 Infrared . . . 36
2.3.1 James Webb Space Telescope (JWST) . . . 36
2.3.2 Spitzer Space Telescope . . . 37

2.4 Millimetre . . . 38
2.4.1 Atacama Large Millimeter/submillimeter Array . . . 38
2.5 Research methodologies . . . 38
2.5.1 Source Extraction . . . 38
2.5.2 Photutils . . . 40
2.5.3 Starburst99 Stellar Populations Model . . . 40
2.5.4 Other Theoretical Models . . . 41

3 Study of the high-mass Stellar Initial Mass Function in star forming complexes of NGC628 43
3.1 Introduction . . . 43
3.2 NGC 628 and Observations . . . 45
3.3 Data Analysis . . . 46
3.3.1 Source extraction and classification . . . 46
3.3.2 Internal extinction correction . . . 48
3.3.3 Characterization of the SFCs . . . 52
3.3.4 The number of high-mass stars and their ratios in the SFCs 54
3.4 Results . . . 59
3.4.1 Distribution of SFCs in NGC 628 in Hα, FUV and NUV emission. . . . 59
3.4.2 UV and Hα luminosity correlation . . . 60
3.4.3 Determing the IMF of the SFCs . . . 63
3.4.4 IMF trends with the properties of the SFCs . . . 65
3.5 Discussion . . . 68
3.6 Conclusions . . . 76

4 Spatial Correlations of PAH, UV, and Hα Emission and IMF-PAH Variations in Star-Forming Complexes of NGC 628 79
4.1 Introduction . . . 79
4.2 Data . . . 82
4.3 Analysis and Results . . . 84
4.3.1 PAH correlation with the UV and Hα emission . . . 84
4.3.2 PAH emission across the different regions of NGC 628 . . . 88
4.3.3 The variation of PAH band ratios with the IMF for the SFCs 90
4.3.4 The variation of PAH band ratios with the colour for the SFCs 93
4.4 Discussion . . . 93
4.5 Summary . . . 100

5 Morphological complexity of NGC 628 - a multiwavelength multiscale analysis using the ordinal pattern framework 103
5.1 Introduction . . . 103
5.2 Framework of ordinal patterns, permutation entropy, statistical complexity, and ordinal networks . . . 106

5.2.1 Permutation Entropy, Statistical Complexity, and the Complexity-Entropy (CH) causality plane . . . 110
5.2.2 Node Entropies from Ordinal Network . . . 113
5.2.3 Ordinal pattern analysis for Gaussian random fields - a toy example . . . 114
5.3 NGC 628 Galaxy - multiwavelength view and observed data . . . 117
5.3.1 Multiwavelength observed data of NGC 628 . . . 117
5.3.2 Multiwavelength view of NGC 628 . . . 118
5.3.3 Coarse graining images . . . 120
5.4 Results for NGC 628 . . . 121
5.4.1 Entropy, Disequilibrium, and Complexity for different wavelength images of NGG 628 across scales . . . 123
5.4.2 Entropy, Disequilibrium, and Complexity of NGC 628 across observing wavelengths . . . 129
5.4.3 Surrogate analysis as a control study to quantitatively determine the transition scale . . . 132
5.4.4 Disorder to order transition for individual wavelength images of NGC 628 and high resolution JWST NIR and MIR images . . . 134
5.4.5 Ordinal Network Global Node entropy S_{gn} . . . 136
5.5 Conclusions . . . 138

6 Comparative FUV Study of Star Forming Complexes in Star Forming Dwarf Galaxy Types 141
6.1 Introduction . . . 141
6.2 Sample Selection . . . 143
6.2.1 Dwarf Spirals . . . 146
6.2.2 Dwarf Irregulars . . . 146
6.2.3 Blue Compact Dwarfs . . . 147
6.3 Observations . . . 147
6.4 Data Analysis . . . 149
6.4.1 Data Reduction and Source Extraction . . . 149
6.4.2 UV Photometry . . . 150
6.4.3 The Host galaxy extinction and Total Star Formation Rate 151
6.4.4 Mean Disk Mass of the SFCs . . . 155
6.5 Results . . . 157
6.5.1 Morphology of Dwarfs in UV emissions . . . 157
6.5.2 FUV and NUV SFCs . . . 163
6.5.3 Observed Radial trends of SFCs . . . 169
6.5.4 Star forming main sequence for SFCs . . . 174
6.5.5 Other results of SFDGs . . . 176
6.6 Discussion . . . 183

6.6.1 Difference in Sizes and Star formation rate densities of SFCs in the different SFDG types . . . 183
6.6.2 Effect of interaction on star formation in SFDGs . . . 187
6.6.3 The Global and local SFMS of SFDGs . . . 189
6.6.4 Difference in SFMS of the different SFDGs and inside-out Evolution of Galaxies . . . 191
6.6.5 Correlation between dust obscuration and specific star formation rate . . . 194
6.6.6 The nature of star formation in SFDGs compared to massive galaxies . . . 195
6.7 Conclusions . . . 197

7 Ultraviolet Properties of the Ultra-Faint Dwarf Galaxy Leo T: Insights from UVIT Observations 199
7.1 Introduction . . . 199
7.2 Observations . . . 201
7.3 UV Star forming Clusters . . . 203
7.3.1 Extent of UV SFCs in Leo T . . . 203
7.3.2 Properties of UV Star forming Clusters . . . 204
7.4 Possible UV-emitting stars in Leo T . . . 207
7.4.1 Cross-matching with HST catalog . . . 207
7.4.2 Cross-matching with MUSE sources . . . 208
7.4.3 Distribution of UV-emitting stars in Leo T . . . 210
7.5 Radial Profiles of Young and Old Stellar Population Tracers . . . 214
7.6 Indications of Leo T infall into the MW from UV . . . 215
7.7 The Star Formation Rate and Star Formation Efficiency in Leo T . 217
7.7.1 Leo T Star Formation Rate . . . 217
7.7.2 Correlation with molecular hydrogen and star formation efficiency . . . 219
7.8 Summary . . . 220

8 Conclusions & Future Work 223
8.1 Summary and Conclusions . . . 223
8.2 Future work . . . 227

Bibliography 231

List of Figures

1.1 The first JWST NIRCam's deep field view of galaxy cluster SMACS 0723. Credit: NASA, ESA, CSA, and STScI; composite by E. Siegel. 2
1.2 Hubble tuning fork diagram. Credit: Karen Masters, galaxies are from the Sloan Digital Sky Survey gri colour image as used in Galaxy Zoo. 5
1.3 The reddening-corrected u - r colour–mass diagram from Schawinski et al. (2014). 8
1.4 Classification of dwarf galaxies based on the presence of gas and SF. 11
1.5 Sculptor Dwarf Galaxy. Credit: NASA, ESA/Hubble, DSS2. . . . 13
1.6 Baryonic cycle in MW from Draine (2011). 14
1.7 Multiwavelength View of MW. Credit: NASA. 17

2.1 Schematic representation of the UVIT instrument from Kathiravan et al. (2021). 33
2.2 Splitting and slicing of the MUSE FOV (Credit: ESO). 35
2.3 Observing Modes with JWST (Credit: STSci). 37
2.4 A schematic diagram of the method used to deblend a source in SExtractor from Bertin & Arnouts (1996). 40
2.5 Synthetic spectrum of massive star generated using ATLAS9 stellar atmosphere model Castelli & Kurucz (2004). 42

3.1 UVIT FUV, NUV, and MUSE Hα images of galaxy NGC 628 tracing recent SF. 46
3.2 The above images show the classification of SFCs based on their region(different colors) and their emission in different filters (different markers). Image (a): The locations of the arm (black markers) and interarm (green markers) SFCs overplotted on the UVIT NUV image. Image (b): The locations of spurs(red markers) SFCs overplotted on the ALMA CO(J=2-1) image. 48

3.3 Figures on the left (a, b, and c) and on the right (d, e, and f) illustrate the correlation of Hα luminosity with FUV and NUV luminosities, respectively, for the SFCs. Figures a and d: Luminosities presented without any correction for internal dust attenuation. Figures b and e: Luminosities are corrected for internal dust attenuation using different methods indicated with different symbols and colors. Figures c and f: Luminosities corrected for internal dust attenuation using the Balmer decrement method for the SFCs with Hα emission, and the scaling relation is used to find the FUV extinction coefficient. The fitted relations related to these plots are given in Section 3.4.2. 49
3.4 The distribution of SF properties across different regions (arms, spurs, and interarm) for all available SFCs (first two rows) and specifically for the SFCs used in the IMF analysis. 53
3.5 Observed Hα and FUV SFR correlation for SFCs corrected for extinction with the Balmer decrement and JWST 21μm method. The linear fit for the Balmer decrement and JWST 21μm method are given as equations 3.13 and 3.14, respectively. 62
3.6 The distribution of $\frac{\mathrm{N(O)}}{\mathrm{N(B0)}}$, α_1, $\frac{\mathrm{N(B0)}}{\mathrm{N(B1)}}$ and α_2. The vertical lines represent the median value of the distribution, which is mentioned in Table 3.2. 63
3.7 Variation of IMF index (α_1 and α_2) with the different properties of IMF like FUV and NUV color, stellar mass density, molecular mass density, and SF rate density (from left). 68

4.1 Multiwavelength images of NGC 628. 82
4.2 Correlation of Hα, FUV and NUV luminosities with different PAH luminosities (7.7 μm, 11.3 μm and 3.3 μm). This correlation is for extracted SFCs, whose UV and Hα luminosities are corrected for extinction with (i) the Balmer decrement method and (ii) MIRI 21 μm. 85
4.3 (i) Association of 3.3 μm PAH emission with arm (a), interarm (b), and spur (c) SFCs. We also plotted the association of 3.3 μm PAH with NUV-only SFCs(d), Hα-only SFCs(e), and FUV emitting SFCs detected with a 3σ threshold (f). The SFCs are overlaid on the continuum-subtracted JWST F335M image. Yellow rectangles in Figure (b) show an example of the spurs, and the brown rectangle indicates the position of the phantom void in NGC 628. 87
4.4 Correlation of NUV luminosity of SFCs with NUV-only emission and NUV with other counterparts with the different PAH luminosities (From left: 3.3 μm, 7.7 μm, and 11.3 μm). The NUV luminosities of these SFCs are corrected for extinction using the MIRI F2100W μm band. 89

4.5 The phantom void region of NGC 628. The blue superbubble is the phantom void, and the two green ellipses represent the connecting bubbles. The red markers represent the position of SFCs emitting at different wavelengths. The SFCs with both UV and Hα emission are numbered. 89
4.6 Variation of IMF index (α_1 and α_2) with the PAH band ratios - F335M/F1130W, F770W/F1130W, and F335M/F770W (from left). 92
4.7 Variation of FUV-NUV with the PAH band ratios - F335M/F1130W, F770W/F1130W, and F335M/F770W (from left). 92
4.8 The distribution of PAH band ratios (F335M/F1130W, F770W/F1130W, and F335M/F770W) for only NUV-emitting SFCs and NUV-emitting SFCs with counterparts in UV and/or Hα. 97

A.1 *Top row*: One realization of a two-dimensional isotropic Gaussian random field generated on a grid of 500^2 pixels, with increasing smoothing scales (left to right) given in units of pixel numbers. *Middle row*: Permutation entropy, H, (left) and statistical complexity, C, (middle), as functions of the smoothing scale, for the fields in the top row. The right panel shows the CH-plane. The arrows in the right panel indicate the direction of increasing s. *Bottom row*: Horizontal, $\mathrm{S}_{\mathrm{gn}}^{\mathrm{hor}}$, (dotted) and vertical, $\mathrm{S}_{\mathrm{gn}}^{\mathrm{ver}}$, (dashed) global node entropies (left), global node entropy difference, $\Delta\mathrm{S}_{\mathrm{gn}}$, (middle), as functions of the smoothing scale, for $(d_x, d_y) = (2, 3)$. The log-log plot of the right panel shows an inverse power law fit (solid line) to $\Delta\mathrm{S}_{\mathrm{gn}}$ (triangles) as a function of smoothing scale. 115
A.2 *Top row of (a)*: Images of the galaxy NGC 628 observed at NUV, NIR, MIR, and mm wavelengths (left to right) obtained from UVIT, JWST (NIR and MIR), and ALMA, respectively. All images cover identical fields of view. The intensity values of each image has been normalized by the respective standard deviation. All images are smoothed identically using a Gaussian kernel with a smoothing scale $\sigma = 2$ (in pixels). *Bottom row of (a)*: Same as the top row but for $\sigma = 10$. Image parameters are provided in table 5.1. (b) PDFs of the field values of the four images in (a) corresponding to the top row (blue), and bottom row (yellow). 119
A.3 Ordinal probabilities $\{\rho_k(\psi_k)\}$ of the four NGC 628 images when $(d_x, d_y) = (2, 2)$ at smoothing scale $\sigma = 2$. 122
A.4 *First, second and third rows*: H, D_E and C computed using $(d_x, d_y) =$ (2,2) (red), (2,3) green and (2,4) (purple) for the four images of NGC 628 shown in Figure A.2 smoothed at different scales σ (in units of 10 pc). The details of the images are provided in table 5.1. *Bottom row*: Values of C and H shown on the CH-causality plane for the three cases of (d_x, d_y) of the four NGC 628 images at different smoothing scales. The black arrows indicate the direction of increasing σ. 124

A.5 Comparison of H ((a)), D_E ((b)) and C ((c)) as functions of observing wavelength λ (in nm), for each smoothing scale. 126
A.6 (a) D_E versus H for the four images of NGC 628 shown in the same panel (same markers as Figure A.5), for different σ and (d_x, d_y). (b) CH-plane for different σ. (c) C and H values for all wavelengths and σ are plotted on the same CH-plane. The color bars at the bottom indicate larger σ towards lighter hues. 127
A.7 (a) CH-planes for comparison between the four wavelength images of NGC 628 and Gaussian random fields (GRFs) with power spectra of the form $P(k) \propto k^{-n}$ with $n = 0, 1, 2$, and 3. In each panel, we use the same markers and colors (indicated by the color bar) as in Figure A.6(c) for the four wavelengths, whereas the lighter-colored curves now correspond to the GRFs at the three different embedding dimensions $(d_x, d_y) = (2, 2), (2, 3)$ and $(2, 4)$. (b) *Surrogate fields:* In the upper panel, we plot the (C, H) values of the four images of NGC 628 along with the corresponding plots for the surrogate fields (indicated at the top of the panel). The bottom panels show the zoomed-in views of the boxed regions. Black arrows indicate the direction of increasing σ. 128
A.8 (a) $dH/d(\log\sigma)$ and $dD_E/d(\log\sigma)$ versus $L_{\rm FWHM}$ for the four images of NGC 628. The black dotted vertical line marks $L^{(c)}_{\rm FWHM} = 196\,{\rm pc}$. (b) Similar plots as in (a) but for high-resolution JWST NIR and MIR images. Insets display the corresponding plots with error bars shown as colored shaded regions. Embedding dimensions are indicated in the legend. 135
A.9 Variation of global node entropy $\mathrm{S_{gn}}$ with smoothing scale σ for embedding dimension $(d_x, d_y) = (2, 3)$: Horizontal global node entropy, $\mathrm{S^{hor}_{gn}}$ (*Top*), vertical global node entropy, $\mathrm{S^{ver}_{gn}}$ (*Middle*), global node entropy difference, $\Delta\mathrm{S_{gn}} = \mathrm{S^{hor}_{gn}} - \mathrm{S^{ver}_{gn}}$, (*Bottom*) versus σ on log-log plots. In the bottom panel, dashed lines represent inverse power-law fits ($\Delta\mathrm{S_{gn}}(\sigma) = a\sigma^{-b}$) with corresponding R^2-values for the goodness of fit (indicated in the legend). Values of power-law exponents b are: 0.8705 (NUV), 0.6730 (MIR), and 0.4854 (mm). For NIR, we have fitted in two regimes with $b = 0.6650$ & 1.2920. . 137

A.1 Types of SFDGs. From left: Dwarf Spiral (NGC 5474), Dwarf irregular (NGC 1427A), and a BCD (UGC 11411). Credit: GALEX and ESA/NASA. 142
A.2 Properties of the sample galaxies. The grey colour with '*' as a pattern represents dwarf spirals, the teal with the pattern 'o' represents dwarf irregulars, and the orange with pattern dots represents BCDs. In these histograms, we see that the dwarf spirals have relatively higher mass and metallicity compared to other types, But they all have similar rotational velocities. All galaxies have subsolar metallicities. 144

A.3 UVIT image of NGC 4625. The red ellipses are fitted to sources using SExtractor (Bertin & Arnouts 1996). The detection threshold is 8 σ. Black circles have a radius of r_{25}, which is mentioned for this galaxy in Table 6.1. 150
A.4 Elliptical annuli of equal area are fitted to the convolved UVIT image of NGC 4618, with the position angle as listed in Table 6.1. . 152
A.5 The radial variation of the sSFR is represented as a blue solid line. Whereas 24 μm and convolved UV flux ratio (α as in subsection 6.4.3) is represented as a red dashed line. The black dotted line represents the average α calculated for each galaxy, taking the integrated 24 μm and convolved UV flux within the outer ellipse. The galaxy UGCA 130 is not included. 153
A.6 Radial variation of Stellar mass density for galaxy NGC 4618. From this, we associated the stellar mass density with the SFCs by looking at their galactocentric distance. 158
A.7 First, second, and third columns in Figure A.7 are a variation of area, star formation rate density, and the mass of the SFCs, respectively, with respect to the deprojected galactocentric radius scaled with the optical size of the galaxy. 165
A.8 The above figures show the scatter plot of $log(\Sigma(SFR))$ for dwarf spiral (NGC 4618) (left), dwarf irregular (UGC 4305) (middle), and a BCD (NGC 3738) (right). 170
A.9 Radial variation of the star formation rate density of SFCs for all the sample galaxies, except NGC 6822. 171
A.10 Radial variation of the log(size) of SFCs for some galaxies with approximately equal distances. The median size value for dwarf spiral (NGC 4136, NGC 4395), irregular (UGC 7608, IC 2574), and BCDs (Haro 36, VIIZw403) at a distance D $\approx$ 10.5 Mpc is 85.11 pc, 96.96 pc, and 104 pc, respectively. And at distance D $\approx$ 4.1 Mpc, it is 27.9 pc, 43.54 pc, and 51.29 pc, respectively. 172
A.11 Radial variation of the specific star formation rate of SFCs for all the sample galaxies. 172
A.12 SFMS of SFCs for all the sample galaxies. 175
A.13 Star forming the main sequence of SFCs for all of our sample galaxies except UGCA 130, as it has only 2 complexes. We see that the inner SFCs with yellow circles (r< r_{25}/2), middle SFCs with purple plus (r_{25}/2<r < r_{25}), and outer SFCs with blue stars (r > r_{25}) have different SFMS for many galaxies. Outer SFCs have higher specific star formation rates, indicating the inside-out evolution of the galaxies. 177
A.14 Blue squares are our sample SFDGs, and red stars are dwarf LSBs from McGaugh et al. (2017). The black solid line is a linear fit for SFMS of SFDGs with the slope of $\alpha = 0.8989$. The dashed line is the linear fit for dwarf LSBs with the slope of $\alpha = 1.05$. 180

A.15 Metallicity-mass plot for SFDGs. Values of errors associated with metallicity can be found in Table 6.6. 181
A.16 Metallicity-colour plot for SFDGs. We find a positive correlation only for BCDs. 182
A.17 Top panel: UVIT FUV and UVIT NUV images. Bottom panel: Siptzer IRAC 3.6 μm, and Optical CTIO b band images of NGC 6822. 185
A.18 Distribution of log(Σ(SFR)) for SFCs of all sample galaxies (except NGC 6822). The mode of log(Σ(SFR)) for dwarf spirals, dwarf irregulars, and BCDs is -1.84 $M_{\odot}yr^{-1}kpc^{-2}$, -2.09 $M_{\odot}yr^{-1}kpc^{-2}$, and -1.5 $M_{\odot}yr^{-1}kpc^{-2}$ respectively. 186
A.19 UVIT FUV image of interacting galaxies NGC 4625, NGC 4625A, and NGC 4618 from left 188
A.20 sSFR and stellar disk mass correlation for SFCs. The black dash-dotted line is the fit from Leroy et al. 2019. The blue dash-dotted line is its extrapolated fit for lower mass. 191

A.1 The background image is the UVIT FUV image of Leo T. The optical center is marked as a black cross. The red ellipses are the extracted FUV SFCs. The black contours represent HI intensity contours from deep Westerbork Synthesis Radio Telescope observations (Adams & Oosterloo 2018), ranging from 5%, 10% to 90% of the peak flux with a step size of 10%. The peak HI column density is 4.2 $\times 10^{-20} cm^{-2}$. The green polygon is an HST FOV (Weisz et al. 2012), and the blue one is MUSE FOV (Vaz, Daniel et al. 2023). The black dashed circle is the FOV of Atacama Compact Array, and brown circles are the molecular cloud locations as mentioned in Villanueva et al. (2025). 202
A.2 Distribution of SFCs along the galactocentric radius. Vertical blue and red lines are half light radius $R_{1/2}$=115 pc (Wolf et al. 2010) and HI extent of the galaxy (400pc; Adams & Oosterloo (2018)). . 204
A.3 The background image is the UVIT FUV image of Leo T. The black contours are the HI intensity contours (Adams & Oosterloo 2018). The image shows how Σ(SFR) and the radius of SFCs are distributed in the galaxy. The image also shows the SFC radii and Σ(SFR) histograms. The black solid lines are the median values. The dashed blue line in the SFC radii histogram is the resolution limit, and in the Σ(SFR) histogram, it is the lower Σ(SFR) limit for dwarf irregular galaxies in Amrutha et al. (2024). 205
A.4 Histogram of FUV luminosity of SFCs. The black solid line is the median value. 206
A.5 The deep HST/WFPC2 CMD of Leo T with select Padova isochrones for UV sources. Isochrones of different colors represent different ages, and markers of different colors represent different populations. 210

A.6 Distribution of UV emitting stellar population of Leo T. Background image is UVIT FUV image of Leo T. Black contours are high-intensity contours (Adams & Oosterloo 2018). Different markers in the image represent different stellar populations emitting UV. 211
A.7 FUV Luminosity (Top panel) and Area distribution of SFCs with respect to the type of star present in it. The star and triangular markers represent SFC with Upper MS and Lower MS, respectively. '+' marker represents SFC containing both lower and upper MS. BL and HB have square and circular markers, respectively. Whereas SFCs with cross and diamond markers have EL and both EL and lower MS stars. 213
A.8 Radial variation of GALEX FUV and NUV magnitudes (from Top panel), Decals r-band magnitude and NUV-r color. 216

A.1 The GALEX FUV image of the interacting galaxies -Mrk 1508 (Left) and Mrk 691. We see interaction features and associated star formation in both galaxies. 228
A.2 The UVIT images of type II XUV disk galaxies from Das et al. (2021) - NGC 2541 (left), and ESO406-042. We can see resolved star-forming knots in these UVIT images of type two XUV galaxies. 229

List of Tables

3.1 FUV and NUV luminosities of massive stars 58
3.2 IMF parameters in different regions 65
3.3 Fitting parameters for α_2 and FUV-NUV plot (equation 3.15) and α_2 and $\log_{10}(\Sigma(\mathrm{SFR}))$ plot (equation 3.16) 66
3.4 IMF parameters in different regions for SFCs with FUV-NUV $\leq$ 0.3. 74

4.1 Fitting parameters for equation 4.2. 86
4.2 Fitting parameters for equation 4.3. 94

5.1 Image parameters 117

6.1 Properties of the sample galaxies. 145
6.2 UVIT Filter and Image Information. 148
6.3 Calculated parameters for extinction-free SFR 156
6.4 Number of FUV and NUV bright SFCs inside and outside optical radius r_{25}. 169
6.5 Star forming main sequence parameters for sample galaxies. 178
6.6 Calculated parameters of Sample galaxies. 179

7.1 Properties of UV Star-forming Complexes 209
7.2 Physical quantities of the CO clouds in Leo T. 220

Abbreviations

ALMA	**A**tacama **L**arge **M**illimetre/submillimeter **A**rray
BCD	**B**lue **C**ompact **D**warf
CDM	**C**old **D**ark **M**atter
CMD	**C**olor **M**agnitude **D**iagram
DECaLS	**D**ark **E**nergy **C**amera **L**egacy **S**urvey
DECam	**D**ark **E**nergy **C**amera
ESA	**E**uropean **S**pace **A**gency
ESO	**E**uropean **S**outhern **O**bservatory
Gaia	**G**lobal **A**strometric **I**nterferometer for **A**strophysics
GALEX	**G**alaxy **E**volution **E**xplorer
HST	**H**ubble **S**pace **T**elescope
IFU	**I**ntegral **F**ield **U**nits
IMF	**I**nitial **M**ass **F**unction
IRAF	**I**mage **R**eduction and **A**nalysis **F**acility
IRAC	**I**nfra-**R**ed **A**rray **C**amera
ISM	**I**nter**S**tellar **M**edium
ISRO	**I**ndian **S**pace **R**esearch **O**rganisation
JWST	**J**ames **W**ebb **S**pace **T**elescope
LSB	**L**ow **S**urface **B**rightness
MIPS	**M**ulti-band **I**maging **P**hotometer for **S**pitzer
MIRI	**M**id-**I**nfra**R**ed **I**nstrument
MS	**M**ain **S**equence

MUSE	**M**ulti **U**nit **S**pectroscopic **E**xplorer
MW	**M**ilky **W**ay
NIRCam	**N**ear-**I**nfra**R**ed **C**amera
PARSEC	**PA**dova and t**R**ieste **S**tellar **E**volutionary **C**ode
PHANGS	**P**hysics at **H**igh **A**ngular resolution in **N**earby **G**alaxie**S**
PM	**P**roper **M**otion
RGB	**R**ed **G**iant **B**ranch
SF	**S**tar **F**ormation
SFC	**S**tar **F**orming **C**omplex
SFDG	**S**tar **F**orming **D**warf **G**alaxy
SFH	**S**tar **F**ormation **H**istory
SFR	**S**tar **F**ormation **R**ate
SFE	**S**tar **F**ormation **E**fficiency
UVIT	**U**ltra **V**iolet **I**maging **T**elescope
UFDG	**U**ltra **F**aint **D**warf **G**alaxy
VLT	**V**ery **L**arge **T**elescope

Chapter 1

Introduction

1.1 Galaxies

Galaxies are fundamental units of the universe on a large scale. They are systems of baryonic and dark matter that are gravitationally bound, with baryonic matter consisting of stars, the interstellar medium (ISM), and stellar remnants. Our Earth is a part of the Milky Way (MW) Galaxy, and the MW is one among the billions of galaxies in our observable universe. Earlier in 1920, there was a debate between the scientists Harlow Shapley and Heber Curtis regarding the nature of the nebulae (or galaxies) outside the MW; this was called the Shapley-Curtis debate. Shapley proposed that these nebulae are part of our MW, whereas Curtis contended that these constitute separate galaxies and do not belong to the MW. In 1926, Hubble (1926) confirmed that they are 'extragalactic nebulae' by studying Cepheid variable stars in one of the galaxies. Now, the study of objects outside the MW comes under the branch of Extragalactic astronomy.



FIGURE 1.1: The first JWST NIRCam's deep field view of galaxy cluster SMACS 0723. Credit: NASA, ESA, CSA, and STScI; composite by E. Siegel.

Figure 1.1 is the first James Webb Space Telescope (JWST) Near-InfraRed (NIR) deep field image of a galaxy cluster, SMACS 0723. This field covers an angular area of 2.4 arcminutes and was observed with 12.5 hours of exposure time. There are nearly 40000 galaxies in this small field. Hence, it is crucial to understand how these galaxies form and evolve to comprehend the formation of large-scale structures in the universe, and also to understand the distribution of invisible dark matter. We discuss the formation, classification, and composition of the galaxies in the sections below.

1.1.1 Galaxy formation theories

There are different theories to explain the formation of galaxies (Mo et al. 2010). The two important theories are the Top-down or Monolithic Collapse Model and the Bottom-up or Hierarchical Clustering Model. The top-down model was first proposed by Eggen et al. (1962). The theory posits that disk galaxies formed rapidly from the collapse of a single, massive primordial gas cloud shortly after the Big Bang. During this collapse, the very first stars form. As the collapse accelerates, the nascent stars and globular clusters that formed early on are ejected into the outer regions of the collapsing cloud. They are left with random, highly elliptical orbits and do not settle into a flattened structure. These older, metal-poor stars form the galactic halo and the central bulge. The remaining gas, which has dissipated energy through radiation (cooling), settles into a much flatter, rotationally supported disk due to the conservation of angular momentum. Stars continue to form in this disk, creating younger, more metal-rich stellar populations. While the luminous, baryonic matter (the gas) dissipates energy and collapses, the dark matter, which only interacts gravitationally, does not. It is assumed to remain in a large, diffuse halo surrounding the disk. Although the theory explains some of the concepts observed in the universe, it fails to explain the age spread in the stellar halo (Searle & Zinn 1978), the lack of early massive galaxies, and predicts a lower angular momentum for galaxies than is observed.

The recent and well-accepted galaxy formation theory is the Bottom-up or Hierarchical Clustering Model (Blumenthal et al. 1984; Bromm et al. 2009). This theory is a core component of the standard Lambda-cold dark matter (CDM) cosmological model, and is supported by a large body of evidence from both observational astronomy and large-scale computer simulations. It describes a gradual process in which smaller structures merge and accrete matter over billions of years to build the large galaxies and clusters seen today. The gravitational influence of dark matter drives the entire process. In the aftermath of the Big Bang, the distribution of

matter was nearly uniform, with only tiny quantum fluctuations in density. The CDM model proposes that dark matter, being cold (moving slowly) and dissipationless, gravitates and clumps much more easily than usual, or baryonic matter. These early, small fluctuations in the dark matter density grew through gravity, forming a cosmic web of filaments and nodes. The densest regions collapsed first to create small, self-gravitating dark matter structures known as "dark matter halos". Gravity pulls the baryonic matter into these dark matter halos. The cool and dense gas forms the first stars and small dwarf galaxies. These dwarf galaxies and dark matter halos merge, forming increasingly larger and more massive structures. This hierarchical merging of galaxies is an important characteristic of the model. Through mergers and mass accretion processes, galaxies continue to grow, evolving into the varied and complex structures observed in the present-day universe, which is predominantly composed of spiral and elliptical galaxies.

However, recent JWST observations have revealed ultra-massive galaxies at redshifts ($z > 7$), including some with well-developed spiral arms (Xiao et al. 2024; Carnall et al. 2024; Xiao et al. 2025; Jain & Wadadekar 2025). The existence of such massive and morphologically evolved systems within the first billion years after the Big Bang poses a challenge to the standard hierarchical clustering paradigm, in which galaxies are expected to assemble progressively through the merger and accretion of smaller systems. These discoveries suggest that massive galaxy assembly and structural evolution may have proceeded more rapidly than predicted by current models, motivating refinements to our understanding of galaxy formation and evolution.

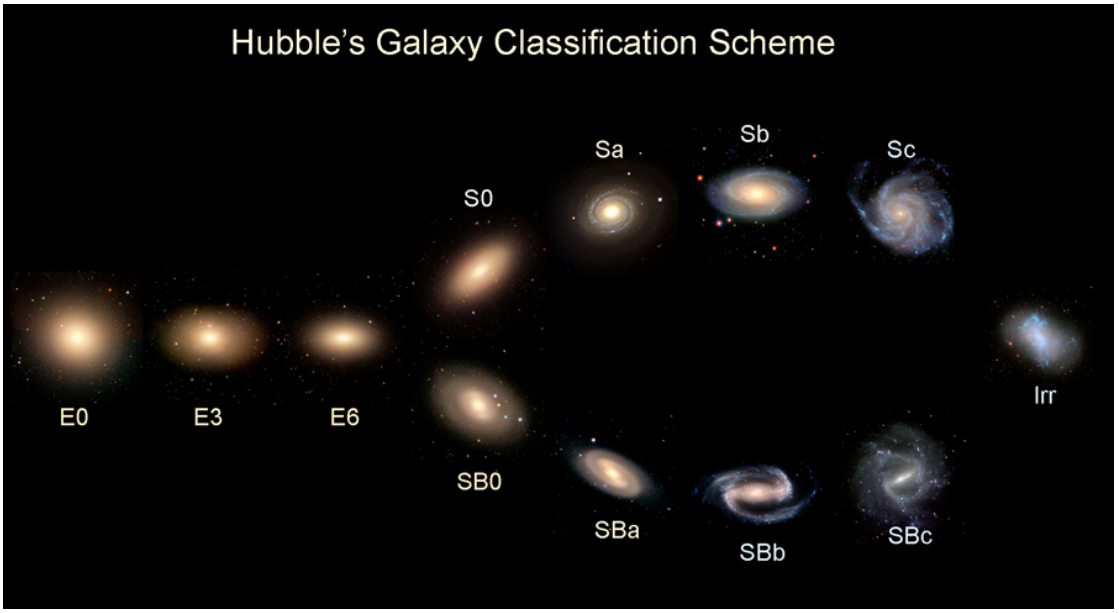


FIGURE 1.2: Hubble tuning fork diagram. Credit: Karen Masters, galaxies are from the Sloan Digital Sky Survey gri colour image as used in Galaxy Zoo.

1.1.2 Classification of galaxies

Morphological classification

With the advent of photography, the study of galaxy structure and morphology began. One of the most notable and popular schemes is 'Hubble Tuning Fork' by Hubble (Hubble 1926, 1936). Hubble classified the galaxies into four major types based on their morphology: Elliptical, Spiral, Lenticular, and Irregular galaxies, as shown in Figure 1.2.

Elliptical galaxies are morphologically elongated galaxies that appear elliptical or spheroidal in shape. They are denoted as En, where n can take values from 0 to 6. E0 means that the galaxy is nearly spheroidal. The n increases as the ellipticity of the galaxy increases. These galaxies are at the left of the bifurcation in the tuning fork, or at the beginning of the tuning fork (See Figure 1.2), so they are also called early-type galaxies.

In contrast, spiral galaxies are characterized by their visible spiral arms. They consist of flat, rotating disks containing stars, gas, and dust, surrounded by an extended stellar halo. Some of the spirals also have a central spheroidal structure, known as a bulge. Spiral galaxies are again classified based on the presence (SB) or absence (S) of an elongated structure called a bar at the centre. Additionally, these galaxies are further categorized by the tightness of their spiral arms, which results in classifications of Sa/SBa (tightly wound), Sb/SBb (moderately wound), Sc/SBc, and Sd/SBd (loosely wound). These latter types of spirals are often referred to as late-type galaxies. There are also lenticular galaxies (S0), which fall between elliptical and spiral galaxies. They have a large disk but lack spiral arms. Lastly, there are irregular galaxies (Irr/Im) with no distinct shape.

Subsequently, new methods were developed for classification based on visual inspection. de Vaucouleurs (1959) highlighted prominent internal features such as bars and rings. Several studies, including those by Sandage (1961), van den Bergh (1976), and Elmegreen & Elmegreen (1987), have extended these classification schemes.

These morphological classifications were reasoned with physics to understand the origin and evolution of these galaxies. Elliptical galaxies are found to be massive and red in color (Holmberg 1958), and show minimal star formation (SF). In comparison, spirals are generally less massive than elliptical galaxies. They are often blue in color and have evidence for ongoing SF. The ellipticals and lenticulars are generally found towards the centres of galaxy clusters, where the galaxy density is very high. Hence, the rate of galaxy mergers/interactions is high, and galaxies grow in mass via mergers over time (Dressler 1980; Bekki 1998). These mergers will trigger intense SF activity, which consumes the available gas, and transforms the galaxies into passive, red galaxies (Larson 1975). However, studies suggest that lenticulars could also be spiral galaxies with faded arms (Aguerri 2012; Marquez-Lugo et al. 2025).

Studies suggest that the spiral arms in disk galaxies are density waves that propagate with a velocity called the pattern speed in the disk (Lindblad 1959; Lin & Shu 1964). Galaxies also exhibit differential rotation, hence their inner disk moves faster than the pattern speed of the spiral arm. As a result, gas and dust in the inner disk pass through the spiral arms, undergoing shocks that heat up the gas. The compression of gas leads to SF, giving the galaxy a blue color. The spiral arms can be formed due to secular evolution, ie, due to excitation by a bar in the galaxy center. Or by the tidal force of fly-by interaction that triggers the formation of spiral arms. The grand design galaxies have two well-defined spiral arms (Lin & Shu 1966), whereas flocculent galaxies have patchy, discontinuous spiral arms (Elmegreen 1981). Most galaxies without central concentration are found to have multiple spiral arms, whereas the bulge-dominated galaxies generally have two spiral arms (Díaz-García, S. et al. 2019; Yu & Ho 2020).

Quantitative methods of classification

Given the large number of galaxies, it is impractical to classify them visually. A wide range of quantitative parameters and methods are now used to classify galaxies. Modern extragalactic astronomy has moved toward multi-parameter, quantitative classification schemes that capture structure, stellar populations, kinematics, and spectral properties.

The galaxy color is indicated by broadband indices such as (B - V) or (U - B), which trace stellar population age and metallicity. Bluer colors in late-type systems represent younger stars and active SF, while redder colors in ellipticals indicate older, metal-rich stars. This is formalized in the color–magnitude relation (CMR), which categorizes galaxies into "red sequence" and the "blue cloud", with transitional "green valley" objects in between (Strateva et al. (2001); Baldry et al. (2004)). The red sequence comprises quiescent galaxies, whereas the blue cloud consists of

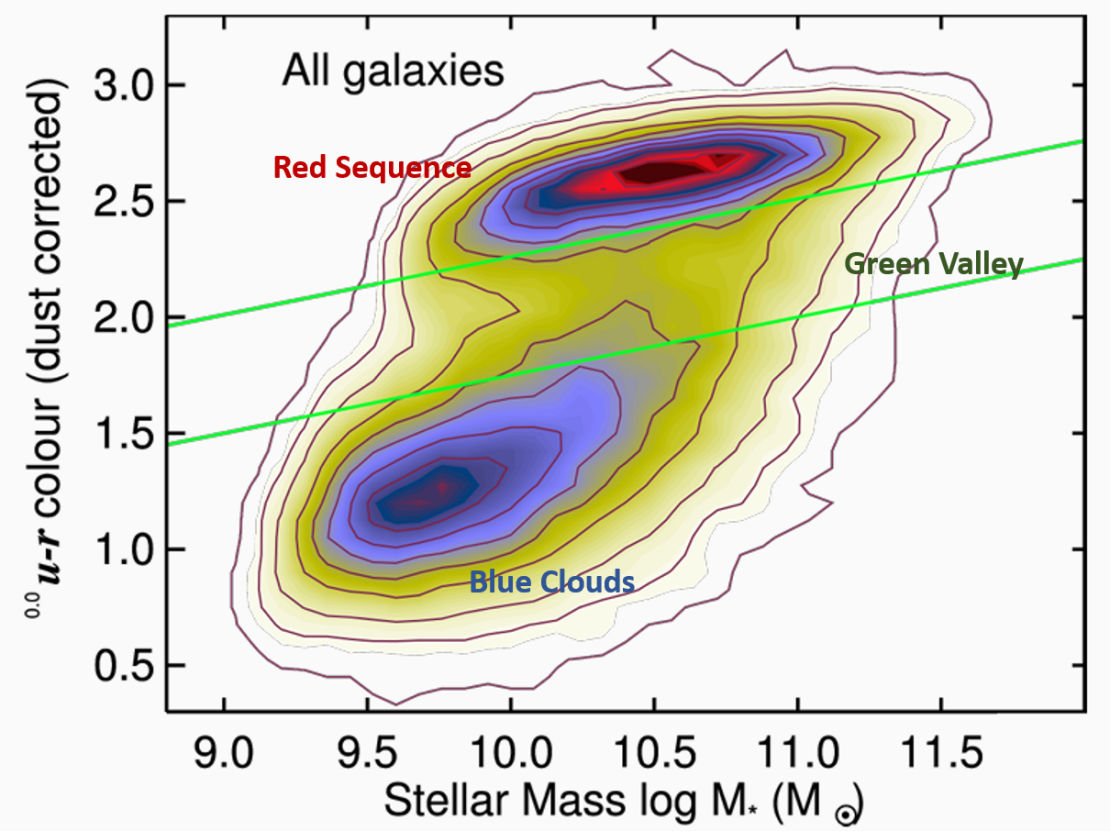


FIGURE 1.3: The reddening-corrected u - r colour–mass diagram from Schawinski et al. (2014).

star-forming galaxies. The HI gas mass-to-light (M_{HI}/L_B) ratio can also be used to classify galaxies, as it increases from elliptical to spiral. This trend indicates that late-type galaxies are relatively more gas-rich and have higher fractions of neutral hydrogen available for SF (Cornett et al. (1994); Catinella et al. (2010)).

There are other Structural (Morphometric) Quantitative Classifications, non parametric techniques describing the shape and light distribution of galaxies, such as Concentration, Asymmetry, and Clumpiness (CAS) System, which distinguishes ellipticals (high C, low A, low S), spirals (moderate A, S), and irregulars (high A, S) (Conselice 2006). The Gini Coefficient quantifies how light is distributed among pixels (Lotz et al. 2004), and the Sérsic Index, derived from surface brightness profiles, serves as a quantitative substitute for the Hubble sequence classification

(Graham & Driver 2005). The Bulge-to-Total Ratio (B/T), derived from two-dimensional light profile decompositions using GALFIT, GIM2D, can also be used to classify galaxies (Simard et al. 2011).

There are many automatic morphological classifications using machine learning and statistical methods, which can classify a large number of galaxies together (Huertas-Company et al. 2011; Dieleman et al. 2015).

1.1.3 Dwarf galaxy

Studies have shown that the properties of galaxies also depend on their mass. Galaxies which have stellar mass (M_*) $\geq 10^{10}$ $M_\odot$ are massive and galaxies below that M_* are considered as dwarf galaxies. Dwarf galaxies are an important part of this thesis. Hence, we discuss dwarf galaxies and their different morphologies in detail in this section.

Dwarf galaxies are low mass ($M_* < 10^{10}$ $M_\odot$) galaxies that have smaller sizes and lower dynamical masses compared to normal galaxies on the Hubble sequence (Lelli 2022). Due to their low stellar masses, they usually have shallower gravitational potential wells. Hence, dwarfs often lose a significant amount of metal content via ejection by stellar winds, and supernova bursts (Bergvall 2011), making them often metal-poor and gas-poor (Mac Low & Ferrara 1999). Most dwarfs do not appear to have molecular hydrogen (H_2) gas as they are not detected in CO emission (Leroy et al. 2005; Das et al. 2006; Schruba et al. 2012). They also have thick/flared disks, resulting in a low mid-plane pressure in the disk gas.

It is well known that dwarf galaxies dominate the galaxy population in the universe (Loveday 1997). The ΛCDM models and cosmological simulations of the large-scale structure show that they are important for the hierarchical growth of

galaxies through SF and mergers (White & Rees 1978; Deason et al. 2014; Wheeler et al. 2019). Due to their abundance, most mergers at all redshifts are between dwarf galaxies (De Lucia et al. 2006). The nearest example of such a merger is the infall of the Large Magellanic Cloud (LMC) and Small Magellanic Cloud (SMC) into our Galaxy (Nidever et al. 2017). The two galaxies are connected by a gaseous bridge composed of HI complexes, and the entire structure is called the Magellanic Stream (D'Onghia & Fox 2016). Such studies of nearby dwarfs in our Local Group, combined with simulations (as in the TiNy Titans (TNT) program), help to understand the redistribution of stellar and gaseous material in interacting/merging dwarf galaxies (Besla et al. 2010; Stierwalt et al. 2015).

Surveys over the past two decades show that dwarf galaxies are not only abundant, but they also span a wide variety of galaxy types. Broadly speaking, dwarfs can be classified into gas-poor and gas-rich based on the presence of gas, as shown in Figure 1.4. The gas-poor dwarf galaxies consist of early-type dwarf spheroidals, dwarf ellipticals, and gas-free ultra-diffuse or ultra-faint galaxies (UDGs). Most of these dwarf galaxies are satellites of giant host galaxies and are very faint. Their low luminosity makes them hard to detect, and it is only recently that they have been detected in large numbers (Koda et al. 2015). There are many theories explaining why satellite galaxies are gas-poor, but the most probable explanation is gas stripping due to interaction with massive galaxies (Putman et al. 2021).

A large fraction of the gas-rich dwarfs are low surface brightness (LSB) galaxies. Such galaxies have low luminosities, diffuse stellar disks, and high dark matter content (Honey et al. 2018). LSB dwarfs include both disky and irregular dwarfs. Their HI masses are very high, and some of them have HI gas mass fractions that are close to 100% of their dynamical mass (Begum et al. 2008; Schombert et al. 2001). They have very low star formation rates (SFRs) and consume gas at a very slow pace (Lee et al. 2009). However, studies show that a significant fraction of LSB dwarfs have some SF and follow a star-forming main sequence (Thilker et al.

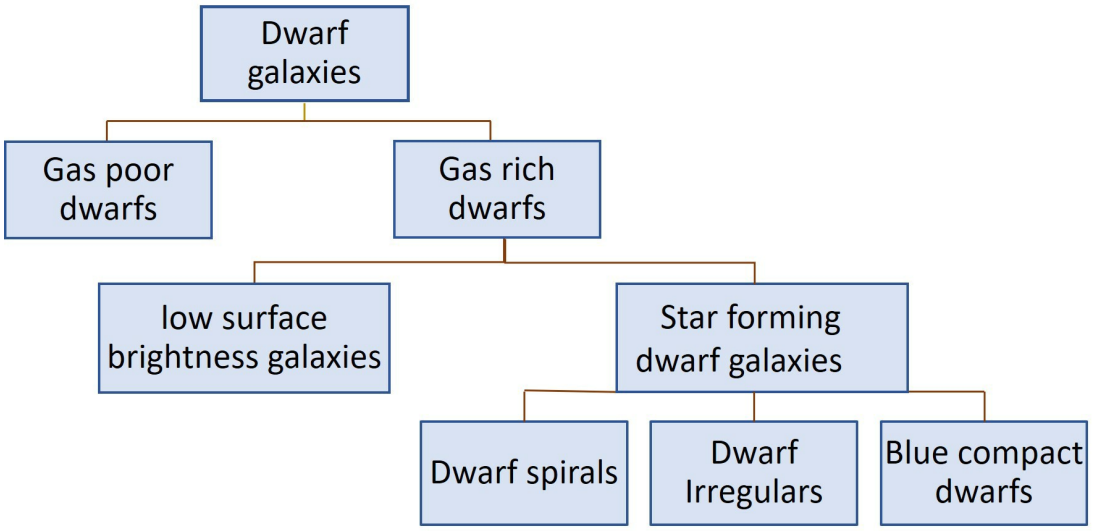


FIGURE 1.4: Classification of dwarf galaxies based on the presence of gas and SF.

2007; McGaugh et al. 2017).

Although dwarfs present extreme environments for SF, about 70% of them are star-forming (Karachentsev et al. 2004) and are called star-forming dwarf galaxies (SFDGs). Their small sizes, slow rotational velocities, and hence low shear, as well as overall low metallicities, result in SF being very distinct from that observed in regular disk galaxies (Bergvall 2011). Feedback and the environment of SFDGs also contribute to the differences (Meurer et al. 1995). The properties of SFDGs are studied and discussed in the Chapter 6.

Ultra faint Dwarf Galaxies

The ultra-faint dwarf galaxies (UFDGs) are faintest in the galaxy luminosity function ($L < 10^5$ $L_\odot$). These galaxies are dark matter-dominated, extremely metal-poor, and perhaps the least chemically evolved stellar systems in our local universe (Simon 2019). They provide a laboratory for understanding the formation of the first galaxies and can be used to constrain the nature of dark matter. UFDGs have

the smallest dark matter halos, with the mass concentrated at the center of the halo. UFDGs are systems with the absolute magnitudes fainter than $M_v = -7.7$ (Bullock & Boylan-Kolchin 2017). UFDGs were first discovered in 2005 (Willman et al. 2005, 2011). Subsequently, using wide-field image surveys, astronomers confirmed about 30 UFDGs and found 40 more as candidates.

Dark matter-dominated systems, such as UFDGs, can provide insights into the core-cusp problem (see, for example, Bullock & Boylan-Kolchin (2017)). Dark matter-only simulations predict a cusp profile at its center (Navarro et al. 1996). However, observations indicate that dwarf galaxies have a core profile with constant density (Brooks & Zolotov 2014; Di Cintio et al. 2014). This discrepancy may result from supernova feedback or can be attributed to self-interacting dark matter, with or without baryonic feedback (Fitts et al. 2017). UFDGs are expected to have a cusp profile if the former explanation is valid, as they generally lack sufficient stars to produce effective feedback (Peñarrubia et al. 2014).

Due to their low luminosity, most of the UFDGs detected are MW satellite galaxies. A few UFDGs are discovered around the nearby massive galaxies. LSB dwarfs can be identified by their diffuse light in the Local Volume; however, it will be challenging to perform stellar population analysis. It is seen that SF in massive dwarf galaxies is generally shut off due to environmental effects (Geha 2012). However, some recently accreted UFDGs have also stopped forming stars long ago (Fritz, T. K. et al. 2018; Simon 2018). In addition to these, reionisation is also suggested as a reason for shutting down the SF in such extremely low-mass systems (Brown et al. 2014; Fitts et al. 2017; Rodriguez Wimberly et al. 2018), indicating that UFDGs need not be formed only closer to massive galaxies. We discuss more on SF in one of the MW UFDGs, Leo-T, in our thesis chapter 7.

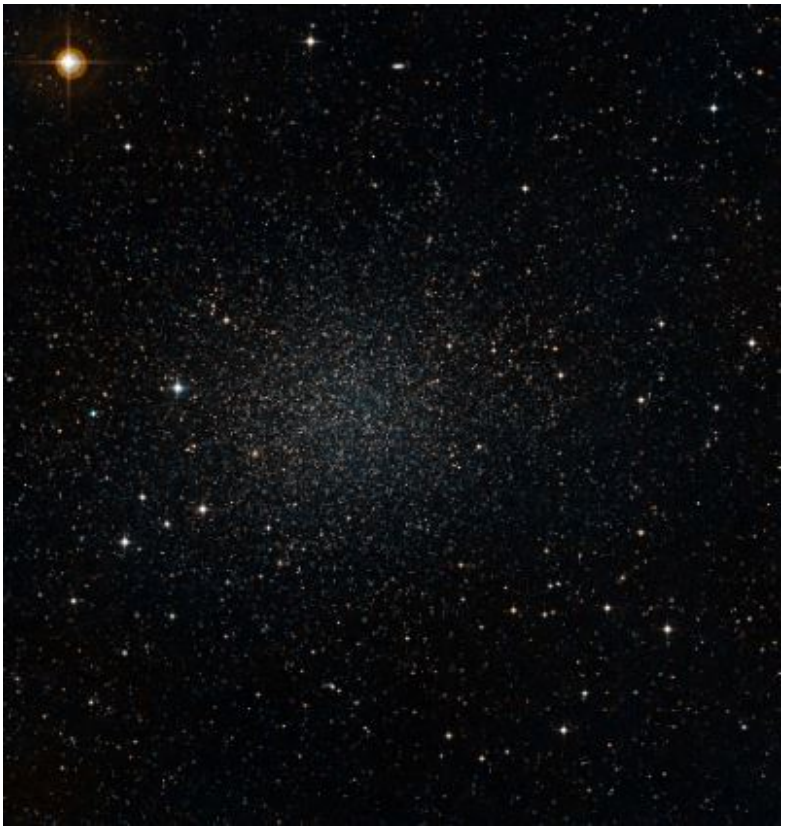


FIGURE 1.5: Sculptor Dwarf Galaxy. Credit: NASA, ESA/Hubble, DSS2.

1.1.4 Galaxy and ISM Composition

Baryons in galaxies determine how galaxies appear. In the early stages of galaxy formation, most of the baryonic mass was in the ISM gas. As galaxies evolved, this gas transformed into stars, while some may have been expelled as galactic winds or stripped by the ram pressure of the intergalactic medium. Gas can also flow into the ISM from the intergalactic medium, adding to its mass. This flow of baryons, especially in the MW, is shown in Figure 1.6.

The ISM is made up of approximately 99% gas and 1% dust by mass, with the gas dominated by hydrogen (about 75%) in atomic, ionized, and molecular forms (Draine 2011). Interstellar dust grains are small ($< 1\,\mu$m), but play a crucial role in extinction, scattering, and regulating the thermal balance of the ISM. However, highly energetic charged particles in galaxies known as cosmic rays influence the

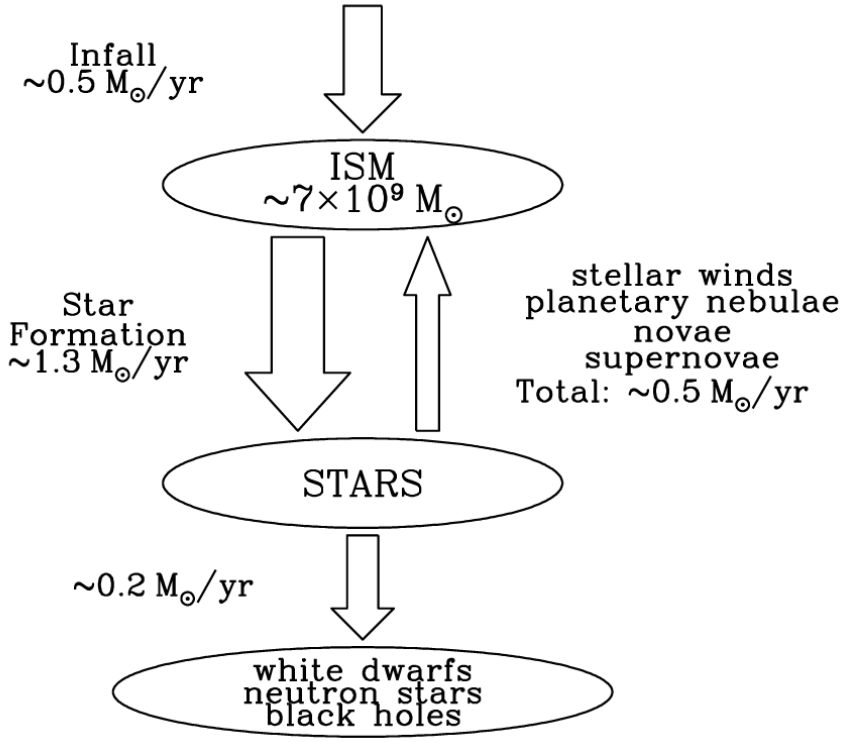


FIGURE 1.6: Baryonic cycle in MW from Draine (2011).

heating, ionization, and magnetic coupling of the ISM (Ferrière 2001; Draine 2011). The ISM is a multiphase system and consists of several components that are in approximate pressure equilibrium.

The hot ionized medium (HIM), or coronal gas, is produced by supernova heating and exhibits temperatures above $10^{5.5}$ K and densities of $\sim 0.004\,\mathrm{cm}^{-3}$. The coronal gas needs a Myr to cool down. **H II regions**, created by ultraviolet (UV) radiation from massive O-type stars, contain ionized hydrogen with characteristic temperatures of 10^4 K and densities between 0.3 and $10^4\,\mathrm{cm}^{-3}$. **warm ionized medium** or **WIM** are low-density photoionized regions that contain more total mass than the high-density regions. **Neutral atomic hydrogen** exists in both the **warm neutral medium (WNM),** with temperatures around 5×10^3 K and densities of $\sim 0.6\,\mathrm{cm}^{-3}$, and the **cool neutral medium (CNM)**, which is colder ($\sim$ 100 K) and denser ($\sim 30\,\mathrm{cm}^{-3}$). **Molecular gas** forms in

regions with sufficient shielding from UV radiation, beginning as **diffuse molecular gas** at densities of $\sim 100\,\mathrm{cm}^{-3}$, and transitioning into **dense molecular gas** within gravitationally bound molecular clouds and giant molecular clouds (GMCs), which have densities of 10^3–$10^6\,\mathrm{cm}^{-3}$ and temperatures of 10–50 K. These GMCs dominate the cold ISM and act as the primary sites for SF.

The interplay of these phases, along with stellar feedback, cosmic rays, and magnetic fields, regulates SF and governs the cycling of matter and energy within galaxies, making the ISM a key driver of galactic evolution (Ferrière 2001; Kennicutt & Evans 2012).

1.1.5 Multiwavelength view of Galaxies

To understand the different components of a galaxy and the ISM, it is essential to use multiwavelength observations. As illustrated in Figure 1.7, each region of the electromagnetic spectrum traces a distinct physical component, allowing us to build a comprehensive picture of galactic structure, SF, and energetic processes.

Neutral atomic hydrogen (H I) is traced by the 21- cm hyperfine transition, revealing the large-scale distribution of cold and warm diffuse gas (Walter et al. 2008). Radio continuum emission originates from both thermal free-free radiation from ionized gas and non-thermal synchrotron emission produced by cosmic-ray electrons accelerated in supernova remnants; it also highlights compact nuclear sources such as active galactic nuclei (AGN) (Condon 1992). Molecular gas is the raw material for star formation, and its distribution and physical properties regulate where and how efficiently stars form within galaxies (Bigiel et al. 2008; Leroy et al. 2009). It is typically traced using CO rotational transitions (e.g., CO: $\mathrm{J} = 1 \rightarrow 0$), which serve as proxies for cold, dense H_2 clouds.

At mid-IR (MIR) and far-IR (MIR) wavelengths, dust grains re-radiate absorbed starlight, providing direct insight into dust mass, temperature, and obscured SF (Draine 2003; Calzetti et al. 2007). NIR emission is dominated by old, low-mass stellar populations, which contribute significantly to the total stellar mass and trace the underlying stellar structure of galaxies (Jarrett et al. 2003). Optical wavelengths trace intermediate-age stars and nebular emission lines (e.g., Hα), which reveal warm ionized gas associated with ongoing SF (Kennicutt & Evans 2012).

UV emission arises from short-lived, massive O and B-type stars, making it a sensitive tracer of unobscured and very recent SF on timescales of $\sim$ 10 to 200 Myr (Gil de Paz et al. 2007; Salim et al. 2007). At higher energies, X-ray observations probe hot gas heated by supernova feedback, stellar winds, and AGN activity (Fabbiano 1989). Gamma rays are produced by the most energetic processes in the universe, including gamma-ray bursts, relativistic jets from AGN, pulsars, and interactions of cosmic rays with the ISM (Ackermann et al. 2012).

Because the Earth's atmosphere is transparent only to specific wavelength ranges, many of these observations require specialized facilities. Radio and optical/NIR wavelengths can be observed from the ground, whereas MIR, FIR, UV, X-ray, and gamma-ray emissions require space-based observatories. Each wavelength provides complementary information and, together, they enable a complete multiphase view of galactic evolution and the physical processes governing the ISM.

1.2 Star formation

Stars are the basic units of visible matter; Hence, they trace the structure of the universe, as well as its contents. The formation of stars is one of the crucial

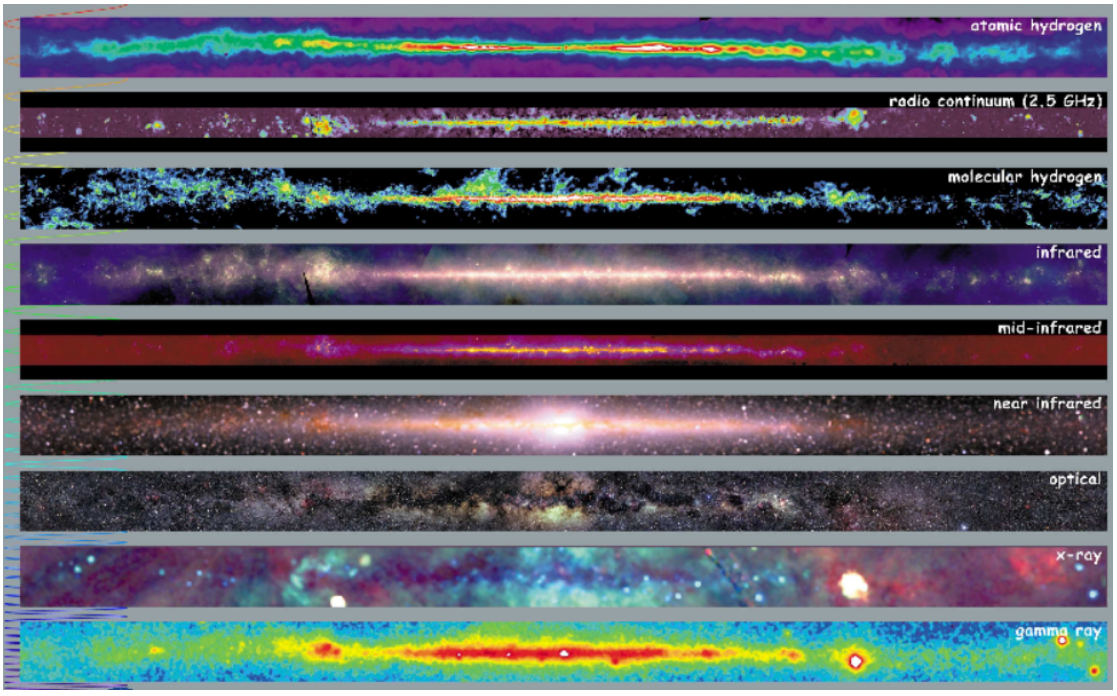


FIGURE 1.7: Multiwavelength View of MW. Credit: NASA.

questions of astrophysics.

SF occurs due to the interplay between gravity and opposing forces across various scales, with different mechanisms becoming significant at each level. This concept is thoroughly explained in the work of Larson (2003).

At the scale of each prestellar cloud core, thermal pressure is necessary for resisting gravitational collapse. This establishes a minimum mass required for a cloud to collapse and form stars. Once a cloud core begins to collapse, the centrifugal force generated by its angular momentum can potentially halt its contraction and lead to the formation of multiple star systems. In the final stages of star formation, magnetic fields become crucial as they mediate gas accretion and assist in launching bipolar jets from newly formed stars. On the intermediate scale of GMCs, turbulence and magnetic fields predominantly counteract gravity. On a larger galactic scale, ISM collapses under the influence of gravity, forming star-forming clouds that are resisted by the tidal forces of galaxies. SF can occur in

regions where the gas surface density is sufficient for its own gravity to overcome these tidal forces, such as in the spiral arms of galaxies.

Turbulance and Magnetic field

The internal motion in molecular clouds can be supersonic and subsonic in diffuse gas, causing them to be highly turbulent. Supersonic turbulent motions inject kinetic pressure that can counteract gravity and prevent the immediate collapse of GMCs. But turbulence can also trigger the collapse by generating density fluctuations (shocks, filaments, clumps), which can make high-density regions gravitationally unstable (Mac Low & Klessen 2004). In this way, turbulence simultaneously supports clouds globally and initiates collapse locally. The sources of turbulence include gravitationally driven large-scale motions, and, at the smaller scales, stellar feedback and supernova explosions are the sources. Different star-forming regions indeed exhibit varying levels of turbulence (Larson 1981). At the same time, Magnetic fields are dynamically significant in the ISM. Magnetic pressures oppose gravitational collapse (McKee & Ostriker 2007; Pattle et al. 2022). They channel gas flows along field lines, making collapse anisotropic and leading to filamentary structures aligned with the magnetic fields. They also regulate angular momentum from the collapsing core. Thus, both turbulence and magnetic fields play important roles in the formation and evolution of molecular clouds and, hence, SF.

Gravitational instability

A small density fluctuation in a uniform medium is amplified by gravity through a mechanism known as 'gravitational instability'. This is where the SF starts. Jeans

(1902, 1929) investigated how plane density perturbations behave in an infinite, uniform medium that possesses finite pressure. However, he did not consider the rotation, magnetic fields, or turbulence. He demonstrated that short-wavelength perturbations are dominated by pressure propagating as sound waves. Perturbations with wavelengths longer than a specific threshold, known as the 'Jeans length' (λ_J), are dominated by gravity. These longer-wavelength perturbations do not propagate; instead, they grow exponentially over time. The minimum mass for gravitationally unstable density fluctuations is the 'Jeans mass' (M_J). This criterion is Jeans' instability criterion.

$$\lambda_J = \pi^{1/2} c (G\rho)^{-1/2} \tag{1.1}$$

$$M_J = \frac{5.57 c^3}{G^{3/2} \rho^{1/2}} \tag{1.2}$$

In reality, galaxies rotate differentially, which leads to the shearing of any overdensity in the disk. In this context, both thermal pressure and rotation work together to prevent clouds from collapsing. To address this, the Toomre criteria were introduced (Toomre 1964). The Toomre Q parameter measures the stability of a differentially rotating disk. The condition $Q < 1$ indicates instability. This instability refers to the tendency of regions with higher density to form SF.

$$Q = \frac{c_s k}{\pi G \Sigma} \tag{1.3}$$

The condition $Q > 1$ is known as Toomre's stability criterion, which accounts for a disk's rotation and its self-gravity. In the context of molecular clouds, a value greater than 1 indicates no SF, implying a stable disk.

Spontaneous and triggered star formation

SF in molecular clouds can occur through both spontaneous and triggered processes (Shu et al. 1987). **Spontaneous SF** takes place when internal conditions within a molecular cloud naturally lead to gravitational collapse by exceeding either Jeans or Toomre criteria without any external perturbation. This mode of SF reflects the intrinsic evolution of molecular clouds and generally produces filamentary or distributed star-forming structures.

In contrast, **triggered SF** is initiated by an external agent that compresses or destabilizes the cloud, pushing it past the threshold for gravitational collapse. Typical triggers include shock waves from supernova explosions, expanding H II regions around massive stars, strong stellar winds, cloud-cloud collisions, and spiral density waves in galactic disks. These mechanisms enhance local gas densities, promote sequential or propagating SF, and can produce characteristic age gradients across star-forming complexes.

In many environments, both spontaneous and triggered mechanisms may operate together, with internal turbulence creating density fluctuations, while external feedback further compresses the gas, thereby accelerating the onset of SF.

1.3 Initial Mass Function

Stars in galaxies are generally found in star clusters and stellar associations (Scalo 1986a). The masses of the stars formed in a cluster vary over a wide range and depend on several factors, such as the environment, metallicity, and density of the parent molecular cloud. This distribution of stellar masses formed during the star-formation event in a given volume is called the initial mass function (IMF)

(Kroupa 2002). The IMF is a crucial ingredient for the stellar evolution models of star-forming galaxies (e.g., Leitherer et al. (1999); Maraston (2005)) and is thus essential for understanding SF as well as galaxy formation and evolution (Bastian et al. 2010).

Over the past few decades, many studies have tried to understand the IMF using resolved populations of stellar clusters in the solar neighbourhood, within the MW, and in nearby galaxies lying in the Local Group (Weisz et al. 2015; Wainer et al. 2024). The IMF is commonly described by a power-law, $dN/dm = Am^{-\alpha}$, where A is a constant, and dN/dm represents the number of stars formed in a mass range dm, and the index α =2.35 (Salpeter 1955). More recently, the canonical stellar IMF has been derived from observations of field stars and nearby star-forming regions of sizes approximately equal to one parsec and has an index value close to α=2.3 for stars with $M_* > 0.5\ M_\odot$ (Jeřábková et al. 2018). In general α is observed to be shallower for low mass stars ($M_* < 0.5\ M_\odot$) (Kroupa 2001; Chabrier 2003). Determining the uniformity of the IMF for all stellar populations involves combining IMF estimates for different resolved populations. However, the estimation of IMF in different mass ranges has its own challenges (Kroupa 2002).

Several studies have tried to understand the universality of the IMF (e.g., Hoversten & Glazebrook 2008; Meurer et al. 2009; Dib 2014). Recent studies have shown that the IMF is non-universal and depends on environmental and statistical effects (Pflamm-Altenburg & Kroupa 2008; Krumholz 2014; Tanvir et al. 2022). The denser starburst galaxies have a top-heavy IMF, i.e., a large number of massive stars and hence an IMF that is flatter than the canonical IMF. In comparison, the less dense, LSB galaxies show a bottom-heavy IMF (i.e., steeper than the canonical IMF) (Scalo 1990; Weidner et al. 2011; Meurer et al. 2009). Even within galaxies, there are regions with low stellar surface mass densities, such as the outer disks of extended UV (XUV) galaxies or the inter-arm regions of spiral galaxies, where the IMF can be different compared to that of the spiral arms (Thilker et al. 2007;

Kroupa et al. 2024).

1.4 Star formation in nearby galaxies

The structure of galaxies is highly dependent upon the conditions under which stars form and the rate of SF. The evolution of galaxies, in turn, depends on the IMF. Faint low-mass stars evolve slowly, while massive stars burn quickly and release significant amounts of matter and energy, which can heat and ionize the ISM, enriching it with heavy elements (Larson 2003).

SF in nearby galaxies helps us understand processes that convert gas into stars across diverse galactic environments. Here we have the advantage of spatially resolving star-forming regions in these galaxies on scales of sub-kiloparsecs or even parsecs. They are ideal laboratories for studying the interplay between gas dynamics, feedback, metallicity, and galactic structure. Multiwavelength observations from the far-UV (FUV) to the radio, with state-of-the-art facilities such as the Hubble Space Telescope (HST), JWST, and ALMA, have advanced our understanding of how the ISM cycles through phases and fuels SF in the local Universe.

As explained in previous sections, SF is associated with cold molecular gas, which is traced by CO emission or dust continuum. High-resolution surveys such as HERACLES and PHANGS-ALMA, JWST reveal that the molecular ISM in nearby galaxies is highly structured, consisting of filaments, clumps, and gravitationally bound clouds with properties that vary with environment (Sun et al. 2018; Leroy et al. 2021).

It is seen that the ISM and SF in galaxies exhibit a hierarchical structure. Turbulence, gravity, and feedback together create a fractal-like distribution of structures, from large-scale atomic gas flows and GMCs to smaller clumps, dense cores, and ultimately, individual star-forming systems (Elmegreen & Falgarone 1996; Grasha et al. 2017). Understanding this hierarchical organization is essential for linking galaxy-scale processes such as spiral structure, disk instability, and gas accretion to the small-scale physics that governs the formation of stars and stellar clusters (Menon et al. 2021).

Star Formation Laws and Scaling Relations

Schmidt (1959) first proposed that the SFR scales with gas density ($\Sigma_{\rm gas}$) as a power law. Building on this, Kennicutt (1998) established the empirical Kennicutt-Schmidt law for disk galaxies and starbursts:

$$\Sigma_{\rm SFR} \propto \Sigma_{\rm gas}^{1.4}. \tag{1.4}$$

Modern spatially resolved studies indicate that SF is more strongly correlated with molecular gas than with total gas. Observations by Bigiel et al. (2008) and Leroy et al. (2008) demonstrate that the star formation efficiency (SFE) and gas depletion times are relatively constant for the normal spiral galaxies, but vary significantly with environment, pressure, and metallicity. Dwarf galaxies have low molecular fractions and bursty SF due to inefficient H_2 formation in their low-metallicity ISM.

There is also an established relationship between stellar mass and SFR observed in star-forming galaxies across cosmic time. This is referred to as the star-forming main sequence (SFMS) (Brinchmann et al. 2004). Galaxies on the SFMS form stars in a steady and regulated manner, with a slope that evolves with redshift

(Speagle et al. 2014). This scaling relation suggests that most star-forming galaxies grow through self-regulated processes in which gas accretion, feedback, and internal dynamics maintain a balance between fuel supply and SFE. Galaxies that lie significantly above the main sequence are typically undergoing starbursts, often triggered by mergers or compaction events. At the same time, those below it experience quenching due to environmental effects, AGN feedback, or declining gas fractions. The SFMS, therefore, provides a fundamental framework for understanding galaxy growth and its stage of evolution.

Feedback and the Regulation of Star Formation

Massive stars inject large amounts of energy and momentum into their surroundings through stellar winds, ionizing radiation, and supernova explosions (Maeder & Conti 1994). This stellar feedback disrupts GMCs, drives turbulence, and can create large ionized bubbles and superbubbles observable in nearby galaxies (Watkins et al. 2023). Feedback regulates SF by reducing cloud lifetimes and preventing unchecked gravitational collapse. Multiwavelength studies, especially using Hα, FUV, and infrared emission, reveal evidence for expanding H II regions and hot gas in galactic disks. In some cases, positive feedback can trigger new SF by compressing surrounding gas, such as in the collect-and-collapse scenario or during cloud-cloud collisions (Mayya et al. 2023).

Environmental Dependence

SF in nearby galaxies varies strongly with galactic environment. Spiral arms organize gas into dense ridges through density-wave compression, enhancing cloud formation and subsequent SF (Elmegreen 2011). Bars can efficiently funnel gas

into the central kiloparsec regions, often leading to nuclear starbursts. We also detect SF at the bar ends, where usually stellar orbits collide (Díaz-García et al. 2020). In contrast, the outer disks of galaxies (e.g., XUV disks) and low-mass dwarf galaxies typically show low SFEs and display a more stochastic SF distributed in localized regions. Dynamical factors such as shear, tidal forces, and mid-plane pressure in the disks play a significant role in shaping cloud stability and collapse in dwarf galaxies(Elmegreen 2015).

Resolved Star Formation Histories

Nearby galaxies also allow us to create their star formation histories (SFHs) using resolved stellar populations. Colour-magnitude diagrams (CMDs) from high-resolution data enable the measurement of SFHs over Gyr timescales. These studies show that SF in dwarf galaxies is highly episodic, while massive spirals form stars more steadily (Weisz et al. 2014). This approach links present-day SF to long-term evolutionary pathways.

1.5 Star formation rate tracers

Recent SF can be traced across a wide range of wavelengths. Most commonly used tracers are UV and Hα regions, each sensitive to different stages of stars and physical conditions in the ISM. **UV continuum** emission directly comes from young, massive O and B stars, making it a tracer of recent ($\lesssim$ 100 Myr) SF. However, hydrogen recombination lines such as **H**α trace ionizing photon production from the most massive and short-lived stars ($\lesssim$ 10 Myr), providing a nearly instantaneous measure of SF activity (Calzetti 2013). Both of these tracers should be corrected for extinction. In the **IR**, dust absorbs UV/optical light from young

stars and re-emits it thermally; thus, MIR and FIR emission serve as robust tracers of embedded SF, especially in dusty star-forming regions and starburst galaxies (Kennicutt 1998). There are also **polyaromatic hydrocarbons (PAHs)** that vibrationally excite upon the absorption of UV and high-energy visible photons and emit at discrete wavelengths in IR, indirectly tracing SF (Peeters et al. 2004). **Radio continuum emission**, arising from synchrotron radiation of cosmic-ray electrons, is accelerated in denser cores of supernova remnants. This emission trace SF on longer timescales (∼100 Myr) and is unaffected by dust, making it a powerful tracer in highly obscured systems (Condon 1992). Combined multi-wavelength indicators provide the most reliable measurements by capturing both obscured and unobscured SF across diverse galactic environments.

1.6 Motivation and goals of the thesis

As mentioned earlier, understanding SF is very important for understanding galaxy evolution. The environments within galaxies can vary over different parts of galaxies, such as spiral arms, interarm regions, spurs, and extended disk regions (Kreckel et al. 2016; Yadav et al. 2021). Additionally, variations also exist among different types of galaxies, including massive galaxies, dwarf galaxies, ultra-faint dwarfs, interacting galaxies, and accreting galaxies (Melena et al. 2009; Vaz, Daniel et al. 2023; Yadav et al. 2023). This variation in star-forming environment within a galaxy primarily affects the local SF properties of the galaxy. However, variation among different galaxy types can help us understand both local and global variations in SF properties.

Multiwavelength studies have tried to understand the SF process both locally and globally. Hα and UV emission are most commonly used tracers of SF in galaxies. The UV emission can trace recent SF for a longer time than the Hα emission. The

Hα emission also depends on the availability of gas around the stars to undergo recombination (Hunter et al. 2010). Whereas UV emission comes directly from the star. Hence, a thorough UV study of galaxies, along with multiwavelength observations, is crucial for observational studies of SF.

The Galaxy Evolution Explorer (GALEX) and HST have greatly enhanced our understanding of nearby galaxies. In particular, GALEX's UV images of star-forming galaxies have made a remarkable contribution over the past decade (Gil de Paz et al. 2007; Thilker et al. 2007). Although GALEX has good sensitivity, it offers spatial resolution of 4.5″ to 5.3″, which is very poor compared to the resolution of complementary existing optical, IR, and even submillimeter telescopes. HST, on the other hand, has an excellent resolution which has helped to identify stars in nearby galaxies (McQuinn et al. 2010; Weisz et al. 2014). There are HST UV surveys, such as the HST Legacy ExtraGalactic UV Survey (LEGUS, Calzetti et al. (2015)), that have studied resolved SF in nearly 50 nearby galaxies. However, HST has a very narrow field of view (FOV), which can cover only a small part of a galaxy. Hence, Ultraviolet Imaging Telescope (UVIT) provides a very good alternative to these two with better resolution 1.2-1.5″ and FOV (28′) to understand the SF in nearby galaxies on sub-kiloparsec scales.

The main goals of our thesis are:
(i) Understanding the SF process at the smaller scale ($<$ 100 pc).
(ii) Understanding SF in different galactic environments within a galaxy.
(ii) Understanding SF among different types of galaxies, such as dwarfs, low luminosity metal-poor galaxies, and massive galaxies (such as NGC628).

1.7 Overview of the thesis

- **Chapter 1:** In this chapter, we introduce the galaxies, their formation theories, morphological types, and also their compositions. We then explain the SF, SF in the galaxies, including environmental effects. We present important SF relationships, and discuss the recent SF tracers. The aim and motivation of the thesis are also outlined.

- **Chapter 2:** In this chapter, we discuss the multiwavelength datasets used in our studies. This chapter also provides details of the common research methodologies employed for data analysis.

- **Chapter 3:** This chapter presents the pilot study, which aims to assess the universality of high-mass IMF across different star-forming environments within the galaxy NGC 628 and its variation with the star-forming properties of star-forming complexes (SFCs). We used UV and Hα data from UVIT and the Multi-Unit Spectroscopic Explorer (MUSE) instrument. By extracting SFCs and comparing UV and Hα luminosities, we estimated the high-mass IMF values.

- **Chapter 4:** Here, we discuss the PAH correlation with UV and Hα emission in the different regions of NGC 628 and also obtain the PAH trend with the IMF we estimated in our previous study. We even explored bubble regions (mainly the Phantom void), which are more evident in JWST imaging, to understand the distinct stellar populations within and around them.

- **Chapter 5:** In this chapter, we explore ordinal patterns, permutation entropy, statistical complexity, and ordinal network node entropy to understand the structures in the galaxy NGC 628 with high-resolution, multiwavelength data suitable for two-dimensional analysis. We assess its morphological complexity across these wavelengths using near-ultraviolet (NUV), NIR, MIR, and millimeter (mm) images.

- **Chapter 6:** In this chapter, we investigated recent SF in 16 nearby SFDGs and compare properties in different morphological types (Dwarf spirals, Dwarf irregulars, and Blue Compact Dwarfs (BCDs)) at the global and at the scale of SFCs.

- **Chapter 7:** This chapter is dedicated to understanding the UV populations of the UFDG galaxy Leo T (409 kpc), one of the faintest known gas-rich satellites of the MW. We extract SFCs from UVIT data and compare them to those from the HST and MUSE star catalogs.

- **Chapter 8:** We summarize the key findings as the conclusions of the thesis and outline the potential directions for future research.

Chapter 2

Data and Methodologies

Observing galaxies at various wavelengths provides unique insights into their properties. Hence, multiwavelength observations of galaxies are essential for understanding their nature. In this chapter, we describe the details of these observations, the resulting data products, and the procedures used to analyze the information obtained at different wavelengths.

2.1 Ultraviolet

2.1.1 UltraViolet Imaging Telescope (UVIT)

The UVIT is one of the instruments aboard AstroSat, a multiwavelength space observatory developed by the Indian Space Research Organisation (ISRO). This instrument has twin telescopes equipped with co-aligned Ritchey-Chrétien (RC)

optics. One telescope operates in the FUV range (1300–1800 Å), while the other covers the NUV (2000–3000 Å) and visible (VIS) bands. UVIT can simultaneously observe across all three bands with a FOV of 28′.

During observations, the instrument can experience slight drifts in its pointing for a few seconds. We use the VIS channel or the NUV imager to correct for these drifts. The FUV and NUV telescopes operate in photon-counting mode, whereas the VIS channel functions in integrated mode. The complementary metal-oxide-semiconductor (CMOS) imagers have 512 x 512 pixels, with each pixel mapped to 8 x 8 subpixels in the final image, resulting in a plate scale of 0.416″ per subpixel. The FUV and NUV telescopes have resolutions $\leq 1.5''$, which is three times better than the GALEX (Martin et al. 2005).

Additionally, the FUV and NUV telescopes have filter wheels that allow for the selection of multiple narrow-band photometric filters (Tandon et al. 2020). However, since 2018, the UVIT NUV filter has been non-operational due to issues related to the payload, resulting in limited availability of NUV images for certain galaxies.

We downloaded Level 1 data from the Indian Space Science Data Centre (ISSDC) website*. This data consists of photon count centroids that must be stacked to form an image. Before doing so, the centroids require corrections for drift, as well as other instrumental and calibration adjustments, to produce science-ready images.

By knowing the precise timing of the FUV/NUV detector clocks in relation to the VIS detector clock and the spacecraft clock, we can do the required drift correction. Subsequently, specialized software is used to perform drift tracking and shift-and-stack operations. In addition to these corrections, flat-fielding and

*https://astrobrowse.issdc.gov.in/astro_archive/archive/Home.jsp

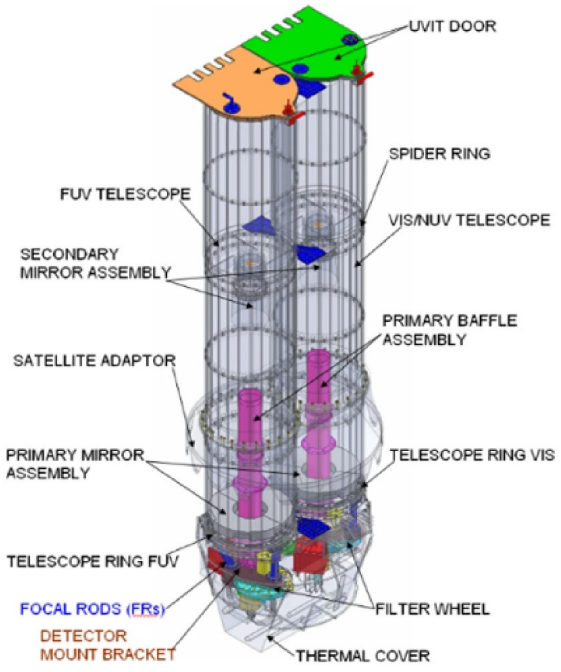


FIGURE 2.1: Schematic representation of the UVIT instrument from Kathiravan et al. (2021).

distortion mitigation are also performed. We utilised CCDLAB (Postma & Leahy 2017, 2021), the graphical user interface to reduce the raw UVIT data.

After processing the data, we combined the orbit-wise UVIT images to create a final composite image. We used the same interface to perform astrometry and conducted background subtraction on these images with the Image Reduction and Analysis Facility (IRAF; Tody 1993). This process involved measuring the counts in several regions surrounding the galaxy and then subtracting the mean of these counts from the scientific image. To determine the resolution of the UV images, we analyzed the mean point spread function (PSF) using approximately 5 to 6 stars in the FUV and NUV image fields.

2.1.2 Galaxy Evolution Explorer (GALEX)

We utilized archival GALEX data obtained from the Mikulski Archive for the Space Telescopes (MAST) portal [†]. GALEX is a National Aeronautics and Space Administration (NASA) Small Explorer mission that conducts an all-sky UV survey in the FUV band (134.4–178.6 nm) and the NUV band (177.1–283.1 nm) (Martin et al. 2005). It offers a resolution of 4–6″ and features an effective area of 50cm^2. The instrument has a wide FOV measuring 1.2° and is sensitive to an apparent magnitude of $m_{AB} = 21$ in the All-Sky Imaging Survey (AIS). In the Deep Imaging Survey (DIS), its sensitivity extends to $m_{AB} = 25$. Several survey programs conducted with GALEX together cover about two-thirds of the sky.

The primary data consist of the lists of photon positions on the detector and their corresponding arrival times. This is because the detector operates in photon-counting mode. These data are corrected for satellite motion and other detector-related effects. Following this, they are flat-fielded and background-subtracted using a ground-based pipeline to create science-ready images (Morrissey et al. 2007).

2.2 Optical

2.2.1 Multi-Unit Spectroscopic Explorer (MUSE)

MUSE is a second-generation instrument on the Very Large Telescope (VLT) of the European Southern Observatory (ESO) (Bacon et al. 2010). It is an integral-field spectrograph (IFS) operating in the visible wavelength range. MUSE features

[†] https://mast.stsci.edu/portal/Mashup/Clients/Mast/Portal.html

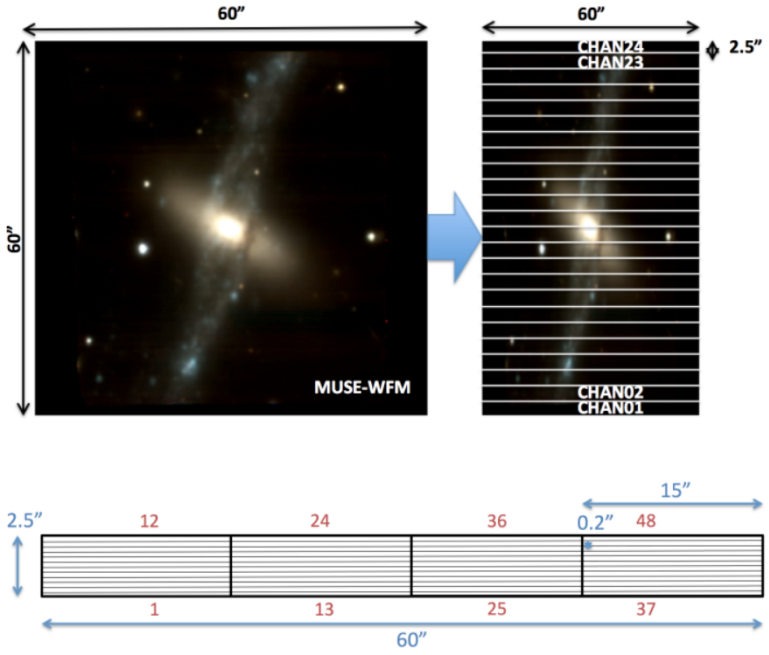


FIGURE 2.2: Splitting and slicing of the MUSE FOV (Credit: ESO).

a Wide Field Mode (WFM) with a FOV covering $1' \times 1'$ and a Narrow Field Mode (NFM) with a FOV of $7.5 \times 7.5''$. MUSE has a spatial resolution of 0.3–0.4 $''$ in WFM, with each pixel covering $0.2''$ of sky. As shown in Figure 2.2, MUSE splits the FOV into 24 channels, which are each split further into 48 slices or "mini slits", resulting in a total of 1,152 mini slits. Each set of 48 mini slits is directed into a spectrograph, which functions as a disperser. Hence, it has a spectral range from 465 nm to 930 nm. The resolving power is $\sim$ 1800 at 465 nm and $\sim$ 3600 at 930 nm. We used publicly available data for our analysis.

2.2.2 Hubble Space Telescope (HST)

HST is a 2.4 m space-based observatory, providing high-angular-resolution imaging over wavelengths ranging from UV to NIR. Owing to its diffraction-limited optics, HST achieves an angular resolution of $\sim 0.05''$ in the optical, with a typical imaging FWHM of $\sim 0.07''$, depending on the instrument and wavelength. Currently, HST

has five main instruments, including the Advanced Camera for Surveys (ACS; Sirianni et al. 2005) and the Wide Field Camera 3 (WFC3; Kimble et al. 2008), which are widely used for high-resolution imaging of resolved stellar populations and galactic structures.

For this work, we used the HST/WFPC2 stellar photometric catalogue of Leo T observed in the F606W (wide V) and F814W (I) filters. The catalogue provides the positions and calibrated F606W and F814W magnitudes of resolved stars and was obtained from Weisz et al. (2009).

2.3 Infrared

2.3.1 James Webb Space Telescope (JWST)

We used archival science-ready imaging data from JWST for our work. JWST provides three imaging modes: broadband imaging in the Mid-IR instrument (MIRI; Argyriou, Ioannis et al. (2023)), Near-IR Camera (NIRCam; Rieke et al. (2023)) imaging, and Near-Infrared Imager and Slitless Spectrograph (NIRISS). We use MIRI and NIRCam observations. MIRI imaging observes in nine filters from 5.6 (resolution $\sim$ 0.2 $''$) to 25.5 μm (resolution $\sim$ 0.8 $''$). It has a FOV of 74$''$x113$''$, with a pixel scale of 0.11$''$. NIRcam imaging observes 0.6–2.3 μm (0.031 $''$/pix) and 2.4–5.0 μm (0.063 $''$/pix) simultaneously over a 9.7 arcmin^2 FOV. The spatial resolution is around 2 pixels. Apart from the imaging modes discussed, JWST has other instruments, as shown in Figure 2.3.

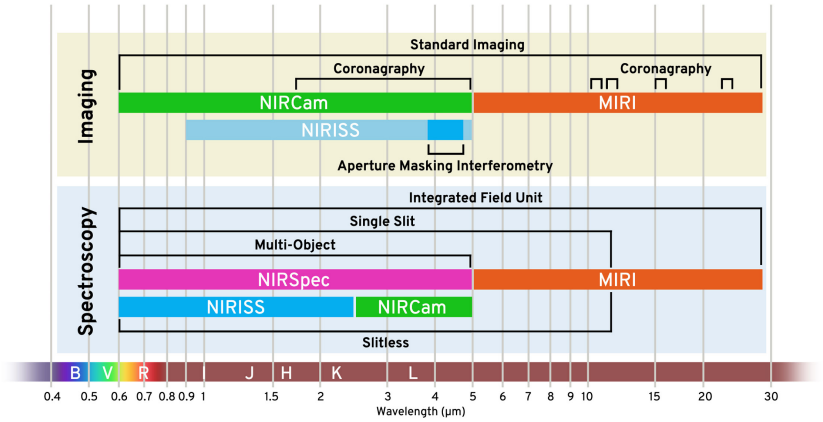


FIGURE 2.3: Observing Modes with JWST (Credit: STSci).

2.3.2 Spitzer Space Telescope

We used archival broadband imaging data from the Spitzer Space Telescope, which has three primary instruments: the Infrared Array Camera (IRAC; Fazio et al. (2004)), the Infrared Spectrograph (IRS), and the Multiband Imaging Photometer for Spitzer (MIPS; Rieke et al. (2004)). IRAC has four broadband filters: IRAC 1, 2, 3, and 4, which operate at wavelengths 3.6, 4.5, 5.8, and 8.0 μm, respectively. Meanwhile, MIPS detects signals in the FIR at the wavelengths 24, 70, and 160 μm. For our analysis, we utilized IRAC 1 and MIPS-24 μm observations. IRAC 1 has $5.2 \times 5.2'$ FOV, with $1.22''$ pixel size, and $2''$ spatial resolution. MIPS-24 has a spatial resolution of $6''$. The pipeline-processed archival images were retrieved from the Spitzer Heritage Archive[‡].

[‡] https://irsa.ipac.caltech.edu/Missions/spitzer.html

2.4 Millimetre

2.4.1 Atacama Large Millimeter/submillimeter Array

We used archival ALMA 12CO(2-1) mapped over a large array. ALMA is an interferometer consisting of an array of 12-m antennas, with baselines extending up to 16 km (Wootten & Thompson 2009). It also has an additional compact array of 7-m and 12-m antennas to enhance the ability to image extended targets. With compact 12-m array configurations resolutions range from 0.5″ at 950 GHz to 4.3″ at 110 GHz. It is around 1.3″ at 230 GHz, which is also the frequency for the CO(2-1) transition.

2.5 Research methodologies

For our study, we employed various techniques and models to analyze the data. The following subsections provide a detailed explanation of these standard techniques and models.

2.5.1 Source Extraction

The closest galaxy in our study is located at a distance of 400 kpc. Using the UVIT, we were able to resolve SFCs only when they were larger than 2 pc. To extract these SFCs, we utilized Source Extractor (SExtractor, Bertin & Arnouts (1996)), a widely-used command-line Program that performs multiple tasks, including background estimation, source detection, deblending, and aperture photometry.

SExtractor estimates the background and identifies which pixels belong to the background versus those that belong to objects. It then segregates the non-background area into distinct objects and determines the properties of each, compiling the results into a catalog. We set the detection threshold to a few times the global background noise (σ), ensuring that pixels with values exceeding this threshold are classified as objects. If two peaks in the light distribution are sufficiently distinct, SExtractor separates them into different entries in the catalog.

Input parameters include the deblending threshold and deblending ratio, which allow for the identification of detected objects as separate sources. Additionally, we specify a minimum area requirement for source detection.

Given that our galaxies are extended, we conducted background subtraction using IRAF (Tody 1993). The process involves measuring the counts in several regions around the galaxy and subtracting the average of these counts from the scientific image. Following this subtraction, we estimated σ from the image. We adjust detection threshold and minimum area parameters to ensure clean and confident detection, varying according to different observations, the extent of the galaxy, and the spatial resolution of the observed data.

For the UVIT images, we typically adopt a minimum area of 10 pixels (for 1.2 $''$) and a detection threshold of 3–8 σ, depending on the strength and spatial distribution of the galaxy emission. The default value of 32 is used for the deblending threshold, while the deblending contrast parameter is varied based on source crowding to minimise overlap between neighbouring detections.

SExtractor fits an ellipse around each source, providing us with the position, position angle, and size parameters of the SFCs. For photometry, we utilize Photutils, which will be discussed in the next section.

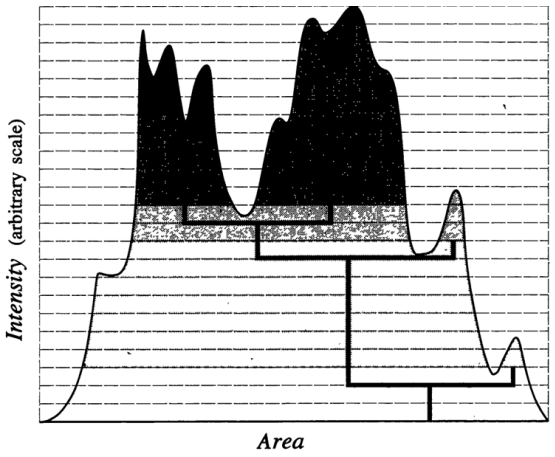


FIGURE 2.4: A schematic diagram of the method used to deblend a source in SExtractor from Bertin & Arnouts (1996).

2.5.2 Photutils

Photutils is an Astropy package for Photometry (Bradley et al. 2022). This tool provides background estimation, star finding, source detection and extraction, aperture photometry, PSF photometry, image segmentation, centroids, radial profiles, and elliptical isophote fitting. We mainly use this tool for aperture photometry. We provide input parameters, such as position, position angle, and size, derived from SExtractor. As an output, we extract the aperture sum, which is the sum of the values within the aperture. We use this parameter (total flux or counts) for our further analysis.

2.5.3 Starburst99 Stellar Populations Model

We utilised the Starburst99, a spectrophotometric Simple Stellar Populations (SSP) model, to estimate the age and mass of the extracted SFCs in actively star-forming galaxies (Leitherer et al. 1999). This model provides a synthetic stellar spectrum for star clusters of various ages, covering a wavelength range from 91 Å to 160 μm. The critical parameters that can be adjusted to generate the desired

model spectrum are the SF law, total cluster mass, IMF, mass boundaries for the IMF, metallicity, and the type of stellar evolutionary tracks, such as Padova and Geneva.

We use the Starburst99 SSP models to estimate the masses of the SFCs. Since the galaxies in our sample exhibit recent star formation, we adopt an instantaneous burst star formation history. Model spectra are generated for a grid of SFC masses ranging from 10^3 to 10^8 $M_\odot$, assuming solar metallicity (Z = 0.020) for the inner disks of massive galaxies and a Kroupa initial mass function (Kroupa 2001) with stellar mass limits of 0.1–100 $M_\odot$. The model spectra are then convolved with the UVIT filter transmission curves to obtain synthetic FUV and NUV magnitudes and colours. The observed extinction-corrected FUV magnitudes and FUV−NUV colours of the SFCs are compared with the resulting model predictions on the CMD. Since the models are computed only for discrete masses, interpolation between adjacent model grid points is performed to estimate the mass corresponding to the observed colour and magnitude of each SFC. Similar model grids are generated for different metallicities while keeping the SFC mass range unchanged.

2.5.4 Other Theoretical Models

We used the ATLAS9 stellar atmosphere model Castelli & Kurucz (2004) to obtain the synthetic spectrum of a specific type of star. This atlas comprises approximately 4,300 stellar atmosphere models that span a wide range of metallicities, effective temperatures, and gravities. These local thermal equilibrium models do not incorporate convective overshooting and have enhanced opacities and abundances. The ATLAS9 models cover metal abundances [M/H] ranging from −2.5 to +0.5, with increments of 0.5. The gravity range extends from log g = 0.0 to +5.0, also in steps of 0.5. Additionally, the effective temperature range stretches from 3,500 K to 50,000 K, and the model spectra cover the UV (1000 Å) to IR

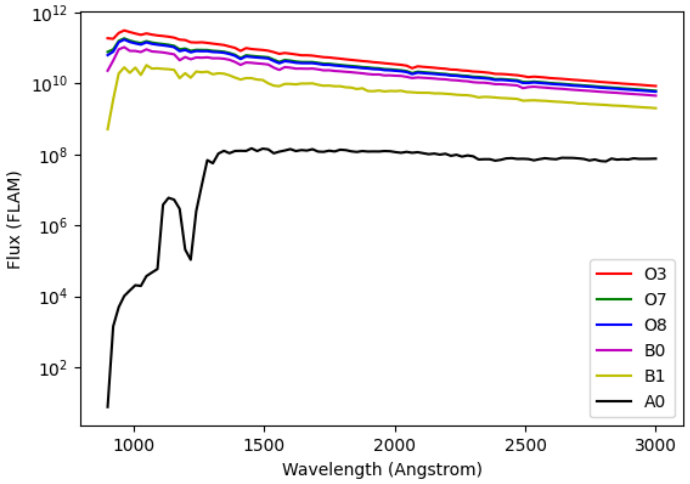


FIGURE 2.5: Synthetic spectrum of massive star generated using ATLAS9 stellar atmosphere model Castelli & Kurucz (2004).

(10 μm). However, the temperature and spectral range have an uneven grid and non-uniform wavelength spacing.

For the work presented in Chapter 3, we selected the ATLAS9 model spectra with the closest effective temperature ($T_{\rm eff}$) and surface gravity ($\log g$) corresponding to representative O, B0, and B1 stars. The selected spectra were convolved with the UVIT filter transmission curves to obtain synthetic FUV and NUV luminosities for each stellar type. These synthetic luminosities served as templates to estimate the numbers of O, B0, and B1 stars within each SFC from the observed UV luminosities (see Section 3.3.4). The resulting stellar populations were subsequently used to derive the high-mass end slope of the stellar IMF.

Chapter 3

Study of the high-mass Stellar Initial Mass Function in star forming complexes of NGC 628

3.1 Introduction

Massive stars significantly impact the chemical enrichment of the ISM due to their strong stellar winds and feedback process (Chappell & Scalo 2001; Freyer et al. 2003). Hence, it is essential to understand the upper or high-mass end of the IMF, even though the low-mass stars contribute more to cluster masses, as well as the overall mass of a galaxy. Young massive stars emit most of their energy at FUV wavelengths and have a short main sequence. However, it is difficult to distinguish between the two main types of massive stars (O and B, $M_* > 20M_\odot$) based on just magnitude alone (Kroupa 2002). Even with UV colors, it is challenging to

distinguish massive B stars from O stars (Koda et al. 2012). Massive O-type stars give out FUV, NUV, and Hα emission. The Hα emission from O and massive B stars is a well-known tracer of SF in galaxies (Kennicutt et al. 2009; Lee et al. 2009). But Hα can trace SF for only 10 Myr, since O star lifetimes vary from 1 to 10 Myr. However, UV traces O, B, and even some red and cold stars, which makes them trace SF for around 200 Myr (Thilker et al. 2005). Therefore, recent studies have used both UV and Hα measurements to understand the universality of the high-mass end of the IMF by considering the relative strength of their emission in external galaxies (Meurer et al. 2009; Lee et al. 2009; Koda et al. 2012).

Previous studies have used GALEX data to show that there is a correlation between the SFR and the Hα to UV flux ratios in galaxies (Meurer et al. 2009; Lee et al. 2009; Hunter et al. 2010). They also show that the galaxies with low SFRs have a deficit of O stars and hence have a bottom-heavy IMF due to stochastic sampling. Boselli et al. (2009) used Hα to UV ratios to show that the high-mass end of late-type normal galaxies follows the standard IMF. Calzetti et al. (2010) showed that a universal IMF exists by comparing the Hα flux with the cluster mass. Some studies have investigated the high end of the IMF in the outskirts of XUV galaxies and find that the bottom-heavy IMF dominates (Gogarten et al. 2009; Bruzzese et al. 2019). In contrast, some studies show that it follows the standard IMF (Koda et al. 2012). A few studies analyzed the IMF in XUV disks by assuming that the Hα to UV flux ratios are approximately equal to the ratios between the lifetime of the stars that can produce Hα to those that produce UV emission (i.e., mainly O and B types stars) (Zaritsky & Christlein 2007). Bruzzese et al. (2019) have used HST measurements and compared them with the simulations to obtain the high-mass end of the IMF.

This paper presents a new method to determine the slope α of the high-mass end of the IMF using observations of individual SFCs. We leverage the high sensitivity and spatial resolution of UVIT and MUSE to extract the SFCs of a nearby galaxy

to determine the ratio of O and B stars to derive α. We investigate whether α varies with regions, i.e., spiral arms, spurs, and interarm regions, since the mechanisms leading to SF in these regions are different. Spiral arms are global disk instabilities, whereas SF in the spurs or feathers is due to local gas instabilities, where diffuse gas is transformed into dense gas when it flows into the spiral arm. The inflow shocks the gas near the arm and causes SF in these spur regions (Kim & Ostriker 2002; Shetty & Ostriker 2006). The interarm regions have isolated SFCs, and the star-forming mechanism may be more local. Many studies have attempted to understand SF in both the spiral arm and interarm regions, but our analysis focuses on the IMF (Stedman & Knapen 2001; Foyle et al. 2010; Eden et al. 2013). Studying the IMF over different regions of a galaxy will also help us understand the universality of the IMF within a galaxy.

3.2 NGC 628 and Observations

NGC 628, also known as M74 or the Phantom Galaxy, is a grand design spiral galaxy of Hubble type SA(s)c (de Vaucouleurs et al. 1991), and is at a distance of 9.84 Mpc (Anand et al. 2020). This massive galaxy ($\log(M_*/M_\odot)$=10.34; Leroy et al. (2019)) is nearly face-on (i=8.9°; Lang et al. (2020)) with a position angle of 20.7°(Lang et al. 2020). Hence, it is the perfect target for studying SF properties in different regions of a galaxy. The SF in NGC 628 is well studied (Kreckel et al. 2016, 2018; Lomaeva et al. 2022) and the SFCs on kpc scales have also been characterized (Yadav et al. 2021; Ujjwal et al. 2022). We used archival, deep UV imaging observations obtained using the UVIT on board the AstroSat telescope (Kumar et al. 2012) to understand IMF. The UVIT observed NGC 628 in multiple filters, but we used the CaF2 F148W FUV image with an exposure time of 1810 s and a bandwidth of 500 Å, and the NUVB4 N263M image, which has an exposure time of 2086 s and a bandwidth of 275 Å, for our analysis. We also used two close

filters, F172M (bandwidth and exposure time are 125 Å and 5881 s respectively) and N219M (bandwidth and exposure time are 270 Å and 1365 s respectively), to correct internal extinction using the Beta slope as described in Section 3.3.2.

We obtained archival MUSE (Emsellem, Eric et al. 2022) Hα and Hβ maps, archival ALMA (Leroy et al. 2021a,b) CO(J=2 - 1) moment 0 map, and also the JWST (Lee et al. 2023) F2100W map, from the Physics at High Angular Resolution in Nearby GalaxieS (PHANGS Treasury Program*). The specifications of instruments are discussed in Chapter 2.

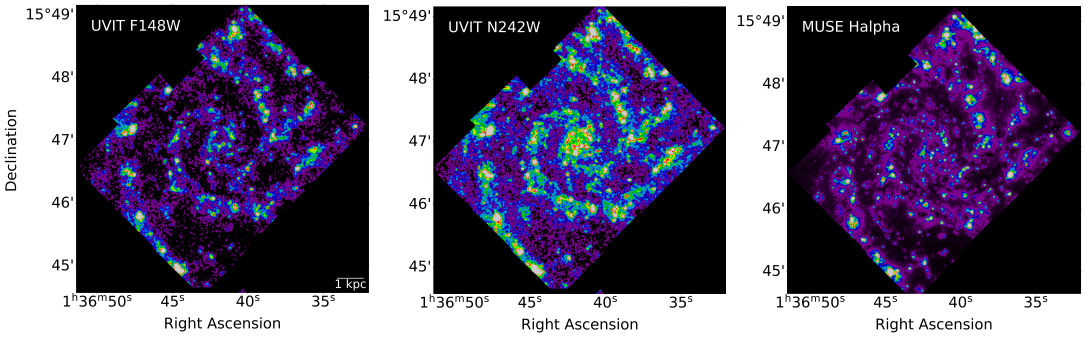


FIGURE 3.1: UVIT FUV, NUV, and MUSE Hα images of galaxy NGC 628 tracing recent SF.

3.3 Data Analysis

3.3.1 Source extraction and classification

We reduced the raw UVIT data using the CCDLAB graphical user interface (Postma & Leahy 2017). We then did the astrometry using the same interface. We did background subtraction of these images using IRAF as outlined in Chapter 2. Using around 5-6 stars in the FUV and NUV image fields, we found that the mean PSF of the field stars is around 1.2″. Hence, this is assumed to be the resolution

*https://sites.google.com/view/phangs/home

of the UV images. This resolution corresponds to a physical scale of 57 pc at the distance of NGC 628, which is moderately high resolution and cannot resolve star clusters, because clusters have radii of a few parsec (Ryon et al. 2015). However, we can resolve OB associations and SFCs with this resolution, because they correspond to a scale of a few hundred parsec (Elmegreen et al. 2014; Amrutha et al. 2024).

Since we are interested in comparing the Hα and UV emission, we made cutouts of the UVIT FUV and NUV images that match the size of the MUSE Hα map. The cutout images of the FUV, NUV, and Hα maps are shown in Figure 3.1. We convolved the Hα map to the UV resolution of 1.2″. We extracted SFCs in all three images using the command line program SExtractor (Bertin & Arnouts 1996). We set the detection threshold to five times the estimated global background noise for confident detection. Then, we masked the foreground sources (with high parallax and high proper motion) by comparing the extracted SFCs with the bright sources in the Gaia catalog using TOPCAT (Taylor 2005). We also convolved the Hβ and JWST map to the UVIT resolution.

We determined the total counts from the extracted SFCs using the Photutils module (Astropy Collaboration et al. 2018). The UV fluxes were derived using the conversion relation $Flux = UC \times CPS_{corr}$ as mentioned in Tandon et al. (2017), where UC is unit conversion factor in ergs^{-1}cm^{-2} Å^{-1} and CPS_{corr} is the counts per second corrected for MW extinction (Schlafly & Finkbeiner 2011) for the FUV and NUV filters (Bayo et al. 2008). We determined the UV and Hα luminosities in $ergs^{-1}$ units using the distance of the galaxy and the bandwidth of the UV filters.

We matched the UV and Hα images and found the SFCs that are present in all three filters. We also determined the SFCs that are detected only in the FUV and Hα filters, the SFCs detected only in the NUV and Hα filters, and finally, the SFCs detected in only the FUV and NUV filters. We also found the SFCs that

are visible only in FUV, only in NUV, and also only in Hα. This classification was necessary because we needed emissions from all three bands to estimate the IMF value.

We noted the SExtractor parameters of the SFCs with larger areas present in at least two filters. We also classified them as arm, interarm, and spur SFCs based on location. This classification helps us understand the universality of the IMF within the galaxy. Hence, we first classified the SFCs as arms and interarm sources based on their location in the NUV image (see Figure 3.2a). Then, we again checked which SFCs lie in and around the spur regions of the ALMA observations (Figure 3.2b).

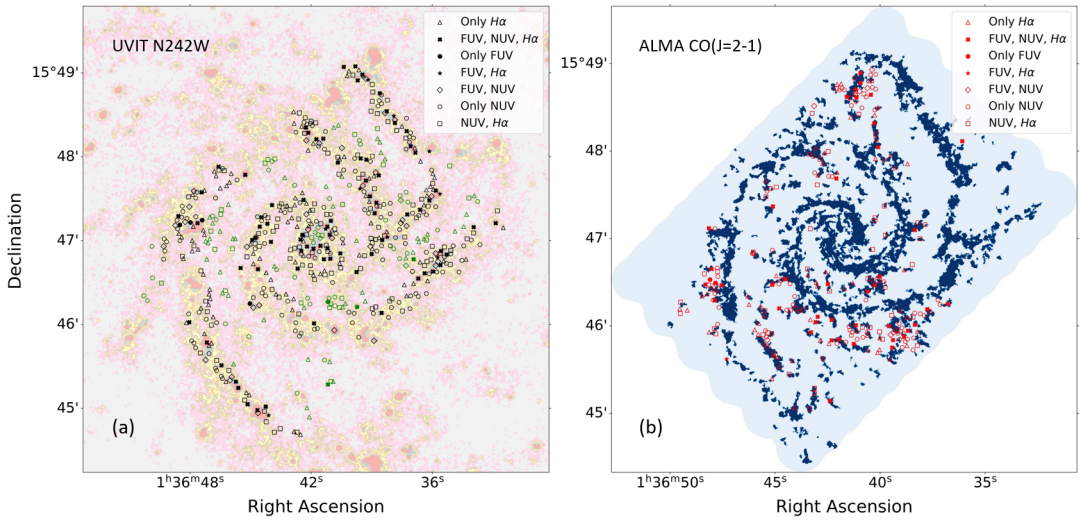


FIGURE 3.2: The above images show the classification of SFCs based on their region(different colors) and their emission in different filters (different markers). Image (a): The locations of the arm (black markers) and interarm (green markers) SFCs overplotted on the UVIT NUV image. Image (b): The locations of spurs(red markers) SFCs overplotted on the ALMA CO(J=2-1) image.

3.3.2 Internal extinction correction

An accurate extinction correction of observed Hα and UV luminosities is crucial for IMF analysis. Since there are different methods to correct the galaxy's internal

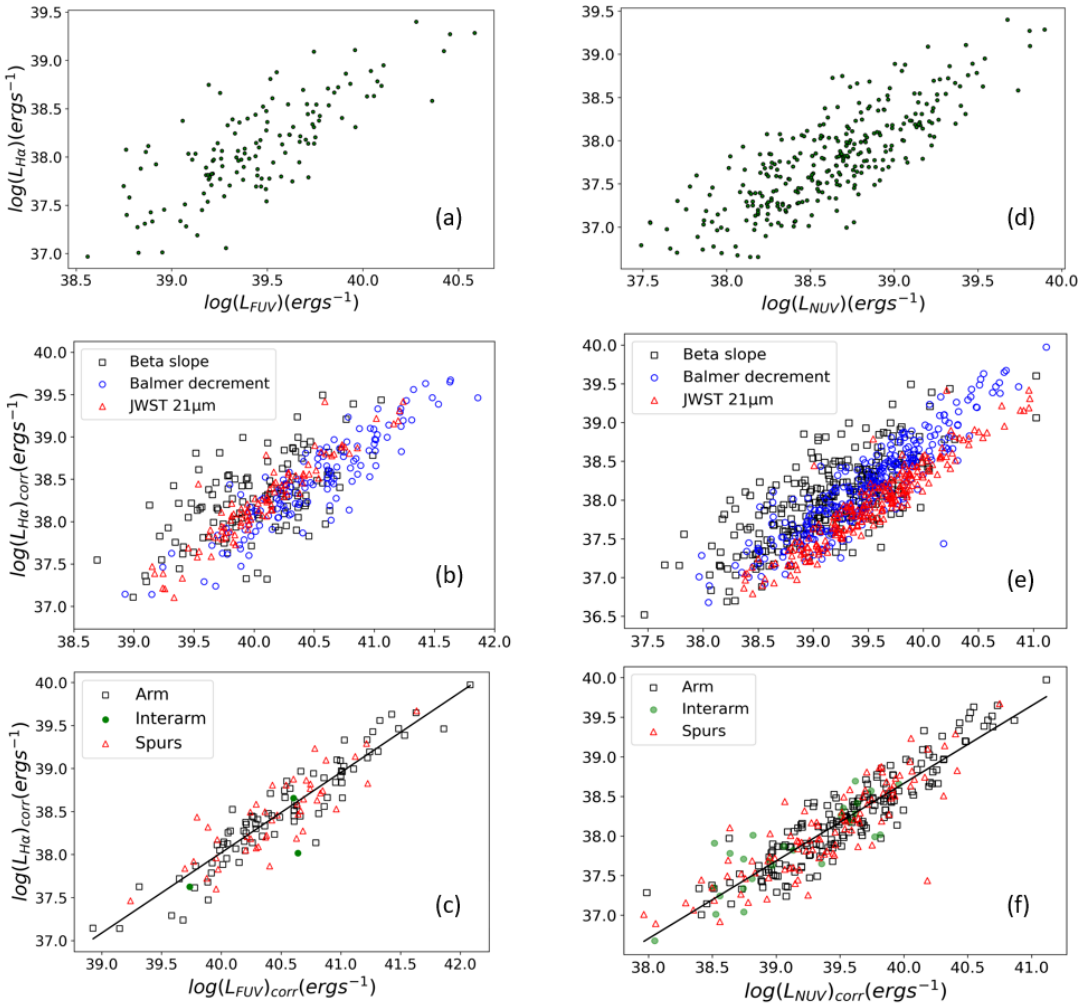


FIGURE 3.3: Figures on the left (a, b, and c) and on the right (d, e, and f) illustrate the correlation of Hα luminosity with FUV and NUV luminosities, respectively, for the SFCs. Figures a and d: Luminosities presented without any correction for internal dust attenuation. Figures b and e: Luminosities are corrected for internal dust attenuation using different methods indicated with different symbols and colors. Figures c and f: Luminosities corrected for internal dust attenuation using the Balmer decrement method for the SFCs with Hα emission, and the scaling relation is used to find the FUV extinction coefficient. The fitted relations related to these plots are given in Section 3.4.2.

extinction, we corrected SFC luminosities for internal extinction using the Balmer decrement, Beta slope, and JWST 21 μm methods to see which method gives a better correlation for Hα and UV luminosities. We used Hα and Hβ maps of MUSE to find the Balmer decrement, which is one of the most successful techniques for determining dust extinction. It uses the ratio of two nebular Balmer emission lines such as Hα and Hβ at low redshifts (Kennicutt 1992; Moustakas et al. 2006; Garn &

Best 2010). The intrinsic ratio of the two lines remains roughly constant for typical gas conditions in star-forming galaxies and $(\frac{H\alpha}{H\beta})_{int} = 2.86$, at the temperature 10^4 K and an electron density $n_e = 10^2 \mathrm{cm}^{-3}$ for Case B recombination (Osterbrock 1989). Hence, the corresponding color excess E(B − V) is given by,

$$\mathrm{E(B-V)} = 1.97 \log_{10} \left[\frac{(\frac{H\alpha}{H\beta})_{obs}}{2.86} \right] \tag{3.1}$$

and using the Calzetti et al. (2000) reddening curve, we find the $H\alpha$ extinction to be, $\mathrm{A_{H\alpha}} = (3.33 \pm 0.80) \times \mathrm{E(B-V)}$.

For the SFCs with FUV and Hα emission, we found FUV extinction using the relation, $\mathrm{A_{FUV}} = 3.6\mathrm{A_{H\alpha}}$, assuming that the FUV emission arises mainly from the young stellar population as mentioned in Leroy et al. (2008), and we corrected for the extinction in NUV band using the relation $\mathrm{A_{NUV}} = 0.8\mathrm{A_{FUV}}$ (Calzetti et al. 2000). The extinction-corrected Hα and UV luminosity is given by

$$\mathrm{L}(\lambda)_{\mathrm{corr}} = 10^{0.4\mathrm{A}_\lambda} \mathrm{L}(\lambda)_{\mathrm{obs}} \tag{3.2}$$

where $\mathrm{L}(\lambda)_{\mathrm{obs}}$ is observed luminosity at the wavelength λ. The correlation of extinction-corrected Hα and UV luminosity for SFCs using the Balmer decrement method is shown in Figure 3.3c and 3.3f.

The Beta slope method can be used for the SFCs with FUV and NUV emission to correct the internal extinction (Calzetti et al. 1994). The extinction curve in the UV band (1300-2600 Å) can be fitted by a power law with the slope β ($f_\lambda \propto \lambda^\beta$). The UV spectral slope is filter-dependent, and we can get a better estimate for β when we consider the two close filters. Hence, β for UVIT filters m_{F172M} and

m_{N219M} is given by,

$$\beta = \frac{m_{F172M} - m_{N219M}}{-2.5log(\frac{\lambda_{F172M}}{\lambda_{N219M}})} - 2 \tag{3.3}$$

where m_{F172M} and m_{N219M} are the Galactic extinction-corrected magnitudes of SFCs in the F172M and N219M filters with λ_{F172M} and λ_{N219M} as their central wavelengths respectively. Then, we used filters F148W and N263M and found the SFC's extinction $A_\lambda = (0.44 \pm 0.03)E(B-V)k(\lambda)$ as given by Calzetti et al. (2000). The color excess E(B-V) is then found using $\beta = -2.616 + 4.594E(B-V)$ as given by Reddy et al. (2018) and $k(\lambda)$ as given in Calzetti et al. (2000) for filters F148W and N263M, and for SFCs with Hα emission. We again calculated extinction-corrected Hα and UV luminosities for this method using equation 3.2.

Apart from the two methods mentioned above, we use 24 μm to measure the embedded Hα and UV luminosities, as mid-IR peaks around 24 μm and trace the hot dust component that is due to the young stellar population. Also, Jang, In Sung et al. (2020) showed that the F2100W filter of JWST is better for extinction correction than any of the other mid-IR bands in JWST. Hence, here we corrected for extinction using a convolved JWST 21μm map. We used the extinction correction relation for Hα as given in Kennicutt et al. (2009) and for FUV and NUV as in Hao et al. (2011). The relation for finding the extinction-corrected luminosity is $L(\lambda)_{corr} = L(\lambda)_{obs} + cL(24\mu m)$. Here $L(\lambda)_{corr}$ and $L(\lambda)_{obs}$ are the corrected luminosity and observed luminosity in ergs^{-1} respectively. The parameter c is 3.89, 2.26, and 0.0024 when we correct the FUV, NUV, and Hα luminosities, respectively. L(24μm) is the Spitzer MIPS 24 μm luminosity in ergs^{-1}. Since we are using the JWST 21 μm map, we took the ratio of JWST 21 μm and MIPS 24 μm luminosity for some of the SFCs on both maps. We find that the ratio is approximately equal to 4.54. We multiplied this value by L(21μm) to obtain the L(24μm).

We plotted the extinction-corrected Hα and UV luminosity correlation for all three methods in Figure 3.3b and 3.3e. The extinction-corrected luminosities strongly

correlate for SFCs corrected with the Balmer decrement and JWST methods. However, we see the clear difference between the three methods in Figure 3.3, which reveals that each method uniquely compensates for extinction at varying depths. Hence, it is necessary to use a single method to correct extinction. The SFC luminosities corrected with the Beta slope method show more scatter ($\sigma_{\rm FUV}$=0.38 and $\sigma_{\rm NUV}$=0.37), making it less preferable. Although the JWST 21 μm method showed a tight Hα and UV luminosity correlation ($\sigma_{\rm FUV}$=0.17 and $\sigma_{\rm NUV}$=0.17), due to its limited field of view, very few SFCs had 21 μm emission. Hence, we mainly used the Balmer decrement method ($\sigma_{\rm FUV}$=0.21 and $\sigma_{\rm NUV}$=0.25) for the extinction correction for SFCs with Hα luminosity; the SFCs without Hα luminosity were not used for further analysis, wherever Hα and UV luminosities are involved. However, we have shown the extinction-corrected Hα and UV luminosity correlation for the Balmer decrement method and also the SFR correlations for the Balmer decrement and JWST methods in Section 3.4.2.

3.3.3 Characterization of the SFCs

We calculated the FUV SFR for the SFCs using Salim et al. (2007). The FUV SFR in $M_{\odot}yr^{-1}$ is given by $SFR_{FUV} = 0.68 \times 10^{-28} \times L(FUV)_{corr}$. Similarly, we calculated the Hα SFR using $SFR_{H\alpha} = 5.3 \times 10^{-42} \times L(H\alpha)_{corr}$ (Calzetti et al. 2007) . Here $L(FUV)_{corr}$ and $L(H\alpha)_{corr}$ are the extinction-corrected luminosities in $ergs^{-1}$. As mentioned in Section 3.3.2, we only derived both FUV and Hα SFRs for SFCs with associated Hα luminosity. We calculated the SFR density Σ(SFR) by dividing the SFRs by their respective areas. $\Sigma_{\rm SFR}$ is used to characterise the local intensity of star formation within an SFC. Normalising the SFR by the physical area of the SFC enables a more meaningful comparison among star-forming regions of different physical sizes and across different galactic environments.

We also derived the corresponding stellar masses of the SFCs using Starburst99,

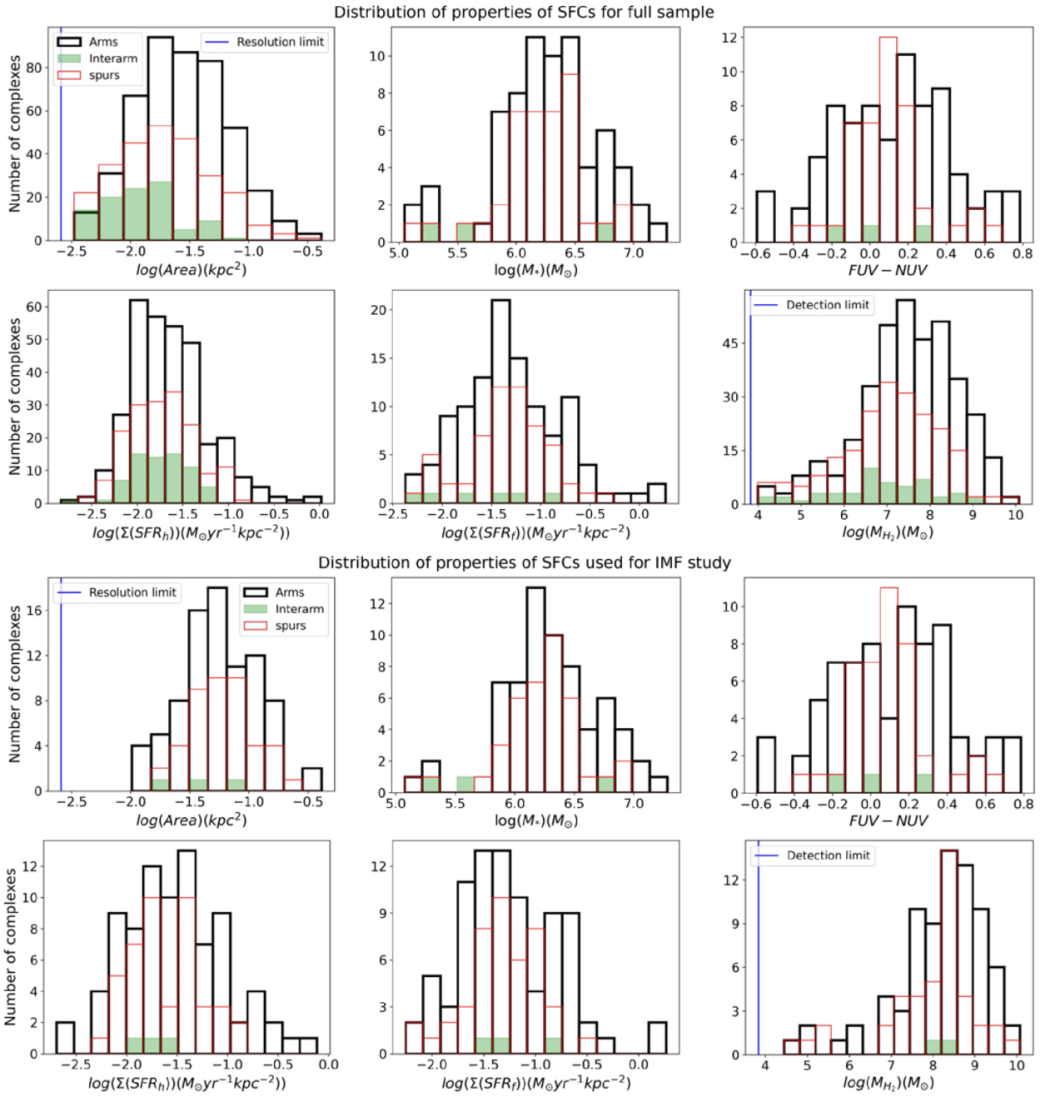


FIGURE 3.4: The distribution of SF properties across different regions (arms, spurs, and interarm) for all available SFCs (first two rows) and specifically for the SFCs used in the IMF analysis.

an SSP model (Leitherer et al. 1999). We ran starburst99 assuming Padova tracks with asymptotic giant branch stars and standard Salpeter IMF (Salpeter 1955) with the lower cutoff mass set to $m_l = 0.1M_\odot$ and the upper cutoff mass to be $m_u = 100M_\odot$. We adopted a solar metallicity (Z=0.02; Leitherer et al. (1999)), which is closer to the value mentioned in Calzetti et al. (2015). We evolved the model from 1 Myr to 200 Myr, as UV can trace up to 200 Myr. We plotted the observed extinction-corrected UV colour and FUV magnitudes of the SFCs on the theoretically predicted values from Starburst99. We then interpolated the values

for each SFC to find the mass.

We estimated the molecular hydrogen mass using the ALMA CO(J=2-1) map. We converted the CO flux to H_2 mass using the conversion factor α_{CO} =4.35$M_\odot$ $pc^{-2}(Kkms^{-1})^{-1}$ and $R_{21} = 0.62$ (Sandstrom et al. 2013; Kreckel et al. 2018).

We plotted the distribution of different properties of SFCs, like the area (from SExtractor), molecular hydrogen mass (M_{H_2}), extinction-corrected FUV and NUV color (FUV-NUV), stellar mass (M_*), and Σ(SFR) for both Hα and FUV emission for all the possible SFCs (For area and M_{H_2} distribution, we included even the SFCs which did not have emission in all three bands) and also for the SFCs used for IMF analysis as shown in the Figure 3.4. We also observed that the median estimated values of properties like (M_*) and area of SFCs are more than what we see in resolved studies of stellar clusters in NGC 628 with HST in LEGUS (Adamo et al. 2017), as SFCs contain multiple individual star-forming clusters and smaller OB associations.

3.3.4 The number of high-mass stars and their ratios in the SFCs

This section describes how we estimated the approximate number of O and B stars in the SFCs. It depends crucially on the difference in time scales over which Hα and UV emission trace SF. The Hα and FUV emission arises from O stars and massive B stars. But since Hα comes from recombination in the ionisation region around massive stars, it lasts for a few Myr. Even if we consider that there is a contribution from B stars in the Hα emission, we may not get the total count of massive B stars. Hence, for this study, we assume that the Hα emission arises mainly from O stars. The FUV emission arises from O ($M > 21M_\odot$), and also massive B0 stars ($M > 10M_\odot$). We also see that with a 5σ photometric limit of

FUV and NUV filters, we can only detect individual stars after O7 stars. But, since low-mass stars are more numerous, and studies have shown that NUV can significantly detect emission from even low-mass B stars (Das et al. 2021), we assume that the NUV emission arises from O, B0, and B1 stars ($M \leq 10 M_{\odot}$). All of this information can be used to estimate the number of O, B0, and B1 stars as described below.

As we do not know what kind of O stars produce the Hα emission from the SFCs, we randomly populate O stars in the SFCs by assigning a fraction of the Hα luminosity for each type of O star we are considering. Here, we present the three cases. (i) First, we consider that Hα arises from only O8V-type stars (31 $M_{\odot}$). (ii) Secondly, we consider that Hα comes from only O7V, O8V and O9V stars. We included these types of O stars because previous studies show that the median Hα luminosity of the SFCs in NGC 628 corresponds to the luminosity of a single O8V star (Kreckel et al. 2016). (iii) Apart from these two combinations, we tried a third case in which we populate the SFCs with a combination of O9V (23 $M_{\odot}$) to O3V stars (88 $M_{\odot}$). In this way, we include different combinations of O-type stars to estimate how the IMF varies. We used the Hα Lyman photon flux Q_H for each stellar type from Sternberg et al. (2003). We consider Case-B recombination with electron temperature 10^4 K (Gavazzi et al. 2002). The Hα luminosity in ergs^{-1} is given by $1.37 \times 10^{-12} Q_H[s^{-1}]$. The Castelli & Kurucz (2004) model was used to find the FUV and NUV luminosities for these stars. We chose the closest parameters, such as effective temperature (T_{eff}), surface gravity (g), and radius (R) from the grid of all types of O, B0, and B1 star models from Sternberg et al. (2003) and Leitherer et al. (2010), where the B1 stars parameter are from the second paper and the rest from the first paper. The parameters (T_{eff}, log(g), R), along with the UV luminosities for the solar metallicity, are given in Table 3.1.

Initially, the algorithm carried out 10,000 iterations for each SFC, drawing a random $H\alpha$ luminosity probability for each type of O star from a uniform distribution

between 0 and 1. For the third case, we ensured that there should be at least one of each type of O star in a SFC. Then, the total number of O stars present in a SFC for each of the three cases is,

$$\mathrm{N(O)} = \sum_{\mathrm{n=3}}^{9} \frac{\mathrm{P(On)} \times \mathrm{L_{H\alpha}}}{\mathrm{L_{H\alpha}(On)}} \tag{3.4}$$

where, $\mathrm{L_{H\alpha}}$ is the Hα luminosity of a SFC and $\mathrm{L_{H\alpha}(On)}$ is the Hα luminosity of single On star, where n is the class (e.g. n=3, O3 type star). P(On) is the randomly generated probability for an On-type star, such that $\sum_{\mathrm{n=3}}^{9} \mathrm{P(On)} = 1$. For the second case, we generated the P(On) only for the combination of O7, O8, and O9 stars. And for the first case, the P(O8)=1. The number of B0 stars in the SFC derived from the FUV luminosity is,

$$\mathrm{N(B0)} = \frac{\mathrm{L_{FUV}} - \sum_{\mathrm{n=3}}^{9}(\mathrm{N(On)} \times \mathrm{L_{FUV}(On)})}{\mathrm{L_{FUV}(B0)}} \tag{3.5}$$

where $\mathrm{L_{FUV}}$ and $\mathrm{L_{FUV}(On)}$ are the FUV luminosity of a SFC and a single On-type star, respectively. The $\mathrm{L_{FUV}(B0)}$ is the FUV luminosity of the B0 star, and N(On) is the number of On-type stars. The total number of O stars is $\mathrm{N(O)} = \sum_{\mathrm{n=3}}^{9} \mathrm{N(On)}$. The number of B1 stars (N(B1)) in a SFC will then be

$$\mathrm{N(B1)} = \frac{\mathrm{L_{NUV}} - (\mathrm{N(B0)} \times \mathrm{L_{NUV}(B0)}) - \sum_{\mathrm{n=3}}^{9}(\mathrm{N(On)} \times \mathrm{L_{NUV}(On)})}{\mathrm{L_{NUV}(B1)}} \tag{3.6}$$

where $\mathrm{L_{NUV}}$ and $\mathrm{L_{NUV}(On)}$ are the NUV luminosity of a SFC and single On stars, respectively. Also, $\mathrm{L_{NUV}(B0)}$ and $\mathrm{L_{NUV}(B1)}$ are the NUV luminosities of the B0 and B1 stars, respectively.

It should be noted that this method does not distinguish the O, B0, and B1-type populations based on their FUV/NUV luminosity ratios. Instead, we use the absolute FUV and NUV luminosities derived from the ATLAS9 models and sequentially account for the contribution of the previously estimated higher-mass stellar populations. B0 and B1 stars are adopted as representative populations of the massive and relatively lower-mass B stars contributing to the UV emission, respectively. Therefore, the derived numbers represent approximate estimates of these stellar populations rather than a unique spectral classification of individual stars.

Further, we took the ratio of N(O) to N(B0) ($\frac{\mathrm{N(O)}}{\mathrm{N(B0)}}$) and the ratio of N(B0) to N(B1) ($\frac{\mathrm{N(B0)}}{\mathrm{N(B1)}}$) to obtain the IMF indices α_1 and α_2 respectively. We assume that the IMF can be represented as a distribution function in linear mass units as,

$$\frac{\mathrm{dN}}{\mathrm{dm}} = \mathrm{Am}^{-\alpha} \tag{3.7}$$

where α is the power law index of the IMF. The number of stars N in the mass range m_u to m_l is

$$\mathrm{N} = \mathrm{A}\int_{\mathrm{m_l}}^{\mathrm{m_u}} \mathrm{m}^{-\alpha}\mathrm{dm} \tag{3.8}$$

and $\frac{N(O)}{N(B0)}$ is given by,

$$\frac{\mathrm{N(O)}}{\mathrm{N(B0)}} = \frac{\mathrm{m_u(O)}^{1-\alpha_1} - \mathrm{m_l(O)}^{1-\alpha_1}}{\mathrm{m_u(B0)}^{1-\alpha_1} - \mathrm{m_l(B0)}^{1-\alpha_1}} \tag{3.9}$$

where $\mathrm{m_u(O)}$ and $\mathrm{m_u(B0)}$ are the upper mass limit for O and B0 stars. Similarly, the lower mass limits for O and B0 stars are $\mathrm{m_l(O)}$, $\mathrm{m_l(B0)}$. $\mathrm{m_u}$ and $\mathrm{m_l}$ for the SFCs that are fully populated with O9 to O3 type stars is 21 $\mathrm{M_\odot}$ to 100 $\mathrm{M_\odot}$ respectively. And for B0 stars, it is 21 $\mathrm{M_\odot}$ and 10 $\mathrm{M_\odot}$. When we took O7, O8

TABLE 3.1: FUV and NUV luminosities of massive stars

OV star Type	T_{eff} (kK)	log(g) (cms^{-2})	L_{FUV} ($ergs^{-1}$)	L_{NUV} ($ergs^{-1}$)
O3	50	5	4.6×10^{38}	3.96×10^{37}
O4	47.5	5	$3.5\ \times10^{38}$	3.1×10^{37}
O5	45	4.5	2.75×10^{38}	2.48×10^{37}
O6	42.5	4.5	2.18×10^{38}	2×10^{37}
O7	40	4.5	1.67×10^{38}	1.65×10^{37}
O8	38.5	4.5	1.27×10^{38}	1.29×10^{37}
O9	35.5	4	9.13×10^{37}	1.01×10^{37}
B0	33.3	4	7.26×10^{37}	8.17×10^{36}
B1	25	3.9	6.2×10^{36}	8.02×10^{35}

Note: T_{eff} and log(g) are the effective temperature and surface gravity parameters given to the Castelli & Kurucz (2004) model to get FUV luminosities (L_{FUV}) and NUV luminosities (L_{NUV}). We took the distance 9.84 Mpc, and the star's radius as mentioned in Sternberg et al. (2003).

and O9 stars, the m_u and m_l is 38 $M_\odot$ and 21 $M_\odot$. When considering only the O8 star, the limits are 31 $M_\odot$ and 21 $M_\odot$. All these values are adopted from Sternberg et al. (2003).

We also found $\frac{N(B0)}{N(B1)}$ along with the IMF index α_2.

$$\frac{N(B0)}{N(B1)} = \frac{m_u(B0)^{1-\alpha_2} - m_l(B0)^{1-\alpha_2}}{m_u(B1)^{1-\alpha_2} - m_l(B1)^{1-\alpha_2}} \tag{3.10}$$

The m_u and m_l for B1 stars is 10 $M_\odot$ and 3 $M_\odot$ respectively. Using the IMF index for all the SFCs, we obtained the distribution of $\frac{N(O)}{N(B0)}$ and $\frac{N(B0)}{N(B1)}$.

3.4 Results

3.4.1 Distribution of SFCs in NGC 628 in Hα, FUV and NUV emission.

Although NGC 628 has been observed over the whole spectrum, we focus on the bands that trace SF in this study, i.e., FUV, NUV, and Hα. We can interpret the SF distribution and its propagation by studying the emission at these wavelengths as they trace different timescales. Here, these emissions are characterized as SFCs, which we detected separately from each band. But the number of SFCs detected in each band depends on the threshold we have taken in SExtractor. Although taking a 5σ threshold for all bands gives us a confident bright source detection, the different sensitivity of each band may affect the number of SFCs detected and sometimes even the area of the SFCs. However, taking SFCs that are detected in all three bands and taking the same area for all SFCs (the largest area of SFCs of the three bands) for IMF estimation makes us confident of our analysis.

The 3σ flux sensitivity of MUSE Hα is around $4-7\times10^{37}$ ergs^{-1}kpc^{-2} (Emsellem, Eric et al. 2022). With a 5σ threshold, we could detect around 560 SFCs in this band. The Hα emission is more prominent in the arm and interarm regions. More than 200 SFCs are detected in the Hα map, but have no associated UV emission. Some of the Hα emission could be associated with diffuse ionized gas (DIG), as indicated in previous studies (Kreckel et al. 2016).

The 5σ photometric limit of the UVIT F148W filter is 22.78. The FUV SFCs detected are the least numerous (around 190 SFCs) compared to the other two bands with a 5σ threshold. As mentioned above, one of the reasons could be the difference in sensitivity, which might have made us lose some faint SFCs. We see that more than 96% of the FUV SFCs are associated with SFCs in the other

two bands, where only six SFCs are associated with FUV in the interarm region (out of 100 interarm SFCs). The reasons for the other 4% of FUV SFCs not having associated emissions in other bands could be due to the way SFCs are detected, such that associated SFCs could have a center that is a bit farther than the FUV SFCs. Besides this, the shock-excited accretion disk around extremely eruptive young stars emits mainly in FUV and might lack in the other two bands (Carvalho et al. 2024). Additionally, the enhancement in Hα emission from the interarm regions indicates that there could be young SFCs embedded in dust, which obscures the FUV emission. The FUV bright SFCs are also associated with the spurs along the spiral arms, which are prominent in the ALMA images.

The NUV image has brighter SFCs and a smooth diffuse emission over the entire field. The galaxy center is especially bright in NUV, which we do not see in the other two bands. More NUV emission indicates that the galaxy center has older and cooler stellar populations and fewer massive O and B stars. The 5σ photometric limit of the UVIT N263M filter is 23.36. Of the 650 SFCs with NUV emission, more than 200 SFCs emit only NUV emission. These could be associated with evolved SFCs. The other SFCs are associated with either FUV or Hα emission or both.

3.4.2 UV and Hα luminosity correlation

Any IMF study involving UV and Hα luminosities is susceptible to extinction correction (Boselli et al. 2009). Hence, choosing a method for the extinction correction is critical. When we compared the correlation of extinction-corrected luminosities using different methods, we found more scatter for luminosities corrected for extinction using the Beta slope method as seen in Figure 3.3b and 3.3e. Previous studies such as Lee et al. (2009); Hao et al. (2011) have shown that extinction-corrected UV and Hα luminosities have a strong correlation. Hence, we

obtained the least square fit for UV (FUV and NUV) and Hα luminosities, which is corrected for extinction using the Balmer decrement method. This correlation is shown in Figure 3.3c and 3.3f for FUV and NUV, respectively. The equations we get by fitting a regression are

$$\log(\mathrm{L(FUV)}) = (0.933 \pm 0.034)\log(\mathrm{L(H}\alpha)) + (-0.684 \pm 1.409) \tag{3.11}$$

$$\log(\mathrm{L(NUV)}) = (0.980 \pm 0.028)\log(\mathrm{L(H}\alpha)) + (-0.551 \pm 1.096) \tag{3.12}$$

Here, equations 3.11 and 3.12 correspond to the correlation of FUV and NUV luminosities with Hα. All luminosities in equations are in ergs^{-1}. We also found a correlation for FUV and Hα SFRs for the Balmer decrement and also for JWST 21 μm method as shown in Figure 3.5. The linear fit for the Balmer decrement is

$$\log(\mathrm{SFR_{FUV}}) = (0.934 \pm 0.035)\log(\mathrm{SFR_{H\alpha}}) + (-0.455 \pm 0.09) \tag{3.13}$$

and the linear fit for the JWST 21 μm method is,

$$\log(\mathrm{SFR_{FUV}}) = (0.849 \pm 0.043)\log(\mathrm{SFR_{H\alpha}}) + (-1.081 \pm 0.101) \tag{3.14}$$

From Figure 3.5 and equations 3.13 and 3.14, we can see that the Hα SFR estimated for the Balmer decrement is higher than the JWST method. This again indicates that the different extinction methods correct for extinction at different depths.

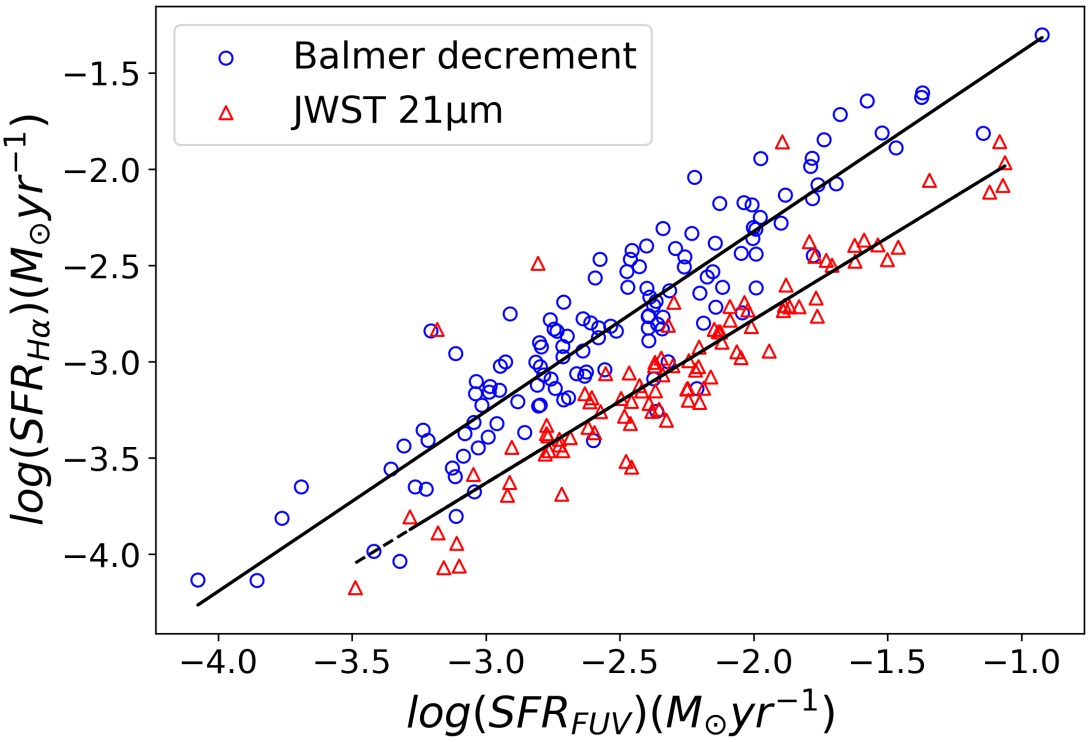


FIGURE 3.5: Observed Hα and FUV SFR correlation for SFCs corrected for extinction with the Balmer decrement and JWST 21μm method. The linear fit for the Balmer decrement and JWST 21μm method are given as equations 3.13 and 3.14, respectively.

We also see that the SFCs in the interarm region do not have higher luminosities than those in the arms and spurs (see Figure 3.3c and d). This could be because interarm SFCs have smaller areas, as seen in Figure 3.4. The luminosity of SFCs in the arm and spurs spans a wide range of values.

The estimated extinction-corrected Hα luminosity of SFCs is between $10^{37} \leq (L_{H\alpha}/ergs^{-1}) \leq 10^{40}$, which is ten times greater than the values in Kreckel et al. (2016). This increase in luminosity could be because we have convolved the Hα image to a lower resolution, which can cause some clusters to blend into larger ones and potentially increase the contribution of DIGs.

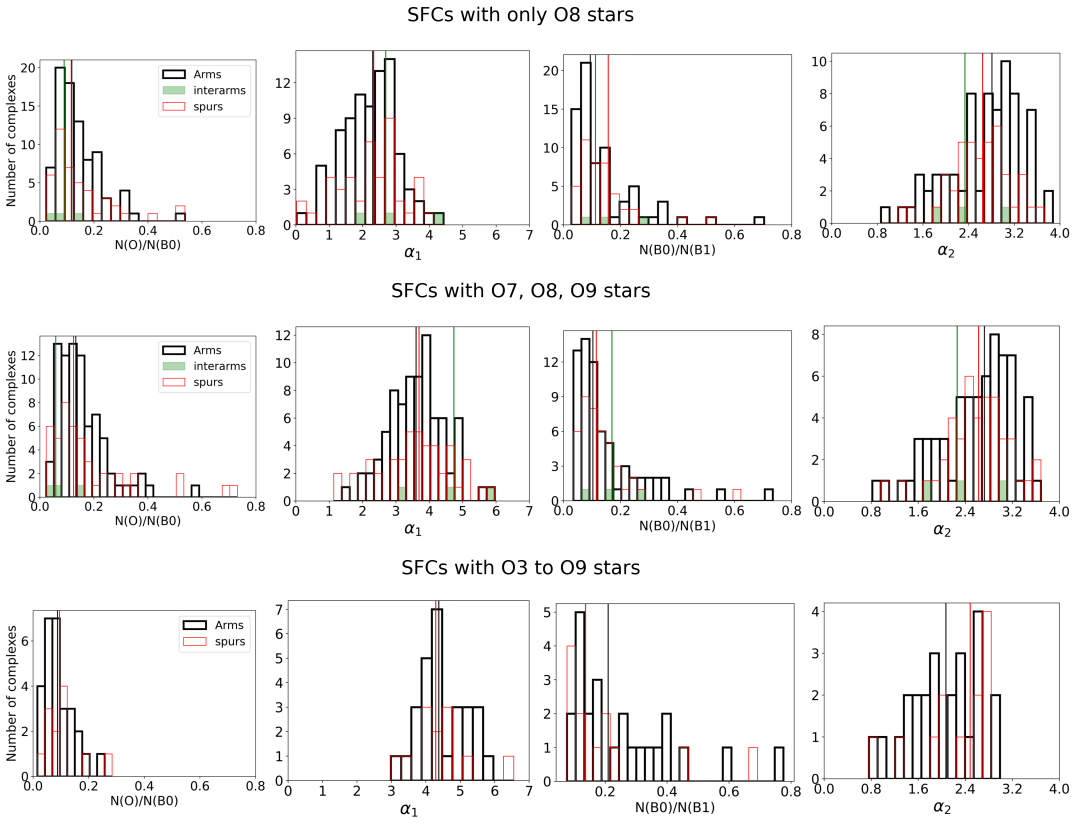


FIGURE 3.6: The distribution of $\frac{N(O)}{N(B0)}$, α_1, $\frac{N(B0)}{N(B1)}$ and α_2. The vertical lines represent the median value of the distribution, which is mentioned in Table 3.2.

3.4.3 Determing the IMF of the SFCs

We estimate $\frac{N(O)}{N(B0)}$ and $\frac{N(B0)}{N(B1)}$ and their respective IMF indices α_1 and α_2 in Section 3.3.4. The distribution of the stellar ratios and IMF indices for the three choices of O-type stars is shown in Figure 3.6, and the median ratios and IMF index for all the cases are given in Table 3.2. We used the bootstrapping method to determine the standard error associated with the median ratios and median IMF indices.

When we consider that Hα arises from only the O8V stars, we find that $\alpha_1 = 2.32$ for the arms and spurs, which is closer to the canonical stellar IMF ($\alpha = 2.3$) (Kroupa et al. 2024). But when we populate with more types of O stars, such as O7V, O8V, and O9V, and calculate the median ratio for each SFC, we find that the median α_1 becomes steeper ($\alpha_1 = 3.66$) than the canonical IMF, and

for the arms and spurs, again it is nearly the same. We also noticed that only 2% of SFCs decreased when populated with three types of O stars (O7V, O8V, O9V), but when we considered the range of O stars (O3V to O9V), we observed a significant decrease in the number of SFCs (69%). Also, the number of SFCs reduced to 34% in the arms and 27% in the spurs, giving the slope a much steeper value of ($\alpha_1 = 4.35$), with no contribution from interarm SFCs. The decrease in the number of SFCs is because not all SFCs have luminosities large enough to accommodate the different types of massive stars. It should be noted that the observed number of SFCs remains unchanged; only the number of SFCs that can be modelled under the adopted assumptions changes.

However, in contrast to α_1, we find that $\frac{\mathrm{N(B0)}}{\mathrm{N(B1)}}$ and α_2 do not vary much with different populations of O-type stars. The variation in α_2 is significantly less for the first two cases. But, we see that α_2 is steeper for the arms compared to the interarm SFCs, which is contradictory to what is expected. However, this result is statistically insignificant as we have only three SFCs for the first two cases, and the error is also very high for interarm SFCs. When we populate SFCs with O3V to O9V stars, we find that the SFCs in the arms have IMF slopes that are flatter than the spurs. The arms show a more significant variation in α_2 for the third case compared to the first two cases (which can be up to 0.74). But variation in α_2 is lesser for spurs (up to 0.16). Nonetheless, the reduced variation and smaller uncertainties associated with it make α_2 a more reliable indicator of the IMF index. We have discussed more on this topic in Section 3.5.

It is also important to note that the different evolutionary timescales of O and B-type stars can affect the stellar number ratios used in Equations 3.10 and 3.15. The Hα emission used to estimate the O-star population primarily traces very recent star formation ($\lesssim$ 10 Myr), owing to the short lifetimes of the massive ionising stars. In comparison, the UV emission traces stellar populations over longer timescales, with FUV emission remaining sensitive to young stars over

$\sim$ 100 Myr and NUV emission extending to somewhat older stellar populations. Therefore, the currently observed N(O)/N(B0) and N(B0)/N(B1) ratios may be affected by the different evolutionary timescales of these stellar populations and may not exactly represent their initially formed relative numbers. This age effect should therefore be considered when interpreting the derived IMF indices.

TABLE 3.2: IMF parameters in different regions

O star Type	Region	No of SFCs	Median $\frac{N(O)}{N(B0)}$	Median α_1	No of SFCs	Median $\frac{N(B0)}{N(B1)}$	Median (α_2)
	Arm	84	0.12 ± 0.01	2.30 ± 0.12	71	0.09 ± 0.01	2.81 ± 0.09
O8	Spurs	44	0.12 ± 0.01	2.33 ± 0.18	42	0.11 ± 0.01	2.64 ± 0.10
	Interarm	3	0.09 ± 0.04	2.69 ± 0.88	3	0.16 ± 0.07	2.34 ± 0.44
(Weighted Mean)			0.12 ± 0.00	2.32 ± 0.06		0.10 ± 0.01	2.74 ± 0.10
	Arm	80	0.13 ± 0.01	3.60 ± 0.12	67	0.10 ± 0.01	2.72 ± 0.10
O7, O8, O9	Spurs	44	0.12 ± 0.02	3.69 ± 0.19	42	0.12 ± 0.01	2.62 ± 0.10
	Interarm	3	0.06 ± 0.05	4.73 ± 0.94	3	0.17 ± 0.08	2.26 ± 0.44
(Weighted Mean)			0.12 ± 0.01	3.66 ± 0.18		0.11 ± 0.01	2.67 ± 0.08
	Arm	28	0.09 ± 0.01	4.38 ± 0.19	24	0.21 ± 0.04	2.07 ± 0.20
O3 to O9	Spurs	12	0.09 ± 0.02	4.29 ± 0.24	12	0.14 ± 0.05	2.48 ± 0.27
	Interarm	0	-	-	0		-
(Weighted Mean)			0.09 ± 0.00	4.35 ± 0.05		0.19 ± 0.04	2.21 ± 0.21

Note: The weighted mean α_1 and α_2 for all three cases combined is 3.16 ± 0.62 and 2.64 ± 0.14 respectively.

3.4.4 IMF trends with the properties of the SFCs

We plotted the variation of our calculated IMF indices (α_1 and α_2) with the properties of the SFCs as shown in Figure 3.7. For the first case (SFCs with only O8 stars), the correlation of with α_1 with SFC properties such as FUV-NUV color, $\log_{10}(\Sigma(M_*))$, $\log_{10}(\Sigma(M_{H_2}))$, and $\log_{10}(\Sigma(SFR))$ are given by the Spearman correlation coefficient of -0.2, -0.1, -0.1 and -0.3 respectively, which are weak negative correlations. Only with $\log_{10}(\Sigma(SFR))$, does α_1 show a slightly better correlation. We observed that for the second case (SFCs with O9, O8, and O7 stars),

the $\log_{10}(\Sigma(\mathrm{SFR}))$ correlation with α_1 became stronger with the correlation coefficient -0.5, which indicates that as the SFR increases, the IMF becomes flatter, i.e., the number of massive stars increases. The other three properties show similar correlations with α_1 for the second case as for the first one.

In contrast, α_2 shows strong correlations with the properties of the SFCs, the most prominent being the correlation with FUV-NUV color. It has a high Spearman correlation coefficient value of nearly +1 for all the cases. We fitted a quadratic equation to it as shown below (equation 3.15), and the fitting parameters are given in Table 3.3 for the different cases.

$$\alpha_2 = \mathrm{a}(\mathrm{FUV} - \mathrm{NUV})^2 + \mathrm{b}(\mathrm{FUV} - \mathrm{NUV}) + \mathrm{c} \tag{3.15}$$

TABLE 3.3: Fitting parameters for α_2 and FUV-NUV plot (equation 3.15) and α_2 and $\log_{10}(\Sigma(\mathrm{SFR}))$ plot (equation 3.16)

O star Type	a	b	c	d ($\mathrm{M}_\odot^{-1}\mathrm{yrkpc}^2$)	e
O8	-1.57 ± 0.15	2.71 ± 0.07	2.42 ± 0.02	-0.78 ± 0.11	1.40 ± 0.18
O7, O8, O9	-1.89 ± 0.18	2.80 ± 0.08	2.41 ± 0.02	-0.74 ± 0.12	1.43 ± 0.19
O3 to O9	-3.75 ± 0.52	2.62 ± 0.11	2.42 ± 0.02	-	-

Note: a, b and c are fitting parameters for α_2 and FUV-NUV plot. Whereas, d and e are fitting parameters for α_2 and $\log_{10}(\Sigma(\mathrm{SFR}))$ plot. The first row or only O8 stars gives the best fit for the α_2 and (FUV-NUV) relation.

The correlation coefficients of $\Sigma(\mathrm{SFR})$ with α_2 are found to be -0.5 and -0.4 for the first two cases. We also fitted a linear regression for the α_2 and $\Sigma(\mathrm{SFR})$ correlations. The equation is given by,

$$\alpha_2 = \mathrm{d} \times \log_{10}(\Sigma(\mathrm{SFR})) + \mathrm{e} \tag{3.16}$$

where the fitting parameters d and e are given in Table 3.3.

As the canonical IMF is considered a universal probability density distribution function (Jeřábková et al. 2018), we found the corresponding parameters of the SFCs associated with this IMF index so that we can compare it with our estimated IMF. We determined the color and $\log_{10}(\Sigma(\mathrm{SFR}))$ for the canonical stellar IMF value ($\alpha = 2.3$) from equations 3.15 and 3.16 along with Table 3.3 for all three cases. The color, $\mathrm{FUV}-\mathrm{NUV} \approx -0.04$ and $\log_{10}(\Sigma(\mathrm{SFR})/\mathrm{M_\odot yr^{-1}kpc^{-2}}) \approx -1.16$ was estimated for the canonical IMF value. The values are similar for all three cases. Since our median IMF indices are steeper than the canonical value for arms and spurs, we obtain $\mathrm{FUV} - \mathrm{NUV} > -0.04$ and $\log_{10}(\Sigma(\mathrm{SFR})) < -1.16$ $\mathrm{M_\odot yr^{-1}kpc^{-2}}$ for our values.

Apart from FUV-NUV and $\log_{10}(\Sigma(\mathrm{SFR}))$, the $\log_{10}(\Sigma(\mathrm{M_{H_2}}))$ also has a weak negative correlation with α_2, with a correlation coefficient of -0.4. However, this is stronger than the correlation with α_1. Hence, as $\Sigma(\mathrm{M_{H_2}})$ increases α decreases i.e. the IMF becomes flatter. This indicates that the larger the molecular surface mass density in the galaxy disk, the larger are the fraction of high-mass stars. We also see that this correlation generally holds for dense molecular clouds of mass density $\geq 10^8$ $\mathrm{M_\odot kpc^{-2}}$. For less dense clouds, α nearly becomes constant. In Figure 3.7, in α_2 and $\Sigma(\mathrm{M_{H_2}})$ correlation, there is a fairly sharp cutoff at $\log_{10}(\Sigma(\mathrm{H_2})/\mathrm{M_\odot kpc^{-2}}) = 9.5$ for third case. But when it comes to $\Sigma(\mathrm{M_*})$, we observed the increase in α_2 with increasing $\Sigma(\mathrm{M_*})$, which means that the IMF becomes steeper as stellar mass density increases, which is contrary to $\Sigma(\mathrm{M_{H_2}})$. This may indicate that the more massive SFCs (i.e., larger $\Sigma(\mathrm{M_*})$) have evolved stellar populations, and the massive stars have evolved away. We discuss the significance of these trends in Section 3.5.

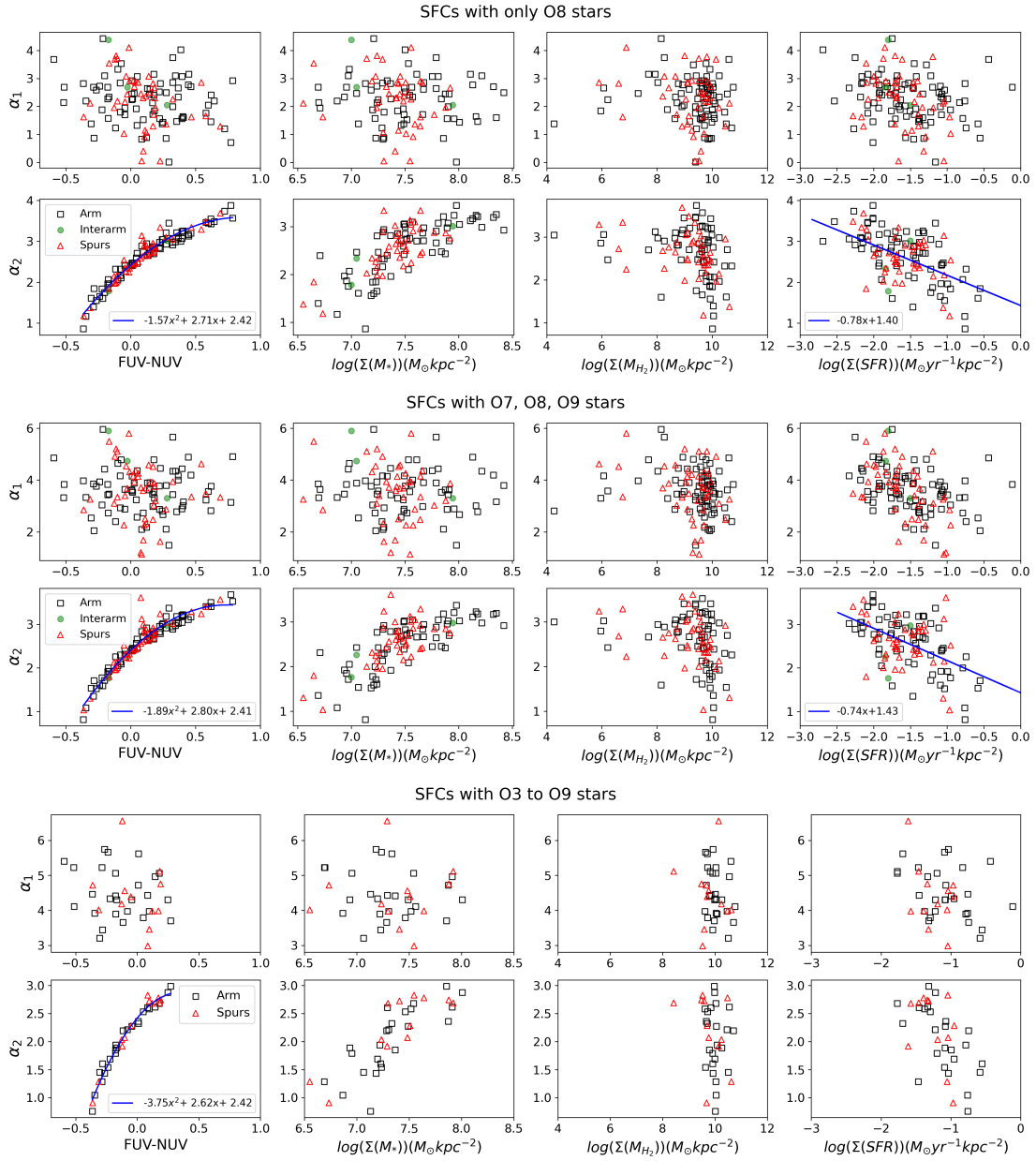


FIGURE 3.7: Variation of IMF index (α_1 and α_2) with the different properties of IMF like FUV and NUV color, stellar mass density, molecular mass density, and SF rate density (from left).

3.5 Discussion

Our study assumes that the Hα emission mainly arises from O-type stars. But, since we have no information on what kind of O stars populate each SFC, we populated the SFCs with the following combinations: (i) O8V star whose luminosity

corresponds to the median luminosity of the SFCs in NGC 628; (ii) a combination of O7V, O8V, and O9V stars; and (iii) a combination of OV stars with a mass limit of 100 $M_{\odot}$ (O3V to O9V stars). Then we generated different possible stellar ratios $\frac{N(O)}{N(B0)}$ and $\frac{N(B0)}{N(B1)}$ for each SFC and noted the median values for each SFC. Hence, there is a range of possibilities for the high-mass IMF, which depends on how we populate O stars in the SFCs. Apart from O stars, there can also be some contribution from very massive B stars in Hα, and we are aware of the degeneracy present in considering the type of the population. But for this study, we will go with the above assumption to see if we can get some estimate of the IMF. Even if we consider the contribution from B stars in Hα emission, we might see a variation in the result for option (iii), where we consider populating with all types of O stars.

When we populated the SFCs with different types of O stars, we ensured that all types were present in each SFC. But in reality, this may not be the case. However, it does help us to understand how steep the IMF can go. Studies show that massive O-type stars of mass more than 100 $M_{\odot}$ are detected in nearby galaxies (Kalari et al. 2022). Koda et al. (2012) have shown that, statistically, for the cluster to have a star as massive as 100 $M_{\odot}$, it should have a cluster of mass at least 10^5 $M_{\odot}$.

But stochastically, massive stars can form in less massive clusters; alternatively, massive stars might not form in massive clusters. With high stellar density, the inner disk may host clusters with one or more massive stars. In addition, it must be noted that although we see in Figure 3.4 that the SFC stellar masses are above 10^5 $M_{\odot}$, the SFCs may be hosting multiple clusters that cannot be individually resolved. However, low-mass O stars are more likely to form rather than high-mass stars. We also find that the number of SFCs decreases when we try to populate with higher masses of O stars. So, we conclude that the existence of SFCs with very massive O-type stars in NGC 628 is less probable than the existence of low-mass

O-type stars such as O9 to O7 stars.

When considering fully populated SFCs (option (iii)), the IMF becomes top-heavy (i.e., $\alpha > 2.3$, so a steeper IMF) compared to only for O8V stars (option (i)), which is nearly canonical. Hence, the IMF index is steeper than the canonical value at the high-mass end of stellar populations (O stars and massive B stars). But we know that the more massive the stars are, the shorter is their lifetime. Hence, many massive stars must have already passed their main sequence, which could be why the present-day IMF that we observe in NGC 628 appears to be a top-light IMF.

We have derived two IMF indices, α_1 and α_2. Since α_1 is derived from O-type stars that have short lifetimes ($< 10^7$ yr), it represents the present-day IMF index. On the other hand, α_2 is more dependent on the B-type stars, which have longer lifetimes ($\leq 10^8$yr) and hence represent the general high-mass IMF index. However, some emissions from NUV might come from the evolved stellar populations. But as the contribution from main sequence stars will be higher, and since we are taking the SFCs that have emission in other bands too, we can say that the SFCs we have considered have massive stars in them. The α_1 values in Table 3.2 show a significant variation for different populations of O stars (cases (i), (ii), and (iii)). In contrast, the ratio of high-mass to low-mass B stars, i.e., N(B0)/N(B1), gives a consistent value for all the scenarios. This shows that $\frac{\mathrm{N(B0)}}{\mathrm{N(B1)}}$ does not depend strongly on what kind of O stars are present in the SFCs. This suggests that the average of α_2 could be a better indicator of the high-mass stellar IMF than the present-day IMF index α_1. The mean value for the IMF index we obtain is $\alpha_2 = 2.64 \pm 0.14$, which is a steeper or top-light IMF compared to the canonical IMF.

Various studies have obtained a top-light IMF compared to the canonical IMF for the massive stars (Kroupa 2002). The Miller & Scalo (1979) and Kennicutt (1983)

predicted $\alpha = 2.5$ for masses above $1M_{\odot}$. Scalo (1986b) predicted α is between 2.3 and 3.3 for the high-mass end. Apart from these, Weisz et al. (2015) found $\alpha = 2.45$ for 85 clusters in M31 and Wainer et al. (2024) found $\alpha = 2.5$ for the 34 clusters in M33. These studies used the resolved population in clusters to find the high-mass IMF. Most of these studies have the low-mass cutoff for the high-mass IMF as $1M_{\odot}$. In our study, there is an overlap in the mass for both $\frac{N(O)}{N(B0)}$ and $\frac{N(B0)}{N(B1)}$ ratios, and we see that both α_1 and α_2 have an average value within the range predicted in Scalo (1986b).

Studying the stellar IMF in external galaxies is crucial because it allows us to investigate the universality of the IMF within the galaxy as well. Klessen et al. (2007) showed that the IMF in the star-forming regions of the MW's bulge differs from the IMF in the disk. Multiple studies utilize the complete field of the galaxy and try to understand if there is any IMF variation in the XUV disk of the galaxy compared to the inner disk (Koda et al. 2012; Bruzzese et al. 2019). This is because the IMF can be inferred from galaxy properties such as stellar and gas densities and metallicity.

The MUSE observations of NGC 628 cover only the inner region. Hence, we try to understand the properties of SFCs in the arm, interarm, and spurs, which are expected to have different environments and star-forming conditions. Unfortunately, only three interarm SFCs have FUV, NUV, and the Hα emission, which is necessary to obtain the IMF index. Hence, the IMF index values we estimated for the interarm region in this study are statistically insignificant. However, as discussed below, our results agree with those of the previous studies.

The SFCs in the interarm regions have smaller areas and mass densities compared to the arms and spurs. Hence, it is expected that the IMF in the interarms will not have enough cluster mass to have more massive stars, making it top-light IMF (Kroupa et al. 2024). However, several studies, including Kreckel et al. (2016), have

shown that there is little difference in SF properties between arm and interarm SFCs. Our studies show that the IMF value for the interarm region is steeper than the arm and spur regions for $\frac{\mathrm{N(O)}}{\mathrm{N(B0)}}$, and for $\frac{\mathrm{N(B0)}}{\mathrm{N(B1)}}$, it is flatter. However, fewer SFCs in the interarm regions make the error bars prominent. Scalo (1986b) showed that the variation in the IMF with region to region is smaller than ± 0.5. Here, the variation of the IMF index α_1 in the interarm compared to the arm and spurs is less than 0.5 for case one, but it becomes more significant for case two. Apart from the three SFCs in the interarm for which we found the high-mass stars ratio, there are more SFCs with only Hα and only NUV emission and no counterparts in the two wavelengths. This shows that there could be stars in the very early stage surrounded by gas and dust, causing extinction in lower wavelengths, and the presence of only NUV in some SFCs indicates that there are even older populations in this region.

There is no statistically significant difference between α_1 in the spurs and the arms for any three cases. The present-day IMF α_1 of the SFCs in the spurs is slightly steeper than the IMF in the arms. The variation is between 0.03 and 0.09. It becomes flatter for α_2, making the arms top-light compared to the spurs and interarms. The spurs have nearly the same IMF index for the third case as the first two, but the arms become much flatter, making it top-heavy, contrary to what we see for α_1. So α_1 might be the right indicator to check for the universality and compare the nature of high-mass IMF across the region. Meanwhile, how steep or flat α_2 can get might depend on how we populate the O stars, though variation in values for different cases is lesser in α_2.

The variation of high-mass IMF indices with the properties of SFCs such as SFR, metallicity, and mass of the clusters or galaxies, helps us understand the massive SF in different environments. The (Σ(SFR)) variation with the IMF is commonly discussed (Gunawardhana et al. 2011; Jeřábková et al. 2018; Kroupa et al. 2024). Studies have shown that the higher the galaxy or cluster SFR, the more likely it

will form high-mass stars because they will have enough mass to produce them (Larson 2006; Gunawardhana et al. 2011). We see that our SFCs also follow a similar trend. Even α_1, which does not show much trend with any other properties, shows the trend with $\log_{10}(\Sigma(\mathrm{SFR}))$. We fitted a linear regression to the α_2 and $\log_{10}(\Sigma(\mathrm{SFR}))$, and found the relation as in equation 3.16 with the parameters mentioned in Table 3.3. Gunawardhana et al. (2011) also fitted a linear fit for α and $\log_{10}(\Sigma(\mathrm{SFR}))$ for galaxies, which is

$$\alpha = -0.3 \times \log_{10}(\Sigma(\mathrm{SFR})) + 1.7 \tag{3.17}$$

where α is the IMF index as mentioned in the introduction (Section 4.1). We find that this relation gives $\log_{10}(\Sigma(\mathrm{SFR}))$ because for the α corresponding to the canonical IMF is equal to -2$\mathrm{M_\odot yr^{-1}kpc^{-2}}$, which is lower than what we obtain for our SFCs for high-mass α. This implies that the $\log_{10}(\Sigma(\mathrm{SFR}))$ for the SFCs to produce the canonical IMF is greater than what we see for galaxies. The $\log_{10}(\Sigma(\mathrm{SFR})/\mathrm{M_\odot yr^{-1}kpc^{-2}})$ of the inner regions of the MW varies between 0 and -3 (Elia et al. 2022). The $\log_{10}(\Sigma(\mathrm{SFR})/\mathrm{M_\odot yr^{-1}kpc^{-2}})$ corresponding to canonical IMF found using relation from Gunawardhana et al. (2011) and even our values fall within this range. However, in this study, we estimate for SFCs and not for the whole galaxy.

We find a strong correlation between α_2 and the extinction-corrected UV color, FUV-NUV. We see in our distribution in Figure 3.4 that the SFCs have a wide range of colors from -0.6 to 0.8. The median color for the SFC distribution in the arms is 0.14, and 0.08 in spurs. Koda et al. (2012) discussed that if a cluster has FUV-NUV $< 0.2 - 0.3$, ie, is blue in color, it must contain O and/or B stars. However, it is difficult to differentiate clusters with and without O stars just by looking at the UV colors. Even SFCs with FUV-NUV$>$ 0.3 might have O and B stars. Hence, we took blue SFCs with FUV-NUV $\leq$ 0.3. We found the median O

to B0 and B0 to B1 stellar ratios, along with median α_1 and α_2 values as seen in Table 3.4. We found that it significantly affects the arm SFC numbers. For the first two cases, the number of SFCs is the same. We also found that taking only blue SFCs does not affect α_1 much. However, α_2 values became less steep, making α_2 closer to the canonical value. For the first two cases, the arms and spurs have nearly the same α_2 values. We also find that spurs become steeper than arms for α_2. We found that the IMF index and FUV-NUV correlations are strong only for α_2. One of the reasons for this could be because we obtain the number of B stars from the FUV and NUV emissions.

TABLE 3.4: IMF parameters in different regions for SFCs with FUV-NUV $\leq$ 0.3.

O star Type	Region	No of SFCs	Median $\frac{N(O)}{N(B0)}$	Median α_1	No of SFCs	Median $\frac{N(B0)}{N(B1)}$	Median (α_2)
	Arm	51	0.12 ± 0.01	2.27 ± 0.15	48	0.14 ± 0.02	2.47 ± 0.10
O8	Spurs	37	0.11 ± 0.02	2.36 ± 0.18	37	0.12 ± 0.01	2.54 ± 0.09
	Interarm	3	0.09 ± 0.04	2.69 ± 0.88	3	0.16 ± 0.08	2.34 ± 0.44
(Weighted Mean)			0.12 ± 0.01	2.32 ± 0.08		0.13 ± 0.01	2.49 ± 0.04
	Arm	51	0.14 ± 0.01	3.55 ± 0.13	48	0.14 ± 0.02	2.43 ± 0.11
O7, O8, O9	Spurs	37	0.12 ± 0.02	3.68 ± 0.22	37	0.12 ± 0.01	2.54 ± 0.09
	Interarm	3	0.06 ± 0.05	4.73 ± 0.94	3	0.17 ± 0.08	2.26 ± 0.44
(Weighted Mean)			0.13 ± 0.02	3.64 ± 0.20		0.13 ± 0.01	2.47 ± 0.06
	Arm	27	0.09 ± 0.01	4.33 ± 0.18	24	0.21 ± 0.04	2.07 ± 0.20
O3 to O9	Spurs	12	0.09 ± 0.02	4.29 ± 0.24	12	0.14 ± 0.05	2.48 ± 0.27
	Interarm	0	-	-	0		-
(Weighted Mean)			0.09 ± 0.00	4.32 ± 0.05		0.19 ± 0.04	2.21 ± 0.21

Note: The weighted mean α_1 and α_2 for all three cases combined is 3.22 ± 0.6 and 2.43 ± 0.06 respectively.

The color FUV − NUV > 0 implies that the NUV emission is more than the FUV. That is, there are fewer massive stars. NUV also comes from some evolved stars that can contribute and make SFCs redder. This can also be seen in the trend. The IMF gets steeper as the SFCs become redder, again showing the bottom heaviness. And for the cases, it starts getting bottom heavy at FUV − NUV > −0.04. Hence, color can also indicate the nature of the IMF.

From our results, we also find that the weak correlation of α_2 with $\Sigma(M_{H_2})$ is as expected, i.e., as molecular hydrogen mass density increases, the IMF index increases. The more massive and dense the clouds, the higher the probability of forming high-mass stars. The reason for the scatter in the correlation could be that a single conversion factor was considered to obtain the molecular hydrogen mass for all the SFCs. It also seems like the less dense clouds cannot fully populate the O stars. In Figure 3.7, for case three, molecular clouds barely form massive O stars for $\log(\Sigma(M_{H_2})/M_\odot kpc^{-2}) < 9.5$ and none below $\log(\Sigma(M_{H_2})/M_\odot kpc^{-2}) = 8.5$. We also see that most of the data points in all three runs are still clumped between α_2 =2 to 3, as expected from canonical or Salpeter, and some region-to-region variation. The tail to α_1 only appears at the highest $\Sigma(M_{H_2})$ measured. This shows the importance of molecular cloud surface density in forming massive stars.

The correlation of α_2 with $\Sigma(M_*)$ in our plot seems contradictory to the previous studies. As the SFC $\Sigma(M_*)$ increases, the IMF steepens, implying fewer massive stars are produced. However, we estimated SFC masses from the starburst99 model, and the redder the SFCs, the more massive the complexes are, i.e., they are composed of cooler and older stars. But this does not mean that there were no massive stars before. As said before, the more massive the stars are, the shorter their time in the main sequence will be. Even if these SFCs had very massive stars, they might already be exhausted. Hence, this trend is quite understandable. However, a more accurate estimation of stellar mass might help us understand it better.

We find very few FUV excess young SFCs with low stellar mass that show top-heavy IMF (see α_2 correlation with FUV-NUV in Figure 3.7.) There are very few in arms and spurs. Some even show nearly Salpeter IMF. These SFCs have large Σ(SFR). This could be an indication of recent starbursts in these SFCs.

Apart from these factors, the IMF also depends upon the metallicity and temperature of the molecular clouds. As we look at the inner disk of a massive galaxy, we expect solar metallicity to be a reasonable assumption, and we do not expect it to vary much. Although not knowing the exact population is a major drawback, this study gives an idea of the IMF in galaxies where the Hα mainly comes only from O stars. This result is specific to the galaxy NGC 628, which is a massive grand design spiral galaxy. In future studies, we will apply the same method to explore the IMF in galaxies in different environments and check its universality.

3.6 Conclusions

In this project, we used Hα from MUSE and FUV and NUV emission from UVIT to determine the IMF of the SFCs in the inner disk of the galaxy NGC 628 by estimating the approximate number of O stars and B stars from each SFC. We also derived some important trends of the IMF index with the properties of the SFCs. The main results of this study are summarized below:

1. There is less FUV emission in the inner disk of NGC 628 compared to $H\alpha$ and NUV emission, indicating strong extinction and/or more dust-embedded SF, mainly in the interarm regions.

2. We see a strong correlation between the extinction-corrected UV and Hα luminosities for the Balmer decrement method and 21 μm JWST correction compared to the extinction correction done by the Beta slope method.

3. The properties of SFCs in the arm, spurs, and interarms do not vary much and are consistent with previous studies. However, the area of the SFCs in the interarms is smaller compared to the distribution of SFC areas in arms and spurs.

4. The present-day IMF index α_1 corresponding to $\frac{\mathrm{N(O)}}{\mathrm{N(B0)}}$ stellar ratio becomes steeper ($\alpha_1 = 4.35 \pm 0.05$) as we populate the SFCs with O-type stars up to stellar masses of 100 $\mathrm{M}_\odot$ (option 3, Table 3.2), which is much steeper than the values found in the previous studies. The mean α_1 is around 3.16 ± 0.52. However, the general high-mass IMF index α_2 corresponding to the $\frac{\mathrm{N(B0)}}{\mathrm{N(B1)}}$ ratio has mean slope of $\alpha_2 = 2.64 \pm 0.14$. The α_2 values are consistent for different O-type stellar populations. However, α_1 for the case where SFCs were populated with only O8 stars has a mean value closer to the canonical stellar IMF.

5. The present-day IMF index α_1 from massive stars ($\mathrm{M} > 10\mathrm{M}_\odot$) is steeper than high-mass IMF index α_2, which we estimated from stars of mass, $10\mathrm{M}_\odot \geq \mathrm{M} \geq 3\mathrm{M}_\odot$. This is because the more massive the star is, the shorter is its lifetime in the main sequence.

6. The IMF index in the arms and spurs are similar, showing a variation $< \pm\, 0.2$. The IMF index α_1 is steeper for the interarm than the IMF index for the arm and spurs. Whereas α_2 gets steeper for the arm than spurs and interarm.

7. The extinction-corrected UV color (FUV-NUV) strongly correlates with α_2. But for FUV-NUV> -0.04, the IMF becomes steeper. Hence, the UV color can also indicate the nature of the IMF.

8. The median value of α_1, when considered SFCs with FUV-NUV ≤ 0.3 is consistent with the value when considered all the SFCs. But the median value of α_2 becomes less steeper with median value $\alpha_2 = 2.43 \pm 0.06$.

9. The $\log_{10}(\Sigma(\mathrm{SFR}))$ versus α_2 shows a similar trend as previous studies for galaxies. But the value $\log_{10}(\Sigma(\mathrm{SFR}))$ for galaxies corresponding to the Salpeter IMF is smaller than what we see for SFCs.

10. In our study, α_2 shows a cutoff at $M_{H_2} \sim 10^{9.5} M_\odot$. On closer inspection, α_2 increases with the increase in the density of molecular gas with a weak correlation, suggesting that low-density clouds cannot support high-mass stars, and most of the SFCs clump around the canonical IMF value.

11. The α_2 and $\Sigma(M_*)$ trend shows that massive and old SFCs must have gone through episodes of SF. Hence, some high-mass stars must already be in the main sequence turn-off.

12. Young SFCs (FUV-NUV< -0.04) with less stellar mass densities show the top-heavy IMF. They also show the high $\log_{10}(\Sigma(\mathrm{SFR}))$, which suggests the starburst in these SFCs.

Chapter 4

Spatial Correlations of PAH, UV, and Hα Emission and IMF- PAH Variations in Star-Forming Complexes of NGC 628

4.1 Introduction

PAHs are organic molecules with multiple aromatic rings containing 20-1000 carbon atoms (Allamandola et al. 1989; Rigopoulou et al. 2024). These molecules are an essential part of the ISM, and up to 20% of the total IR emission in star-forming galaxies comes from these molecules (Smith et al. 2007; Li 2020). They emit in distinctive IR bands at 3.3, 6.2, 7.7, 11.3, 12.7, and 17 μm (Leger & Puget 1984;

Allamandola et al. 1989). These molecules can be vibrationally excited with a single UV photon, and they de-excite, emitting the distinctive PAH features (Tielens 2008). Both stretching and bending vibrational modes contribute to these features. The 3.3 μm feature is seen when C-H bonds stretch, whereas C-C bending and C-H out-of-plane bending contribute to the features at 6-9 μm and features beyond 11 μm, respectively (Leger & Puget 1984; Allamandola et al. 1989).

The UV and visible photons from massive stars excite the PAH molecules in star-forming regions. Their emission traces the front of the photodissociation regions (PDRs) around stars, which separates the ionised gas from the surrounding molecular gas (Tielens et al. 1993). Hence, their emission is associated with recent SF. Their band ratios can be used to investigate the properties of the molecules, such as size and charge, which in turn helps us understand the source of UV photons (Draine et al. 2021; Rigopoulou et al. 2021; Maragkoudakis et al. 2022; Chastenet et al. 2023). Small PAH molecules emit strongly at 3.3 μm. Larger molecules emit at longer wavelengths, specifically around 11.3 and 17 μm. Ionised PAHs are associated with C-C vibrational modes, leading to 6.2 and 7.7 μm emissions. Meanwhile, neutral PAHs emit at 3.3, 11.3, and 17 μm, which are primarily linked to C-H vibrational modes. This is why the combination of the bands' trace size and charge (or degree of ionisation) of PAH molecules (Allamandola et al. 1999).

PAHs have been deeply studied in various astrophysical regions, from planetary, protoplanetary, and reflection nebulae to the H II regions and ISM of galaxies (Tielens 2008). The 6.2, 7.7, and 11.3 μm features have been mostly used to study the PAH properties in galaxies (Rigopoulou et al. 1999; Peeters et al. 2004; Draine et al. 2021; Rigopoulou et al. 2024). Early-type and active galaxies show an abundance of neutral larger molecules, whereas star-forming galaxies have more ionised molecules (Kaneda et al. 2008; Vega et al. 2010; García-Bernete, I. et al. 2022, 2024). Smaller molecules might undergo preferential destruction from a harsh environment (Smith et al. 2007) or, due to the shattering of large grains,

their abundance could also increase(Yamagishi et al. 2012). There can also be the destruction of PAHs in starbursts and regions with strong emission from AGNs. But some studies have also shown that there is no preferential destruction of smaller molecules (Rigopoulou et al. 2024) and shown that PAHs are also present in the close vicinity of AGNs (García-Bernete, I. et al. 2022; Armus et al. 2023). In addition to this, properties such as metallicity affect the production and emission of PAH molecules (Madden, S. C. et al. 2006). With the JWST, there are several large surveys dedicated to understanding PAH molecules and emissions in detail. These include spectroscopic (Lai et al. 2023; Donnan et al. 2022; García-Bernete, I. et al. 2022, 2024) and photometric studies of nearby galaxies (Sandstrom et al. 2023; Egorov et al. 2023; Pedrini et al. 2024; Rodríguez et al. 2025) and also those focusing on high redshift (z) galaxies (Shen et al. 2023; Shivaei et al. 2024; Shivaei & Boogaard 2024).

Our study uses JWST PAH maps (F335M, F770W, and F1130W) of NGC 628 to compare the spatial distribution of PAH with UV, using observations from the UVIT as well as the Hα distribution obtained from the MUSE instrument. Our aim is to understand how the physical properties of the smaller dust constituents, the PAHs in SFCs, vary with different stellar IMFs. The latter have been obtained using the catalogue of SF properties of NGC 628 from Amrutha & Das (2025), which is described in Chapter 3. We investigated how the PAH properties vary over the different regions (arms and spurs). We also closely examined the PAH distribution around the phantom void, which is prominent in the PAH bands of NGC 628 (also known as the Phantom galaxy).

NGC 628 is a well-known grand design spiral galaxy that is nearly face-on (i=8°.9; Lang et al. (2020)) and shows young and massive SF (Yadav et al. 2021), and thus widely used for studying SF, including PAH emission, using the broadband filters of JWST. Most studies have focused on understanding the PAH fraction as a function of the properties of the ISM and PAH molecules, along with their

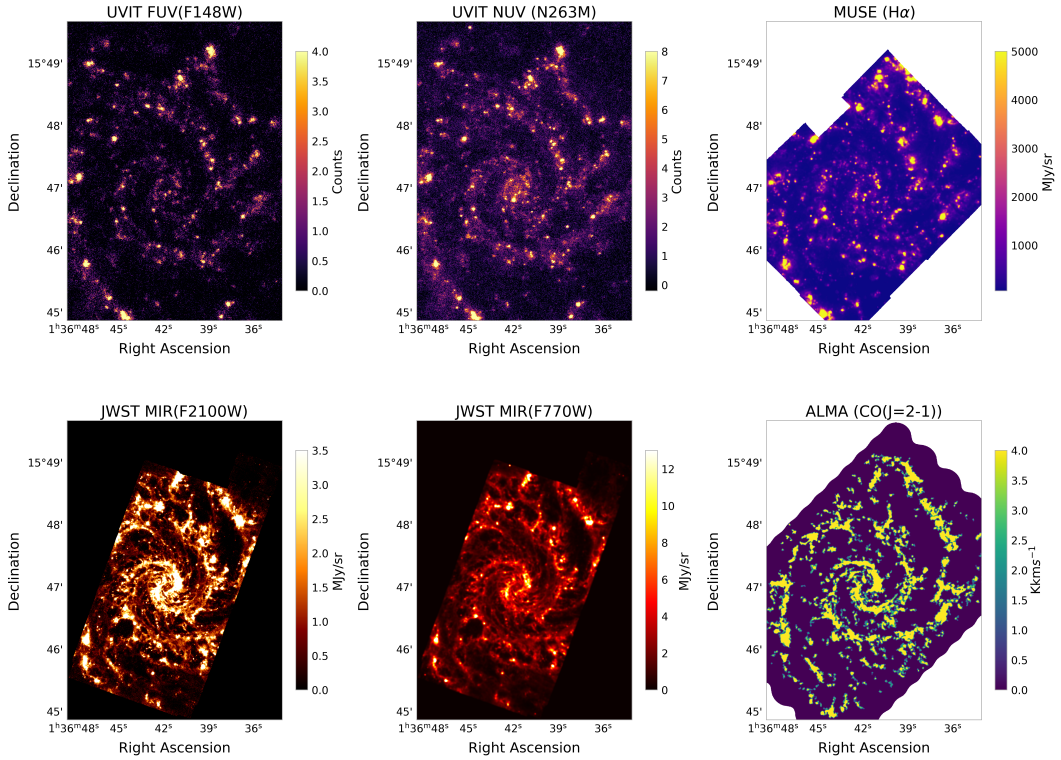


FIGURE 4.1: Multiwavelength images of NGC 628.

variation with properties such as SFR, stellar age, and metallicity (Chastenet et al. 2023; Dale et al. 2023; Ujjwal, Krishnan et al. 2024; Sutter et al. 2024). Thilker et al. (2023) examined the diffuse and filamentary emissions seen in PAH emissions and their relationship to SF. One of the striking features seen in the JWST MIRI (Argyriou, Ioannis et al. 2023) is bubbles and superbubbles formed due to feedback from massive stars and supernovae (SNe) explosions, which has also been the key research topic in galaxies like NGC 628 (Mayya et al. 2023; Barnes et al. 2023; Watkins et al. 2023).

4.2 Data

We used archival JWST MIRI F770W, F1130W images, and NIRCAM F300M, F335M, F360M images to study the PAH emission in NGC 628. We also used

MIRI F2100W for extinction correction. These images are part of PHANGS-JWST (Lee et al. 2023) treasury survey. The F770W and F1130W images have an angular resolution of 0″.269 and 0″.375, respectively. The NIRCAM filters F300M, F335M, and F360M have an approximate angular resolution of 0″.11. We use F770W ($\Delta\lambda = 1.95\mu m$), F1130W ($\Delta\lambda = 0.73\mu m$), and continuum-subtracted F335M ($\Delta\lambda = 0.38\mu m$) images for the PAH analysis. Filters F300M and F360M are used to remove the starlight continuum from F335M by linearly interpolating between F300M and F360M with a varying slope as mentioned in Lai et al. (2020) and as given below.

$$\mathrm{F335M_{PAH}} = \mathrm{F335M} - (\mathrm{A} \times \mathrm{F300M} + \mathrm{B} \times \mathrm{F360M}) \tag{4.1}$$

The coefficients A and B in equation 4.1 are 0.35 and 0.65, respectively, as mentioned in Lai et al. (2020). However, it is observed that the F335M continuum is oversubtracted in the regions where PAH emission is dominant. This is due to the presence of PAH contribution in the F360M band in such regions (Sandstrom et al. 2023).

We used MUSE and UVIT observations of NGC 628 as discussed in the Chapter 3, Section 3.2. All the JWST and MUSE images have been convolved to match the UVIT resolution, with a Full Width at Half Maximum (FWHM) of approximately 1″.2. We utilise these convolved images for further analysis. With this resolution, we are able to resolve OB associations that are approximately 57 parsecs in size.

4.3 Analysis and Results

4.3.1 PAH correlation with the UV and Hα emission

PAHs have been used as SFR tracers (e.g. Rigopoulou et al. (1999); Peeters et al. (2004)), hence we expect that there should be some correlation with the other SFR tracers like UV and Hα emission. The correlation of PAH with SFR has been established in previous studies (Calzetti et al. 2007; Shipley et al. 2016). Earlier studies have used the Infrared Space Observatory (ISO) and Spitzer low-resolution data and broadband MIR emission to establish the relation (Calzetti et al. 2007; Battisti et al. 2015). Apart from this, they have used integrated luminosities of galaxies to obtain this correlation. Therefore, it is important to verify whether this correlation also applies to local SFCs. With the capabilities of the JWST, we can now examine whether the correlations hold in spatially resolved regions such as SFCs.

Here we investigate how the PAH emission from JWST filters correlates with Hα, FUV, and NUV emission. For this purpose, we used a catalogue of SFCs from Chapter 3, which lists the SF properties of SFCs in NGC 628, including UV and Hα luminosities. The method of extraction and classification of SFCs based on emission and location is also outlined in Chapter 3. We overlaid the SFCs on convolved PAH images (F770W, F1130W, and F335M) and obtained the luminosity from each band. We plotted the correlation of different PAH bands with Hα, FUV, and NUV emission as shown in Figure 4.2. We fitted linear regression as given below,

$$\log(\mathrm{L(PAH)}) = \mathrm{A}\log(\mathrm{L(K)}) + \mathrm{B} \tag{4.2}$$

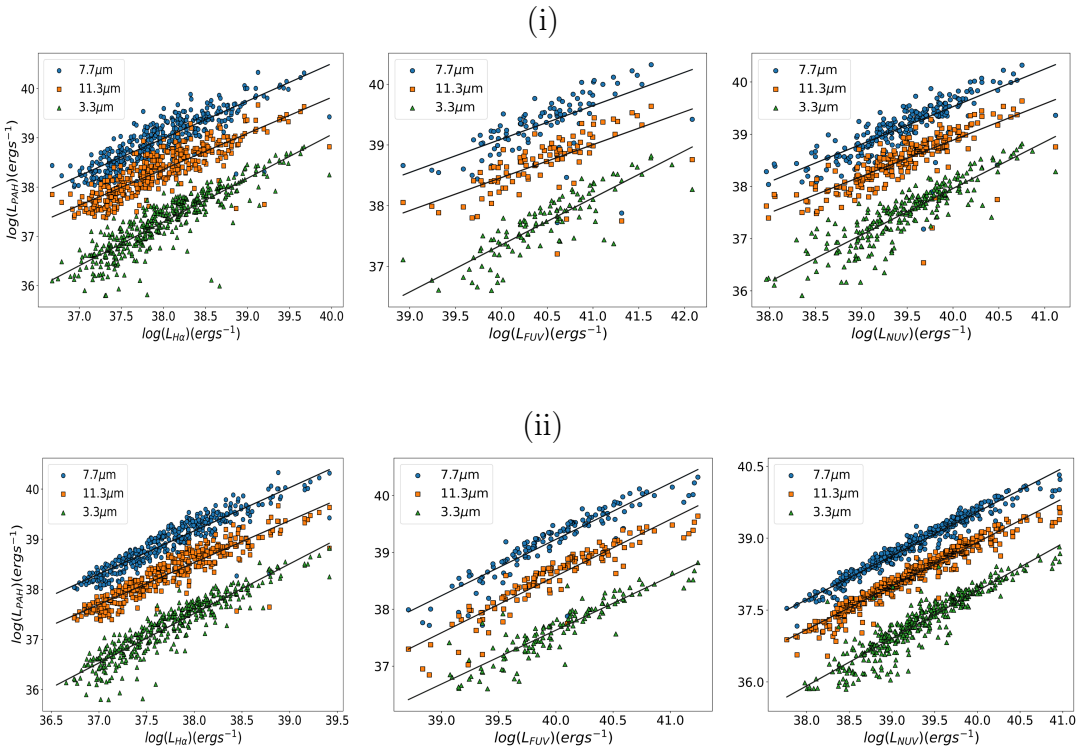


FIGURE 4.2: Correlation of Hα, FUV and NUV luminosities with different PAH luminosities (7.7 μm, 11.3 μm and 3.3 μm). This correlation is for extracted SFCs, whose UV and Hα luminosities are corrected for extinction with (i) the Balmer decrement method and (ii) MIRI 21 μm.

where L(PAH) is PAH luminosity (7.7 μm, 11.3 μm, 3.3 μm) and the term L(K) corresponds to the extinction-corrected luminosity for Hα, FUV, or NUV, with K denoting any of these SF tracers. Both L(PAH) and L(K) are in ergs^{-1}. A and B are fitting parameters as mentioned in Table 4.1.

Shipley et al. (2016) derived the calibration relation between the extinction corrected Hα luminosity and the individual PAH luminosities. The slopes of the linear relation for 7.7 μm and 11.3 μm PAH luminosities are 1 and 0.94 with intercepts of 1.12 and 2.87, respectively. Certainly, there is a clear difference between the parameters of Shipley et al. (2016) calibration relation and those mentioned in Table 4.1. However, the relations mentioned in Shipley et al. (2016) are found for integrated emission from the whole galaxy with very diverse samples, and therefore, there is a lot more scatter in their correlations.

TABLE 4.1: Fitting parameters for equation 4.2.

SF	PAH bands	Balmer decrement method				21 μm method			
Tracer	μm	A	B	σ	ρ	A	B	σ	ρ
Hα	3.3	0.89 ± 0.02	3.11 ± 0.89	0.29	0.89	0.99 ± 0.02	-0.01 ± 0.80	0.23	0.93
	7.7	0.76 ± 0.02	10.12 ± 0.86	0.26	0.87	0.86 ± 0.02	6.43 ± 0.69	0.19	0.93
	11.3	0.73 ± 0.02	10.58 ± 0.89	0.26	0.87	0.84 ± 0.02	6.80 ± 0.72	0.21	0.92
FUV	3.3	0.77 ± 0.04	6.36 ± 1.83	0.27	0.86	0.95 ± 0.04	-0.23 ± 1.59	0.22	0.91
	7.7	0.55 ± 0.07	17.09 ± 2.78	0.37	0.76	0.98 ± 0.04	-0.36 ± 1.5	0.23	0.95
	11.3	0.54 ± 0.06	16.75 ± 2.56	0.34	0.74	0.99 ± 0.04	-1.25 ± 1.48	0.34	0.95
NUV	3.3	0.88 ± 0.03	2.91 ± 1.27	0.28	0.88	0.96 ± 0.02	-0.69 ± 0.87	0.24	0.92
	7.7	0.72 ± 0.03	10.73 ± 1.36	0.29	0.85	0.91 ± 0.01	2.95 ± 0.41	0.14	0.98
	11.3	0.70 ± 0.04	11.02 ± 1.39	0.29	0.84	0.91 ± 0.01	2.47 ± 0.45	0.15	0.98

Note: A and B are the fitting parameters for the equation 4.2, which represents the correlation between PAH bands and SF tracers as shown in the Figure 4.2. σ and ρ represent the standard deviation and Spearman's correlation coefficient of these fits, respectively.

There are very few calibration relations connecting L(PAH) with UV luminosities. Zhang et al. (2021) derived calibration relations for integrated PAH luminosity with both Hα and UV luminosities, and found slopes ranging from 0.865 to 0.842. However, when we examine our correlations for individual PAH bands against Hα and UV luminosities corrected for extinction using the Balmer decrement, we observe significant variations for each PAH band. This variation is primarily driven by the correlation of PAHs with FUV data, as indicated in Table 4.1. FUV shows a shallower slope compared to the other two. One possible reason for this discrepancy is that FUV data exhibit the least sensitivity, which means that, under the same threshold, faint FUV sources may not be included, potentially explaining the limited number of FUV SFCs. We also corrected SFCs for extinction using 21 μm using the MIRI F2100W band as outlined in the previous chapter and found the correlations. We observe that the correlation strengthens and the slope gets steeper than the correlations found for SFCs corrected for extinction using the Balmer decrement as seen in Figure 4.2(ii) and Table 4.1. Despite the discrepancies

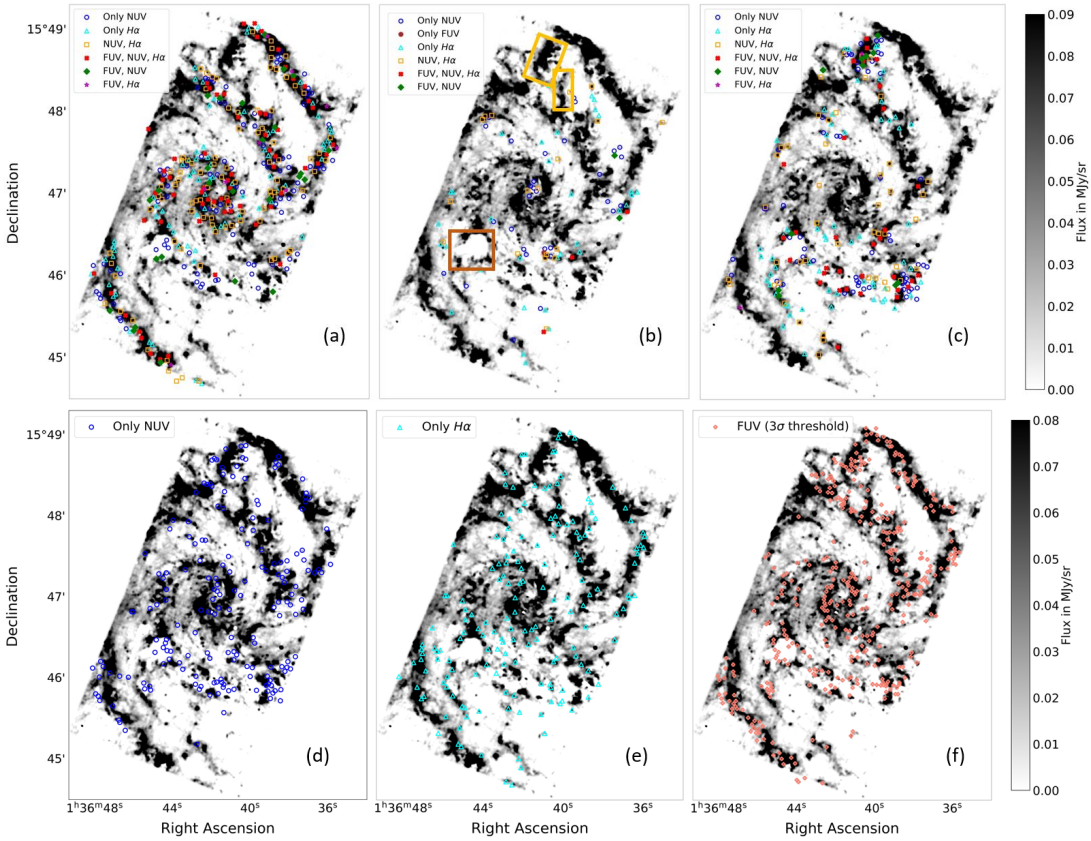


FIGURE 4.3: (i) Association of 3.3 μm PAH emission with arm (a), interarm (b), and spur (c) SFCs. We also plotted the association of 3.3 μm PAH with NUV-only SFCs(d), Hα-only SFCs(e), and FUV emitting SFCs detected with a 3σ threshold (f). The SFCs are overlaid on the continuum-subtracted JWST F335M image. Yellow rectangles in Figure (b) show an example of the spurs, and the brown rectangle indicates the position of the phantom void in NGC 628.

in the correlations, we find that the 7.7 and 11.3 μm PAH luminosity exhibits a flatter linear fit compared to the 3.3 μm luminosity. This indicates that the PAH emitting 3.3 μm is steeply increasing with an increase in UV and Hα luminosity compared to PAH emitting 7.7 and 11.3 μm.

4.3.2 PAH emission across the different regions of NGC 628

In this Section, we investigate the association of arm, spur, and interarm SFCs with PAH emission. For that reason, we overplotted the SFCs on all three PAH images. The association of 3.3 μm PAH emissions with SFCs across the regions, along with NUV-only, Hα-only, and FUV-emitting (3σ threshold) SFCs on the F335M image as shown in Figure 4.3. The association with other PAHs emissions (7.7 and 11.3 μm) is similar to what we see with 3.3 μm.

We find that most of the arm and spur SFCs have associated PAH emissions. The SFCs common in all three wavelengths (Hα, FUV, and NUV), and Hα shows strong PAH emission. However, those that fall on bubbles and superbubbles lack PAH emission as seen in Figure 4.3(d). Most of these SFCs show only NUV emission and are present in the southern arm, which also hosts the phantom void. Very few are FUV-only, and SFCs with both FUV and NUV emissions are also seen in these regions. In Figure 4.3(e), we plotted Hα-only emitting SFCs on the F335M image to see if they also have negligible PAH emission. We found that most of the Hα-only SFCs have a PAH emission. Only some SFCs in the interarm region do not have strong PAH emissions.

As described in Section 4.3.1, SFCs were extracted by applying a constant threshold (5σ) in all three bands. However, SFCs are derived from observations with different sensitivities. The NUV band has a better sensitivity (m_{NUV}=23.36, 690 SFCs) compared to FUV (m_{FUV}=22.78, 195 SFCs). Hence, to see if there are any faint FUV and Hα emitting SFCs in bubble and superbubble regions, we applied a 3σ threshold, which resulted in a FUV sensitivity of $m_{FUV} = 23.4$. We identified 463 SFCs, which is significantly higher than the number we found earlier when the 5σ cut was applied. This sensitivity is comparable to that observed in NUV, where SFCs were detected using a 5σ threshold. However, even by decreasing the

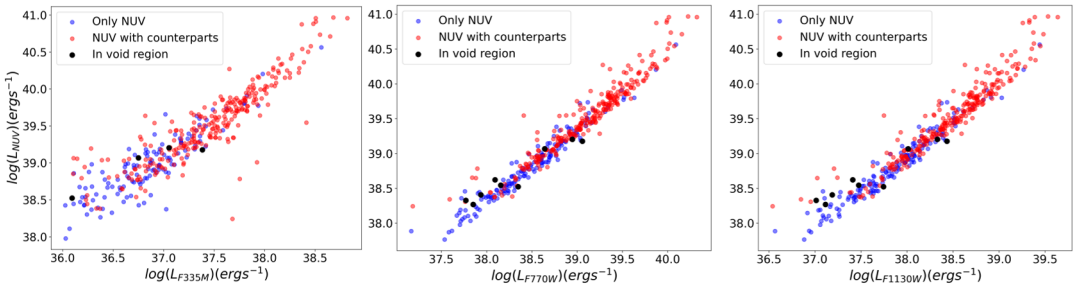


FIGURE 4.4: Correlation of NUV luminosity of SFCs with NUV-only emission and NUV with other counterparts with the different PAH luminosities (From left: 3.3 μm, 7.7 μm, and 11.3 μm). The NUV luminosities of these SFCs are corrected for extinction using the MIRI F2100W μm band.

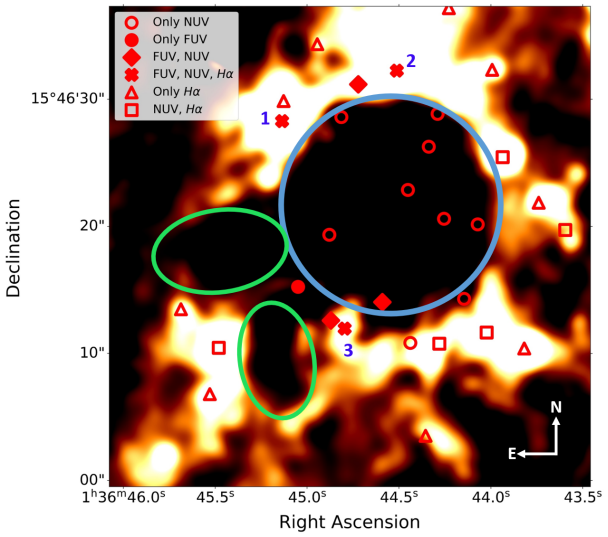


FIGURE 4.5: The phantom void region of NGC 628. The blue superbubble is the phantom void, and the two green ellipses represent the connecting bubbles. The red markers represent the position of SFCs emitting at different wavelengths. The SFCs with both UV and Hα emission are numbered.

threshold, we found that only a few FUV-emitting SFCs are associated with NUV-emitting SFCs in the phantom void. This suggests that the remaining NUV-only emitting SFCs may lack massive stars. A few FUV SFCs are located between the phantom void and two connecting bubbles, as shown in Figure 4.3(f).

We also plotted PAH and NUV luminosity correlations for SFCs with NUV emission, as shown in Figure 4.4. We found that NUV-only emitting SFCs lie at the lower luminosity end of both NUV and PAH luminosity. Since NUV-only emitting SFCs lack Hα emission, we used the MIRI F2100W band for extinction correction

for this correlation. We also checked the correlation for NUV-only emitting SFCs within the void (See Figure 4.5). These also lie in the lower end of both PAH and NUV luminosities.

Only a few interarm SFCs show PAH emission. Many SFCs in the interarm region, especially SFCs with emission in only NUV, only Hα, and SFCs with NUV and Hα emission, do not have much PAH emission (see Figure 4.3(e)). We also find that the region around the galaxy centre is devoid of PAH emission, especially in 3.3 μm. This indicates a dearth of small PAHs in the centre of this galaxy. We found that the SFCs around the centre are either only NUV or with NUV and Hα emission. The presence of Hα emission indicates some recent SF, or it could be emission from diffuse ionised gas.

4.3.3 The variation of PAH band ratios with the IMF for the SFCs

The determination of the IMF indices follows Chapter 3. In this section, we use these IMF values to see how properties of PAH molecules change under different IMF conditions (like when SFCs are top-light or top-heavy).

As explained in Section 4.1, the relative strength of the PAH band ratios gives us information about the size and charge of the PAH molecules in that environment. An increase in the F335M/F1130W ratio indicates that the fraction of small PAH molecules is increasing. Similarly, the fraction of ionised molecules increases with an increase in F770W/F1130W. Recent studies, such as Rigopoulou et al. (2021) and Rigopoulou et al. (2024), use diagnostic grids of PAH band ratios derived using theoretically computed PAH spectra by varying the numbers of carbon atoms, charge, and intensity of exposed radiation fields. These studies reveal the number of carbon atoms in the PAH molecule, the charge composition of the ISM, and

information on what kind of radiation field the molecules are exposed to. Our study uses some of these results to explore the IMF variation with PAH band ratios.

We plotted α_1 and α_2 as a function of PAH band ratios (see Figure 4.6). We found that there is no trend with α_1. It is primarily flat. However, α_2 shows a trend with PAH band ratios. For arms, F335M/F1130W and F770W/F1130W increase as the IMF gets top-heavy, as shown in Figure 4.6. However, the slope is flat for spurs over a range of ratios, and α_2 clumps around values 2.5-3.5. There are a few spur SFCs with a high fraction of smaller and ionised PAH, as seen for arms. This could be the reason for the flattening trend.

For the case where we populated SFCs with O3 to O9 type stars, we retained only SFCs with larger values of PAH ratios. Here again we found that the spurs do not extend to larger values of PAH ratios and are more clumped for α_2.

Besides the correlation of IMF with PAH ratios, we tried to understand the IMF of SFCs in the shell region around the phantom void. Unfortunately, we have only three SFCs with Hα, FUV, and NUV emission. We named these SFCs SFC 1, 2, and 3, as shown in Figure 4.5. The SFCs 1 and 2 have α_2 values of 1.96 and 1.29, respectively, indicating that they are top-heavy. Whereas SFC 3, which is near the connecting elongated bubble, is top-light with a α_2 value of 3.07. We discuss more on the IMF variation with PAH band ratios and the IMF of SFCs in the shell region around the phantom void in Section 4.4.

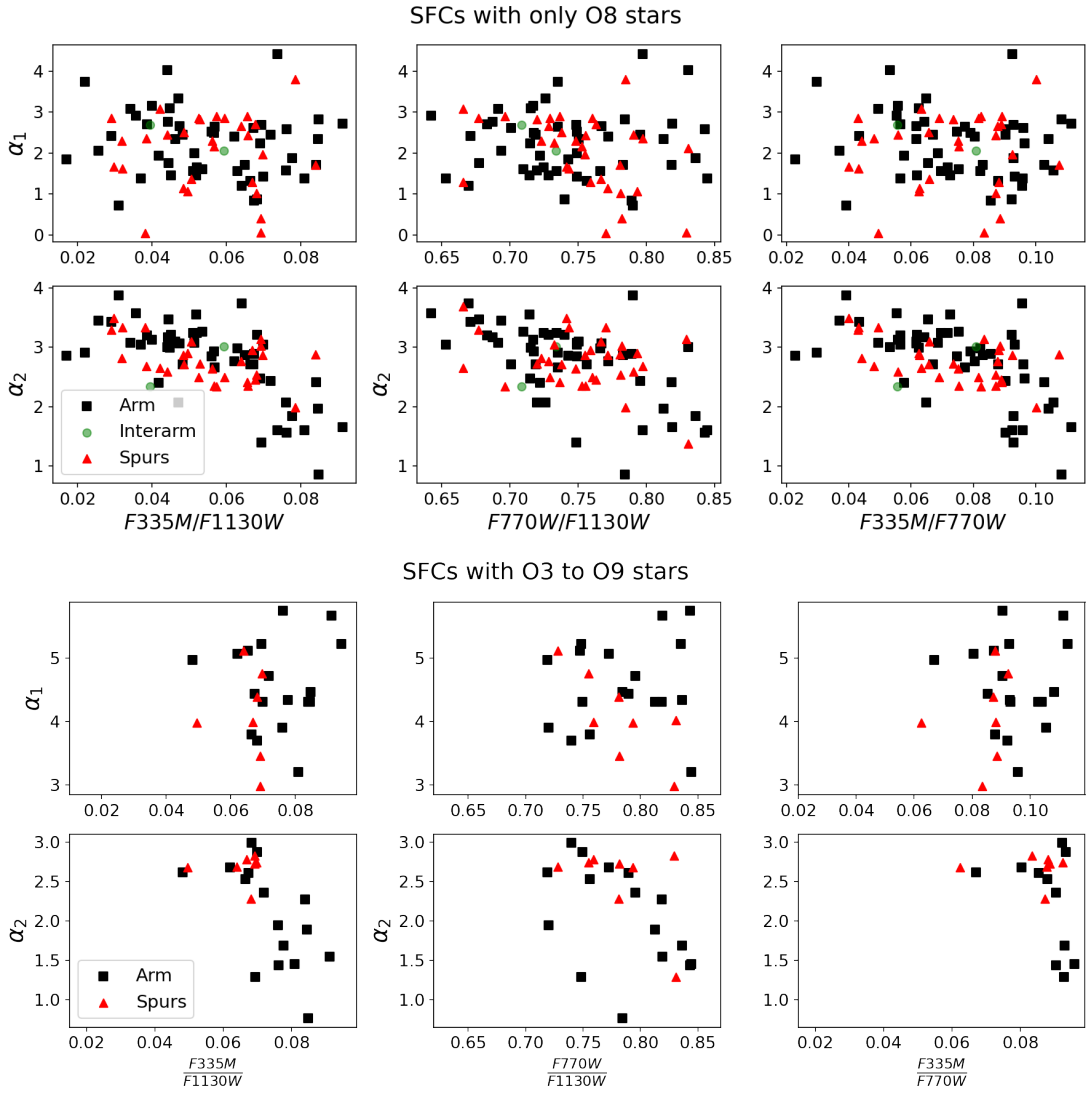


FIGURE 4.6: Variation of IMF index (α_1 and α_2) with the PAH band ratios - F335M/F1130W, F770W/F1130W, and F335M/F770W (from left).

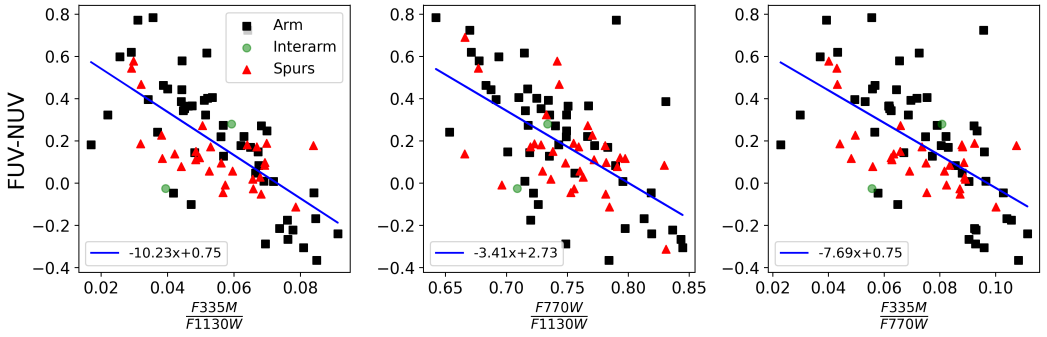


FIGURE 4.7: Variation of FUV-NUV with the PAH band ratios - F335M/F1130W, F770W/F1130W, and F335M/F770W (from left).

4.3.4 The variation of PAH band ratios with the colour for the SFCs

A prominent correlation was observed for α_2 with UV colour FUV-NUV in Chapter 3 (Figure 3.7). It followed a quadratic fit, and FUV-NUV was red for the SFCs with top-light IMF and blue for SFCs with top-heavy IMF, indicating more recent SF in the latter. Therefore, we plotted FUV-NUV as a function of PAH band ratios (see Figure 4.7) for the case with a larger number of SFCs. We fitted linear regression for each ratio as given below.

$$(\mathrm{FUV} - \mathrm{NUV}) = \mathrm{Ck} + \mathrm{D} \tag{4.3}$$

Where C and D are fitting parameters given in the Table 4.2. k is the PAH band flux ratio. As expected, we observe the general trend of the fraction of small and ionised PAH molecules increasing as SFCs get bluer. However, in Figure 4.7, especially for ratios F335M/F1130W and F335M/F770W, we found that more spur SFCs are below the fit than arm in the range $0.1 >$ FUV-NUV> -1. This indicates that for the same colour, the fraction of smaller molecules is higher for arms SFCs than for spurs.

4.4 Discussion

Although PAH emission is used to trace SF, the emission depends on several factors, including the nature of the source exciting the molecules and the surrounding environment. For example, there is less PAH emission from the inter-arm regions. These regions have molecular hydrogen, but SFE is low compared to the spiral

TABLE 4.2: Fitting parameters for equation 4.3.

k	C	D	σ	ρ
F330M/F1130W	-10.23 ± 1.29	0.75 ± 0.08	0.20	0.66
F770W/F1130W	-3.41 ± 0.51	2.73 ± 0.36	0.20	-0.55
F330M/F770W	-7.69 ± 1.15	0.75 ± 0.09	0.20	-0.61

Note: C and D are the fitting parameters for the equation 4.3, which represents the correlation between FUV-NUV and PAH band ratios as shown in the Figure 4.7. σ and ρ represent the standard deviation and Spearman's correlation coefficient, respectively.

arm (Foyle et al. 2010; Kreckel et al. 2016). Besides the inter-arms regions, studies show that there is a central hole in PAH emission in unbarred galaxies (Regan et al. 2006). This absence of PAH emission is attributed to the lack of continuous inflow of gas, which is usually funnelled by a bar. Similarly, in NGC 628, we found that the PAH emission is strong in the compact nuclear region, but is absent in the surroundings 0.1 kpc radius. This could be due to a lack of continuous gas inflow to the central region, which affects the recent SF. Hence, we detect NUV emission from an evolved population, but no FUV emission from recent SF as seen in Figure 4.1.

Apart from the inter-arm and nuclear regions of NGC 628, we also find that the bubbles and super bubbles lack PAH emission. We detected several NUV-only emitting SFCs located within bubble and superbubble regions. A few FUV and NUV-emitting SFCs were also observed in areas lacking PAH emissions. When we lowered the FUV emission threshold, we detected more FUV-emitting SFCs, but very few were found in the PAH-devoid regions (bubbles, superbubbles, and interarm regions). We also found that the FUV-emitting SFCs in such regions have minimal overlap with only NUV-emitting SFCs. The presence of more NUV-only emitting SFCs suggests the presence of stars such as low-mass B stars, A stars,

and other evolved stars in this environment. A few massive stars, such as O-type and massive B stars are found in these regions, potentially contributing to the formation of those bubbles, while more massive ones may have already evolved. This is because NUV emission can trace SF for a more extended period, which is nearly 300 Myr, compared to FUV and Hα (nearly 100 and 10 Myr, respectively). The absence of Hα in these regions may also be due to a lack of ionised gas, which has been expelled by feedback from massive stars or SNe. Hence, the absence of PAH emission and the presence of other SF tracers, such as NUV, can help us understand the progression of SF in different parts of galaxies. However, detailed spectroscopy is needed for understanding the stellar populations.

Interestingly, in the northern arm, some bubbles do not show much association with any of the three emissions, and there are very few NUV-only emitting SFCs. This indicates that these bubbles maybe even older than those in the southern arm and do not show any recent SF. This suggests that the stellar feedback from massive stars of the previous generation, which are now evolved, could have cleared the cold gas necessary for SF. Studies such as Gusev & Efremov (2013); Gusev et al. (2013) have also confirmed the drastic difference in the inner structures between the spiral arms of NGC 628. They suggest that there is a shock wave along the northern arm, which creates high pressure and affects the SF, whereas the regular magnetic field stabilises SF along the southern arm. The other possibility could be that the NGC 628 holes are formed by galactic dynamical processes that include spurring or feathering, and galactic shear caused by the rotation of the galaxy (Watkins et al. 2023).

The prominent super-bubble in the southern arm, the phantom void, has a radius of around 600 pc (Watkins et al. 2023). Two additional bubbles appear to have merged with the phantom void (green ellipses in Figure 4.5). The superbubbles are formed due to the merging of bubbles and are powered by stellar feedback from massive stars, as well as by a series of SNe explosions. They are expected to

be short-lived; hence, low-mass massive stars should still be within them (Mayya et al. 2023). Therefore, we examined SFCs within the phantom void. We find low luminosity, NUV-only emitting SFCs in it (See Figure 4.4), and there are very low luminosity FUV-only emitting SFCs (as we detected only after reducing the threshold) in between the phantom void and the other two connecting bubbles. There is no emission from any of these SF tracers in these connecting bubbles. FUV-emitting SFCs must be much younger than the NUV-only emitting ones, as NUV may come from less massive B and A stars. There is also a clear age-dependent spatial segregation in the stellar population. The study by Mayya et al. (2023) showed that the youngest population is at larger radii up to a radius of 450 pc and is moving away from the centre as the bubble expands. Similar to theirs, we also see that FUV-emitting SFCs are far from the centre of the bubble and the older population, which could be due to the SF triggered in the material swept by the expanding bubble. However, a small number of O, B stars formed in the bubble could explain why faint SFCs are detected.

There is clear evidence of SF in the shell of the phantom void due to positive feedback consistent with Mayya et al. (2023). Figure 4.5 shows that most of the SFCs in the shell having NUV and Hα emission, and very few FUV emitting SFCs. However, we detected a few additional FUV SFCs when we lowered the threshold. This indicates the presence of dust in the shell region, attenuating the FUV emission. Hence, the stars must be very young and embedded in dust. However, PAH is very bright throughout this region, indicating enough PAH molecules and radiation sources to excite the PAHs. We detected only three SFCs with all three emissions and got their IMF. The SFCs marked 1 and 2 show a top-heavy IMF, and SFC 3 shows a bottom-heavy IMF. This could be due to how this structure formed as a whole. We can clearly see in Figure 4.5 that the superbubble in the phantom void is either formed by merging with at least one bubble and/or has been sheared by galaxy rotation. However, bubbles are very short-lived as they are formed by feedback from OB associations. But since we did not find any SFCs in them, the

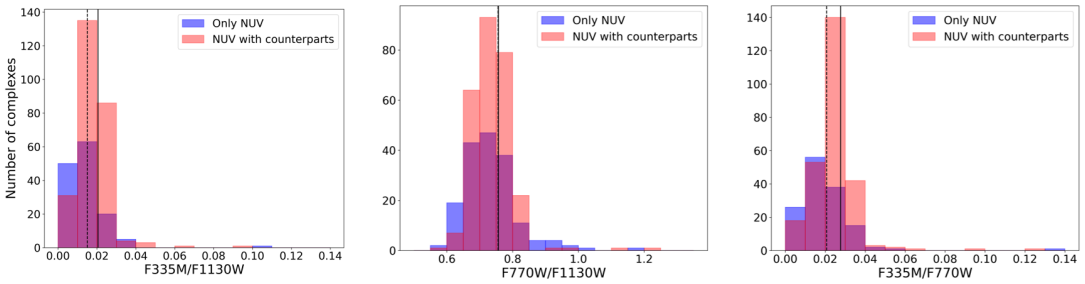


FIGURE 4.8: The distribution of PAH band ratios (F335M/F1130W, F770W/F1130W, and F335M/F770W) for only NUV-emitting SFCs and NUV-emitting SFCs with counterparts in UV and/or Hα.

bubbles must be old and currently powered by massive stars present between them and the phantom void. The elongated shape of bubbles clearly demonstrates the significant impact of shear forces on them. In contrast, the shape of the phantom void near SFC 1 and 2 (at the northeast of the superbubble) is nearly circular, indicating less shear in that region. However, Barnes et al. (2023) have identified the supernova remnants in the shell mainly in the northwest of the superbubble, which might be causing the continued superbubble expansion. Hence, SFC 1 and 2 show top-heavy IMF, as gas here will be very dense, due to the collection of gravitationally bound or unbound gas swept away due to the expansion of the superbubble. The molecular gas near SFC 3, near the elongated bubble, must have experienced some shear, which decreases the gas density and potential to form enough massive stars, making it bottom-heavy. Even in the ALMA map shown in Figure 4.1, we hardly find any molecular gas in that region.

To obtain information on the molecule size and the ionization state of the PAH molecules in different environments, we compared PAH band ratios of NUV-only emitting SFCs with NUV emitting SFCs that have counterparts in at least Hα or FUV to see if there is any difference in PAH molecule properties, as shown in Figure 4.8. We did not find any difference in the median F770W/F1130W ratio; therefore, there is no difference in the charge of PAH molecules for NUV-emitting SFCs with or without any counterparts. However, we find that the median F3350W/F1130W and F335M/F770W ratio for the NUV emitting SFCs with counterparts is slightly

higher than for the NUV-only emitting SFCs, implying a higher fraction of small molecules in the NUV emitting SFCs with counterparts. If we say that NUV-emitting SFCs with counterparts in other bands host massive stars and others do not, then here we see that the presence of massive stars is just slightly influencing the size of molecules present in the ISM, and not the charge.

We even checked the IMF and UV colour trend with the PAH band ratios for arms and spurs. As seen in Chapter 3, only the IMF index α_2 obtained by considering the ratio of B stars shows the trend with PAH band ratios. The trend for cases where we populated Hα SFCs with O7, O8, and O9, and also with only O8, shows a nearly similar trend. Hence, we show only for the former in Figure 4.6. Though the previous chapter showed that there is not much variation between the properties of the arm and spurs, we see that there is some difference in the trends. We find that spurs have only a few SFCs with top-heavy IMF ($\alpha < 2.3$) compared to arm SFCs. As a result, the spurs show a flat trend, mostly clumped between 2 and 4. In contrast, we see decreasing trends in the IMF with the increasing PAH ratios for arms. The lack of SFCs with a top-heavy IMF in the spurs could be due to low molecular gas relative to the arm. Interestingly, we also found that for the SFCs with the same UV colour, the fraction of small PAHs is higher in the arm than in the spurs. However, Schinnerer et al. (2017) showed that the SF is biased towards spurs rather than arms in galaxy M51 and says that the young clusters in spurs are larger, massive, and younger than what we see in the arms. IMF index α_2 is derived from the ratios of massive to less massive B stars, whereas α_1 is from the ratios of the number of O stars to massive B stars. In Figure 4.6, we see that many spur SFCs are top-heavy if we consider α_1, in contrast to α_2. Hence, there might be more young embedded stars in spurs than in arms, as mentioned in Schinnerer et al. (2017). Schinnerer et al. (2017) has also shown that SF in spurs is independent of the spiral arm. However, it is preferred towards the arm within the spurs.

Previous studies on NGC 628 with JWST have shown that star-forming regions or an HII region with a high SFR density show a high value of F335M/F1130W, F770W/F1130W, and F335M/F770W, favouring small and ionised molecules (Chastenet et al. 2023; Egorov et al. 2023; Ujjwal, Krishnan et al. 2024). Even in our study, we found that as the IMF for arm SFCs becomes top-heavy and blue (which indicates recent SF), there is an increase in the fraction of small and ionised PAHs, which is consistent with previous studies. The SFCs with top-heavy IMF will have more massive stars and hence higher UV luminosity. The strong UV radiation density from the compact PDRs of star-forming regions can dominate the particle density, affecting the recombination and ionisation rate. This increases the charged particles in that region (McKinney et al. 2021; Rigopoulou et al. 2024). There will also be an increase in the fraction of shocked gas to total gas in such a high UV radiation region, which can also increase ionised PAHs (Egorov et al. 2023; Chastenet et al. 2023). In contrast, theoretically, small molecules will not survive longer in such an extreme environment (Micelotta et al. 2010). However, with numerical models, it is shown that the shock in dense clouds can cause gas-grain collisions, grain-grain collisions, and also large grain fragmentation, which in turn increases the fraction of small molecules (Jones et al. 1996; Guillet et al. 2011). It is also known that the high UV radiation increases the temperature, resulting in more emissions at lower wavelengths by smaller molecules (Draine et al. 2021).

Chastenet et al. (2023) have shown that the inner disk of NGC 628 does not display much metallicity variation ($8.45 < 12+\log(O/H) < 8.6$). Therefore, properties of PAHs should not be affected by metallicity in different regions of the inner disk. However, trends can vary if there is a contamination by continuum. Though the F335M is continuum subtracted, as discussed in Section 4.2, due to oversubtraction, 3.3 μm PAH might be underestimated. But Sandstrom et al. (2023) also addressed that the aliphatic PAH at 3.4 μm and plateau at 3.47 μm might also contribute slightly to the detected 3.3 μm after continuum subtraction. However,

their strength is very low (8%) compared to 3.3 μm PAH to make a significant variation. Even with the F770W band, approximately 80% of the emissions are from 7.7 μm PAHs, and 70% of the emission seen in the filter F1130W is due to 11.3 μm PAH molecules (Whitcomb et al. 2023). However, Ujjwal, Krishnan et al. (2024) has shown that it doesn't affect the trend.

By comparing PAH emissions with other SF indicators at a resolved scale of 57 pc, we aimed to gain insights into the properties of these star-forming complexes (SFCs) and their surrounding environments. We also observed variations in SF properties across different regions (arms and spurs) in NGC 628 at such small scales. This highlights the significance of examining SF on a local level.

4.5 Summary

In this work, we used PAH maps (F335M, F770W, and F1130W) from JWST observations of NGC 628. We also utilised the catalogue of star formation properties of SFCs of NGC 628 from A&D25, which includes Hα and UV (FUV and NUV) luminosities from MUSE and UVIT, respectively. We used these luminosities to get a correlation with PAH at a scale of 57 pc. We also analysed the PAH emission at the different regions (arm, spurs, interarms, and bubbles) of NGC 628, and the effect of the environment on PAH emission. From the A&D25 catalogue, we used the IMF of the SFCs and derived some important trends with the PAH band ratios (F335M/F1130W, F770W/F1130W, and F335M/F770W) to understand the PAH size and ionised state in arms and spurs. We summarise the main results of our study below,

1. The PAH luminosities show a strong correlation (Spearman's correlation coefficient, $\rho > 0.73$) with FUV, NUV, and Hα luminosities for the extracted SFCs,

even at the scale of SFCs (size $>$ 57 pc).

2. The 7.7 and 11.3 μm PAH luminosities exhibit a flat linear fit compared to the linear fit with the 3.3 μm luminosity. This could be due to a slightly lesser fraction of PAH molecules emitting 7.7 μm and 11.3 μm than the PAH molecules emitting 3.3 μm in the high UV and Hα luminosity region.

3. The PAH emissions are qualitatively well associated with most of the arm and spur SFCs. Most of the only NUV-emitting SFCs lack the PAH emission as they are associated with bubbles and superbubbles. There are also a few FUV-emitting SFCs in the bubbles, in addition to the only NUV-emitting SFCs. This combination of emissions suggests the presence of low-mass B stars, A stars, and a few evolved stars in this environment. Besides, some massive stars like O-type and massive B stars are found in these regions, potentially contributing to the continuous expansion of bubbles and superbubbles.

4. PAH molecules in only NUV-emitting SFCs and in NUV-emitting SFCs with counterparts in at least Hα or FUV exhibit similar charge states, as indicated by their comparable median F770W/F1130W ratios. However, the median F335M/F1130W and F335M/F770W ratios are higher in NUV-emitting SFCs with counterparts than in only NUV-emitting SFCs. This suggests either enhanced emission from small PAH molecules or more efficient excitation of the 3.3 μm PAH feature in the former population. Conversely, the lower ratios in only NUV-emitting SFCs may be consistent with softer radiation fields that reduce PAH excitation.

5. There is a clear age-dependent spatial segregation in the stellar population in the phantom void, consistent with the previous study. The youngest population emitting FUV is at larger radii, far from the bubble's centre, and the older population. This segregation suggests that the recent star formation must have been triggered in the material swept by the expanding bubble.

6. Two SFCs located in the shell region of the phantom void show flatter IMF slopes compared to an SFC near the elongated bubble. This difference may arise from gas accumulation driven by stellar feedback in the shell region, whereas shear in the elongated bubble may hinder the formation of more massive stars.

7. IMF index α_2 derived from the ratio of B stars and UV colour (FUV-NUV), shows a decreasing trend with PAH band ratios (F335M/F1130W, F770W/F1130W, and F335M/F770W). These elevated ratios are commonly associated with enhanced contributions from small and ionised PAHs, although recent studies suggest they may primarily reflect variations in the local radiation field. For a given FUV-NUV colour, arm SFCs exhibit systematically higher PAH band ratios than spur SFCs, indicating stronger PAH excitation and/or different ISM environments in the arm regions.

8. Spur SFCSs have a flat trend with PAH band ratios compared to the arm SFCs. This is because of fewer spur SFCs with a top-heavy IMF.

Chapter 5

Morphological complexity of NGC 628 - a multiwavelength multiscale analysis using the ordinal pattern framework

5.1 Introduction

Complexity of statistical systems is a multifaceted concept, with numerous complexity measures proposed across disciplines (Lloyd 2001; Friedrich et al. 2011; Roli et al. 2019). Traditional complexity measures include Lyapunov exponents (Wolf et al. 1985), entropy (Cover 1999), and fractal dimensions (Mandelbrot 1985), each offering a distinct perspective on the underlying characteristics of complex systems.

Lopez-Ruiz et al. (1995) introduced a statistical measure of complexity based on

the distance of the probability distribution of 'accessible states' of a given system from an equiprobable distribution, multiplied with the Shannon entropy (Shannon 1948). This complexity measure and Shannon entropy encode complementary information of order and disorder. The so-called *complexity-entropy plane* then serves as a phase space on which different physical systems take values, allowing for distinction by their degree of complexity. This characterization of physical systems depends on the 'scale of observations' as the space of accessible states varies with observation scale.

Bandt & Pompe (2002) introduced the so-called *permutation entropy* (H), as an information-theoretic measure of the complexity of one-dimensional empirical data, by constructing accessible states based on comparison of neighboring data values and symbolic dynamics (Balasis et al. 2013). Rosso et al. (2007) extended the formalism and proposed a statistical complexity measure (C) based on the notion of complexity introduced in Lopez-Ruiz et al. (1995), and used the complexity-entropy (CH) plane to distinguish different systems. Ribeiro et al. (2012) and Zunino & Ribeiro (2016) further extended the formalism to two-dimensional (2D) data, which is used to investigate spatial structures (Zunino & Ribeiro 2016; Sigaki et al. 2018, 2019; Morel & Humeau-Heurtier 2021) in image analysis. The formalism of CH-plane has been widely used to distinguish *complex structures* across different physical domains (Mao et al. 2019; Chanu et al. 2024, 2025). Further, one can construct the so-called *ordinal networks* from transitions among accessible states (Pessa & Ribeiro 2019) that can extract additional distinguishing features in different datasets (see e.g., Pessa & Ribeiro (2020, 2021)).

Astrophysical systems - ranging from sunspot cycles, turbulent plasmas, orbital systems to galaxy morphologies and large-scale structure - exhibit rich complexity shaped by nonlinear processes, feedback, and multiscale interactions (Shore & Galli 2003; Regev 2006; Consolini et al. 2009; Aschwanden 2011; Fiore et al. 2024;

Hyman et al. 2025). This paper is focused on the complexity of galaxy morphologies. Galaxies constitute an important dynamical component of our observable universe. Various studies have shown that the morphology of galaxies correlates with their physical properties, including mass, specific star formation rate (sSFR), gas fraction, and integrated colors (e.g., (g–r), (B–V)), among others (Gott & Thuan 1976; Poggianti et al. 2009; Cano-Díaz et al. 2019). For instance, elliptical galaxies are generally more massive than spiral galaxies. Since elliptical galaxies have already consumed most of their gas to form stars, they exhibit low gas fractions and show no recent SF, making them appear red compared to late-type spirals. Thus, morphological classification is crucial for understanding galaxy formation, evolution, and the underlying physical processes.

Existing classification methods primarily rely on visually distinguishing morphological features (Hubble 1936; De Vaucouleurs 1959). More recent approaches use improved photometric and spectroscopic data (Kauffman et al. 1993; Connolly et al. 1995; Yip et al. 2004), and automated intelligent techniques, including machine learning, to classify large numbers of galaxies (Lintott et al. 2011; Zhu et al. 2019; Robertson et al. 2023). There are other non-parametric techniques describing the shape and light distribution of galaxies which are commonly used to classify the galaxies (Lotz et al. 2004; Graham & Driver 2005; Conselice 2006).

The structural and dynamical features of galaxies make them ideal for analysis using tools from the statistical physics of complex systems. In this pilot study, we assess the use of ordinal patterns and associated measures - permutation entropy, statistical complexity, and ordinal network node entropy - for classifying galaxy morphology. We select NGC 628 (the Phantom Galaxy), a well-studied, face-on spiral galaxy with high-resolution, multiwavelength data, meeting criteria for 2D-analysis, emission diversity, and data accessibility. NGC 628 has been extensively studied across a broad spectrum of wavelengths, from radio frequencies to X-rays (see refs Kamphuis & Briggs (1992); Soria & Kong (2002); Kreckel et al. (2018);

Lee et al. (2023)). In this study, we use NUV, NIR, MIR, and mm images to quantify the morphological complexity across wavelengths.

The ordinal pattern framework and in particular the CH-plane has been previously used to study magnetic flux ropes in the corona of the sun (Gekelman et al. 2019), turbulence in the solar wind (Weck et al. 2015; Weygand & Kivelson 2019), electron plasma pressure filaments (Karbashewski et al. (2022)), characterization of exoplanet systems (Gilbert & Fabrycky 2020; Bartlett et al. 2022), x-ray (Lovallo & Telesca 2011) and radio astrophysical sources (Segal et al. 2019). Applying information-theoretic metrics such as entropy and statistical complexity has yielded valuable insights across astrophysical systems. For example, Bartlett et al. (2022) demonstrates that these metrics effectively characterize planetary features and can assist in detecting potential biospheres in exoplanet studies. Weygand & Kivelson (2019) uses them to reveal the stochastic behavior of solar wind structures, including interplanetary coronal mass ejections (ICMEs), co-rotating interaction regions (CIRs), and turbulent magnetic fluctuation intervals. Likewise, Segal et al. (2019) shows their ability to distinguish simple and complex radio galaxy morphologies in the data from the Australia Telescope Large Area Survey.

5.2 Framework of ordinal patterns, permutation entropy, statistical complexity, and ordinal networks

This section introduces the main concepts used in our analysis, namely, ordinal patterns, permutation entropy, statistical complexity, complexity-entropy causality plane, and ordinal networks. This section follows Pessa & Ribeiro (2021).

Consider an $N_x \times N_y$ data matrix Y whose elements are Y_i^j, with $i = 1, 2, \ldots, N_x$, $j = 1, 2, \ldots, N_y$. For a fixed (i, j), let y be a sub-matrix of size $d_x \times d_y$:

$$y = \begin{bmatrix} Y_i^j & Y_i^{j+1} & \ldots & Y_i^{j+(d_y-1)} \\ Y_{i+1}^j & Y_{i+1}^{j+1} & \ldots & Y_{i+1}^{j+(d_y-1)} \\ \vdots & \vdots & \ddots & \vdots \\ Y_{i+(d_x-1)}^j & Y_{i+(d_x-1)}^{j+1} & \ldots & Y_{i+(d_x-1)}^{j+(d_y-1)} \end{bmatrix}. \tag{5.1}$$

d_x, d_y are referred to as 'embedding dimensions'. The smallest choice is $d_x = 2 = d_y$, in which case y is a 2×2 matrix. Moreover, they are chosen to satisfy $d_x \ll N_x$, $d_y \ll N_y$ with $(d_x d_y)! \ll N_x N_y$. This condition is necessary to get a reliable estimate of the ordinal probability distribution, which will be defined shortly.

Let us denote $n_x \equiv N_x - (d_x - 1)$ and $n_y \equiv N_y - (d_y - 1)$. By varying i from 1 to n_x, and j from 1 to n_y in steps of one, we can construct $n_x n_y$ number of such y matrices. In general, the steps for i and j can be arbitrary positive integers, usually known as *embedding delays*. Here we restrict to unit embedding delays.

Permutation state or ordinal pattern: Every sub-matrix y can be mapped to a 'permutation state' or 'ordinal pattern' by the following procedure.

1. *Flatten the elements of y*: Write the elements of y as a one-dimensional sequence denoted by $z = \{z_1, z_2, \ldots, z_{d_x d_y}\}$ (referred to as the 'flattening' step). There is no unique way to flatten y. We choose one way of doing it consistently for all y.

2. *Map z to a symbolic sequence A*: We assign an integer sequentially to each element of z as,

$$\{z_m\} \to \{(m-1)\} \equiv A, \quad m = 1, 2, \ldots, d_x d_y. \tag{5.2}$$

A is a symbolic sequence because its integer elements only serve as position markers or indices for the elements of z.

3. *Sorting and permutation*: Next, the elements of z are sorted in ascending order to get another sequence z_S, resulting in the elements of A getting shuffled or permuted to get another sequence A_S. The new sequence A_S is referred to as a 'permutation state' or 'ordinal pattern'. Other terms such as 'permutation pattern', 'ordinal state', and 'permutation symbol' are also used in the literature.

The steps 1-3 above map every sub-matrix y to a permutation state. We introduce the symbol π_i^j, $i = 1, 2, \ldots, n_x, j = 1, 3, \ldots, n_y$, to denote a permutation state. The sequence $\{\pi_i^j\}_{i=1,2,3,\ldots,n_x}^{j=1,2,3,\ldots,n_y}$ is referred to as the *ordinal sequence*. It is just the set of all $n_x n_y$ number of permutation states obtained from Y. An illustration of the computation of permutation states for an example two-dimensional array is given in below.

Illustration of the construction of ordinal patterns

Let us consider a trivial example where the data Y is a 3×3 matrix given by,

$$Y = \begin{pmatrix} 4 & 9 & 5 \\ 0 & 2 & 7 \\ 2 & 6 & 5 \end{pmatrix}. \tag{5.3}$$

For ease of writing, the data elements are taken to be integers. The actual galaxy data we analyze is real-valued.

Let $d_x = 2 = d_y$ with unit embedding delay. Then $n_x = 2,\ n_y = 2$, which gives 4 sub-matrices. The steps of flattening each sub-matrix y to a sequence z, mapping

z to a symbolic sequence A, sorting z to get z_S, and then obtaining the permuted symbolic sequence A_S, are explicitly demonstrated in the table below.

Sub-matrix		Flatten and map to symbolic sequence		Sort and permute
$y = \begin{pmatrix} 4 & 9 \\ 0 & 2 \end{pmatrix}$	$\Rightarrow$	$z = (4, 9, 0, 2)$ $A = (0, 1, 2, 3)$	$\Rightarrow$	$z_S = (0, 2, 4, 9)$ $A_S = (2, 3, 0, 1)$
$y = \begin{pmatrix} 9 & 5 \\ 2 & 7 \end{pmatrix}$	$\Rightarrow$	$z = (9, 5, 2, 7)$ $A = (0, 1, 2, 3)$	$\Rightarrow$	$z_S = (2, 5, 7, 9)$ $A_S = (2, 1, 3, 0)$
$y = \begin{pmatrix} 0 & 2 \\ 2 & 6 \end{pmatrix}$	$\Rightarrow$	$z = (0, 2, 2, 6)$ $A = (0, 1, 2, 3)$	$\Rightarrow$	$z_S = (0, 2, 2, 6)$ $A_S = (0, 1, 2, 3)$
$y = \begin{pmatrix} 2 & 7 \\ 6 & 5 \end{pmatrix}$	$\Rightarrow$	$z = (2, 7, 6, 5)$ $A = (0, 1, 2, 3)$	$\Rightarrow$	$z_S = (2, 5, 6, 7)$ $A_S = (0, 3, 2, 1)$

We get 4 permutation states (ordinal patterns), which are given by the symbolic sequences A_S. These constitute the ordinal sequence $\{\pi_i^j\}$. Note that $(d_x d_y)! = 4!$ gives 24 possible distinct basis states (ψ_k). The number of elements of $\{\pi_i^j\}$ is less than 24 because Y is 3×3, which violates the requirement $d_x \ll N_x,\ d_y \ll N_y$ with $N_x = 3 = N_y$.

Ordinal probability distribution: Given $d_x d_y$ number of distinct non-negative integers we have $(d_x d_y)!$ distinct states. Under the condition $N_x N_y \sim n_x n_y \gg (d_x d_y)!$, not all states in the ordinal sequence will be distinct. Let us denote each distinct state by ψ_k, where $k = 1, 2, \ldots, (d_x d_y)!$. Let n_k denote the number of occurrences of each ψ_k in the ordinal sequence. Then the probability of occurrence of each ψ_k is given by:

$$\rho_k(\psi_k) = \frac{n_k(\psi_k)}{n_x n_y}. \tag{5.4}$$

The function $P = \{\rho_k(\psi_k)\}$ is referred to as the *ordinal probability distribution*. It satisfies the normalization condition:

$$\sum_{k=1}^{(d_x d_y)!} P = \sum_{k=1}^{(d_x d_y)!} \rho_k(\psi_k) = 1. \tag{5.5}$$

Having introduced the basic concepts of ordinal patterns, we now introduce the statistical quantities that we will use to analyze the galaxy data.

5.2.1 Permutation Entropy, Statistical Complexity, and the Complexity-Entropy (CH) causality plane

Permutation entropy, $H[P]$: The functional $S[P]$ expressed by:

$$S[P] = -\sum_{k=1}^{(d_x d_y)!} \rho_k(\psi_k) \log_2 \rho_k(\psi_k), \tag{5.6}$$

is the entropy of the permutation states (Bandt & Pompe 2002). Then the *normalized* permutation entropy, $H[P]$ (Rosso et al. 2007), is defined as,

$$H = \frac{S[P]}{\log_2(d_x d_y)!}, \tag{5.7}$$

where the normalization factor $\log_2(d_x d_y)!$ is the maximum entropy, thus H satisfies $0 \leq H \leq 1$. H (or S) provides a measure of the degree of disorder or randomness of the data Y, with $H \to 1$ indicating high disorder.

H is exactly one when Y consists of totally random elements and all distinct permutation states are equiprobable, whereas when physical correlations are present in the data across scales set by (d_x, d_y), some states have higher probabilities, hence $H < 1$. The higher the correlation strength, the lower the value of H.

Statistical complexity, $C[P, U]$: Let U denote the uniform probability distribution, $U = \{u_k\}$, with $k = 1, 2, \ldots, (d_x d_y)!$, where $u_k = 1/(d_x d_y)!$. The Jensen-Shannon divergence between the probability distributions P and U is given by,

$$D[P,U] = S\left[\frac{(P+U)}{2}\right] - \frac{S[P]}{2} - \frac{S[U]}{2} \tag{5.8}$$

with permutation entropy of P, $S[P]$ (eq. 5.6), and permutation entropy of U, $S[U]$ given by,

$$S[U] = -\sum_{k=1}^{(d_x d_y)!} u_k \log_2 u_k \tag{5.9}$$

$P+U$ is the mixture distribution of P and U, and its corresponding permutation entropy is

$$S\left[\frac{P+U}{2}\right] = -\sum_{k=1}^{(d_x d_y)!} \left(\frac{\rho_k + u_k}{2}\right) \log_2 \left(\frac{\rho_k + u_k}{2}\right). \tag{5.10}$$

D of eq. (5.8) measures how different P is from U. It is non-zero when there exist more likely states in the space of states constructed from Y.

The so-called *disequilibrium* (Martin et al. 2003), denoted by D_E, is defined as the normalized Jensen-Shannon divergence,

$D_E[P,U] = \frac{D[P,U]}{D_{\max}}$, where $D_{\max}$ denote the maximum possible value of $D[P,U]$ obtained when P is one and U vanishes as: $D_{\max} = -\frac{1}{2}\Big\{\left[\frac{(d_x d_y)!+1}{(d_x d_y)!}\right]\log[(d_x d_y)!+1] - 2\log[2(d_x d_y)!] + \log(d_x d_y)!\Big\}$. D_E (or D) provides a measure of order and organization in the data Y since it measures how far the ordinal probability distribution of Y is from an equiprobable distribution (representing equilibrium). By definition, $0 \leq D_E \leq 1$. Finally, the *statistical complexity*, C, (Rosso et al. 2007) is

defined to be:

$$C = D_E[P, U]\ H[P]. \tag{5.11}$$

Complexity-Entropy (CH) ***plane***: For a given data Y, and for chosen (d_x, d_y) values, the computed values of H and C occupy a point (H, C) on the CH-plane with H on the x-axis and C on the y-axis. Datasets of different physical origins, for example, stochastic processes such as white noise, colored noise, and fractional Brownian motion or chaotic processes such as Lorenz, logistic map will typically occupy distinct regions of the CH-plane and hence can be distinguished (Rosso et al. 2007).

The entropy and complexity measures defined above have various attractive properties (Bandt & Pompe 2002; Rosso et al. 2007). The permutation patterns naturally emerge from the data without the need for any parametrization. Moreover, the results are unaffected by the presence of low levels of noise, invariant under monotonic transformations of the data values, and are also computationally inexpensive.

It is useful to analyze a given 2D-data using different choices of (d_x, d_y) because they probe spatial correlations at varying scales. For a given (N_x, N_y), as we increase d_x and d_y, the total number of permutation states given by $n_x n_y$ decreases, while the number of distinct states $(d_x, d_y)!$ grows factorially. This leads to a decrease of H due to the normalization factor in Eq. 5.7, unless the data contains unusual scale dependence. In comparison, the behavior of C is not straightforward to anticipate. Further, interchanging d_x and d_y is equivalent to rotating the data by 90°, which can yield different H and C if the system lacks rotational symmetry, making such analysis useful for probing anisotropy.

5.2.2 Node Entropies from Ordinal Network

The ordinal patterns from the data matrix Y can be mapped into the nodes of an ordinal network (Small et al. 2018; Pessa & Ribeiro 2019). Each basis state ψ_k corresponds to a node, yielding $k = 1, 2, \ldots, (d_x d_y)!$ nodes. Directed edges connect adjacent basis states (horizontal or vertical), representing *transition* between the states. Suppose $n_{k\to m}$ denotes the total number of occurrences of a transition $\psi_k \to \psi_m$. Then the *weighted adjacency matrix* is:

$$\rho_{k,m} = \frac{n_{k\to m}}{2n_x n_y - n_x - n_y}. \tag{5.12}$$

The denominator represents the total number of horizontal and vertical transitions. Then the normalized transition probability is:

$$\rho^{'}_{k,m} = \frac{\rho_{k,m}}{\sum\limits_{m\in\mathcal{O}_k} \rho_{k,m}}, \tag{5.13}$$

where $\mathcal{O}_k$ is the set of all outgoing edges from node k.

We focus on the entropy measures that take into account the probabilistic nature of nodes and edges *locally*, and *globally* for the ordinal network. The *local node entropy* (McCullough et al. 2017; Small et al. 2018; Pessa & Ribeiro 2020)

$$s_k = -\sum_{m\in\mathcal{O}_k} \rho^{'}_{k,m} \log \rho^{'}_{k,m}, \tag{5.14}$$

measures determinism in the transitions at the node level (Pessa & Ribeiro 2020); $s_k = 0$ if only one edge exits k, and is maximum when all edges leaving k have the same weight (equiprobability).

The *global node entropy* (Pessa & Ribeiro 2020)

$$S_{gn} = \sum_{k=1}^{(d_x d_y)!} \rho_k s_k, \tag{5.15}$$

is the weighted average of local entropies over all nodes of the network, with ρ_k the probability of occurrence of each ψ_k [eq. (5.4)].

5.2.3 Ordinal pattern analysis for Gaussian random fields - a toy example

Before analyzing the morphological complexity of NGC 628, we first evaluate permutation entropy (H), statistical complexity (C), CH-plane, and global node entropy (S_{gn}), as described in subsections 5.2.1 and 5.2.2, for realizations of Gaussian random fields (GRFs), which provide benchmarks for interpreting the galaxy's results.

We simulate GRFs with zero mean and unit variance on a 500×500 pixel grid, approximately comparable to the galaxy data. Uncorrelated, isotropic Gaussian white noise is generated in Fourier space, smoothed using a Gaussian kernel with standard deviation s (in pixel units), and then inverse-transformed. s introduces a characteristic smoothing scale. Hereafter, we refer to this as Gaussian smoothing. Larger s suppresses high-frequency (large k) modes, resulting in smoother, large-scale fluctuations. Conversely, a smaller s retains high-frequency components, producing finer, small-scale structures. We vary s to study how H, C, and S_{gn} change as functions of spatial scale.

Figure A.1 shows realizations of the GRF for a fixed random seed with varying s (top row). We compute H and C for these GRFs, using embedding dimensions: $(d_x, d_y) = (2, 2)$, (2,3), and (2,4). For all (d_x, d_y) pairs, H decreases with increasing

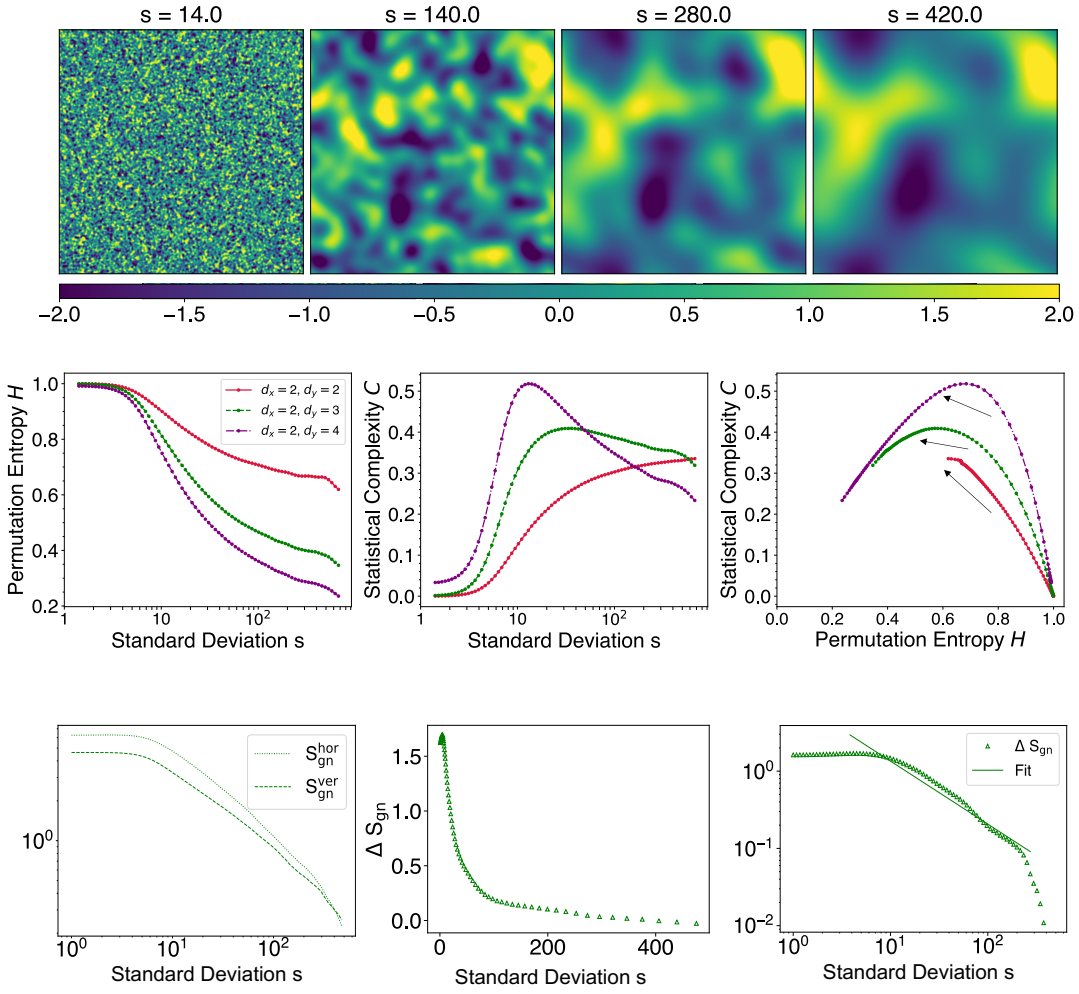


FIGURE A.1: *Top row*: One realization of a two-dimensional isotropic Gaussian random field generated on a grid of 500^2 pixels, with increasing smoothing scales (left to right) given in units of pixel numbers. *Middle row*: Permutation entropy, H, (left) and statistical complexity, C, (middle), as functions of the smoothing scale, for the fields in the top row. The right panel shows the CH-plane. The arrows in the right panel indicate the direction of increasing s. *Bottom row*: Horizontal, S_{gn}^{hor}, (dotted) and vertical, S_{gn}^{ver}, (dashed) global node entropies (left), global node entropy difference, ΔS_{gn}, (middle), as functions of the smoothing scale, for $(d_x, d_y) = (2, 3)$. The log-log plot of the right panel shows an inverse power law fit (solid line) to ΔS_{gn} (triangles) as a function of smoothing scale.

s. This can be visually inferred from the fact that for low s the GRFs contain more modes (hence more information and disorder), while for large s the field becomes smoother and more ordered. For fixed s, H have lower values for higher (d_x, d_y), which is expected (see discussion in sec. 5.2.1).

C exhibits a rapid increase at low s, reaches a maximum (seen for the higher (d_x, d_y) values in Figure A.1, and then tends to decrease. The curves for different embedding dimensions cross each other due to different rates of increase and subsequent decrease with increasing s. For improved visual clarity, we show these H and C results in semi-log plots in the left and middle panels of the second row of Figure A.1.

The right panel presents the CH-plane for the three embedding dimensions, with the black arrows indicating the direction of increasing s.

Limit of perfect correlation: In the above discussion, we focus on smoothing scales s that are in the ballpark range appropriate for the galaxy data in the next section. In the limit $s \to \infty$ (a completely uniform field), the field tends to a constant function, and $H \to 0$, $C \to 0$.

We now map the GRFs at each s to ordinal networks and calculate the horizontal and vertical global node entropies, $\mathrm{S}_{\mathrm{gn}}^{\mathrm{hor}}$ and $\mathrm{S}_{\mathrm{gn}}^{\mathrm{ver}}$, respectively. In the bottom row of Figure A.1, we plot the variation of $\mathrm{S}_{\mathrm{gn}}^{\mathrm{hor}}$ (dotted), and $\mathrm{S}_{\mathrm{gn}}^{\mathrm{ver}}$ (dashed) with s (left), along with their difference, $\Delta\mathrm{S}_{\mathrm{gn}}$ (middle). $\Delta\mathrm{S}_{\mathrm{gn}}$ decreases with s and approaches zero, capturing directional asymmetries at small scales. Next, in the right panel, we fit an inverse power-law function (solid green line) to $\Delta\mathrm{S}_{\mathrm{gn}}(s)$ (green triangles) in a log-log plot, yielding $\Delta\mathrm{S}_{\mathrm{gn}}(s)$=18.58 $\times s^{-1.18}$ with a goodness-of-fit value of R^2 =0.166, indicating not particularly good fit. Investigating similar relations in the NGC 628 data may reveal signatures of self-organization arising from multiscale physical interactions in the galaxy.

5.3 NGC 628 Galaxy - multiwavelength view and observed data

In this section, we describe the multiwavelength imaging data used in our study and also overview physical features observed across the wavelengths of NUV, NIR, MIR, and mm, as shown in Figure A.2(a).

5.3.1 Multiwavelength observed data of NGC 628

We use archival UV observations from the UVIT on board the AstroSat telescope (Kumar et al. 2012). The raw UVIT data is reduced following Amrutha & Das (2025). Multiple filter observations are available for NGC 628. We use only the NUVB4 N263M filter (1365s exposure time).

We use reduced archival data from PHANGS-ALMA (Leroy et al. 2021a,b) CO ($J = 2 \rightarrow 1$) moment 0 map and PHANGS-JWST (Lee et al. 2023) MIRI F2100W * and NIRCam F360M images, both obtained from the PHANGS Treasury. Table 5.1 lists relevant image parameters for the data used in our study.

TABLE 5.1: Image parameters

Image	Central wavelength (nm)	Image PSF (")	Platescale ("/pix)	Pixel unit
UVIT NUV	2.63×10^2	1.2	0.417	counts
JWST NIR	3.6×10^3	0.12	0.063	$MJysr^{-1}$
JWST MIR	2.1×10^4	0.67	0.11	$MJysr^{-1}$
ALMA mm	1.3×10^6	1	0.2	$Kkms^{-1}$

*https://jwst-docs.stsci.edu/jwst-mid-infrared-instrument/miri-observing-modes/miri-imaging#gsc.tab=0

To ensure consistent spatial scales across all four images, we apply interpolation so that the plate size would cover the same area of the galaxy (0.417"/pix). Each pixel corresponds to a physical size of 19.89 pc. We convolve all images to a common resolution of 1.2″ (UVIT) (the poorest resolution among the maps), corresponding to the physical scale of 57 pc. The final images, displayed in Figure A.2(a), consist of 530×311 pixels, spanning $10.54 \times 6.19\,\mathrm{kpc}^2$.

5.3.2 Multiwavelength view of NGC 628

NUV: This emission traces recent SF, predominantly from O, B, and massive A stars over timescales of 200-300 Myr (Thilker et al. 2005). In NGC 628, large NUV star-forming complexes are found in the wider arms and inter-arm regions. A faint UV emission is observed across the disk, especially at the galaxy's center, indicating some evolved stellar populations and scattered dust. NGC 628 has experienced self-regulated SF over the last 500 Myr (Cornett et al. 1994; Zaragoza-Cardiel et al. 2019), owing to the lack of interactions in the past Gyr.

NIR (3.6 μm): This emission traces the bulk of low-mass stars and evolved giants (which have moved off the main sequence), producing smoother, less clumpy arms. The center is bright, with two prominent spiral arms and a visible bifurcation in the top-right arm.

MIR: The emission in MIR is due to re-emission of UV and visible light absorbed by the dust, tracing embedded SF. The MIRI F2100W band (includes 24,μm) reveals bright spiral arms, spurs (Williams et al. 2022), bubbles (Watkins et al. 2023), and web-like inter-arm structures.

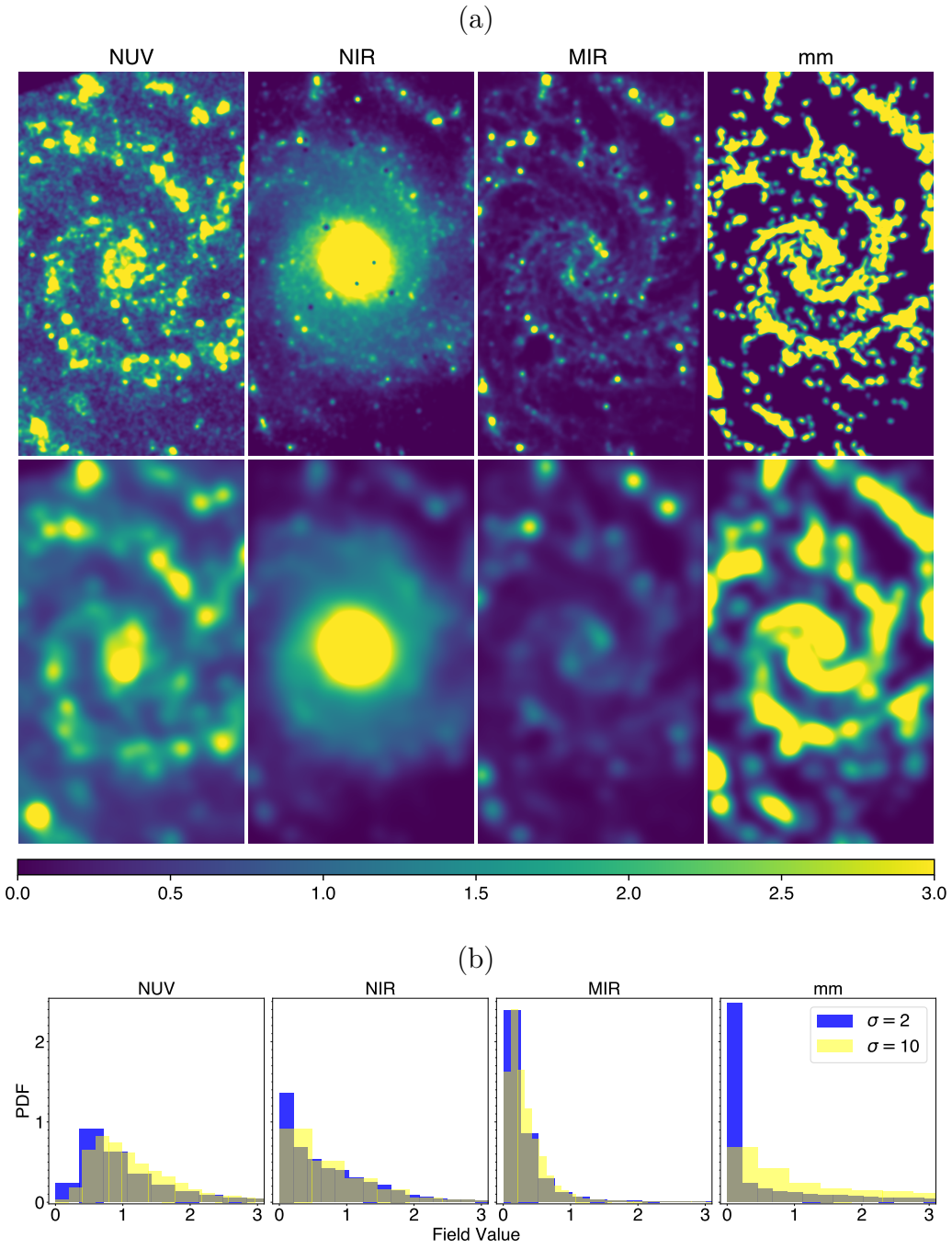


FIGURE A.2: *Top row of (a)*: Images of the galaxy NGC 628 observed at NUV, NIR, MIR, and mm wavelengths (left to right) obtained from UVIT, JWST (NIR and MIR), and ALMA, respectively. All images cover identical fields of view. The intensity values of each image has been normalized by the respective standard deviation. All images are smoothed identically using a Gaussian kernel with a smoothing scale $\sigma = 2$ (in pixels). *Bottom row of (a)*: Same as the top row but for $\sigma = 10$. Image parameters are provided in table 5.1. (b) PDFs of the field values of the four images in (a) corresponding to the top row (blue), and bottom row (yellow).

Millimeter (mm): The mm emission of our data corresponds to the $J = 2 \rightarrow 1$ transition of carbon monoxide (CO) molecules, which indirectly traces cold molecular hydrogen clouds that exhibit clumpy structures. With the ALMA strict map, diffuse emission is filtered out (Leroy et al. 2021a). CO emission is bright throughout the spiral arms and spurs.

5.3.3 Coarse graining images

To carry out a multiscale probe of the structural properties of NGC 628, we systematically perform coarse-graining (smoothening) of the multiwavelength images using Gaussian kernels with different standard deviations σ (in units of pixel numbers). Throughout this paper, we use 'smoothing scale' to mean the standard deviation of the smoothing kernel. This process mimics telescope beam smoothing and enables analysis at varying resolutions. By varying σ, we study small and large-scale morphological features arising from multiscale physical interactions. Figure A.2(a) displays the images smoothed with $\sigma = 2$ (first row) and 10 (second row).

Effective physical scale: The PSF values quoted in Table 5.1 are FWHM values. The common smoothing of all images by FWHM 1.2" corresponds to 57 pc in physical scale, and the corresponding smoothing scale is 24.2 pc. In pixel units, this corresponds to a smoothing scale, denoted by σ_a, of 1.22. Since the smoothing by σ discussed above is in addition to the common smoothing by σ_a, the effective smoothing scale, in pixel units, is $\sigma_{\rm eff} = \sigma\sqrt{1 + (\sigma_a/\sigma)^2}$.

For $\sigma \gg \sigma_a$, we have $\sigma_{\rm eff} \sim \sigma$. Then the physical length scales, which we denote by $L_{\rm FWHM}$, associated with the FWHM value corresponding to $\sigma_{\rm eff}$ is given by

$$L_{\rm FWHM} = 2\sqrt{2\ln 2} \times \sigma_{\rm eff} \times 19.89\,{\rm pc}. \tag{5.16}$$

In section 5.4 we will primarily use the smoothing scale σ for plotting and presenting our results, unless stated otherwise. However, for interpretation in terms of physical length scales we will use $L_{\rm FWHM}$ which is the length corresponding to the smoothing FWHM.

Probability distribution functions at multiwavelengths

The panels in Figure A.2 (b) show the probability density functions (PDFs) of the emissions of NGC 628 at NUV, NIR, MIR, and mm wavelengths, for smoothing scales $\sigma = 2$ (blue) and $\sigma = 10$ (yellow). We observe that all PDFs are right-skewed. For the mm image, we observe a sharp drop in the PDF values for lower field values. A precise modelling of the PDFs is not important for our discussion here.

5.4 Results for NGC 628

In this section, we present the results obtained for permutation entropy H, disequilibrium D_E, statistical complexity C, and network global node entropy $\rm S_{gn}$ for the multiwavelength images of NGC 628. We probe the multiscale nature by smoothing the galaxy field data at different scales σ and using different choices of embedding dimensions (d_x, d_y).

Choice of embedding dimensions: We use combinations of $(d_x, d_y) = (2,2)$, $(2,3)$, and $(2,4)$. These choices are constrained by the total number of available pixels in the data, and the condition for statistical reliability: $(d_x d_y)! \ll 164,830$. Different embedding dimensions explore correlations for varying chunks of data, and this

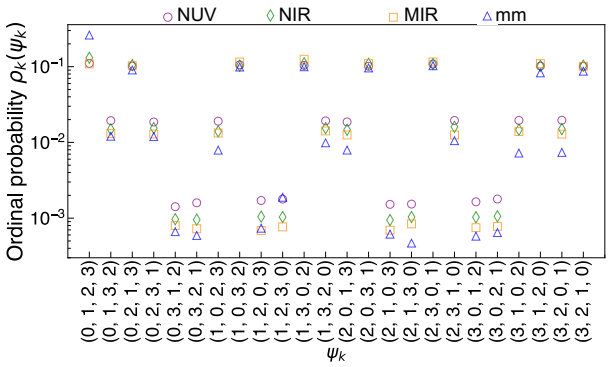


FIGURE A.3: Ordinal probabilities $\{\rho_k(\psi_k)\}$ of the four NGC 628 images when $(d_x, d_y) = (2, 2)$ at smoothing scale $\sigma = 2$.

can potentially reveal distinct structural features that may not be apparent at a single embedding dimension.

The numbers of distinct states, permutation states, and the physical sizes (each pixel rounded off to 20 pc) associated with the three (d_x, d_y) choices are listed as:

(d_x, d_y)	No. of distinct states	No. of permutation states	Physical size in pc^2
(2, 2)	24	163,990	40×40
(2, 3)	720	163,461	40×60
(2, 4)	40,320	162,932	40×80

As a demonstration, we present the ordinal probabilities $\{\rho_k(\psi_k)\}$ for the four images of NGC 628 at $\sigma = 2$ for $(d_x, d_y) = (2, 2)$ in Figure A.3. The x-axis shows the 24 distinct states ψ_k. We see that some states are more probable than others. The manner in which the ordinal probabilities deviate from equi-probable distribution results in distinctive behavior of the statistical quantities (H, D_E, C, and S_{gn}) introduced in section 5.2.

Estimation of errors: We estimate errors associated with the computed values of

H, D_E and C values of NGC 628 as follows. We divide the data into 20 equal-sized patches, each having an area roughly $2.11 \times 1.53\,\mathrm{kpc}^2$. Then treating each patch as independent data, we compute H, D_E and C, and treat the standard deviations from the 20 values as the statistical uncertainties. Note that this way of estimating the errors will slightly underestimate the true errors since the different patches are actually correlated.

The errors of H and D_E will propagate to give the error of C. To quantify this, let σ_H, σ_{D_E} and σ_C denote the standard deviations (errors). Then,

$$\sigma_C^2 = \bar{D}_E \sigma_H^2 + \bar{H} \sigma_{D_E}^2 + 2\bar{H}\bar{D}_E \mathrm{Cov}\,(H, D_E)\,, \tag{5.17}$$

where the bar indicates mean values, and $\mathrm{Cov}\,(H, D_E)$ is the covariance between H and D_E. Intuitively, we expect H and D_E to be anti-correlated, with $\mathrm{Cov}\,(H, D_E)$ being negative. We explicitly compute the covariance and confirm that this is so. Then, σ_C will not be simply related to the quadrature sum of σ_H and σ_{D_E}. For all results shown henceforth, we will use σ_H, σ_{D_E} and σ_C to show the error bars.

5.4.1 Entropy, Disequilibrium, and Complexity for different wavelength images of NGG 628 across scales

Figure A.4 shows permutation entropy (H), disequilibrium (D_E), and statistical complexity (C) as functions of smoothing scale σ at $(d_x, d_y) = (2, 2)$, $(2, 3)$ and $(2, 4)$. From the top row, at all embedding dimensions (d_x, d_y) and in all bands except the mm band, H decreases with increasing σ, consistent with the loss of small-scale structures observed in the images. In the NUV, the emission primarily traces the young and some evolved stellar populations, as well as scattered light from dust. In the NIR, the emission is dominated by low-mass stellar light, with additional contributions from dust continuum and scattered light. In the MIR, the

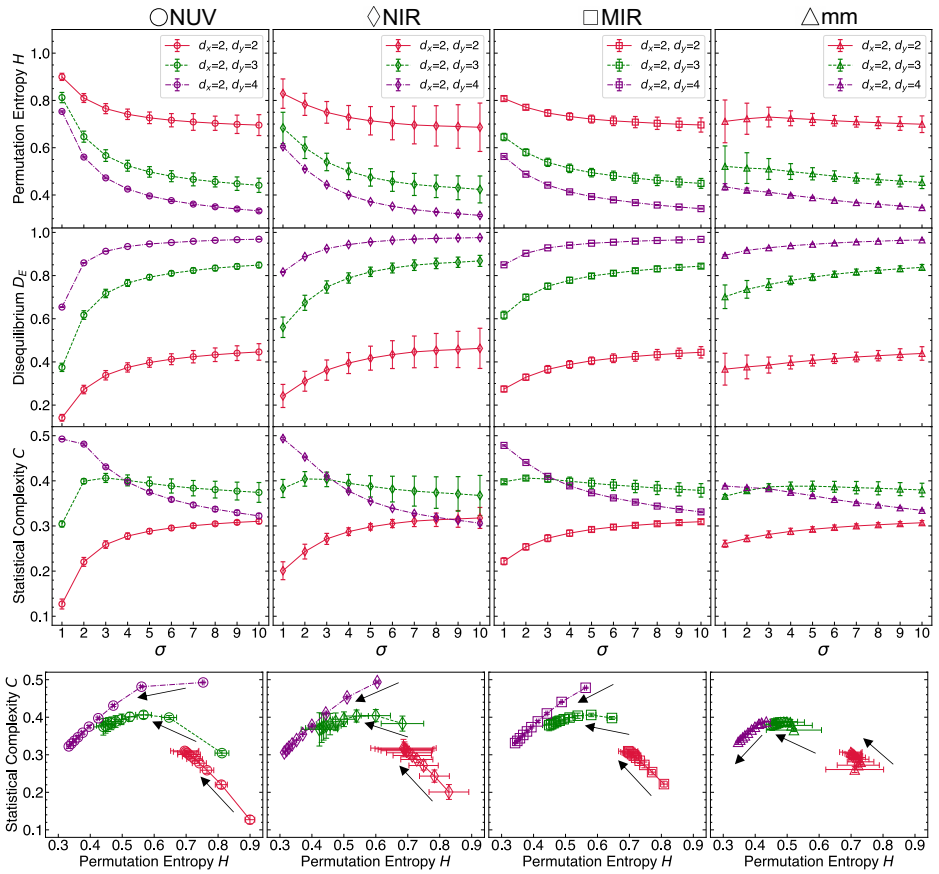


FIGURE A.4: *First, second and third rows*: H, D_E and C computed using (d_x, d_y) = (2,2) (red), (2,3) green and (2,4) (purple) for the four images of NGC 628 shown in Figure A.2 smoothed at different scales σ (in units of 10 pc). The details of the images are provided in table 5.1. *Bottom row*: Values of C and H shown on the CH-causality plane for the three cases of (d_x, d_y) of the four NGC 628 images at different smoothing scales. The black arrows indicate the direction of increasing σ.

emission is dominated by bright, clumpy dust structures associated with the spiral arms, together with diffuse web-like structures in the interarm regions. At mm wavelength, however, H shows only mild variation with σ, reflecting the cold and clumpy nature of the emission and the lack of diffuse structures, as also evident in the PDFs of Figure A.2(b), where mm and MIR have most of the field values around 0. A mild non-monotonic behavior for $(d_x, d_y) = (2, 2)$ at small σ is further explained by the clumpy nature of regions that emit in mm wavelengths, making them less disordered. The second row shows increasing D_E with σ across all wavelengths and (d_x, d_y), indicating greater structural order as fluctuations are

washed out with smoothing. The third row shows the behaviour of C, encoding information of both H and D_E, with σ at different (d_x, d_y), highlighting that different embedding dimensions capture distinct aspects of the galaxy's complexity inherent in different spatial structures of the galaxy field at the given scale.

We observe that for H and D_E, $(d_x, d_y) = (2, 2)$ has the largest error bars, with a drop towards higher embedding dimensions across all wavelengths. The errors tend to increase with σ, except for mm, which shows the opposite trend. Moreover, NIR shows larger error bars relative to other wavelengths, indicating larger fluctuations across the galaxy. MIR shows the smallest error bars, indicating relative uniformity of the fluctuations across the galaxy. We also observe that for C the sizes of error bars do not follow the trends of H and D_E, which is because of $\mathrm{Cov}\,(H, D_E)$ being negative.

The bottom row of Figure A.4 shows the CH-planes parametrised by σ, with the black arrows indicating increasing σ. Across different embedding dimensions, H consistently decreases with increasing smoothing for all images (except mm at $(d_x, d_y) = (2, 2)$). However, complexity C exhibits interesting behaviors: for $(d_x, d_y) = (2, 2)$, C shows increasing trends; for $(d_x, d_y) = (2, 4)$, C decreases; and for $(d_x, d_y) = (2, 3)$, C follows non-monotonic behaviors. Since C $(= D_E \times H)$ reflects the interplay between order (organization) and disorder (randomness), these variations of C reflect distinct complexity inherent in different spatial structures and scales of the galaxy. These results, therefore, highlight the morphological complexity of NGC 628 at multiscales.

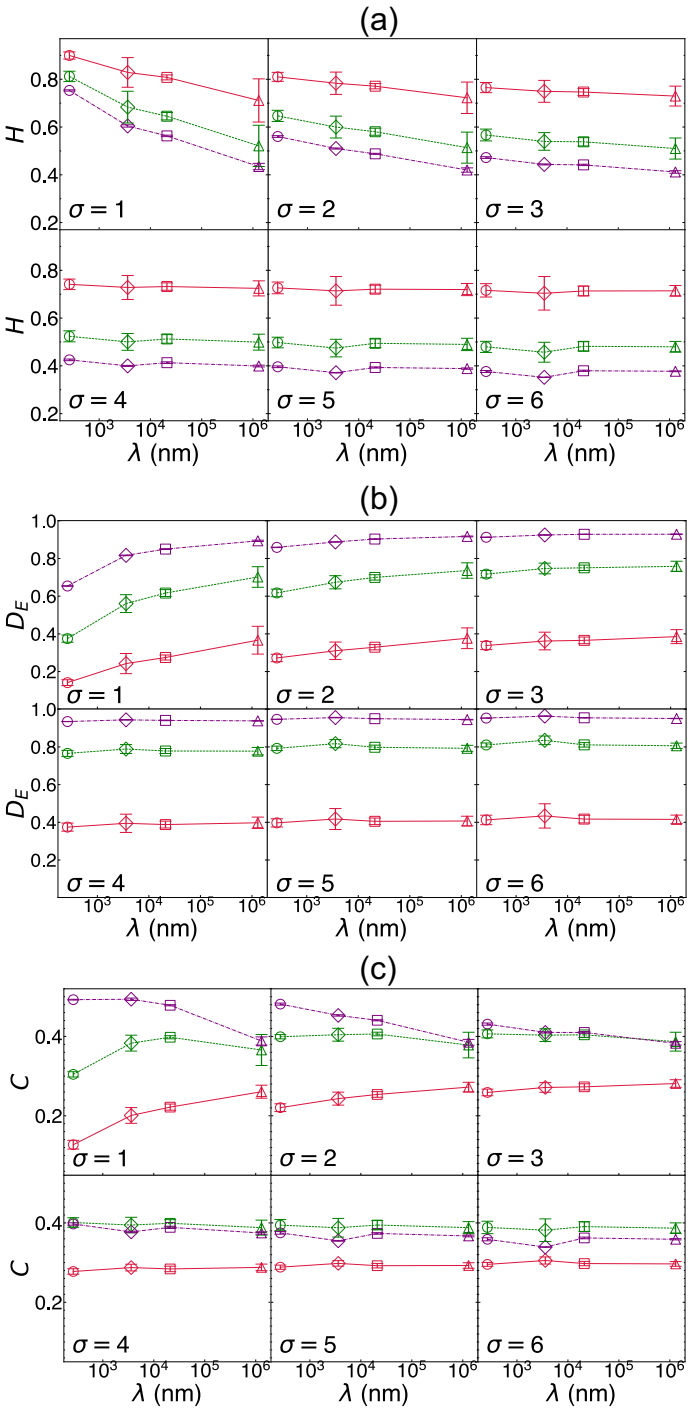


FIGURE A.5: Comparison of H ((a)), D_E ((b)) and C ((c)) as functions of observing wavelength λ (in nm), for each smoothing scale.

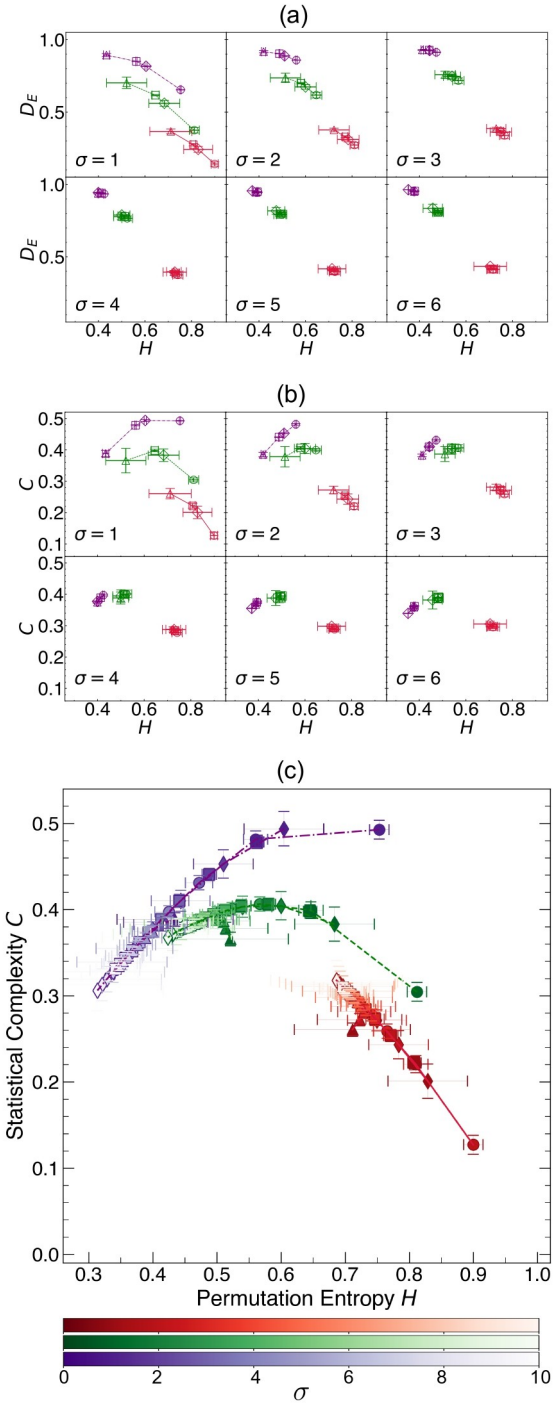


FIGURE A.6: (a) D_E versus H for the four images of NGC 628 shown in the same panel (same markers as Figure A.5), for different σ and (d_x, d_y). (b) CH-plane for different σ. (c) C and H values for all wavelengths and σ are plotted on the same CH-plane. The color bars at the bottom indicate larger σ towards lighter hues.

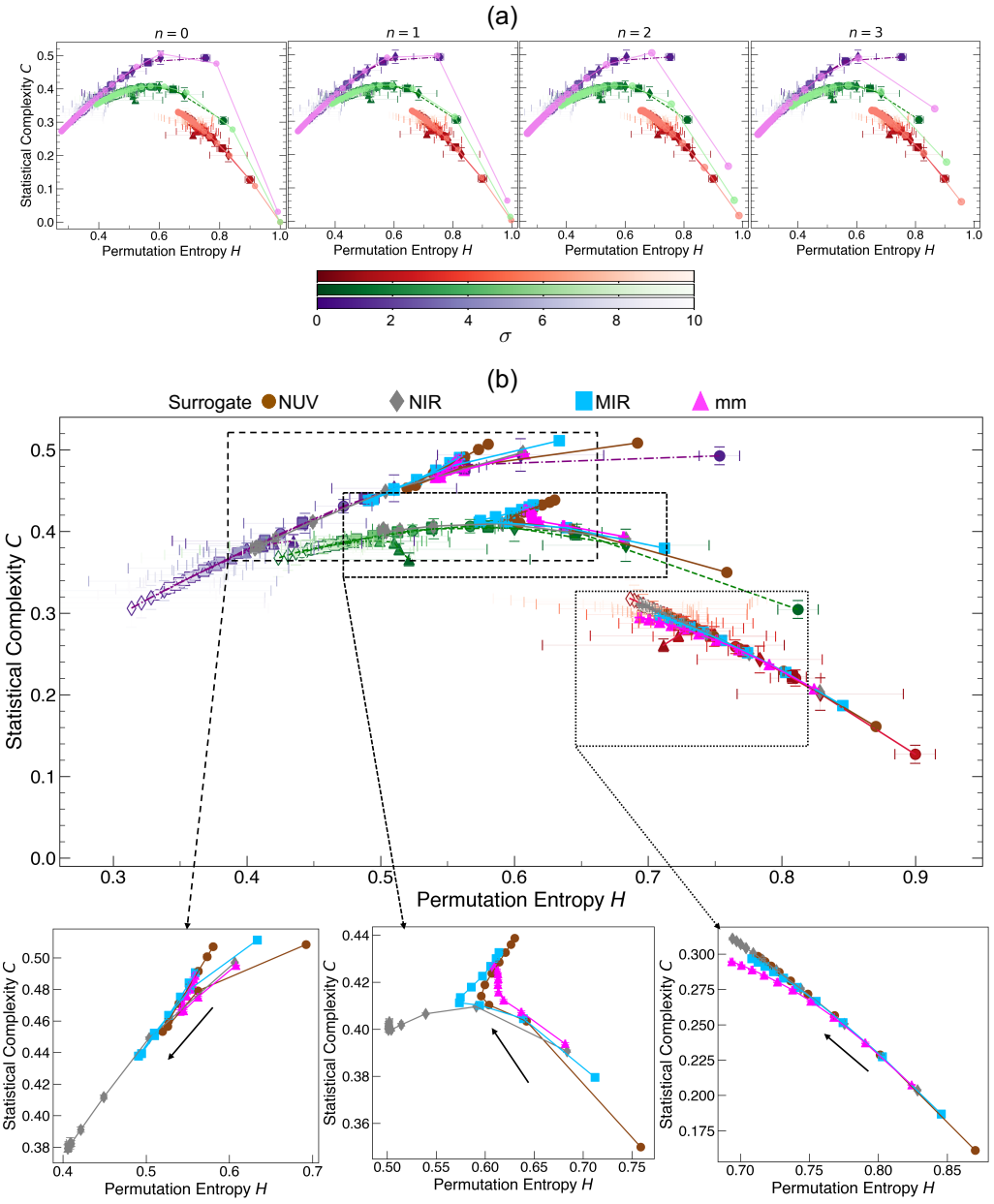


FIGURE A.7: (a) CH-planes for comparison between the four wavelength images of NGC 628 and Gaussian random fields (GRFs) with power spectra of the form $P(k) \propto k^{-n}$ with $n = 0, 1, 2$, and 3. In each panel, we use the same markers and colors (indicated by the color bar) as in Figure A.6(c) for the four wavelengths, whereas the lighter-colored curves now correspond to the GRFs at the three different embedding dimensions $(d_x, d_y) = (2, 2), (2, 3)$ and $(2, 4)$. (b) *Surrogate fields:* In the upper panel, we plot the (C, H) values of the four images of NGC 628 along with the corresponding plots for the surrogate fields (indicated at the top of the panel). The bottom panels show the zoomed-in views of the boxed regions. Black arrows indicate the direction of increasing σ.

5.4.2 Entropy, Disequilibrium, and Complexity of NGC 628 across observing wavelengths

We next examine how H, D_E, and C vary with observing wavelength λ. Figure A.5 shows H, D_E, and C versus λ for $\sigma = 1, 2, \ldots, 6$. The markers and colour codes are the same as in Figure A.4. Figure A.5 reveals two different behaviors in the variation of H, D_E, and C with σ for all λ. For scales $\sigma < 4$, H decreases with increasing wavelength for all embedding dimensions, as seen in panel (a). NUV has the highest entropy, which is explained by the fluctuating nature of star-forming regions across a wide range of spatial scales with diffuse emissions in the entire disk. In comparison, there is a drop of diffuse emissions in NIR and further in MIR, which results in lower values of H. The mm image has the lowest value of H because the emissions primarily originate from cold clumpy regions, and diffuse emissions are not present. Besides, UV emission from massive star associations can photoionize the surrounding gas (Vacca et al. 1996), making fluctuations particularly prominent in the NUV band. Previous studies have also indicated that these associations drive large-scale motions, contributing to turbulence and structure in ISM (Elmegreen & Scalo 2004; Kim & Park 2007). Through stellar winds and supernova explosions, these stars inject energy (Maeder & Conti 1994), and create bubbles and superbubbles, ranging from a few parsecs to several kiloparsecs, which are evident in the JWST MIR observations of NGC 628 (Barnes et al. 2023; Watkins et al. 2023). However, for scales $\sigma \geq 4$, H does not significantly vary with the variation of wavelength as both small-scale structures and diffuse emissions get washed out due to the effect of larger smoothing. Further examination of D_E and C also shows similar constant behavior as H for $\sigma \geq 4$.

Emergence of a transition scale: In Figure A.6(a) and (b), we present the $D_E H$- and CH-planes, where data points corresponding to all four wavelengths (distinguished by different markers) are plotted together for each value of σ. We observe

that, for all embedding dimensions, the values across the four wavelengths converge for $\sigma \geq 4$. This observation reinforces the conclusion drawn earlier from Figure A.5. Hence, based on visual inspection, $\sigma = \sigma^{(c)} \sim 4$ emerges as a critical transition scale beyond which the degrees of order and disorder in NGC 628 exhibit universal behavior across all four wavelengths. Converting $\sigma^{(c)}$ to a physical scale which we denote by $L^{(c)}_{\rm FWHM}$ using Eq. 5.16, we get $L^{(c)}_{\rm FWHM} \simeq 196$ pc as the effective transition length scale.

Physical significance of the transition scale: At scales below $L^{(c)}_{\rm FWHM}$, NUV has the highest H and lowest D_E, with decrease/increase of H/D_E towards higher wavelengths. This trend supports the physical expectation that UV photons generated by stars transfer energy to the ISM, and have a cascading (but delayed in terms of a shift in the values of H and D_E) effect. There exists a hierarchy of scales related to star clusters such as OB associations and stellar aggregates (see e.g. Gusev (2014)); and characteristic scales associated with distinct features of the ISM such as clumps and holes related to stellar winds, supernova bubbles and super-bubbles (arising from multiple supernova explosions) (Kim & Park 2007). The hierarchy of these scales is revealed as the increasing/decreasing part of the plots of H/D_E versus σ. At $L^{(c)}_{\rm FWHM}$ and higher, all wavelengths share the same values of H and D_E, implying that they trace the same structural features. Therefore, $L^{(c)}_{\rm FWHM} \sim 196\,$pc captures the transition from scales affected by SF and stellar feedback, to larger scales where the galaxy's morphology is shaped by global gravitational dynamics.

Attractor curves: An attractor curve refers to a locus in the complexity-entropy (CH)-plane traced by the (H, C) values, where H denotes normalized permutation entropy and C denotes statistical complexity, as a control or observational parameter is varied. Systems with similar underlying dynamical or spatial organization can trace similar loci. Rosso et al. (2007) showed that varying the correlation or control parameters of stochastic processes, such as fractional Brownian motion and

($1/f^k$-noise), and deterministic systems, such as the chaotic Schuster map, produces characteristic CH-curves occupying distinct regions of the CH-plane. In the context of NGC628, the attractor curve is traced by the (H, C) values obtained as the observational wavelength or spatial scale is varied. Therefore, it represents an empirical statistical signature of how disorder and structural organization vary within the galaxy.

The existence of an attractor curve across multiple wavelengths and spatial scales in NGC 628 implies that observations tracing different physical processes, including molecular gas, stars, and dust, share a common multiscale statistical organization despite their different emission mechanisms. This common organization is consistent with the physical coupling of these components through processes governing the interstellar medium and star formation, such as turbulence, gravitational collapse, and stellar feedback. The significance of this attractor curve is that it provides a quantitative statistical signature of NGC 628 that can be used to compare with other galaxies.

Emergence of attractor curves: FigureA.6(c) shows the values of C and H for all wavelengths (distinguished by markers) across smoothing scales, plotted on a common CH-plane. The progression toward lighter colors indicates increasing smoothing scales, as shown by the color bars at the bottom. We see that C and H values tend to align along the same curve at each (d_x, d_y), except the mm image towards small σ. This suggests the existence of an *attractor curve* for NGC 628, for each (d_x, d_y). It is noteworthy that for the smallest embedding dimension H and C span relatively smaller region of the phase space, indicating that larger embedding dimensions are necessary to better probe the structural components of the galaxy.

Further, we generate GRFs with power spectra of the form $P(k) \propto k^{-n}$, where $n = 0, 1, 2$, and 3. The three light-colored CH-curves on each panel of Figure A.7(a)

represent the (H, C) values of smoothed GRFs (parametrised by s and increasing in the same direction as σ) for fixed seeds corresponding to the three embedding dimensions. In each panel, we use the same markers and colors (indicated by the color bar) as in Figure A.6(c) for the four wavelength images. We do not make a comparison between s and σ since the GRF is not a physical field, and we cannot compare the pixel sizes directly. What is of interest to observe is that the CH-trajectories of the GRFs with $n = 1$ align most closely with those of the NGC 628 galaxy field, indicating that the galaxy field shares similar correlation properties with a pink-noise $(1/f)$ spectrum. It further suggests an underlying universality of the attractor curves, despite the differing physical processes traced by each wavelength.

Robustness of our results: To test the effect of rotation of the data, we repeat all calculations for the four image data, as well as the GRFs, after interchanging d_x and d_y (except (2,2), which is symmetric). We find negligible effect of the rotations on all the results. We note that the results would remain invariant under any order-preserving transformation of the data due to the ordinal distributions being the same.

5.4.3 Surrogate analysis as a control study to quantitatively determine the transition scale

Next, to test whether the galaxy's CH-curve is determined solely by its power spectrum, we construct realizations of phase-randomized surrogate Gaussian random fields for each wavelength and smoothing scale σ. These surrogates preserve the exact power spectrum of the galaxy but have randomized Fourier phases, thereby destroying nonlinear correlations while retaining all linear correlations. In Figure A.7(b), we show the mean (H, C) results (indicated by markers and colors at the top of the panel) obtained from 60 realizations of surrogate fields

(with error bars) along with the galaxy results. The three panels in the bottom row show the zoomed-in views of the boxed regions. Black arrows indicate the direction of increasing σ. For $(d_x, d_y) = (2, 2)$ (right panel), the phase-randomized surrogates track the galaxy data reasonably well, indicating that low-dimensional embeddings are dominated by linear correlations, which the power spectrum captures. However, for $(d_x, d_y) = (2, 3)$ (middle panel) and $(2, 4)$ (left panel), the (H, C) values of the surrogate fields begin deviating from the galaxy curve already at small σ, and the deviation becomes particularly strong around $\sigma \sim 4$. This further demonstrates that $\sigma = \sigma^{(c)} \sim 4$ marks a critical transition scale, where nonlinear, phase-dependent correlations present in the galaxy data are no longer reproduced by Gaussian surrogates that match the power spectrum. We interpret the results as follows. Below $\sigma < \sigma^{(c)}$, surrogates lie close to the galaxy curve, and much of the small-scale structure is consistent with what the power spectrum captures for small (d_x, d_y). Nonlinear correlations (turbulence, fractal hierarchy) exist to cause significant deviations for larger (d_x, d_y). Around $\sigma = \sigma^{(c)}$, surrogates begin to deviate significantly, marking the emergence of nonlinear, phase-dependent correlations that cannot be captured by the power spectrum alone. For $\sigma > \sigma^{(c)}$, deviations grow substantially. These scales reflect coherent galactic morphology, requiring a phase-organized structure that Gaussian surrogates cannot reproduce. We note that for NIR, $\sigma^{(c)} \sim 5$ and its CH-curve appears different as compared to the other wavelengths that trace younger stellar populations and molecular gas. Older populations are, in general, more dispersed and form larger complexes (Elmegreen et al. 2006). An additional bright, large structure at the center for NIR might be the reason behind the observed difference.

The transition scale $\sigma^{(c)} \sim 4$ is consistent with the correlation length, $l_{\rm corr}$, inferred using the two-point correlation function for NGC 628 (Grasha et al. 2017; Menon et al. 2021). These studies interpret $l_{\rm corr}$ as the maximum separation over which star clusters remain correlated in the scale-free, turbulent fractal hierarchy generated by SF and stellar feedback. Beyond this scale, the fractal hierarchy breaks

down, and large-scale gravitational dynamics begin to shape global morphology. For a spiral galaxy like NGC 628, $l_{\rm corr}$ marks the shift from a fractal distribution influenced by turbulence to larger scales, where galactic dynamics dominate. Thus, below ∼196 pc, the galaxy contains strong turbulent, fractal, nonlinear correlations, whereas above ∼196 pc, the structure transitions to large-scale, phase-organized morphology that cannot be reproduced by Gaussian fields. The close agreement between $L^{(c)}_{\rm FWHM}$ and $l_{\rm corr}$ supports the interpretation that ∼196 pc represents a fundamental physical transition scale in NGC 628: the boundary between turbulence-driven small-scale structure and large-scale galactic organization.

5.4.4 Disorder to order transition for individual wavelength images of NGC 628 and high resolution JWST NIR and MIR images

The value of $\sigma^{(c)}$ quoted in the previous subsection is inferred from the comparative behavior of H, D_E, and C across wavelengths as a function of σ. Since the scale dependence varies across individual wavelengths, we further analyze the slopes of H and D_E with respect to $\log \sigma$ for each wavelength, as shown versus $L_{\rm FWHM}$ in Figure A.8(a). These plots reveal significant variation among the wavelengths, indicating that the observed emissions arise from a mix of physical processes, each dominating at different spatial scales.

The original JWST NIRCam F360M and MIRI F2100W images have plate scales 3 pc and 5.2 pc, respectively, compared to the 19.89 pc used previously. We recompute H and D_E using full-resolution data (see Table 5.1 for angular resolution) over a broader range of smoothing scales than in FigureA.8(a), enabling finer-scale fluctuation detection. With pixel number of the order of $\sim 10^6$, we now use

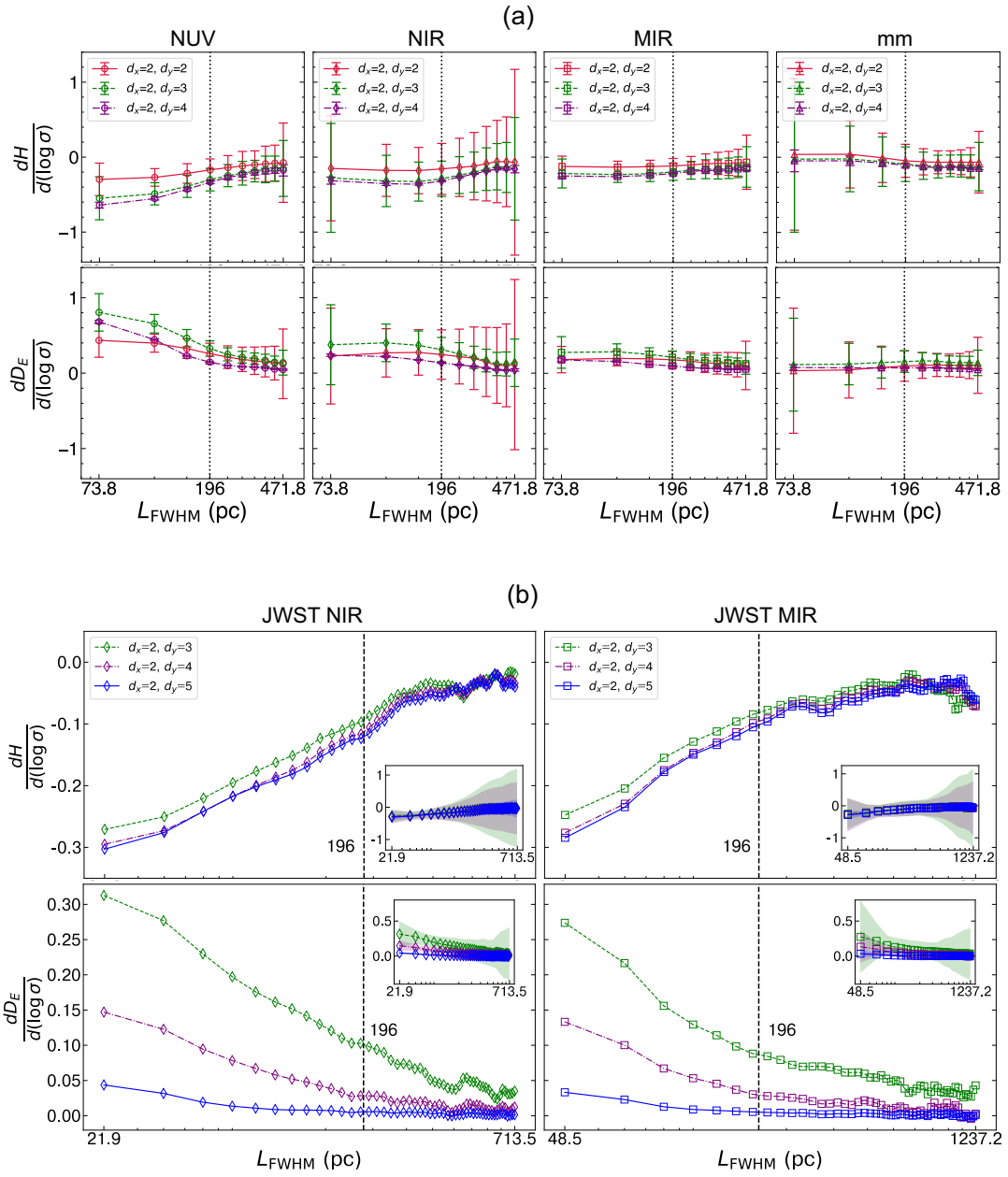


FIGURE A.8: (a) $dH/d(\log\sigma)$ and $dD_E/d(\log\sigma)$ versus $L_{\rm FWHM}$ for the four images of NGC 628. The black dotted vertical line marks $L_{\rm FWHM}^{(c)} = 196\,$pc. (b) Similar plots as in (a) but for high-resolution JWST NIR and MIR images. Insets display the corresponding plots with error bars shown as colored shaded regions. Embedding dimensions are indicated in the legend.

$(d_x, d_y) = (2, 3), (2, 4)$ and $(2, 5)$. The resulting slopes are shown in FigureA.8(b), with uncertainties indicated by the shaded regions in the insets.

While the plots in panel (b) are qualitatively similar to the corresponding NIR and MIR results in Figure A.8(a), they also reveal notable differences that reflect the added sensitivity to small-scale structures. Interestingly, in both NIR and MIR, the slopes of H and D_E flatten and show oscillations on scales larger than 196 pc. This behavior at high σ may reflect statistical fluctuations induced by large-scale galactic structures. Additionally, the associated uncertainties increase with σ, due to the reduced number of independent regions at larger smoothing scales. An important thing to notice is that the embedding dimensions cover a much smaller scale in Figure A.8(b) compared to Figure A.8(a). Hence, small embedding dimensions show more fluctuations at the same large smoothing scales. These fluctuations may also stem from variations in structure size with galactocentric distance, as some large features appear in the galaxy's outskirts. However, this study is limited to the inner disk of NGC 628.

5.4.5 Ordinal Network Global Node entropy S_{gn}

We map the multiwavelength NGC 628 images at different σ (in pixel units) into horizontal and vertical ordinal networks. We compute the corresponding horizontal (S_{gn}^{hor}) and vertical (S_{gn}^{ver}) global node entropies, and their difference ($\Delta S_{gn} = S_{gn}^{hor} - S_{gn}^{ver}$) using $(d_x, d_y) = (2, 3)$ (Figure A.9). The decrease of S_{gn}^{hor}, S_{gn}^{ver} and ΔS_{gn} with σ indicates progressive loss of the overall structural information of the galaxy field with smoothing. We again fit inverse power-law functions: $\Delta S_{gn}(\sigma) = a\sigma^{-b}$ to the data (dashed lines), with exponents: $b = 0.8705$ (NUV), 0.6730 (MIR), and 0.4854 (mm) [R^2-values indicated in the legend]. Entropy decays quickly in NUV (as the structures in this emission seem relatively even without strong clustering), slowly in mm (structures persist across scales with strong

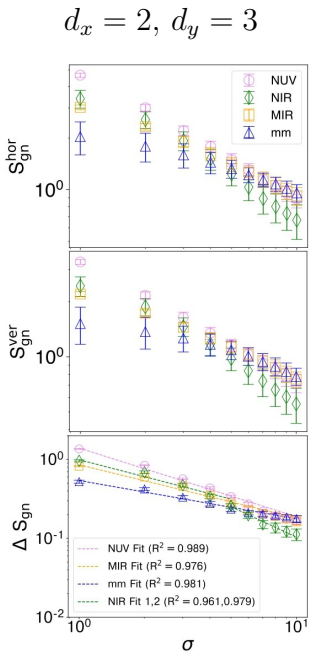


FIGURE A.9: Variation of global node entropy S_{gn} with smoothing scale σ for embedding dimension $(d_x, d_y) = (2, 3)$: Horizontal global node entropy, S_{gn}^{hor} (*Top*), vertical global node entropy, S_{gn}^{ver} (*Middle*), global node entropy difference, $\Delta S_{gn} = S_{gn}^{hor} - S_{gn}^{ver}$, (*Bottom*) versus σ on log-log plots. In the bottom panel, dashed lines represent inverse power-law fits ($\Delta S_{gn}(\sigma) = a\sigma^{-b}$) with corresponding R^2-values for the goodness of fit (indicated in the legend). Values of power-law exponents b are: 0.8705 (NUV), 0.6730 (MIR), and 0.4854 (mm). For NIR, we have fitted in two regimes with $b = 0.6650$ & 1.2920.

clustering), and moderately in MIR (some clustering exists, but not as pronounced as in mm). For NIR, two σ regimes emerge: $b = 0.6650$ for $\sigma < 4$, and $b = 1.2920$ for $\sigma \geq 4$, suggesting a transition from a relatively uniform distribution of low-mass stars at small scales to central bulk emission at larger scales. This result from node entropies further supports the critical transition scale $\sigma^{(c)}$ observed in the preceding subsections.

The observed negative power-law decay of $\Delta S_{gn}(\sigma)$ in NGC 628 indicates a scale-free reduction of structural information, pointing to a hierarchical organization (Barabási & Albert 1999) in the distribution of structures across scales. This hierarchical organization likely emerges from the self-organization (Bak et al. 1988) of various physical processes at multiple scales of the galaxy NGC 628, reflecting

its multiscale complexity.

5.5 Conclusions

This study presents a novel approach to understanding the morphological complexity of the galaxy NGC 628 through the lens of statistical physics of complex systems. We demonstrate how the structural features of NGC 628 can be characterized within the framework of complexity analysis applied to empirical data. Using publicly available multiwavelength imaging data, we systematically analyze NGC 628's morphology across UV, NIR, MIR, and mm wavelengths, probing multiple physical scales. Our analysis employs the framework of ordinal patterns - permutation entropy, disequilibrium, statistical complexity, and ordinal network-based metrics. Taking into account a common field of view - set by the JWST MIR image - and the lowest resolution determined by the UVIT image - for the four images of NGC 628, our analysis probes smoothing scales ranging from 20 to 200 pc, corresponding to a physical extent of approximately 10 kpc.

Our first key finding is the emergence of a characteristic scale near 196 pc, where all structural complexity measures - permutation entropy, disequilibrium, statistical complexity, and global node entropy - show a clear transition. Surrogate field analysis (Figure A.7(b)) further confirms the emergence of this transition scale, marking a shift in the ISM from fluctuations caused by the turbulence acting at the smaller scale to more self-organized structures influenced by galaxy dynamics and global gravitational instability, consistently across all embedding dimensions. The 196 pc scale aligns with the $l_{\rm corr}$, indicating a physical connection and also lends support to the robustness of our method. Our approach quantitatively captures the impact of SF, traced by UV emission, in driving ISM turbulence and enhancing spatial randomness. This effect is weaker in colder, clumpier CO-dominated

regions. Beyond 196 pc, morphological differences across wavelengths become negligible.

Our second main conclusion is that the values of C and H for the four NGC 628 wavelengths trace a single smooth curve on the complexity-entropy plane, which asymptotes towards an 'attractor' trajectory associated with isotropic Gaussian random fields. This suggests a statistically isotropic spatial distribution of the structures in NGC628.

This pilot study demonstrates the effectiveness of ordinal patterns in probing the internal structure of galaxies and linking it to their non-equilibrium statistical states. A natural next step is to extend this analysis to a larger, morphologically diverse galaxy sample. Such a study could identify both distinguishing features for galaxy classification and underlying universal properties. This approach may also be combined with established geometrical and topological methods to uncover finer structural details, e.g., a topological analysis of HI in the Large Magellanic Cloud (Kim & Park 2007) revealed four characteristic scales, each associated with distinct features, clumps, or holes, arising from different physical processes. While our ordinal pattern framework captures structural transition scales, it does not yet differentiate between topological types like holes or clumps or even structures from the SF hierarchy (Gusev 2014). Incorporating such distinctions is a direction we plan to pursue in future work.

Chapter 6

Comparative FUV Study of Star Forming Complexes in Star Forming Dwarf Galaxy Types

6.1 Introduction

Star-forming dwarf galaxies (SFDGs) are abundant in the local universe. They can be classified into dwarf spirals, dwarf irregulars, and BCDs. The dwarf spirals often have spiral arms and small bars or oval bulges (e.g. NGC4136), which are common in normal disk galaxies and are important for triggering SF (Das et al. 2019). However, the spiral arms are not as well-defined as in regular spirals, probably because the stellar disk is not dense enough. Or, as in some cases, the spiral arms can be due to tidal interactions (Stierwalt et al. 2015). On the other hand, dwarf irregulars have a sub-threshold environment for SF, as they generally

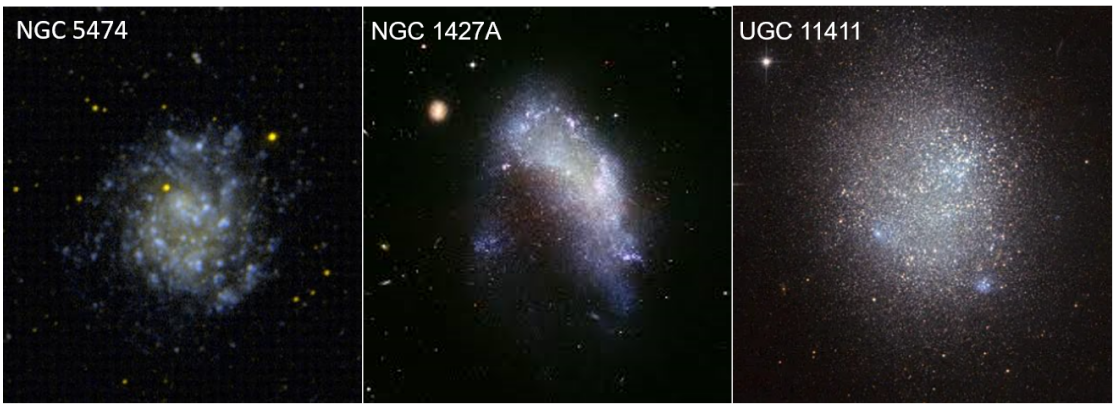


FIGURE A.1: Types of SFDGs. From left: Dwarf Spiral (NGC 5474), Dwarf irregular (NGC 1427A), and a BCD (UGC 11411). Credit: GALEX and ESA/-NASA.

do not have bars or spiral arms nor the critical gas density to form stars (Melena et al. 2009). SF is distributed over their disks and is due to local disk instabilities (Hunter et al. 2010). The third class of SFDGs is the BCDs, which have small, compact star-forming inner disks and diffuse LSB outer disks. The BCDs tend to form superclusters (Adamo et al. 2010; Meurer et al. 1995). Although the origin of the starbursts in BCDs is unknown, one of the main possibilities is that they are merger-driven (Stierwalt et al. 2015). These galaxies are very metal-poor, which gives them a blue appearance.

The main tracers of star formation in galaxies are Hα and Ultraviolet (UV) emission. The Hα is emitted by hot O-type stars, and the emission lasts for 1 to 10 Myr. Far UV (FUV) and near UV (NUV) emission arises from O and B type stars, and the emission lasts for a longer timescale ($\leq 100 - 200$ Myr) compared to Hα (Boissier et al. 2007; Koda et al. 2012). In many galaxies, the UV emission extends far beyond the Hα disk emission (Das et al. 2019), the extreme examples being the extended UV (XUV galaxies) (Thilker et al. 2007). Sensitive observations can trace the Hα and UV emission from the star-forming XUV disks of massive galaxies (Das et al. 2021; Yadav et al. 2021), as well as from nearby dwarf galaxies (Lee et al. 2009a).

In this study, we use UV to trace recent massive SF in nearby SFDGs. We use the UVIT observations of 16 nearby SFDGs to extract and characterize their star-forming regions. The UVIT has a spatial resolution advantage over the previous space UV telescope, GALEX. Previously, Melena et al. (2009) has used GALEX images to characterize the star-forming regions of nearby dwarf irregulars. But as shown by Mondal et al. (2021), the UVIT can extract many more regions than GALEX, giving a better and more accurate idea of the size and distribution of SFCs. Our study uses FUV filters and NUV filters for only a few galaxies, as NUV has not been in operation since 2018.

6.2 Sample Selection

Our study aims to understand SF in dwarf galaxies by resolving their SFCs. Our definition of dwarf galaxies is derived from the study of Leroy et al. (2005), where dwarfs have a stellar mass of $M_* < 10^{10}\,M_\odot$, a typical physical diameter of approximately $10kpc$, and flat rotation velocities of $V_{rot} \leq 100\,kms^{-1}$. To resolve the SFCs, we need high-resolution UV observations of nearby galaxies. For example, galaxies at distances $<$ 20 Mpc are suitable because SFCs of sizes $\sim$ 100 pc in their disks can be resolved. All our sample dwarf galaxies are star-forming and have UVIT data. The sample includes both isolated and interacting galaxies. We proposed some of the UVIT observations, and some were obtained from archival data. In the following paragraphs, we describe our sample, which was mainly derived from the surveys of Leroy et al. (2005) and Hunter et al. (2012). All of them follow the chosen criteria, and the distribution of their properties is shown in Figure A.2.

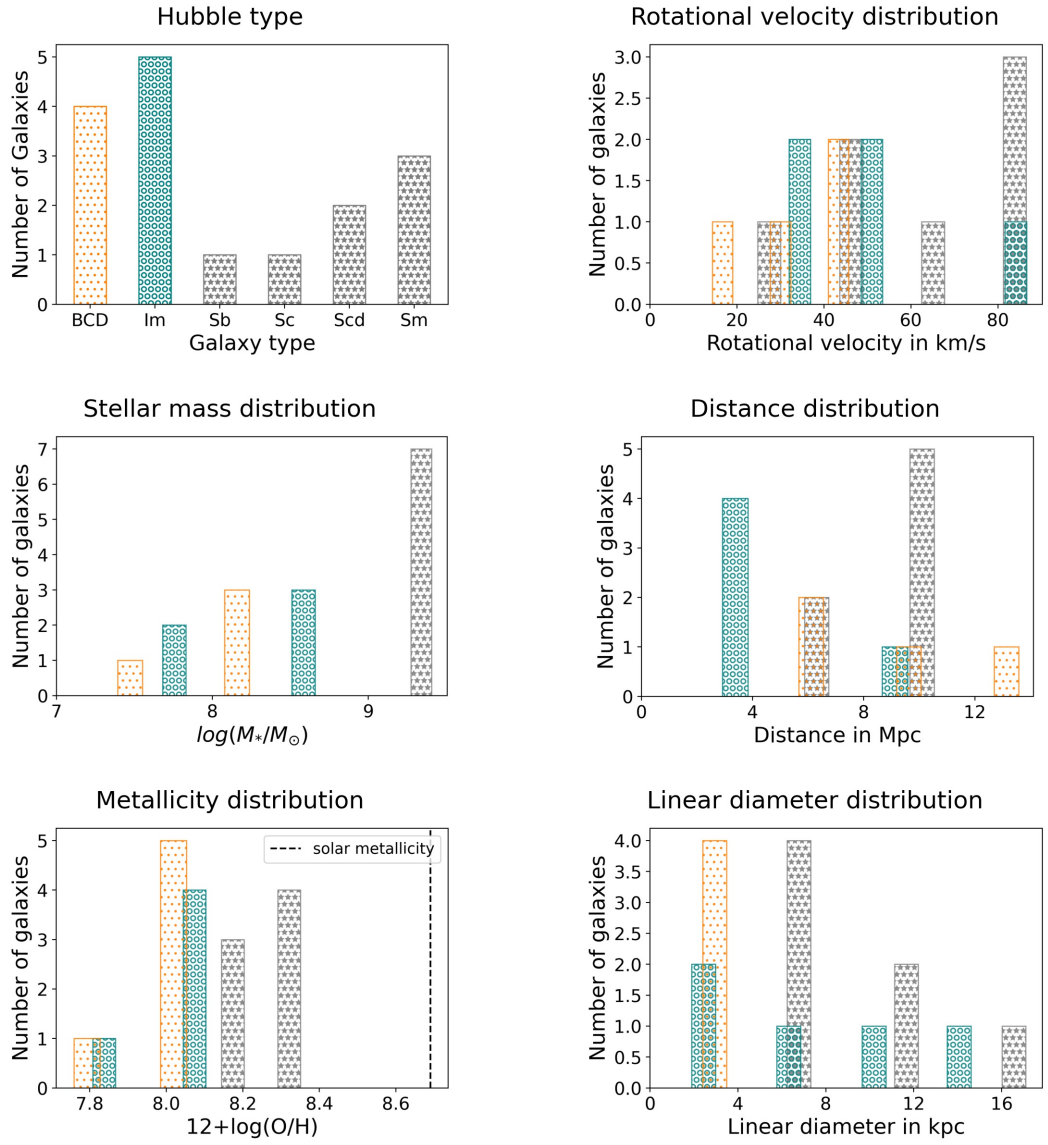


FIGURE A.2: Properties of the sample galaxies. The grey colour with '*' as a pattern represents dwarf spirals, the teal with the pattern 'o' represents dwarf irregulars, and the orange with pattern dots represents BCDs. In these histograms, we see that the dwarf spirals have relatively higher mass and metallicity compared to other types, But they all have similar rotational velocities. All galaxies have subsolar metallicities.

TABLE 6.1: Properties of the sample galaxies.

Galaxy	Type	D (Mpc)	Method	Vrot (kms^{-1})	i (°)	P.A. (°)	r_{25} (')	E(B-V) (mag)	$\log(SFR_{FUV})$ $M_{\odot}yr^{-1}$	$\log(M_{HI})$ $M_{\odot}$
NGC 4136	SAB(r)c	10.9	virgo infall	93.3	0	179	1.17	0.016	-0.80	8.98
NGC 4618	SB(rs)m	9.43	TRGB	67.6	39	25	1.74	0.018	-0.51	9.11
NGC 4625	SAB(rs)m pec	9.43	TRGB	47.4	21	90	0.79	0.016	-1.19	8.68
NGC 5474	SA(s)cd pec	6.8	TGRB	22.1	35	90	1.2	0.01	-0.67	8.96
NGC 5832	SB(rs)b	11	Virgo infall	74.5	47	45	0.93	0.022	-0.96	8.88
NGC 4395	SA(s)m	4.41	TGRB	57.4	35.6	147	6.7	0.015	-0.49	-
NGC 2541	SA(s)cd	12	Cepheids	93.1	64.4	169	1.51	0.043	0.09	9.39
UGC 7608	Im	10.64	virgo infall	46.6	28.9	90	1.73	0.015	-1.22	-
WLM	IB(s)m	0.98	TGRB	26.2	70	1	5.75	0.031	-2.24	7.85
UGC 4305	Im	3.37	TGRB	35.1	52.6	15	3.95	0.027	-1.06	8.85
NGC 6822	IB(s)m	0.5	TGRB	92.4	68	10	7.74	0.203	-1.82	8.11
IC 2574	Irregular	3.9	TRGB	46.9	53.1	50	6.44	0.031	-0.78	9.12
NGC 3738	BCD	5.1	TGRB	52.3	31	155	1.3	0.009	-1.33	8.06
VIIZw403	BCD	4.35	TGRB	14.8	55.8	14	0.75	0.032	-1.94	7.69
Haro 36	BCD	10.53	virgo infall	51.7	43.7	105	0.65	0.013	-1.41	8.16
UGCA 130	BCD	14.9	Virgo infall	35.2	47	8	0.3	0.074	-1.65	7.86

Note: Distance (D), Method and r_{25} (radius of galaxy at 25 B-mag $arcsec^{-2}$) are from Hyperleda * and NED †.

Rotational velocities (Vrot) are from Leroy et al. (2005) and Hyperleda.

Inclination (i) and Position angle (P.A.) are from NED and Hyperleda, respectively.

Galactic reddening E(B-V) is calibrated using Schlafly & Finkbeiner (2011) and taken from IRSA ‡.

$\log(SFR_{FUV})$ is FUV star formation rate as listed in Karachentsev & Kaisina (2013) for all galaxies, except NGC 5832 and UGCA130, for which it is taken from Lee et al. (2009b), and López-Sánchez (2010) respectively.

M_{HI} is neutral hydrogen mass taken from Thilker et al. (2007) for spirals and Hunter et al. (2012) for the irregulars and BCDs except NGC 6822 and UGCA 130, for which it is taken from de Blok & Walter (2000) and López-Sánchez (2010) respectively.

6.2.1 Dwarf Spirals

We have seven star-forming dwarf spirals in our sample, and they are all selected from Leroy et al. (2005). These are the most massive dwarfs with a mass range of $10^9\,M_\odot < M_* < 10^{10}\,M_\odot$, the most massive being NGC 4618 with a mass of $M_* = 10^{9.56}\,M_\odot$ (see Table 6.6). Most of these dwarfs are late-type spiral galaxies, and their metallicity is higher than the other two classes. Some are fairly extended. NGC 4395 has the largest diameter ($D_{25} = 16.9\,kpc$) in our sample. Also, most of our dwarf spirals are classified as Extended Ultraviolet galaxies (Thilker et al. 2007). Some of them are also interacting, such as NGC 4625 and NGC 4618, which are interacting with each other, and with NGC 4625A that lies between them (Gil de Paz et al. 2007). The galaxy NGC 5474 is probably interacting with the giant spiral M101 (Mihos et al. 2013; Bellazzini et al. 2020). For the other 4 spirals, we do not find any sign of interaction.

6.2.2 Dwarf Irregulars

We have 5-star-forming dwarf irregulars in our sample. Most of these are from the Local Irregulars That Trace Luminosity Extremes, The HI Nearby Galaxy Survey (LITTLE THINGS; Hunter et al. 2012). Besides this, we also included UGC 7608 from Smith et al. (2021). Dwarf irregulars have stellar masses $\leq 10^9\ M_\odot$ and are generally smaller than dwarf spirals. The largest in this group is IC 2574, which has a diameter of $D_{25} = 14.61\,kpc$; this is high compared to the typical sizes of dwarf galaxies. The irregulars are at closer distances compared to the other two types of dwarfs. For example, NGC 6822 and WLM are at distances of 0.5 Mpc and 0.98 Mpc, respectively. NGC 6822 is one of the nearest dwarf galaxies around the MW, and it may have interacted with the MW as well as with other dwarf

galaxies (Zhang et al. 2021). The irregular galaxy UGC 4305 is part of the M81 group and is infalling towards M81 (Bureau & Carignan 2002).

6.2.3 Blue Compact Dwarfs

We have 4 BCDs. NGC 3738, VIIZw403, and Haro 36 are from LITTLE THINGS. We included UGCA 130 from Leroy et al. (2005). BCDs have smaller diameters compared to dwarf spirals and irregulars. In our sample, their diameters are less than 1.5′. Hence, they appear to be very compact and very bright in UV. The BCD UGCA 130 is the farthest galaxy in our sample. We do not see any sign of interactions in the BCD sample.

6.3 Observations

We performed deep UV imaging observations of the galaxies NGC 7608, NGC 4136, NGC 4625, NGC 4618, NGC 2541, and NGC 5832 using the UVIT on board the AstroSat telescope (Kumar et al. 2012). For all other galaxies, we used archival UVIT data. The details of the UVIT filter and exposure time of galaxies are given in Table 4.2.

The UV radiation emitted by the young stars is absorbed by interstellar dust and re-emitted in the IR band, mainly around 24 μm. Hence, we used 24 μm images from the MIPS instrument in our study (Rieke et al. 2004). The resolution of this 24 μm image is 6″. The data reduction procedure of the MIPS image is mentioned in Gordon et al. (2005). All the images we used here are reduced archival images. We used background-subtracted images for our analysis.

TABLE 6.2: UVIT Filter and Image Information.

No	Galaxy	Other names	FUV filter	Exptime (s)	PSF	NUV filter	Exptime (s)	PSF
1	NGC 4136	UGC7134	CaF2	3640.447	1	-	-	-
2	NGC 4618	IC3667; UGC7853 ARP23; VV73	CaF2	5893.002	1	Silica15	1576.123	1.2
3	NGC 4625	IC3675; UGC7861	CaF2	5893.002	1	Silica15	1576.123	1.2
4	NGC 5474	UGC 09013; VV 344b	BaF2	1500.408	1	NUVB4	763.004	1.1
5	NGC 5832	UGC 09649	CaF2	1976.753	1.1	NUVB13	1691.195	1.3
6	NGC 4395	UGC 07524	CaF2	709.967	1.1	NUVB15	6386.25	1.2
7	NGC 2541	UGC 04284	BaF2	2660.16	1.1	NUVB15	1759.857	1.2
8	UGC 7608	DDO 129	CaF2	7543.797	1	-	-	-
9	WLM	UGCA 444; DDO 221	CaF2	5078.986	1.2	Silica15	2706.837	1.1
10	UGC 4305	Holmberg II ARP 268; DDO 050	CaF2	18229.966	1.1	NUVB13	9607.65	1.1
11	NGC 6822	IC 4895; DDO 209	CaF2	4085.606	1.1	Silica15	315	0.9
12	IC 2574	UGC 05666 DDO 081; VII Zw 330	CaF2	9871.635	1.1	-	-	-
13	NGC 3738	UGC 06565; ARP 234	BaF2	2659.343	1	-	-	-
14	VIIZw403	UGC 06456; VV 574	BaF2	2649.006	1	Silica15	2792.765	1
15	haro 36	UGC 07950	BaF2	1584.729	1	-	-	-
16	UGCA130	MRK 0005	CaF2	4617.873	1	-	-	-

Note: Other names are as listed in NED. Only few galaxies have UVIT NUV filter information as it has stopped working since 2018.

Emission from older stellar photospheres is studied using 3.6 μm wavelength images. As the stellar mass of a galaxy is mainly due to an older population, we used the 3.6 μm luminosity to calculate the stellar mass density of the galaxies. The 3.6-micron images were from one of the four cameras, the IRAC cameras on Spitzer (Fazio et al. 2004). It has an angular resolution of 2″ and has a FOV of 5′. It has a good sensitivity compared to the other three cameras in the instrument.

*https://leda.univ-lyon1.fr/
†https://ned.ipac.caltech.edu/
‡https://irsa.ipac.caltech.edu/applications/DUST/

6.4 Data Analysis

6.4.1 Data Reduction and Source Extraction

We downloaded UVIT L1 data (raw) from the ISSDC website for all the sample galaxies. We reduced the raw data as outlined in Section 2.1.1 and used a background-subtracted science-ready image for our further analysis. Using Python, we cut out the image of the galaxies from the entire field of view of UVIT. Then we used the SExtractor (Bertin & Arnouts 1996; Barbary 2016) to extract the SFCs from the cutout image. We had set the detection threshold to 8 σ and minimum area to 10 pixels as recommended by Bertin & Arnouts (1996) for clean and confident detection.

While detecting sources, we may even detect some foreground sources. To eliminate such sources, we found bright sources around a galaxy centre in Gaia, within a radius comparable to the field of view of the cutout image. These foreground sources have parallax and high proper motion. We matched the RA and Dec of the SFCs detected with SExtractor with the RA and Dec of the sources obtained from the Gaia catalogue using TOPCAT (Taylor 2005). If the matched sources had high parallax and high proper motion, we masked those sources using Python.

We found the deprojected area of the remaining SFCs, which is given by

$$\text{area} = \frac{\pi \times \text{a} \times \text{b}}{\cos(\text{i})} \tag{6.1}$$

with a and b as the semi-major and semi-minor axes of an ellipse fitted to the SFCs, respectively, and ‘i‘ is the angle of inclination of the galaxy. We found the approximate size or radius of the SFCs by equating this area to the area of a circle.

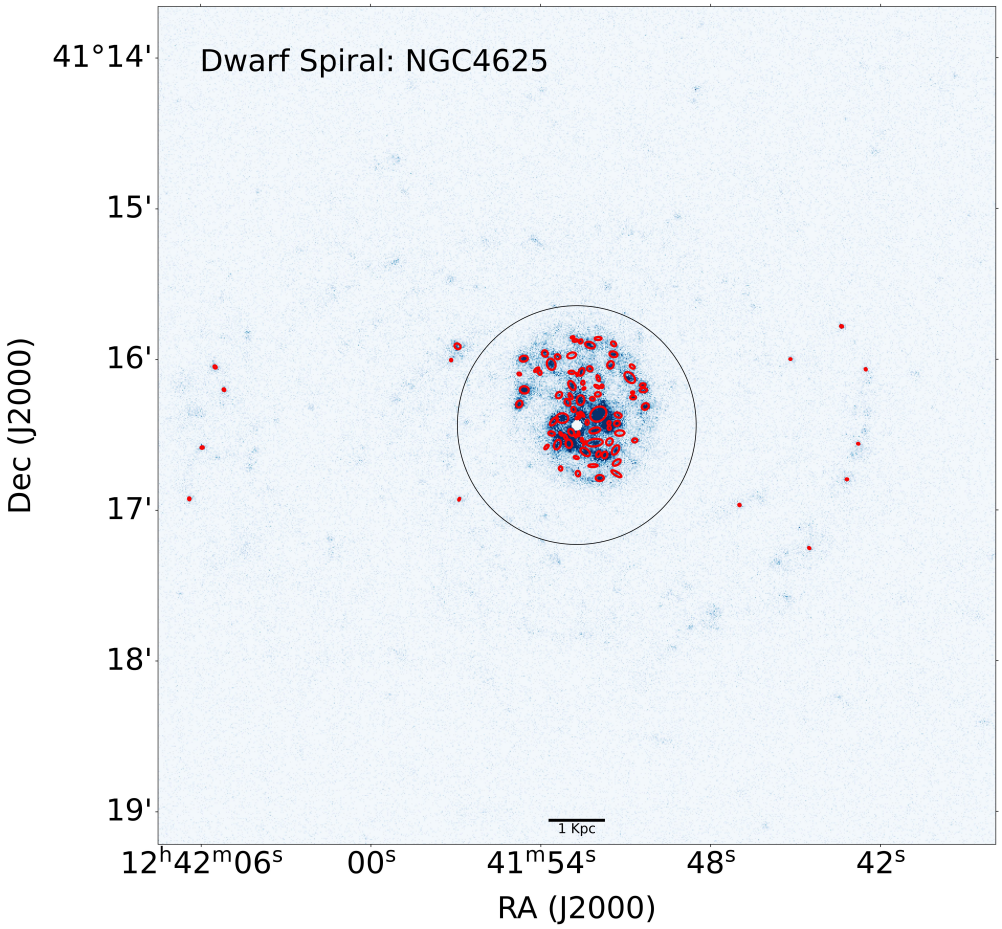


FIGURE A.3: UVIT image of NGC 4625. The red ellipses are fitted to sources using SExtractor (Bertin & Arnouts 1996). The detection threshold is 8 σ. Black circles have a radius of r_{25}, which is mentioned for this galaxy in Table 6.1.

6.4.2 UV Photometry

We performed elliptical aperture photometry on the SFCs using the Python astropy package Photutils (Astropy Collaboration et al. 2013, 2018) and obtained the counts per second CPS from the SFCs. We found the Galactic extinction corrected apparent AB magnitude m_{AB} for each SFC using the formula,

$$m_{AB} = -2.5 \times \log10(CPS) + ZP - A_{FUV} \tag{6.2}$$

Where ZP is zero point magnitude, and A_{FUV} is FUV Extinction, which is calculated using Galactic reddening E(B − V) (Schlafly & Finkbeiner 2011) from IRSA

and using extinction laws (Rodrigo et al. 2012). We found the corrected CPS with this corrected magnitude. We calculated Flux ($ergs^{-1}cm^{-2}Hz^{-1}$) from the corrected CPS using the formula,

$$F_\nu = \frac{\lambda^2}{c} \times UC \times CPS_{corr} \tag{6.3}$$

where λ is the mean wavelength of the FUV filter, c is the speed of light, UC is the unit conversion factor in $ergs^{-1}cm^{-2}Å^{-1}$ for the filter used as given in Tandon et al. (2017), and CPS_{corr} is corrected CPS for the source.

We calculated the extinction-corrected SFR using the FUV luminosities in $ergs^{-1}Hz^{-1}$ and the ratio of 24 μm Flux to FUV flux, using the formula from Leroy et al. (2008). This is explained in detail in the next section. For most galaxies, we obtained the FUV fluxes using the CaF2 filter, which is similar to GALEX. The SFR calculations apply to the CaF2 filter. However, for five galaxies, the filter used is BaF2. We mentioned filter information in Table 6.2. Hence, we calibrated the Flux in the BaF2 filter with the GALEX observations using five stars in the field of the galaxy.

6.4.3 The Host galaxy extinction and Total Star Formation Rate

We calculated the extinction corrected total SFR using 24 μm MIPS observations. As the UVIT resolution is almost five times greater than 24 μm MIPS, we convolved the UVIT image to 24 μm MIPS image resolution. Then we fitted elliptical annuli to the galaxy's 24 μm MIPS image and convolved the UVIT image, such that the annular regions' area should be the same as the inner ellipse, as shown in Figure A.4. The outermost ellipse has a semimajor axis value equal to the distance

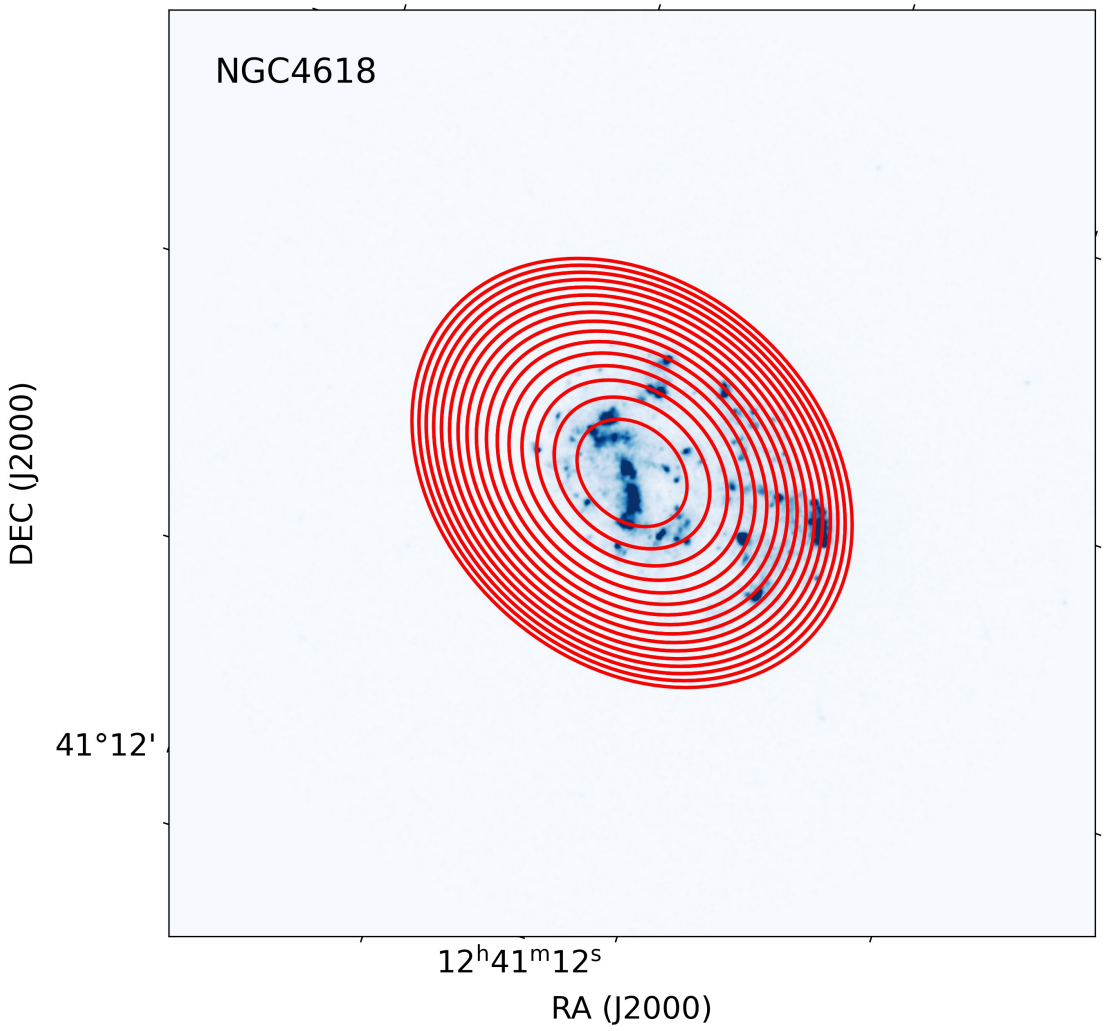


FIGURE A.4: Elliptical annuli of equal area are fitted to the convolved UVIT image of NGC 4618, with the position angle as listed in Table 6.1.

of the farthest SFC, as seen in the UVIT image. We performed aperture photometry on the 24 μm images using `Photutils`. Since the images are calibrated in units of MJy sr^{-1} (surface brightness), the aperture photometry integrates the surface brightness over the aperture. The integrated values were then converted to flux densities in Jy using the pixel solid angle. Similarly, we performed aperture photometry on the convolved UVIT images and followed the same procedure as we followed on 24 μm images to obtain the CPS. As mentioned in the previous section, we calculated the UV Flux in Jy from the CPS.

We calculated the IR flux corresponding to one Jy of UV flux for each annulus

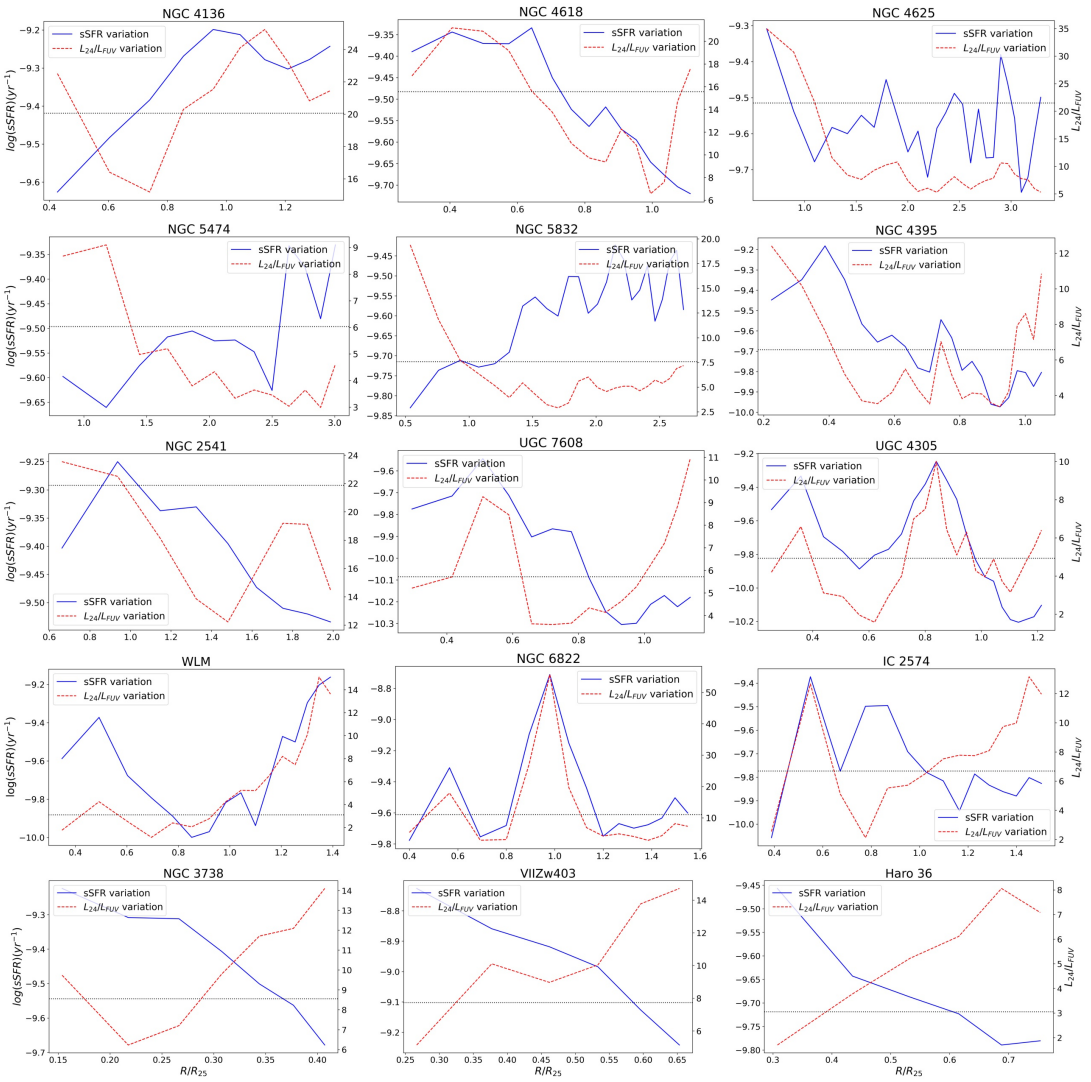


FIGURE A.5: The radial variation of the sSFR is represented as a blue solid line. Whereas 24 μm and convolved UV flux ratio (α as in subsection 6.4.3) is represented as a red dashed line. The black dotted line represents the average α calculated for each galaxy, taking the integrated 24 μm and convolved UV flux within the outer ellipse. The galaxy UGCA 130 is not included.

by dividing the integrated 24 μm flux by the integrated UV flux obtained from that annulus. We denote the ratio as α, and we plotted the variation of α(r) for each galaxy (see Figure A.5). Since we know the deprojected galactocentric distance of the SFCs from the galaxy centre in the UVIT image, we assumed the corresponding radial distance from the plot to determine α(r). In this way, we associated α with all the SFCs in the galaxy.

We found the total SFR for each SFC using the formula mentioned in Leroy et al. (2008), where the FUV SFR is taken from Salim et al. (2007) for sub-solar metallicities (0.8 Z_0) and considered the Chabrier IMF (Chabrier 2003).

$$SFR_{Total} = (0.68 \times 10^{-28} + \alpha\nu_{24} 2.14 \times 10^{-42}) L_{FUV} \tag{6.4}$$

We thus obtain the SFR in $M_\odot yr^{-1}$, where L_{FUV} is the Galactic extinction corrected FUV luminosity in $ergs^{-1}Hz^{-1}$, and $\nu_{24} = 1.25 \times 10^{13}$ Hz. We calculated the SFR density Σ(SFR) by dividing SFR_{Total} by the deprojected area.

In previous studies like Belfiore, Francesco et al. (2023); Leroy et al. (2023), it is mentioned that the MIR flux also comes from the local conditions in a galaxy disk, like reflection heating due to sources other than SF. However, Leroy et al. (2023) showed that 22 μm or 24 μm is more associated with star-forming regions than any other MIR bands. But the conversion factor (C_{24}), which converts UV or Hα flux to 24 μm flux, is higher for the whole galaxy when compared to intense star-forming regions. Hence, the equation 6.4 slightly overestimates the total SFR for the SFCs as it averages the dust from molecular gas, diffuse emissions and emission from star-forming regions.

Figure A.5 shows that the radial variation of α(r) is significant (Red dashed line). For most of the dwarf spirals, α(r) is radially decreasing, with some showing higher values at the end. For irregulars, there is no particular trend. Surprisingly, BCDs show a radially increasing trend. The α considered for the whole galaxy (black dashed line) is in the range of varying $\alpha(r)$. For most of the galaxies, it falls almost at the mean value. But for some, it is either at the high or low end of varying α(r) (See NGC 6822). We used convolved UV and IR images to plot the variation of α(r), which has a resolution of 6". Hence, there is a resolution difference as SFCs have UVIT resolution ($\approx 1.2''$), which is another factor that adds to the uncertainty. Although considering α(r) for SFCs by this method may not be

accurate, it shows how α(r) varies for each type of SFDG and gives approximate α values.

To find the global extinction-free SFR of the galaxies, we took integrated FUV flux and integrated the 24 μm flux from the convolved UVIT images and 24 μm MIPS images, respectively, within the outermost ellipse around the galaxies. Then, we obtained the α value from those fluxes. We have tabulated the fluxes along with α for each galaxy in Table 6.3.

We compared our global SFRs from Table 6.6 with the tabulated global SFRs and stellar masses of Leroy et al. (2019). Although our methods overlap, there is a significant difference in total SFR values. We see that our values are much higher than Leroy et al. (2019). The main reason is the differences in the aperture sizes to obtain the integrated luminosities. Leroy et al. (2019) have considered the optical radius r_{25} as the semimajor axis for the elliptical aperture around galaxies, which is much less than ours. Since there are galaxies with extended disks (and XUV disks), considering r_{25} as the semimajor axis will significantly decrease the total SFR of the galaxies. Also, it should be noted that for some galaxies, the distances considered are slightly different.

6.4.4 Mean Disk Mass of the SFCs

We found the underlying disk masses in the areas covered by the SFCs using 3.6 microns IRAC images. We masked all foreground sources using GAIA data. We used the same method of fitting elliptical annuli to the galaxy as in the subsection 6.4.3.

We determined the 3.6 μm flux from each annulus. We converted the flux to AB absolute magnitude using the distance and then to luminosity. We calculated disk

TABLE 6.3: Calculated parameters for extinction-free SFR

Galaxy	F_{FUV} mJy	F_{24} mJy	α
NGC 4136	10.76±0.10	215.88±2.44	20.06±0.29
NGC 4618	24.75±0.23	384.47±1.74	15.53±0.16
NGC 4625	6.81±0.06	146.46±1.08	21.50±0.26
NGC 5474	27.55±0.31	166.14±1.15	6.03±0.08
NGC 5832	6.49±0.06	49.16±0.62	7.57±0.12
NGC 4395	73.96±0.69	486.02± 1.9	6.57±0.07
NGC 2541	14.36±0.16	0.1419±	21.87±0.29
UGC 7608	4.87±0.04	27.88±0.47	5.72±0.11
WLM	36.15±0.34	112.59±1.12	3.11±0.04
UGC 4305	40.18±0.38	198.18± 1.25	4.93±0.06
NGC 6822	201.41±13.48	2223.49± 4.2	11.04±0.74
IC 2574	53.3±0.5	343.89±1.65	6.45±0.08
NGC 3738	11.31±0.13	96.7±0.88	8.55±0.12
VIIZw403	3.16±0.04	24.43±0.44	7.73±0.17
Haro 36	2.52±0.00	7.7±0.24	3.05±0.05
Mrk 5	1.12±0.01	4.592±0.5	4.1±0.07

Note: F_{FUV} and F_{24} are the FUV and 24 microns integrated flux in mJy estimated within the outer ellipse of the elliptical fitting (see Figure A.4) to the SFDGs. α is ratio of F_{FUV} and F_{24}.

mass M_* using mean 3.6 μm luminosity L_* in $L_\odot$, with mass to light ratio $\Upsilon_{3.6}$ in $M_\odot L_\odot^{-1}$ using relation,

$$M_* = \Upsilon_{3.6} L_* \tag{6.5}$$

Mass to light ratio $\Upsilon_{3.6}$ is the relationship between the mass and luminosity of a disk galaxy. It depends on the FUV-NUV colour for dwarf galaxies. We took approximately $\Upsilon_{3.6}$ from Schombert et al. (2022) based on the colour of the galaxy.

We took $\Upsilon_{3.6} = 0.4\,M_{\odot}L_{\odot}^{-1}$ for galaxies with $0.15 < FUV - NUV < 0.4$ and $\Upsilon_{3.6} = 0.35\,M_{\odot}L_{\odot}^{-1}$ for galaxies with $FUV - NUV < 0.15$.

We derived the stellar mass density $\Sigma(M_*)$ by dividing the stellar disk mass by the area of the bounding ellipse. Then, we plotted the radial variation of $\Sigma(M_*)$ for each galaxy as shown in Figure A.6. Then we associated $\Sigma(M_*)$ with all the SFCs in the galaxy, as explained in the previous section. To find the mean disk mass, we multiplied $\Sigma(M_*)$ with its area. We used the total 3.6-micron luminosity within the outermost ellipse to calculate the total stellar mass of the galaxies.

We compared the total stellar mass of the galaxies from Table 6.6 with the corresponding values in Leroy et al. (2019). Our estimated mass is higher than theirs. Some of the reasons are mentioned in subsection 6.4.3 where we compare the global SFRs. Another important reason is Leroy et al. (2019) have considered the value of $\Upsilon_{3.6}$ from 0.2 to 0.5 $M_{\odot}L_{\odot}^{-1}$, and some of our sample galaxies have $\Upsilon_{3.6}$ value lesser than 0.35 $M_{\odot}L_{\odot}^{-1}$ and the least value we have taken is 0.35 $M_{\odot}L_{\odot}^{-1}$. Hence, this also affects the estimated mass value.

6.5 Results

6.5.1 Morphology of Dwarfs in UV emissions

To understand SF in dwarfs, it is important to compare their UV morphology with the stellar disk at other wavelengths, such as NIR, which traces the old stellar population and hence the main stellar mass distribution, and the optical B band, which traces the overall stellar light distribution from SF. As mentioned earlier, young massive stars emit in the UV band, which can be traced even in distant galaxies (Bianchi 2011). So, by comparing the FUV and NUV emission with the

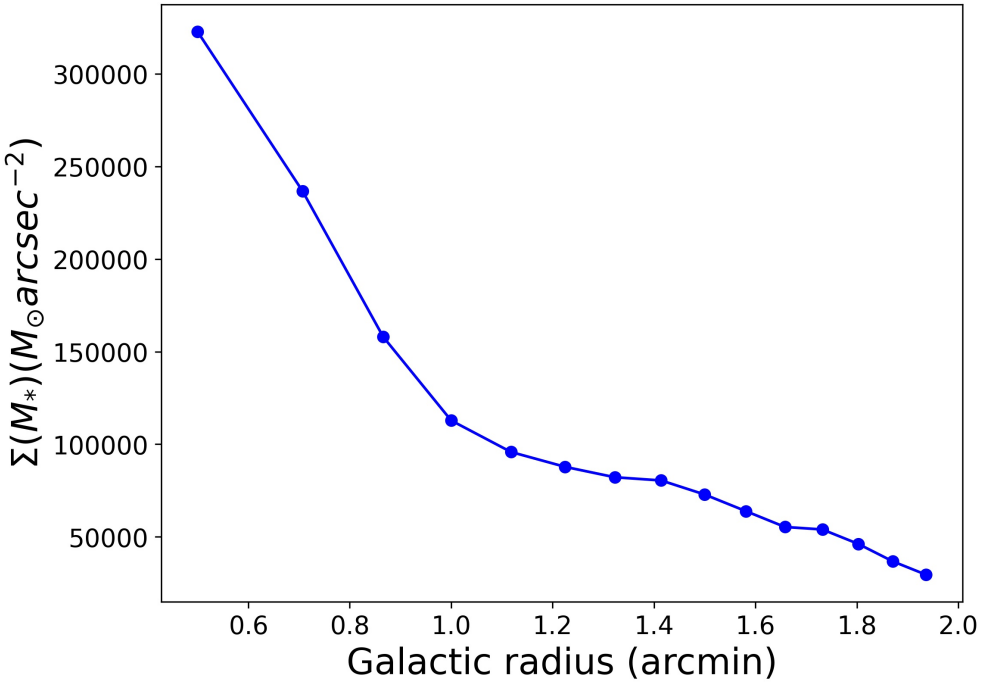


FIGURE A.6: Radial variation of Stellar mass density for galaxy NGC 4618. From this, we associated the stellar mass density with the SFCs by looking at their galactocentric distance.

older stellar population traced in NIR and the intermediate stellar population traced in the optical band, we can understand how SF has propagated in these galaxies.

Dwarf Spirals: We see strong UV emission from the spiral arms of the dwarf spirals, which appear to be very flocculent in nature. However, disk emission in the 3.6 μm NIR band images is poor for most of them, and no well-defined spiral arms are detected. We can see some emission in the optical B or g band images, but it is generally not as extended or bright as the FUV and NUV emission. Hence, these galaxies are forming stars in regions where the stellar density is low (Thilker et al. 2007). Overall, the NIR emission is strong only in the central disk, bar, and bulge regions for some dwarf spirals.

NGC 4136: This galaxy is nearly face-on and has multiple flocculent arms seen in the UV and B band images. The arms are more extended and clearer in the UV

images, especially the southern arm. The galaxy also has a compact oval-shaped bulge (Eskridge et al. 2002). There is no UV emission associated with the short, strong bar, which can be seen in the NIR image. But there is UV emission at the bar ends, and it is loosely associated with the spiral arms since not all the arms are exactly coming from the ends of the bar. This galaxy has a strong inner ring visible in UV emission and a co-rotation ring around a weak bar that is visible in both the B and UV band images. The spiral arms appear to be arising from this ring. There is a bright star-forming nucleus at the centre.

NGC 4618: This galaxy appears very compact in UV. It shows strong UV emission from the bar and has a single spiral arm extending towards the south. The bar is brighter in the NIR and B band images compared to UV, but the spiral arm appears surprisingly faint. The optical centre is slightly offset from the kinematical centre due to the presence of the strong southern spiral arm (Epinat et al. 2008). Although NGC 4618 is classified as a single-armed galaxy, there is a small arm-like structure that can be seen as faint FUV emission extended towards the north and perhaps associated with the bar end. This arm also appears as a faint emission in NUV. The interaction with NGC 4625 could be the reason for the high star formation rate in the bar and the southern arm, and the arm probably formed due to the tidal interaction.

NGC 4625: NGC 4625 shows very bright FUV and NUV emission concentrated towards its centre. This region is also brighter in the NIR and B bands, indicating that the stellar mass is also concentrated in the centre. We see a ring structure in the centre due to the tightly wound spiral arms and also a small bar. The most striking feature in this galaxy is the very extended spiral arms that are bright in FUV and NUV emission and can be traced well beyond the central bright disk. The multiple faint arms extend out to several kiloparsecs around the galaxy but are surprisingly not visible in the NIR image and barely detected in the g band image. The r_{25} of this galaxy is $0.79'$ as per literature. But the UV extends out to

3.2′, which is 4 times more than the r_{25} radius of the galaxy. This was first noted in the GALEX survey by Gil de Paz et al. (2007), which classified it as a Type 1 XUV galaxy. We see some bright regions in the faint arm of this galaxy, and the extended arms seen in UV could be due to the interaction with NGC 4618 and NGC 4625A.

NGC 5474: This galaxy has a peculiar shape due to its highly asymmetric structure. It has a bright central region, which can be seen in UV and the other bands. There are multiple spiral arms arising from the centre, and they all appear distorted in UV emission. To the west and southeast of the galaxy centre, some arms in UV are not connected to the centre and appear to be arising from the other arms. Such bifurcation in spiral arms has been observed in grand design spiral structures (Rahna et al. 2018). In the northern region, we see an arc-like structure. All these peculiar structures are due to interaction with NGC 5457, which may have caused the formation of flocculent spiral arms. We also observe bright star-forming regions or SFCs along these arms. However, in the NIR image, which traces the old stellar population, we can see only one southern arm, and in the B band, only two arms can be detected. This galaxy is classified as a mixed type XUV galaxy (Thilker et al. 2007).

NGC 5832: In this galaxy, there is significant bright UV emission along the bar, but the spiral arms appear flocculent and poorly defined. The multiple arms show diffuse FUV, NUV emission, and a few bright regions with compact UV emission. Some of the spiral arms are connected to the ends of the bar, and some are clearly not. In this galaxy, there are more compact, bright star forming regions in FUV than in NUV. However, the NUV is more extended and smoother. In NIR, we can detect a weak bar with a bright bulge in the centre. The outer disk is barely visible. Hence, this galaxy is classified as a mixed XUV galaxy. In the B band, the galaxy has an S shape with a bright bar and bulge. There are two prominent arms arising from the ends of the bar, but they become fainter at larger radii. There

are also more fainter arms in the southwestern part of the galaxy.

NGC 4395: This is the largest galaxy in our sample, with several bright regions in UV emission. The UV-bright spiral arms are extended but very distorted in shape and do not follow the traditional spiral arm structure. There are multiple arms, at least 3 major ones, all supporting UV bright SFCs. The arm extending southeast of the centre is the brightest in UV emission. We can detect its counterpart in both the NIR and B-band images. There is an oval bulge that is prominent in NIR and hosts a Seyfert 1 type AGN (Epinat et al. 2008). There is an association of bright UV regions around it, and it also appears bright in the B band. This galaxy is brighter in the B band than the other galaxies, but some arms appear fainter than what we observe in UV.

NGC 2541: This galaxy has a flocculent multi-armed structure that is bright in UV emission but does not appear to be connected to the inner disk. At least 3 arms are extended into the outer LSB disk and support many SFCs. The galaxy has a prominent bulge that is bright in the NIR image, but the outer disk is faint and similar to an LSB disk. This galaxy has been classified as a Type 2 XUV galaxy.

Dwarf irregulars: They have very faint and diffuse NIR disks, but show very extended UV emission. We find that some irregulars have spiral arm-like features that are relatively bright in FUV and NUV emission but are not detected or are faint in NIR and B or g band images. Hence, SF is very recent in almost all of these irregular galaxies, as their old stellar population is so faint.

UGC 7608: A bar-like elongated structure is visible in the FUV, NUV, and B bands, but there is no sign of a bar in the NIR image. There are some distinct spiral arm-like structures in the disk that have FUV, NUV bright SFCs distributed along them. The NUV emission appears smoother and has comparatively fewer

bright star forming regions compared to FUV.

UGC 4305: This galaxy is bright in FUV and NUV emission, but the star forming regions are irregularly spread over the galaxy disk. There are four ill-defined arm-like structures in the north and west regions that could be due to clumpy local SF resulting from the effect of some interaction in the M81 group. There is an extended distribution of faint FUV and NUV emission over the galaxy in addition to bright, compact UV arising from the SFCs. Surprisingly, there is hardly any emission in the B and NIR images, suggesting that the old stellar population is very low.

WLM: This is the most inclined galaxy in the sample with an inclination of 70 °. As it is nearby, we can detect many small UV-bright SFCs in this galaxy. The FUV and NUV emission is spread over the disk. The galaxy is classified as barred, but we do not detect a bar in any band (FUV, NUV, B, NIR). However, we detected some disk emission in the NIR, which is also bright in the B band.

NGC 6822: This is the nearest galaxy in the sample; hence, we can detect a larger number of small, UV-bright regions. The tidal features in the southeast region, as well as both northeast and northwest regions, are very prominent in UV, which clearly shows that there have been episodes of interactions associated with this galaxy. This galaxy also shows strong IR and B-band emissions from the central disk.

IC 2574: The galaxy has a very irregular structure. We detect more emission in the UV and B bands. The bright bar in the northeastern region is not visible in the NIR image. A tail-like structure in the southeastern region suggests that the galaxy is tidally interacting with another galaxy. However, we do not detect any close companions.

BCDs: All the BCDs are compact and show strong central emission in all four bands (FUV, NUV, NIR, B). We find a clear UV emission gradient from the centre to the outside BCD, as they are UV bright in the centre but not in the outer LSB disks. The BCDs do not have many SFCs, and we detect no complexes in their outer disks.

6.5.2 FUV and NUV SFCs

The number of FUV and NUV SFCs detected depends on the parameters given in the source extractor, such as exposure time, distance of the galaxy, and the size of the galaxy. We have taken an 8 σ threshold for all our galaxies. The other parameters in the source extractor were chosen to deblend the sources. The galaxies with higher exposure time are brighter, and we are likely to detect more SFCs from them. Also, due to the blending effect, we detect more complexes in nearby galaxies than farther ones. We have summarized the number and parameters of FUV and NUV sources that are detected in Table 6.4. The high resolution of UVIT enables us to detect relatively small SFCs present in the low gas threshold outer regions. For example, NGC 6822, WLM, and UGC 4305 were studied by Melena et al. (2009) using GALEX data, and they detected only 713, 165, and 139 complexes, respectively, which is approximately 78%, 30%, and 7.5% of regions detected using the UVIT.

The optical radius (r_{25}) differentiates most of the stellar disk from the outer disk. After this radius, the stellar disk surface density, and usually the gas surface density both fall rapidly in both massive galaxies and dwarfs (Das et al. 2020). Hence, we expect low SFRs in these regions and the properties of SFCs in the outer and inner regions to be different (Yadav et al. 2021). All the sample galaxies except some BCDs have complexes outside the optical radius. The outer complexes are more than the inner ones in the XUV dwarf spiral NGC 5474 and in NGC 2541.

Other than these dwarfs, NGC 6822 has almost the same number of complexes in both the inner and outer regions. These galaxies must have interacted recently or undergone rapid gas accretion to support such high SF outside the optical radius. The number of outer complexes are much less than the inner ones for all other galaxies. We even find that for most of the galaxies with UVIT NUV data, the number of FUV complexes detected in these galaxies is more than the NUV complexes in both inner and outer regions, while we expect the reverse as NUV can detect complexes till 200 Myrs, whereas FUV only till 100 Myrs. This could be due to the narrower UVIT NUV bands in some cases, or because the SFCs contain stars that are very young and emit more FUV flux than NUV flux in these galaxies. It could also be a combination of both reasons. We have detected more NUV complexes than FUV ones in only the nearby galaxies WLM and UGC 4305. We have detected similar numbers of FUV and NUV complexes in the dwarf irregular UGC 4305. It has 1842 FUV complexes and 1860 NUV complexes. We should note that this galaxy has the highest exposure time (18.23 ks) in our sample.

When we compared the number of complexes in NGC 5474 with the number of complexes in massive galaxies such as NGC 5457 and NGC 0628 from (Yadav et al. 2021), which are at almost similar distances, both NGC 5457 and NGC 0628 have more complexes (1425 and 706 complexes respectively) than NGC 5474 (98 complexes). But NGC 5474 has more outer complexes than inner complexes, whereas the other two have more inner complexes than outer.

In contrast to dwarf spirals and irregulars, BCDs have only one or no complexes outside their optical radius. Even the number of inner complexes is much lower than the other two types. UGCA 130 is the farthest BCD in our sample, which has only two complexes.

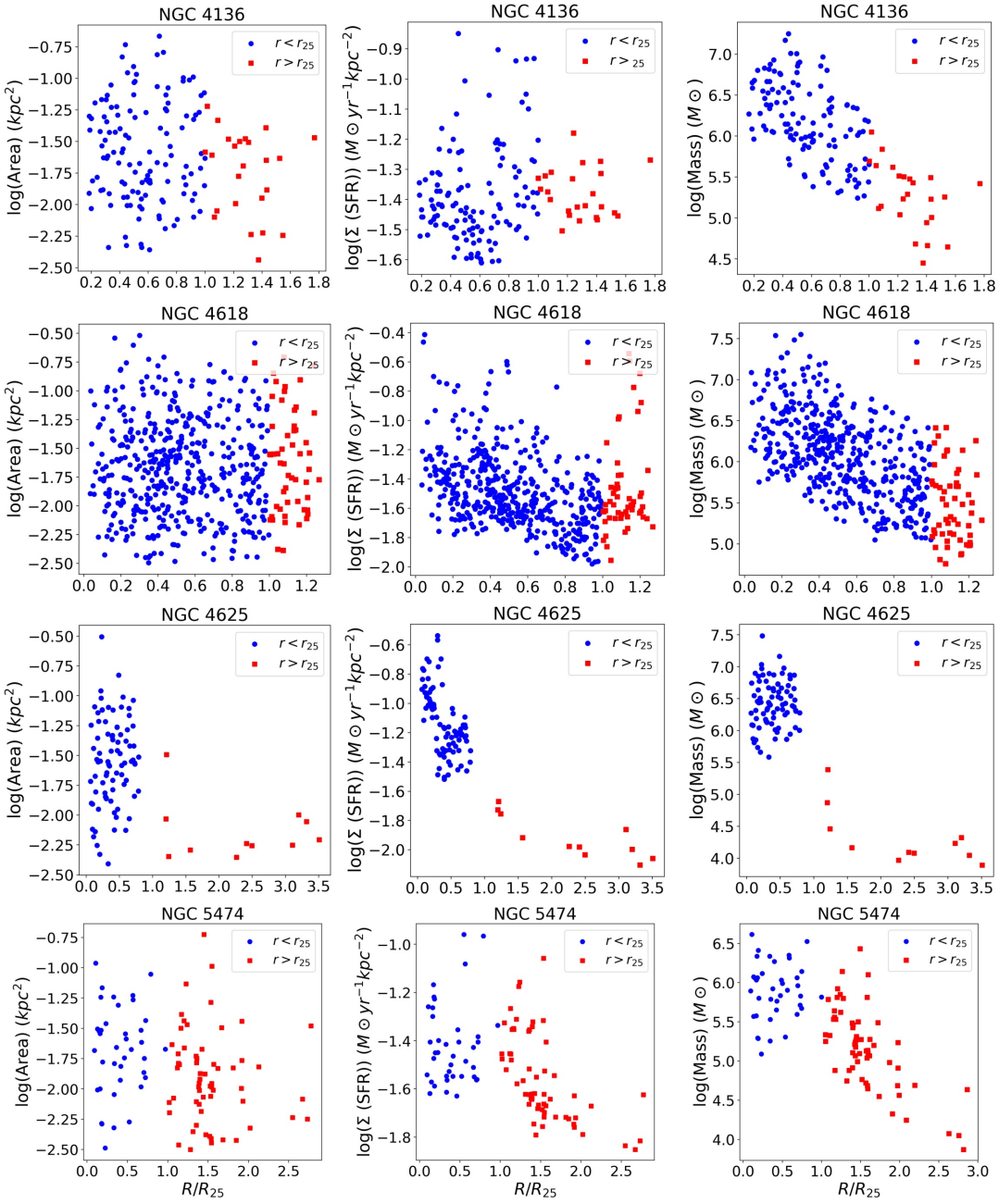
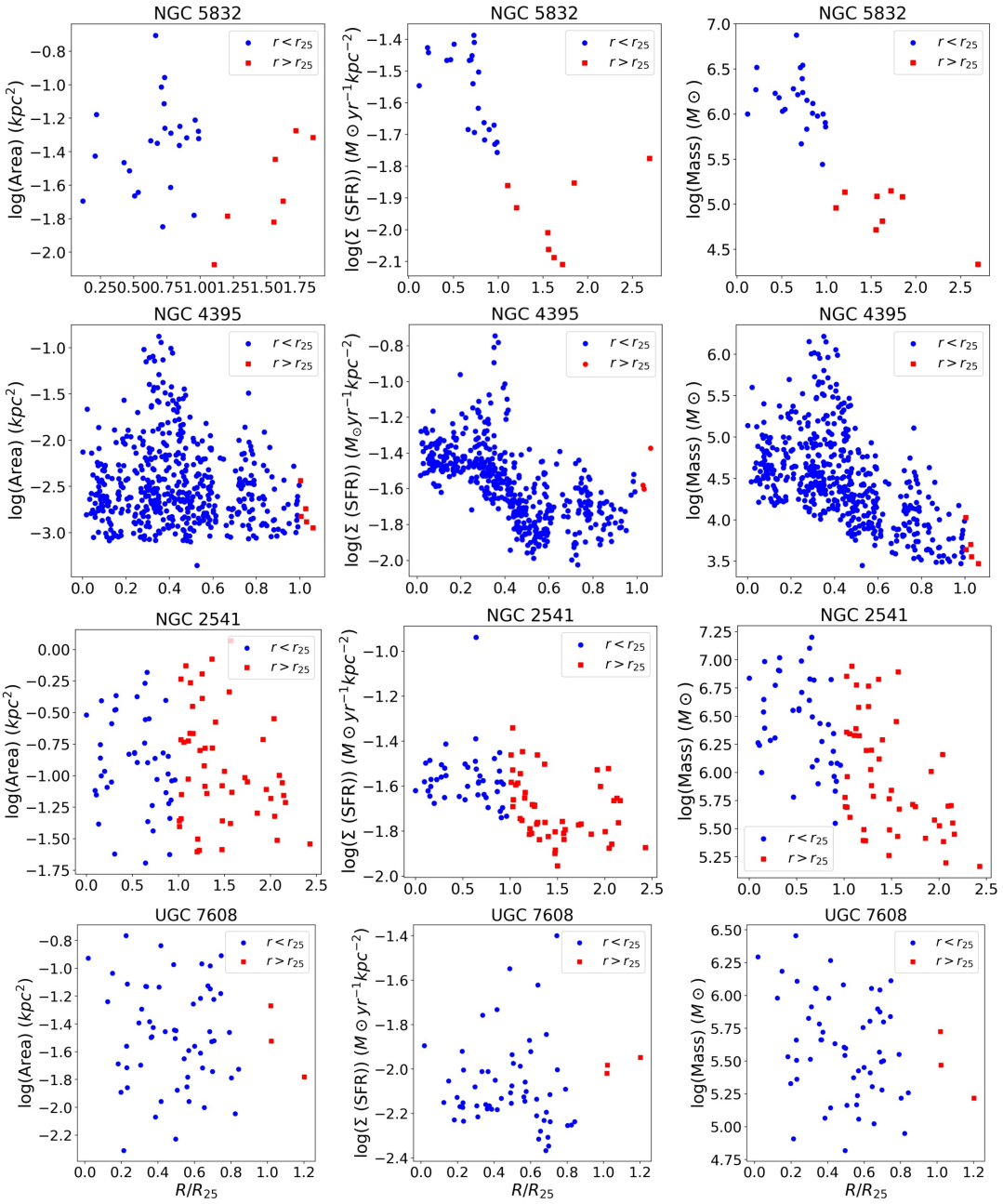
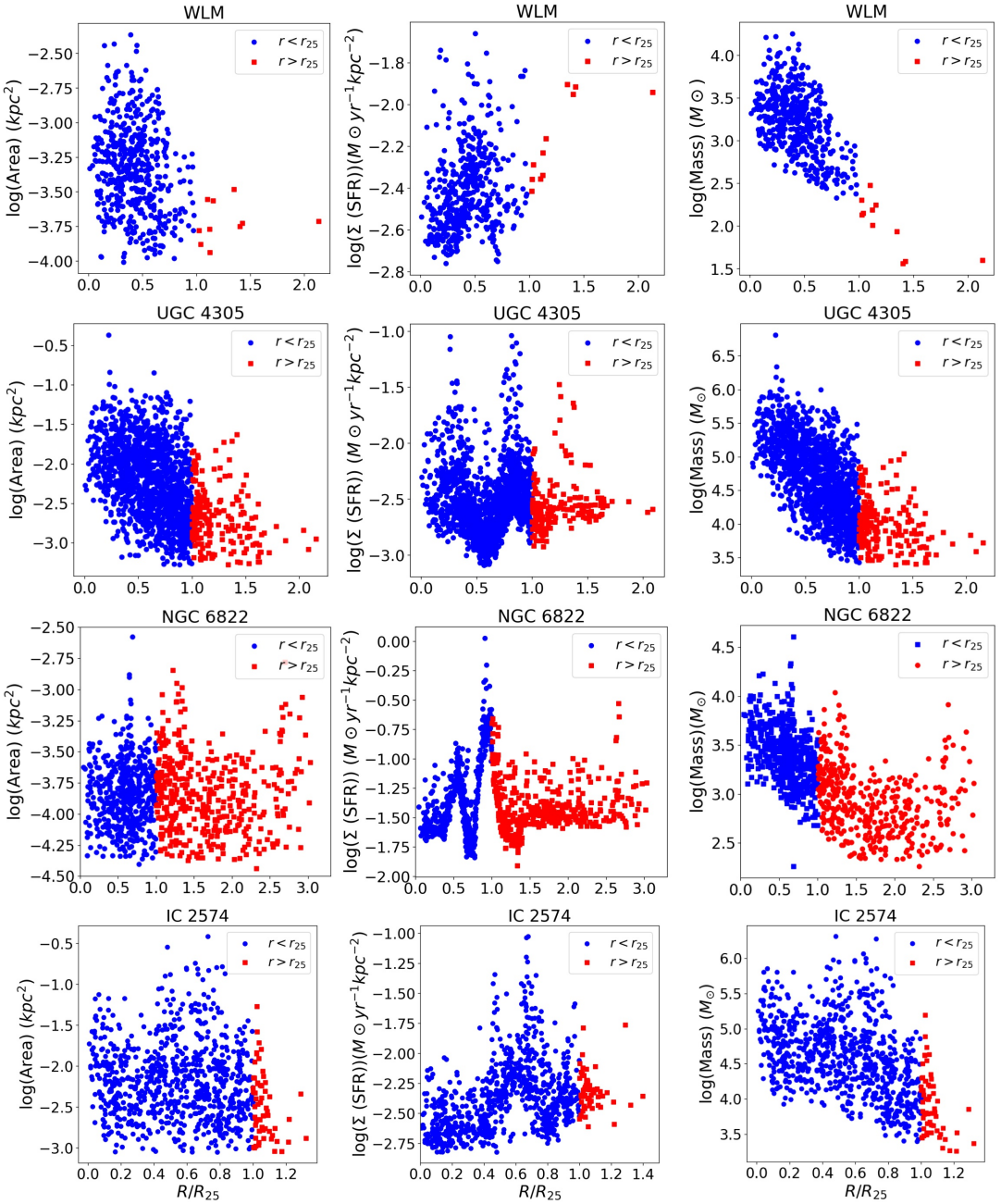


FIGURE A.7: First, second, and third columns in Figure A.7 are a variation of area, star formation rate density, and the mass of the SFCs, respectively, with respect to the deprojected galactocentric radius scaled with the optical size of the galaxy.


NGC 5832
NGC 5832
NGC 5832
NGC 4395
NGC 4395
NGC 4395
NGC 2541
NGC 2541
NGC 2541
UGC 7608
UGC 7608
UGC 7608
$r < r_{25}$
$r > r_{25}$
log(Area) (kpc^2)
log(Σ (SFR)) ($M\odot\, yr^{-1} kpc^{-2}$)
log(Σ (SFR)) ($M_\odot yr^{-1} kpc^{-2}$)
log(Mass) ($M\odot$)
R/R_{25}


WLM
UGC 4305
NGC 6822
IC 2574
$r < r_{25}$
$r > r_{25}$
log(Area) (kpc^2)
log(Σ (SFR))($M\odot\, yr^{-1} kpc^{-2}$)
log(Mass) ($M\odot$)
log(Mass) ($M_\odot$)
R/R_{25}

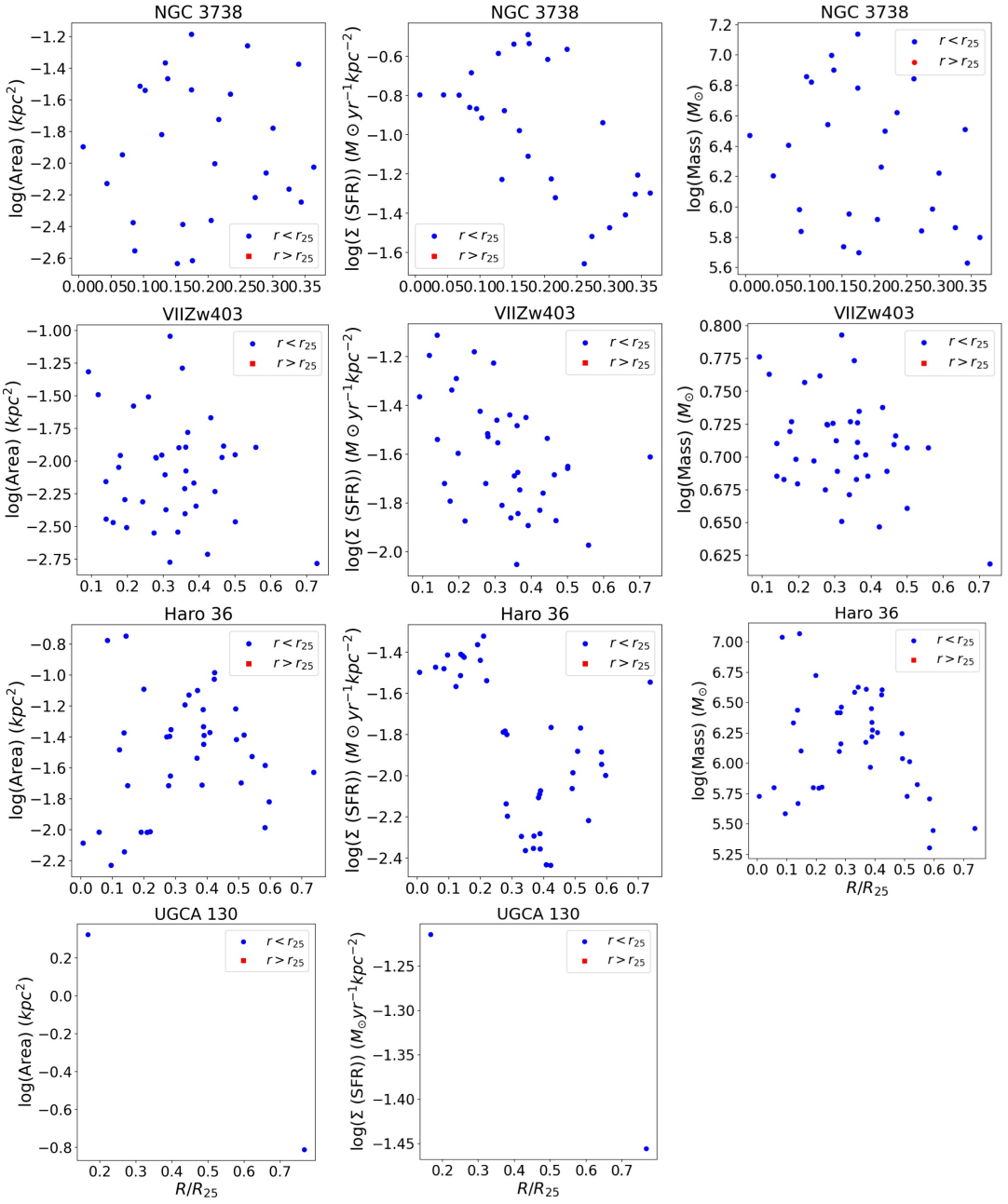

NGC 3738
log(Area) (kpc^2)
log(Σ (SFR)) ($M\odot\, yr^{-1} kpc^{-2}$)
log(Mass) ($M_\odot$)
VIIZw403
Haro 36
UGCA 130
$r < r_{25}$
$r > r_{25}$
R/R_{25}

TABLE 6.4: Number of FUV and NUV bright SFCs inside and outside optical radius r_{25}.

Galaxy	FUV_{in}	FUV_{out}	NUV_{in}	NUV_{out}
NGC 4136	122	24	-	-
NGC 4618	500	12	227	7
NGC 4625	81	11	52	0
NGC 5474	40	58	39	46
NGC 5832	24	8	23	9
NGC 4395	473	3	369	4
NGC 2541	43	49	14	17
UGC 7608	56	2	-	-
WLM	533	10	541	14
UGC 4305	1536	306	1613	247
NGC 6822	507	411	311	348
IC 2574	780	56	-	-
NGC 3738	28	1	-	-
VIIZw403	38	0	29	0
Haro 36	39	0	-	-
UGCA 130	1	1	-	-

Note: FUV_{in} and FUV_{out} are inner and outer FUV bright SFCs respectively. NUV_{in} and NUV_{out} are inner and outer NUV bright SFCs respectively.

6.5.3 Observed Radial trends of SFCs

The radial trends of SFC properties are very important for understanding how a galaxy grows via SF. Hence, we plotted the quantities like SFC area, star formation rate density (Σ(SFR)), and corresponding disk stellar disk masses of SFCs with respect to the deprojected galactocentric radius scaled with the optical size of the

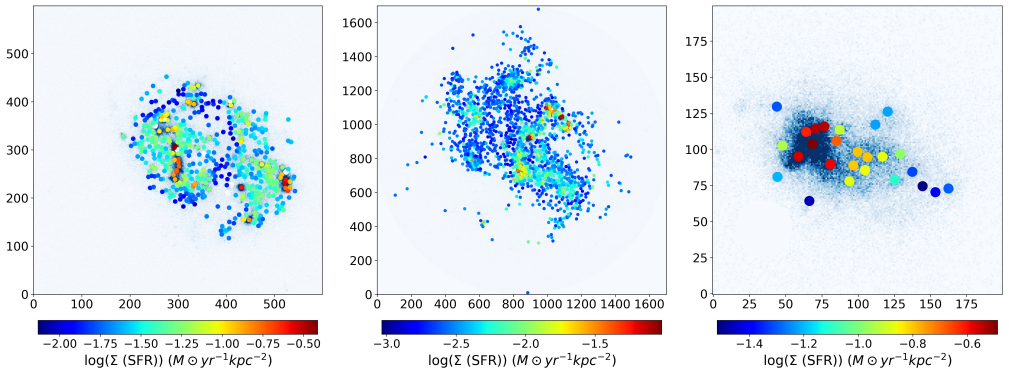


FIGURE A.8: The above figures show the scatter plot of $log(\Sigma(SFR))$ for dwarf spiral (NGC 4618) (left), dwarf irregular (UGC 4305) (middle), and a BCD (NGC 3738) (right).

galaxy. The deprojected galactocentric distance R is

$$\mathrm{R} = \frac{\mathrm{R_{obs}}}{\sqrt{\cos^2(\phi) + \sin^2(\phi)\cos^2(\mathrm{i})}} \tag{6.6}$$

Where $\mathrm{R_{obs}}$ is the observed galactocentric distance, and i is the inclination of the galaxy. ϕ is the angle between the radial distance to the SFC and the semi-major axis in the galaxy's plane.

$$\tan(\phi') = \tan(\phi)\cos(\mathrm{i}) \tag{6.7}$$

where ϕ' is the angle between the radius vector to the SFC and the semi-major axis projected on the sky (Arnaboldi et al. 1995).

The area or the size of the complexes detected depends on the distance of the galaxy. The minimum resolvable area will be smaller for the nearby galaxies and increases with the galaxy distance due to the blending effect. The minimum resolvable radius of SFCs in our sample is for the galaxy NGC 6822, and the value is 2 pc. Whereas for UGCA 130, which is much farther away, it is 87 pc. Hence, the number of complexes detected will decrease with increasing galaxy distance. And we cannot compare the area of the complexes for the galaxies at different distances. This effect is tested in Melena et al. (2009), and it is observed that the

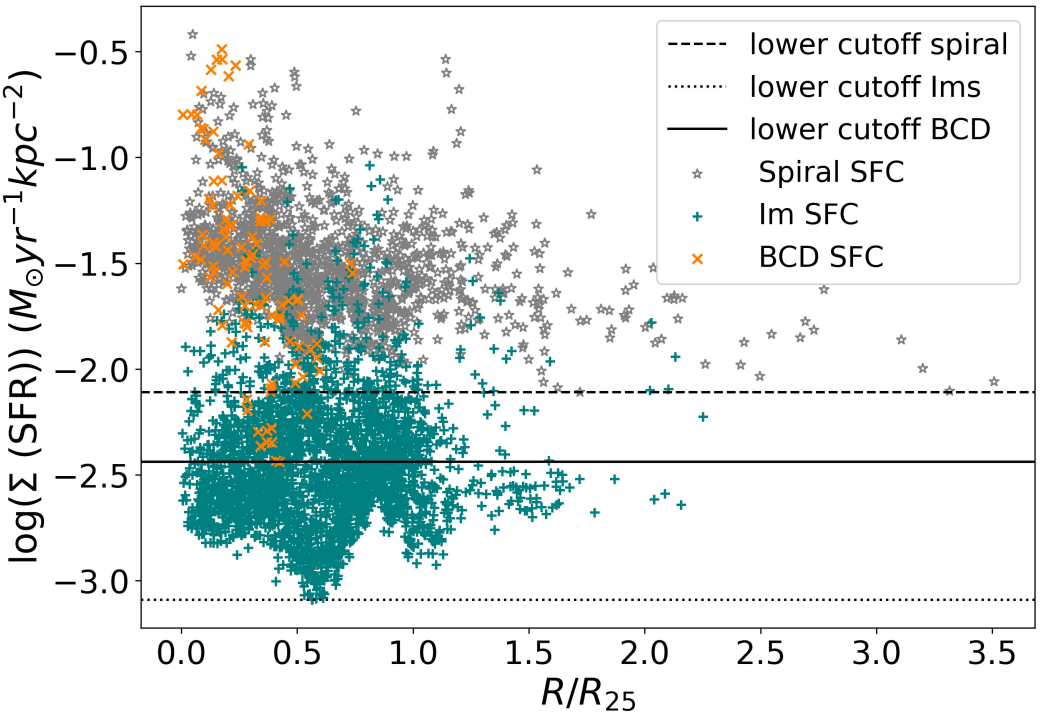


FIGURE A.9: Radial variation of the star formation rate density of SFCs for all the sample galaxies, except NGC 6822.

general trend remains.

Figure A.7 shows the radial variation of the area of the SFCs for the sample. In general, the SFCs have a smaller area beyond the optical radius for most galaxies, except for some galaxies that are either interacting (for example, NGC 4618 and NGC 6822) or are highly extended (NGC 2541), whereas, within the optical radius, both small and relatively larger complexes can be seen. The large SFCs in dwarf spirals, away from the centre, must be associated with structures due to global instabilities such as spiral arms, bars, and bar ends for spiral galaxies. The larger complexes are irregularly spread within the optical radius or associated with ill-defined arms in dwarf irregulars. The distribution of BCDs is entirely irregular.

Unlike the area of the complexes, extinction-corrected Σ(SFR) can be compared between galaxies at different distances. However, differences in physical sensitivity across the sample may introduce selection biases in the detection of faint SFCs.

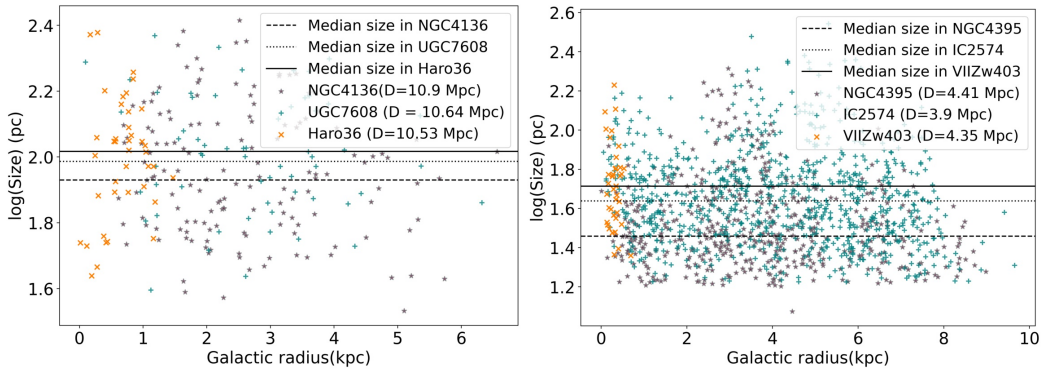


FIGURE A.10: Radial variation of the log(size) of SFCs for some galaxies with approximately equal distances. The median size value for dwarf spiral (NGC 4136, NGC 4395), irregular (UGC 7608, IC 2574), and BCDs (Haro 36, VIIZw403) at a distance D ≈ 10.5 Mpc is 85.11 pc, 96.96 pc, and 104 pc, respectively. And at distance D ≈ 4.1 Mpc, it is 27.9 pc, 43.54 pc, and 51.29 pc, respectively.

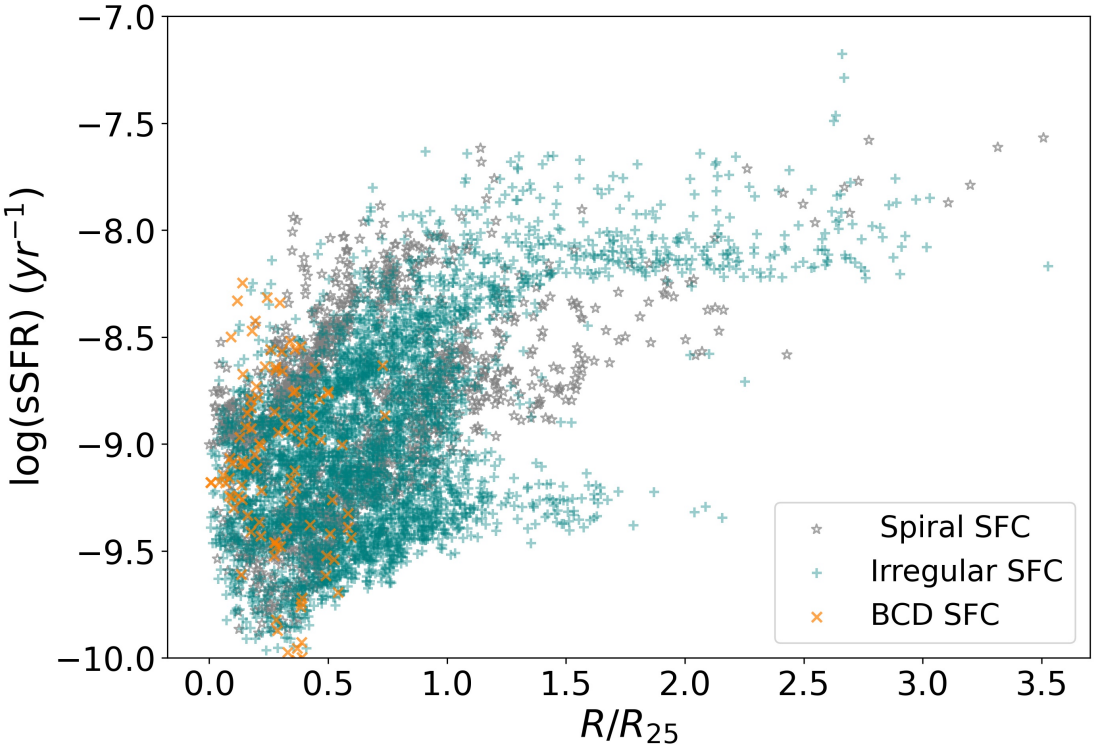


FIGURE A.11: Radial variation of the specific star formation rate of SFCs for all the sample galaxies.

Although normalised quantities such as $\Sigma_{\rm SFR}$ and sSFR are more suitable for comparisons among galaxies than the physical sizes of the detected SFCs, they may still be indirectly affected by distance-dependent source blending, sensitivity, and source identification.

The radial trend here is either oscillatory or radially decreasing. Dwarf spirals show a prominent radially decreasing trend along with some SFCs with high Σ(SFR) values at some radius, primarily associated with spiral arms ends of the bars. In some galaxies, SFCs associated with bar have higher Σ(SFR) (See NGC 4618 in Figure A.8). Even for irregulars, the clumpiness is more only at a certain radii. Hence, they also show the oscillatory trend. Most SFCs with higher Σ(SFR) are associated with larger complexes. The radial trend of Σ(SFR) for SFCs in BCDs mainly drops with increasing galaxy radius. We have shown for each SFDG type an example ($\log \Sigma$(SFR)) scatter plot over the galaxy disk in Figure A.8. This plot shows how the Σ(SFR) distribution differs for the three types of SFDGs.

The stellar disk mass of the SFCs is distance-dependent, and the blending effect is prominent because of it. The larger the complex, the more disk stellar mass it will correspond to. Even the mass radial trend is mainly similar to ($\log(\Sigma$(SFR)) for some galaxies, but the radially decreasing trend is clearly evident for all the galaxies. However, this could also be due to the radial profile of the stellar mass density, which falls off with radius. Hence, we do not find any massive complex in the outer region.

We also plotted the Σ(SFR) for SFCs of all types in a single plot, as shown in Figure A.9, and found that the Σ(SFR) of the dwarf spirals is much higher than the other two types. We have not included data from NGC 6822 as it shows unusually high Σ(SFR) values compared to other dwarf irregulars, and the reason for it is discussed in section 6.6.1. The lowest Σ(SFR) measured for SFC in dwarf spirals is 0.0078 $M_{\odot}yr^{-1}kpc^{-2}$. 0.0008 $M_{\odot}yr^{-1}kpc^{-2}$, and 0.0036 $M_{\odot}yr^{-1}kpc^{-2}$ for

dwarf irregulars and BCDs respectively. There is minimal overlap exists between the dwarf spirals and the dwarf irregulars Σ(SFR)s.

Figure A.10 shows the comparison of the sizes of the SFCs in three different types of SFDGs, which are at roughly the same distance. The left and right panels show the comparison at 10 Mpc and 4 Mpc distances, respectively. The solid, dotted, and dashed lines show the median size of the SFCs in BCDs, irregulars, and spirals. The median sizes of the SFCs are the largest in BCDS. The irregulars host larger SFCs than spirals. One reason for this could be that irregular galaxies lack spiral density waves, and their kinematics are dominated by random gas motions. The discussion on the difference in size and Σ(SFR) of SFDGs is discussed in section 6.6.1.

We even plotted variations of specific star formation rates (sSFRs) of SFCs along the galaxy radius. We plotted the SFCs of all the sample galaxies in the same plot as shown in Figure A.11. The trend is radially increasing till a little beyond r_{25}, and later it becomes nearly constant.

6.5.4 Star forming main sequence for SFCs

The star-forming main sequence (SFMS) is a relation between the SFR and mass of the galaxy, and has important implications for understanding the age and evolutionary states of star-forming galaxies (McGaugh et al. 2017). The equation of the SFMS has a form

$$\log(\mathrm{SFR}) = \alpha \log(\mathrm{M}_*) + \beta \tag{6.8}$$

with α and β likely to be functions of the time (Speagle et al. 2014). Slope α is measured between 0 to 1 (Chen et al. 2009) .

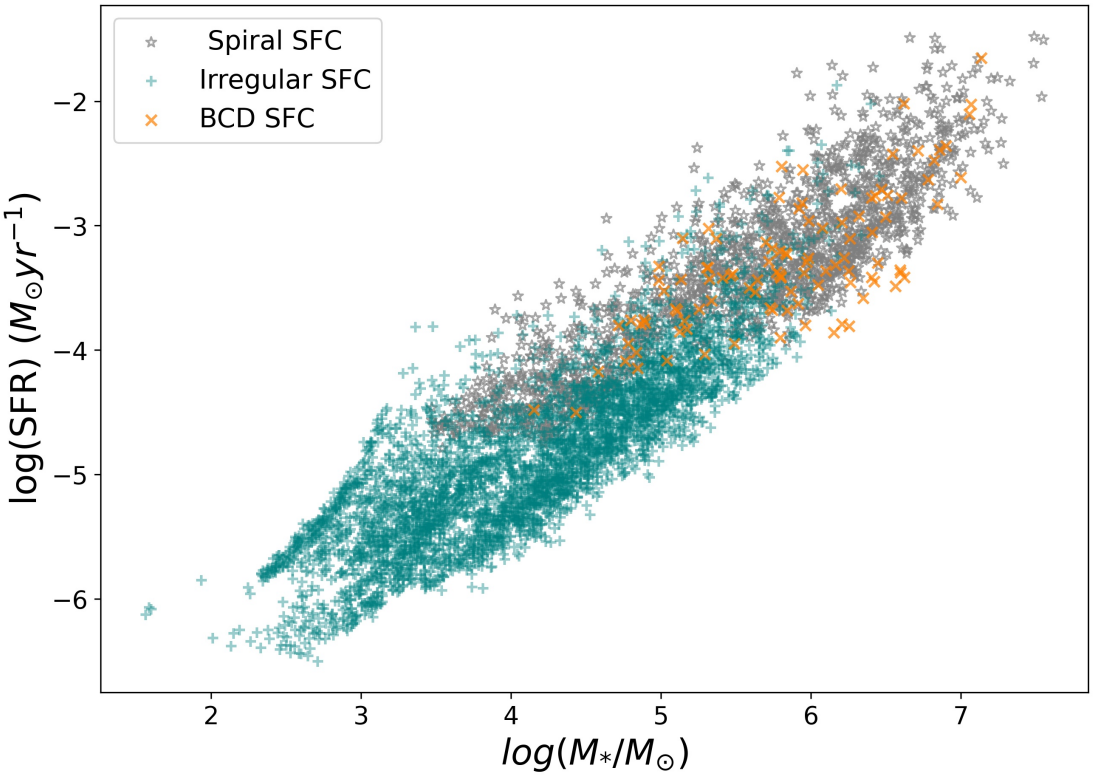


FIGURE A.12: SFMS of SFCs for all the sample galaxies.

In section 6.4, we have extracted SFCs and derived their properties, including the corresponding stellar disk mass for each SFC. We used them to construct the SFMS but on the scale of SFCs for SFDGs. So, we plotted the log of SFR versus the log of corresponding stellar disk mass for the SFCs. We find that they are very well co-related. This tells us that galaxies follow the SFMS globally and even at the level of SFCs, which is on scales well below a kpc. The parameters of the SFMS for the SFCs are given in Table 6.5. However, the slopes of the three types of dwarf galaxies are slightly different. It is clear that the dwarf spirals have a slightly shallower slope than the other two types. The slope of SFMS for dwarf spiral SFCs has a wide range from 0.93 to 0.59, and the mean of the slope is around 0.74. NGC 4136 has the lowest slope of 0.59. The mean slope of the dwarf irregulars is 0.87, and for BCDs, it is 0.8.

From Figure A.11, the sSFR (i.e. SFR/mass) of the SFCs is increasing with

galactic radius for some galaxies and becomes nearly constant at the outer radius. To understand how it varies for each galaxy, we divided the SFCs for all the sample galaxies into inner SFCs (r< $r_{25}/2$), middle SFCs ($r_{25}/2$<r < r_{25}), and outer SFCs (r > r_{25}), where r_{25} is the optical radius. For a given galaxy at any fixed log(M_*), the log(SFR) increases from the inner to outer SFCs for some galaxies. Hence, the sSFR increases as well. This is very clear in Figure A.13 and is more prominent in dwarf spirals, although some irregulars also show this trend. The BCDs do not follow any trend. It is important to note that most of the outer complexes correspond to low stellar mass, and the inner complexes generally correspond to higher stellar mass. But the outer disks have lower stellar surface densities, so for SFCs at outer radii, the sSFR will naturally appear higher. The possible reasons for this gradient is discussed further in subsection 6.6.4.

6.5.5 Other results of SFDGs

6.5.5.1 The Global Star forming main sequence for SFDGs

We took the global SFR and total mass of the SFDGs from Table 6.6. We plotted the SFMS for our sample galaxies and determined the slope of the linear regression fit to our sample. We found that it is shallower than the dwarf LSBs and steeper than that for the massive galaxies, which will be discussed in section 6.6.3. The fit for SFDGs,

$$\log(\mathrm{SFR}) = (0.899 \pm 0.087)\log(\mathrm{M_*}) + (-8.59 \pm 0.75) \tag{6.9}$$

with slope $\alpha = 0.8989$. We see very little deviation of our sample from the fit. The internal scatter of the relation is $\sigma = 0.25$. As the sample has only 16 galaxies, we do not see much deviation between the dwarf types in Figure A.14. But most

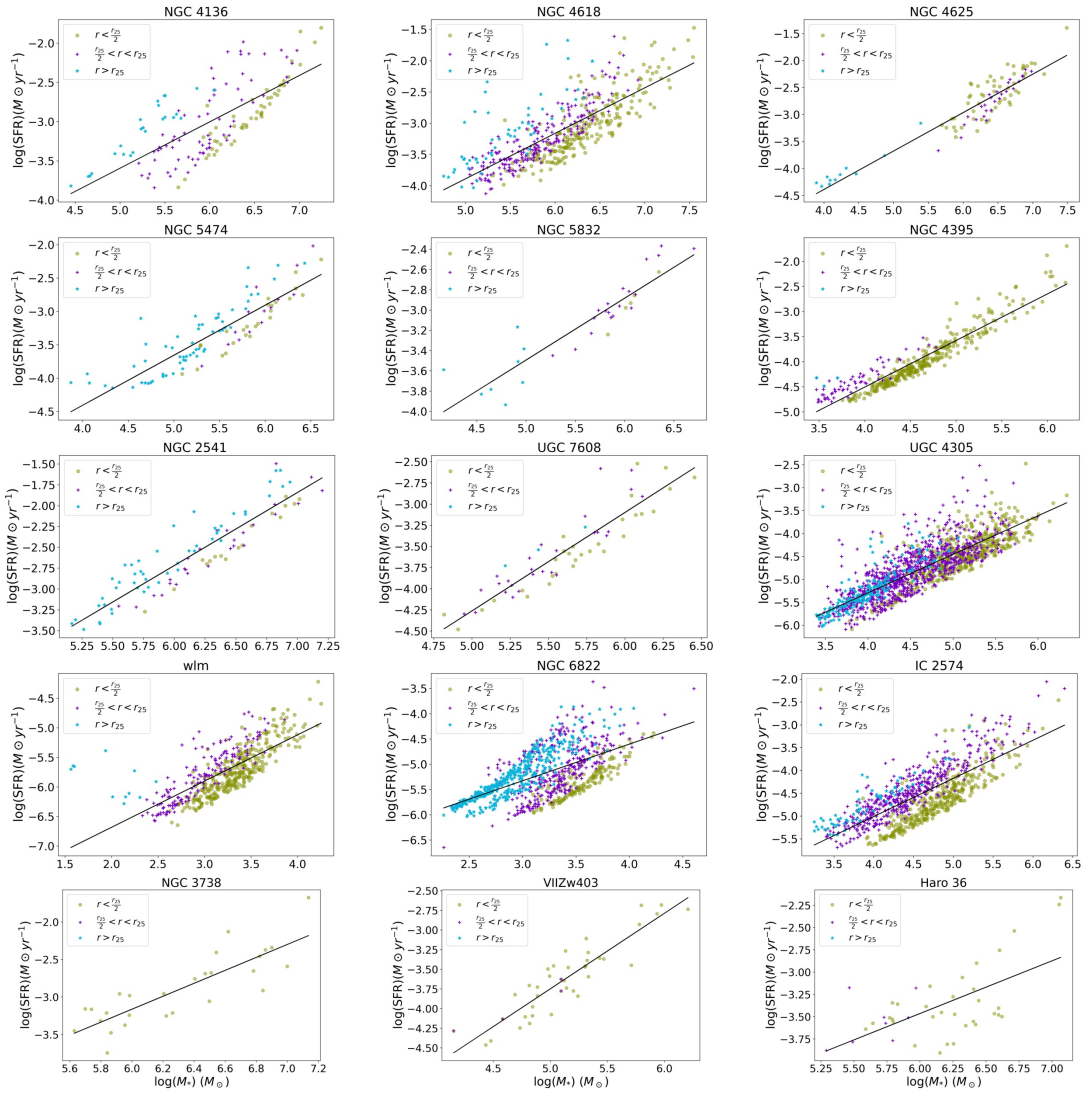


FIGURE A.13: Star forming the main sequence of SFCs for all of our sample galaxies except UGCA 130, as it has only 2 complexes. We see that the inner SFCs with yellow circles (r< $r_{25}/2$), middle SFCs with purple plus ($r_{25}/2$<r < r_{25}), and outer SFCs with blue stars (r > r_{25}) have different SFMS for many galaxies. Outer SFCs have higher specific star formation rates, indicating the inside-out evolution of the galaxies.

TABLE 6.5: Star forming main sequence parameters for sample galaxies.

Galaxy	α	α_{mean}	β	σ
NGC 4136	0.59± 0.05		-6.55± 0.29	0.32
NGC 4618	0.73± 0.03		-7.53± 0.16	0.32
NGC 4625	0.71± 0.03		-7.24± 0.19	0.23
NGC 5474	0.75± 0.04	0.74± 0.13	-7.4± 0.24	0.26
NGC 5832	0.61± 0.05		-6.54± 0.29	0.17
NGC 4395	0.93± 0.02		-8.22± 0.08	0.2
NGC 2541	0.88± 0.04		-7.98± 0.25	0.25
UGC 7608	1.16± 0.07		-10.07± 0.39	0.2
WLM	0.78± 0.03		-8.25± 0.1	0.29
UGC 4305	0.84± 0.01	0.87± 0.16	-8.66± 0.06	0.32
NGC 6822	0.73± 0.03		-7.5± 0.1	0.38
IC 2574	0.84± 0.02		-8.35± 0.1	0.37
NGC 3738	0.86 ±0.1		-8.34± 0.71	0.26
VIIZw403	0.96± 0.07	0.80± 0.19	-8.5± 0.38	0.2
Haro 36	0.59± 0.12		-7.01± 0.74	0.31

Note: α and β represent as mentioned in SFMS equation 6.8. α_{mean} is the mean of slope for each type of SFDGs, and σ is the Standard deviation of the data points.

of the irregulars lie below the fit as they have lower SFRs. Some high-mass dwarf spirals and BCDs are above the fit.

6.5.5.2 Mass Metallicity relation for SFDGs

It is found that for dwarf galaxies with known metallicity, the metallicity strongly correlates with the B-band luminosity (Richer & McCall 1995). Hence, B-band

TABLE 6.6: Calculated parameters of Sample galaxies.

Galaxy	m_B (mag)	12 +log (O/H)	FUV − NUV (mag)	log(M_*) $M_\odot$	log(SFR) $M_\odot yr^{-1}$
NGC 4136	11.69±0.17	8.38±0.02	0.26±0.01	9.38	-0.04
NGC 4618	11.31±0.16	8.39±0.02	0.25±0.01	9.56	0.1
NGC 4625	12.85±0.18	8.17±0.03	0.3±0.01	9.15	0.01
NGC 5474	11.49±0.17	8.27±0.02	0.12±0.01	9.12	-0.46
NGC 5832	12.9±0.3	8.21±0.04	0.39±0.01	9.2	-0.6
NGC 4395	10.3±0.54	8.21±0.08	0.12±0.01	9.14	-0.38
NGC 2541	12.02±0.22	8.37±0.03	0.09±0.01	9.49	0.2
UGC 7608	13.6±0.19	8.1±0.03	0.11±0.01	9	-0.84
WLM	11±0.08	7.72±0.01	0.12±0.01	7.34	-2.2
UGC 4305	10.9±0.2	8.13±0.03	0±0.01	8.64	-0.96
NGC 6822	7±0.3	8.09±0.04	0.4±0.08	8.03	-1.66
IC 2574	10.8±0.3	8.19±0.04	0.03±0.01	9	-0.63
NGC 3738	11.79±0.19	8.13±0.03	0.37±0.01	8.31	-0.98
VIIZw403	14.5±0.19	7.68±0.03	-0.05±0.01	7.13	-1.71
Haro 36	14±0.18	8±0.03	0.27±0.01	8.26	-1.26
UGCA 130	15.1±0.04	7.99±0.01	0.21±0.06	8.1	-1.49

Note: Apparent B magnitude m_B is taken from NED.

luminosity is considered a better predictor of metallicity for dwarf galaxies (Skillman et al. 2003). We found the metallicity for our sample galaxies using a fit derived by Richer & McCall (1995) from local group dwarf irregulars.

$$12 + \log(O/H) = (5.67 \pm 0.48) + (-0.147 \pm 0.029)M_B \tag{6.10}$$

We took apparent B magnitudes from NED, and using distances as listed in Table 6.1, we calculated the absolute B magnitude M_B. The M_B and metallicity of our sample galaxies are listed in Table 6.6.

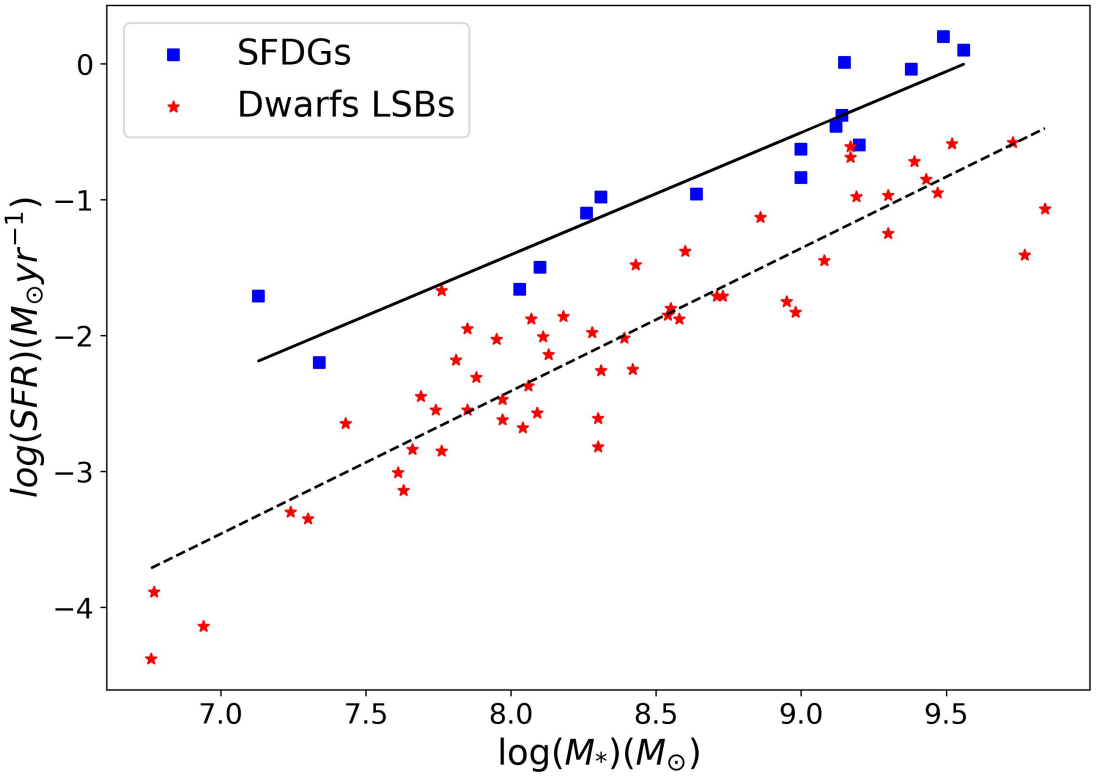


FIGURE A.14: Blue squares are our sample SFDGs, and red stars are dwarf LSBs from McGaugh et al. (2017). The black solid line is a linear fit for SFMS of SFDGs with the slope of $\alpha = 0.8989$. The dashed line is the linear fit for dwarf LSBs with the slope of $\alpha = 1.05$.

We plotted the independently calculated metallicity and mass for SFDGs in Figure A.15. We find that the linear fit for metallicity and mass is given by,

$$12 + \log(\mathrm{O/H}) = (5.85 \pm 0.208) + (0.26 \pm 0.024)\log(\mathrm{M_*}) \tag{6.11}$$

This mass-metallicity relation matches very well with the previous study by Berg et al. (2012), where they found a similar relation for low luminosity galaxies. Our relation lies within its error bars. The B magnitude of his sample has a range ($-10.8 \geq \mathrm{M_B} \geq -18.8$). We find that our galaxies also have a B-magnitude in that range. This indicates that our galaxies have low luminosity in the B band. The intrinsic scatter of the data points from our fit is $\sigma = 0.07$, which is very small. We see that all our sample SFDGs follow this relation irrespective of their type. This supports our mass and metallicity calculations.

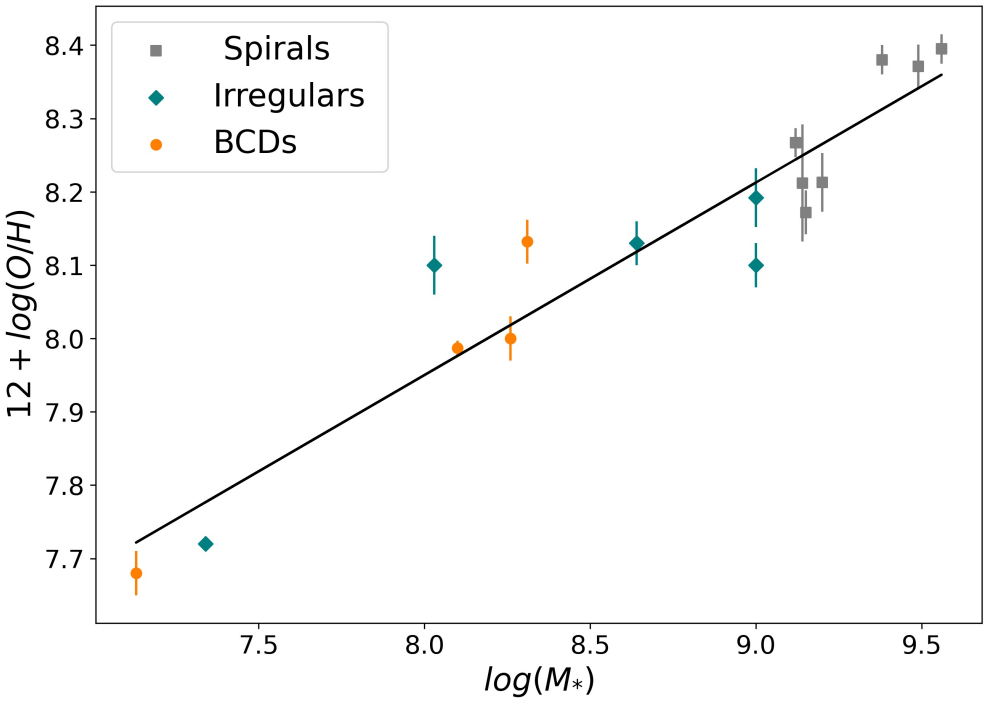


FIGURE A.15: Metallicity-mass plot for SFDGs. Values of errors associated with metallicity can be found in Table 6.6.

6.5.5.3 (FUV-NUV) Colour - Metallicity plot for SFDGs

The (FUV − NUV) colour traces the age of the star-forming galaxies up to a few hundred Myrs. As they get older, the colour reddens (Mondal et al. 2021). The redder galaxies are expected to be comparatively metal-rich as they are more evolved than the bluer ones (Hogg et al. 2004; Pasquali et al. 2010).

We plotted the metallicity against (FUV − NUV) colour, as shown in Figure A.16. We calculated the (FUV − NUV) colour for GALEX data from NED. We neglected the host galaxy extinction as we are calculating the colour, and the difference in the extinction for FUV and NUV bands is negligible. We see a proper co-relation only for BCDs, where we find bluer galaxies are more metal-poor, and as they get redder, they turn metal-rich. The other two types, i.e. dwarf spirals and irregulars, do not show any kind of co-relation.

In Figure A.16, the dwarf spirals have [12 +log (O/H)] >8.1, and their colour is

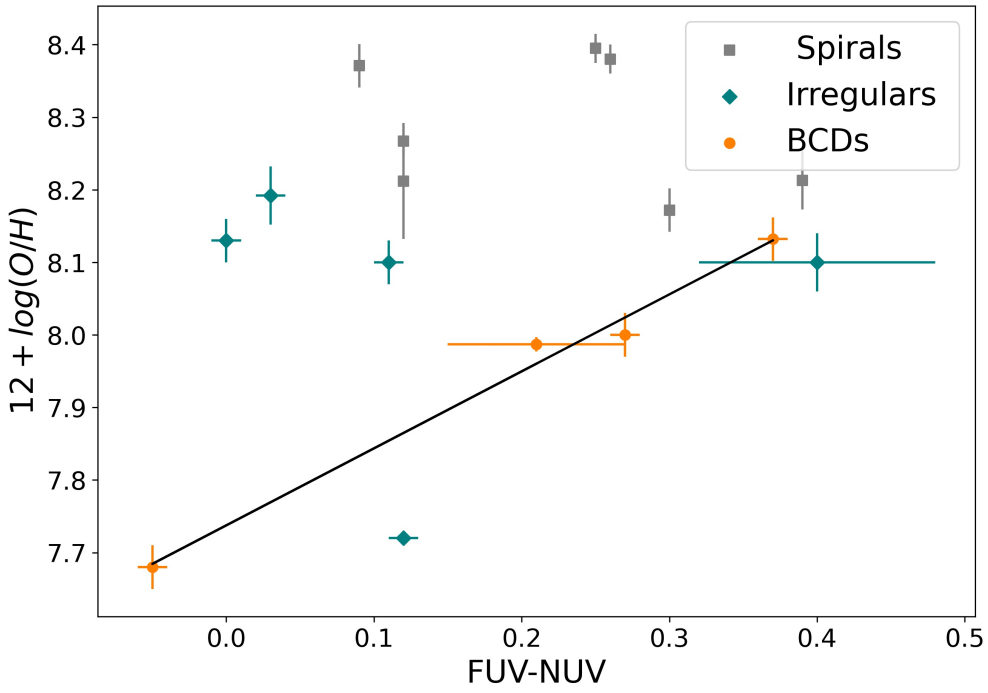


FIGURE A.16: Metallicity-colour plot for SFDGs. We find a positive correlation only for BCDs.

spread between 0.1 to 0.4. For the galaxies with the same colour, galaxies with higher stellar mass have higher metallicity than those with lower stellar mass. The irregulars and BCDs have 12 +log (O/H) $<$ 8.2, where all dwarf irregulars except NGC 6822 have a colour lesser than 0.2, and BCDS except VIIZw403 have a colour greater than 0.2. This indicates that although they are redder than dwarf irregulars, the BCDs are metal-poor compared to dwarf spirals and dwarf irregulars (Kunth & Östlin 2000). The BCD VIIZw403 has a colour less than 0. This indicates that the galaxy is very young and could be a starburst galaxy.

6.5.5.4 The radial variation of sSFR measured over annuli

We calculated the Σ(SFR) from each fitted elliptical annulus of the UVIT image as explained in subsection 6.4.3. Similarly, we estimated $\Sigma(M_*)$ from each fitted elliptical annulus of the 3.6 μm image. We plotted the radial variation of sSFR

for each galaxy by dividing the estimated Σ(SFR) by $\Sigma(M_*)$. We have shown this variation in Figure A.5.

We find that the variation is different for each galaxy, and except for BCDs, we don't see any particular trend for types of SFDG. For BCDs, it clearly decreases radially. However, for dwarf spirals and irregulars, we see a lot of variation in the plots. Galaxies like NGC 4618, NGC 2541, and NGC 6822 show a kind of opposite trend to what we see in their SFCs, which will be briefly discussed in the subsection 6.6.4.

6.6 Discussion

6.6.1 Difference in Sizes and Star formation rate densities of SFCs in the different SFDG types

In previous studies, it has been shown that galaxies show hierarchical SF, and in general, the SFCs correspond to the largest stellar groups with sizes on the scales of 100 s of parsec (Efremov 1995; Elmegreen & Salzer 1999; Elmegreen et al. 2014). But with UVIT resolution, our study resolves smaller star forming units like SFCs and OB associations in nearby galaxies on the scales of a few tens of parsec (Rahna et al. 2018). In section 6.5.3, we find that although the sizes of SFCs are fairly similar over the SFDG types, the SFCs in dwarf irregulars are slightly larger than the SFCs in dwarf spirals. The BCDs have the largest SFCs compared to the dwarf spirals and irregulars. As previously mentioned, random gas motions can significantly contribute to the pressure in irregulars, and in some cases, rotation can be insignificant compared to the gas velocity dispersion. As a result, for effective SF to occur within irregular galaxies, a higher gas surface

density is required to overcome the pressure. This leads to the formation of larger SFCs within irregular galaxies compared to spirals.

However, in general, many factors play a role in the variation of SFC size across different morphological galaxy types, such as the interplay between their inherent kinematic characteristics, feedback from massive stars, the presence of spiral arms and the gas pressure in the disk. A previous study by Elmegreen et al. (1996) mentions that the late-type galaxies (mostly dwarf spirals) and dwarf irregulars have almost similar sizes. And since we have compared galaxies at only two distances, the result is statistically insignificant.

Figure A.7 shows the distribution of the properties of the SFCs, including the radial variation of the Σ(SFR) for the SFDG sample. Although we do not see much difference between the radial trends in dwarf spirals and dwarf irregulars, there is a marked difference in their Σ(SFR) lower cutoff as shown in Figure A.9. The SFCs of dwarf spirals show a higher Σ(SFR) than dwarf irregulars. For BCDs, it varies over a wide range.

To understand this further, we plotted the histogram of Σ(SFR) for the SFCs of the three classes of SFDGs separately, as shown in Figure A.18. The mode of log(Σ(SFR)) for dwarf spirals, dwarf irregulars, and BCDs is -1.84 $M_{\odot}yr^{-1}kpc^{-2}$, -2.09 $M_{\odot}yr^{-1}kpc^{-2}$, and -1.50 $M_{\odot}yr^{-1}kpc^{-2}$ respectively. Hence, most of the SFCs of dwarf irregulars have a lower Σ(SFR) compared to dwarf spirals and BCDs. However, the SFCs with higher Σ(SFR) means that they either have a higher star formation rate than other SFCs in the galaxies or have a smaller area. Hence, the high Σ(SFR) for SFCs in the outer disk could be due to the comparable star formation rate to the inner complexes with minimal areas. But in Figure A.7, we can see that the SFCs in the outer disk, which have higher Σ(SFR), have larger areas, implying a higher star formation rate in the outer disk.

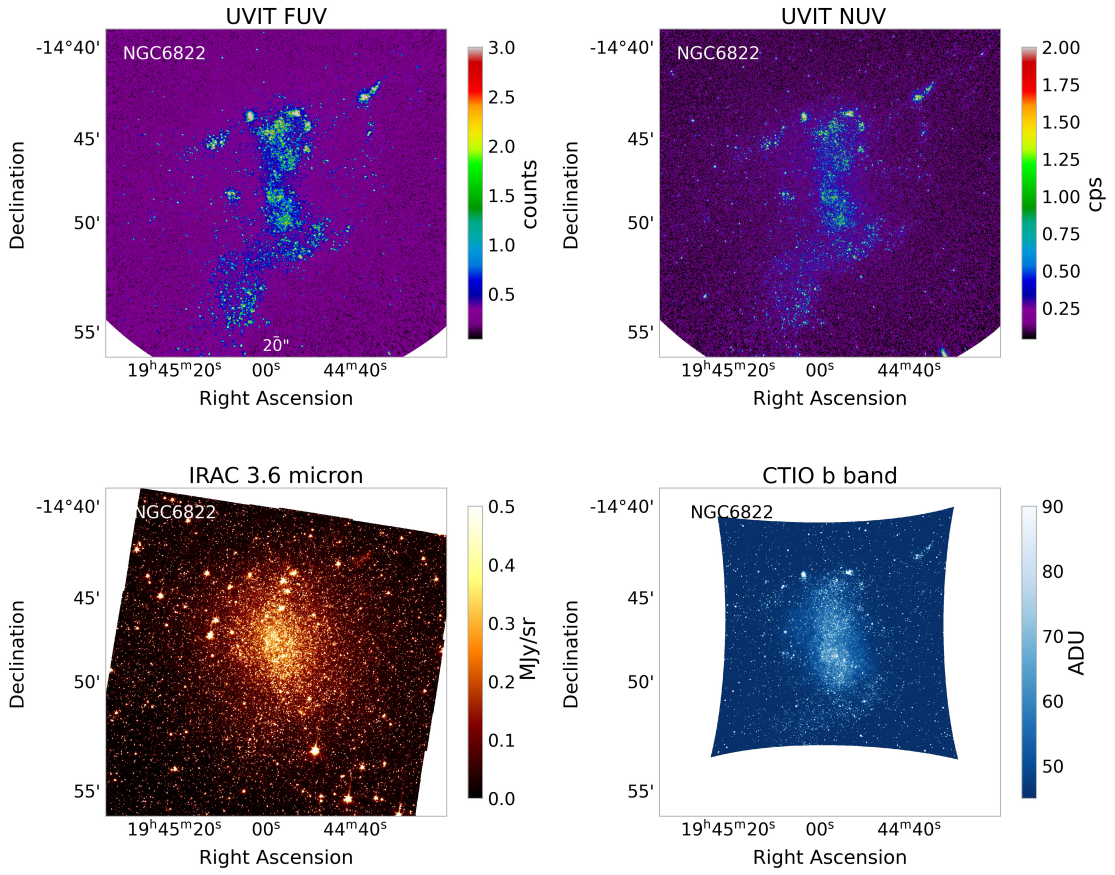


FIGURE A.17: Top panel: UVIT FUV and UVIT NUV images. Bottom panel: Siptzer IRAC 3.6 μm, and Optical CTIO b band images of NGC 6822.

It must be noted that the Σ(SFR) of NGC 6822 is not included as it has an unusually high Σ(SFR) compared to the other dwarf irregulars (See Figure A.7). This could be due to a recent interaction that it has undergone, which is evident from its tidal features that can be seen in FUV and NUV images, as shown in Figure A.17. Another reason could be that the NGC 6822 is very nearby. The SFCs detected in it are very small, which could be smaller unit-like clusters, and bound clusters are densest in the star groups (Elmegreen et al. 2014).

The Σ(SFR) distribution and lower cutoff are clearly connected to a variation in stellar disk surface densities and mean stellar masses in the three types of SFDGs (see Table 6.6). The mean stellar disk surface density is the largest for the BCDs, followed by the dwarf spirals and the irregulars. Also, the mode of Σ(SFR) is the

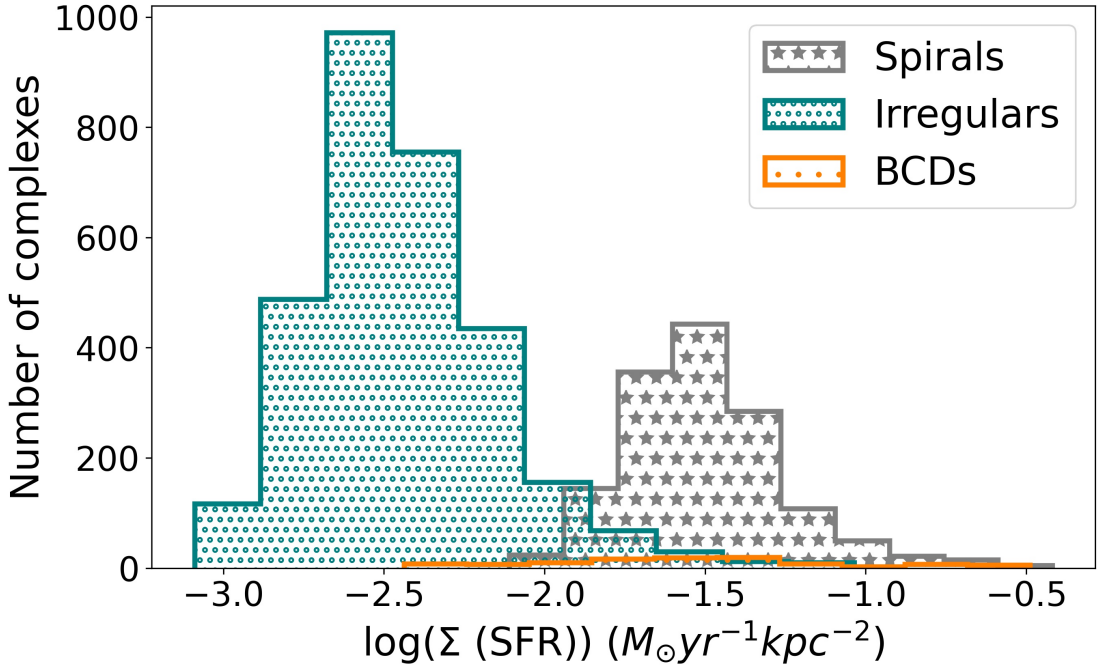


FIGURE A.18: Distribution of log(Σ(SFR)) for SFCs of all sample galaxies (except NGC 6822). The mode of log(Σ(SFR)) for dwarf spirals, dwarf irregulars, and BCDs is -1.84 $M_\odot yr^{-1} kpc^{-2}$, -2.09 $M_\odot yr^{-1} kpc^{-2}$, and -1.5 $M_\odot yr^{-1} kpc^{-2}$ respectively.

highest for the BCDs and is the least for dwarf irregulars. This confirms that the stellar mass is the main factor influencing the SFRs, as shown in earlier studies of the SFMS (Rodrigo et al. 2012; Speagle et al. 2014).

We have also listed log(M_{HI}) in Table 5.1. From those values, we can see that the dwarf irregulars have log(M_{HI}) greater than log(M_*), whereas, for dwarf spirals and BCDs, the stellar mass is greater. Hence, dwarf spirals and BCDs must have used gas to form stars at a higher rate, whereas dwarf irregular do not have stellar disk potentials strong enough to convert M_{HI} to stellar mass at such a rate (Finlator & Davé 2008; Rodrigo et al. 2012).

6.6.2 Effect of interaction on star formation in SFDGs

As our samples have both interacting dwarf galaxies and isolated dwarf galaxies, we could examine the effect of interactions on their SFRs. However, due to their low masses, the effect of interactions on their morphology or SFRs is not very clear (Stierwalt et al. 2015). Some of the signatures of galaxy interaction are starburst activity, gaseous bridges, Magellanic-type streams, and extended tidal arms or tails. In this section, we describe some of these features in our sample.

As discussed in section 6.5.1, in the interacting dwarf galaxies NGC 4625, NGC 4618, and NGC 4625A, the galaxy NGC 4618 is more massive compared to the others. Hence, the extended arm in NGC 4625 could be due to the mass pulled out from the lower mass galaxy NGC 4625. We have even extracted some SFCs from those regions, as shown in Figure A.3. The central disk in NGC 4618 is very bright. This could be due to the funnelling of gas into the central disk, causing it to have enhanced SF. In NGC 4618, the interaction has triggered SF all over the galaxy, including along the bar.

In NGC 5474, the interaction is with the very massive galaxy NGC 5457, with mass $4.1 \pm 1.2 \times 10^{10}\,\mathrm{M}_{\odot}$ (Jang, In Sung et al. 2020). Hence, the galaxy NGC 5474 is completely distorted and extended. The galaxy UGC 4305 also has an extended distorted arm-like structure in UV. NGC 6822 is thought to have undergone interaction twice with a companion galaxy and once with the MW. We can distinguish tidal tails northeast and southwest of the galaxy centre. The southwestern tail looks like a stellar stream and is entirely absent in the IR image. Hence, its UV emission is probably due to a very recent SF triggered by a recent interaction. It is suggested by De Blok & Walter (2003) and Komiyama et al. (2003) that NGC 6822 could be merged system, and the large cloud of gas at northwest could be the location of the other galaxy. It has also been mentioned that the interaction with the MW in the southwestern region has a kinematic age of 100 Myr, and the

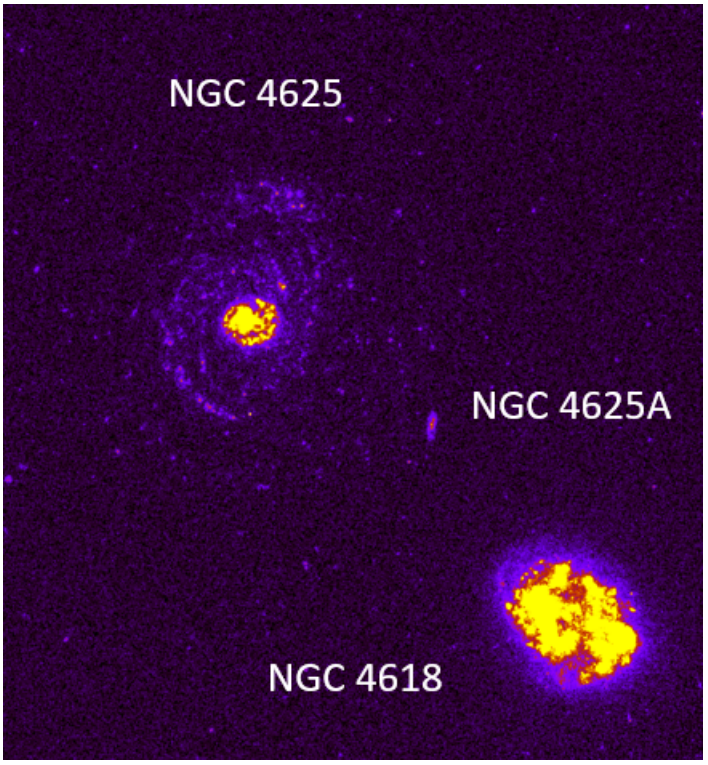


FIGURE A.19: UVIT FUV image of interacting galaxies NGC 4625, NGC 4625A, and NGC 4618 from left .

merger in the Northeast region is 300 Myr.

Using the New Horizon cosmological hydrodynamical simulation, Martin et al. (2020) showed that interactions between dwarf galaxies enhance their overall star formation rates (SFRs) at low redshifts. Observational studies have also found that interacting dwarf galaxy pairs exhibit significantly enhanced SFRs, with the level of enhancement depending on the projected separation between the galaxies (Stierwalt et al. 2015). Since we have very few galaxies that are interacting, and as we have a wide mass distribution for these galaxies, it is difficult to compare and confirm this result. But we do see clear differences in their radial trends compared to non-interacting dwarf galaxies as mentioned in 6.5.3. In NGC 4625, there are small SFCs in the tidal arms, but for NGC 4618, even outer SFCs are relatively large and have larger Σ(SFR). We also see this trend in NGC 5474 and NGC 6822. Hence, interaction affects the size and Σ(SFR) of SFCs of star-forming

dwarf galaxies.

In Figure A.7 and as mentioned in sections 6.5.3 and 6.6.1, SFCs of NGC 6822 has very high Σ(SFR) compared to other dwarf irregulars. The Σ(SFR) is comparable to dwarf spirals. It could be due to the recent interaction of the galaxy. It is believed that mergers can also drive starbursts in these galaxies (Pustilnik et al. 2001; Koleva et al. 2014; Stierwalt et al. 2015). Even in the SFMS parameters of this galaxy (Table 6.5), we can see that it has a shallower SFMS slope α compared to other dwarf irregular galaxies. However, some outer complexes are showing a sudden increase in star formation rate after $10^3\,M_\odot$. Hence, in some cases, this galaxy's SFC SFRs are not included when we have made overall conclusions about dwarf irregulars.

6.6.3 The Global and local SFMS of SFDGs

Studies show that the SFMS slope α in equation 6.8 depends on time (Speagle et al. 2014). This suggests that the galaxies where SF appears quenched could have been actively forming stars back in time.(Daddi et al. 2007; Elbaz, D. et al. 2007; Speagle et al. 2014). Hence the Massive galaxies ($\log(M_*/M_\odot) \geq 10$) at lower redshifts have a shallower slope of $\alpha \approx 0.5$ as SF is slowing in them, which explains the main sequence turnoff (Speagle et al. 2014; McGaugh et al. 2017). As mentioned in Leroy et al. (2019), the time to form the stellar disk in galaxies of mass $\log(M_*/M_\odot) = 10$ is approximately 13-14 Gyr, which was also seen in Speagle et al. (2014). The galaxies with a slope of unity imply that they are formed at an early age in the universe and are forming stars at a constant rate. This has been observed in dwarf low surface brightness galaxies. They also take around 13 Gyr to build their entire stellar disk (McGaugh et al. 2017).

The star-forming main sequence of SFDGs has a slope $\alpha = 0.899$ as seen in

equation 6.9. When we calculated the approximate age for SFDGs using global SFMS equation 6.9, as mentioned in McGaugh et al. (2017), we found the age to be 2-4 Gyr. This implies that the SFDGs are recently formed (McGaugh et al. 2017) or must be forming stars at a very high rate in recent times compared to dwarf LSBs.

The higher sSFRs compared to LSB galaxies (LSBGs), as seen in Figure A.14, could be due to a higher stellar density in SFDGs compared to LSB disks. The sudden bursts of SF can also contribute to the stellar disk formation at a higher rate, leading to a higher gas consumption rate. Due to this, SFDGs may get quenched earlier than LSBGs but not as fast as massive galaxies. Gas can also be lost due to supernova explosions as the dwarfs do not have enough potential to retain the gas.

When we consider the local SFMS in Figure A.12, it is remarkable that over a range of a factor of 10^5 in stellar disk mass, the SFR within a complex is strongly correlated with the local stellar disk mass. We know from Toomre's theory of local disk instability that stellar mass density provides the self-gravity for cloud collapse and SF. We see that SFCs in dwarf irregular have a mean $\log(M_*/M_\odot)$ around 4-4.5, whereas dwarf spirals and BCDs have around mean $\log(M_*/M_\odot)$ around 5.5-6. We used these masses to calculate SF age collectively for SFCs of different SFDG types using the mean equation from Table 6.5. We got an approximate age of 1 Gyr for all the types, which is a little less than the global SFMS of SFDGs but is still comparable. This can also be seen in Figure A.12, where 1/(sSFR) is approximately equal to 1Gyr for the entire sample.

In addition to Figure A.12, we plotted the sSFR with the SFC stellar disk mass as shown in Figure A.20 to further understand the importance of the local stellar disk density for SF in SFDGs. The equation of SFCs for dwarf spirals and dwarf irregulars is very similar to the equation in Leroy et al. (2019) where the mass

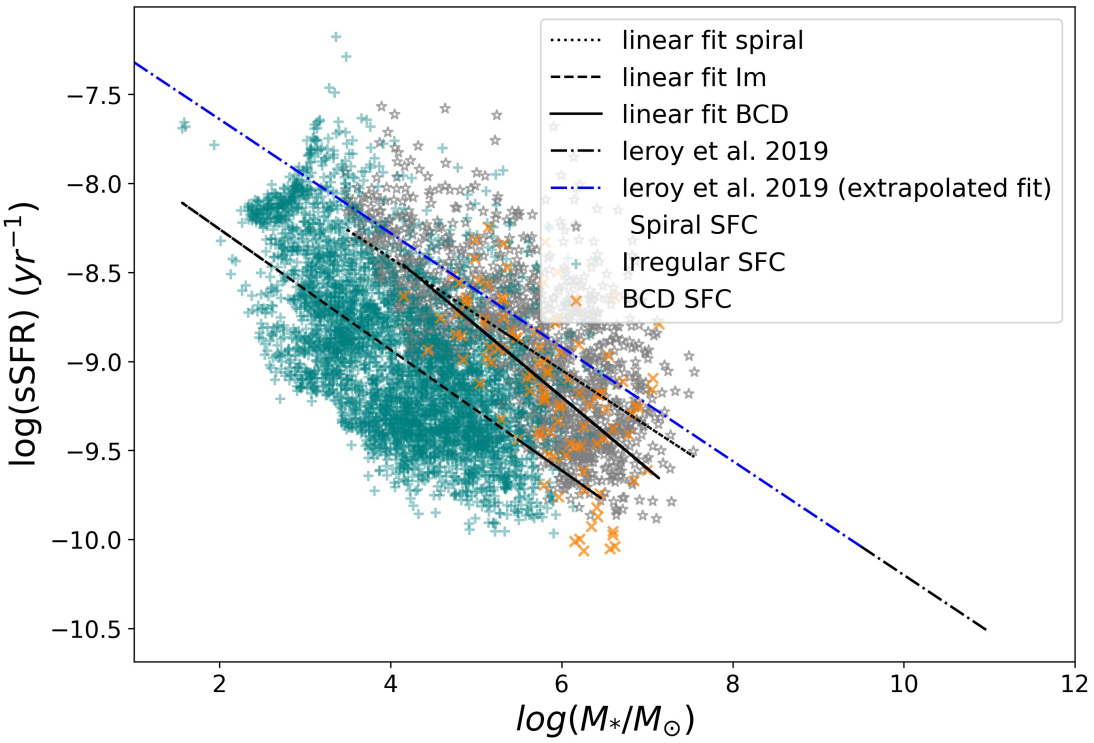


FIGURE A.20: sSFR and stellar disk mass correlation for SFCs. The black dash-dotted line is the fit from Leroy et al. 2019. The blue dash-dotted line is its extrapolated fit for lower mass.

range considered for the fit is $10^{9.5}\,M_\odot$ to $10^{11}\,M_\odot$. So, when we substitute the average mass of the SFCs, we see the difference that the age of local SF in SFDGs is much smaller than the global stellar disk formation time for massive galaxies. It will be interesting to compare the local SFMS of massive galaxies with the global SFMS of massive galaxies.

6.6.4 Difference in SFMS of the different SFDGs and inside-out Evolution of Galaxies

The SFCs following the SFMS give us an idea of how each of our sample galaxies is evolving differently. We see in section 6.5.4, where each SFDG type has a different average value of the SFMS slope, which indicates that the SF process is slightly

different for each type. For dwarf spirals, the slope value is closer to the slope of massive spirals, in which SF quenches and evolves to lower SFRs as gas is depleted (Oemler et al. 2017). But most of the irregulars have a slope closer to or a little less than unity. Galaxies with slope $\alpha = 1$ are expected to evolve at a constant rate, whereas lower α signifies that the galaxies are forming stars at a higher rate in recent times (McGaugh et al. 2017). The BCDs have an α lying somewhere between dwarf spirals and irregulars.However, the approximate time for stellar disk formation is almost the same for all three types, as seen in the previous section.

These galaxies' inner, middle, and outer SFCs, as categorized in section 6.5.4, follow a separate trend. Outer complexes are mostly above the fit, and the inner ones are below. Hence, we find that outer complexes have higher sSFRs than the inner ones, indicating that the star-forming mechanism or evolution of the inner and outer regions of the galaxies are different and depend strongly on the stellar surface density.

Several studies have been conducted to understand the star-forming mechanisms in dwarf galaxies. Previous studies have shown that the spirals mostly have the inside-out SF mechanism (White & Frenk 1991; Bell & de Jong 2000; Brook et al. 2006). The extended UV emission discovered in outer disks by Thilker et al. (2007); Boissier et al. (2007) clearly indicated inside-out disk formation in those galaxies. Some studies have even shown that the late-type spirals, which are less massive, also follow this trend (Dale et al. 2020; Smith et al. 2022). A recent study by Mondal et al. (2021) using UVIT on a dwarf spiral also confirmed it. But studies on dwarf irregulars, like Zhang et al. (2012) studied 34 nearby dwarf irregulars and concluded that the radial profiles of 80% of his samples at shorter wavelengths have shorter disk scale lengths than those at longer wavelengths, indicating the outside-in disk evolution by disk shrinking. Even Dale et al. (2020) showed that irregulars show the opposite evolution trend to the spirals.

In our sample, we have galaxies evolving via ex-situ SF (via gas accretion or interactions)(Chamba et al. 2022). These are expected to grow inside-out, as indicated by previous studies, which is also seen in our results. The galaxies (NGC 5474, NGC 2541, NGC 6822, etc.) have higher sSFR in the outer disk than the inner, and in Figure A.13, we can see a clear distinction between the three regions. Some SFDGs classified as isolated, like NGC 4136 and WLM, have outer complexes with relatively higher sSFR. But in NGC 4625, NGC 4395 and in most dwarf irregulars like UGC 7608, IC 2574, and even in the galaxy UGC 4305, where the SF in the outskirts might have been triggered by external influence, doesn't show much gradient. Although most dwarf spirals and irregulars show inside-out evolution, we find stronger evolution in galaxies where ex-situ SF is observed. The gradient in some galaxies might also depend on how strong the interaction or accretion is. Dwarf irregulars in the sample generally show a moderate gradient or no gradient. Other than accretion and interaction, the local SF in the outer disk of dwarfs can also be supported by dark matter halo (Das et al. 2023).

Unlike the strong gradient observed in SFCs supporting inside-out evolution in Figure A.13 (like in NGC 2541, NGC 4618, and NGC 6822), the radial variation of sSFR over annuli shows a radially decreasing or no specific trend as seen in Figure A.5. One of the reasons is that some galaxies are highly extended, and their tidal tails are spread in a very irregular fashion (NGC 6822). These regions in the outer radius are challenging to consider in elliptical annuli, which results in an underestimation of sSFR. The other reason is that the SFCs depend on the local stellar mass. This does not clearly come out on a radial average.

6.6.5 Correlation between dust obscuration and specific star formation rate

The different trends between sSFR and α seen in Figure A.5, indicate that the relationship between star formation activity and dust attenuation is not uniform across the dwarf sample. Since α is defined as the ratio of the 24 μm luminosity to the UV luminosity, it traces the relative contribution of dust-obscured to unobscured star formation.

A positive correlation between sSFR and α suggests that regions with higher specific star formation rates are also more dust-obscured. In massive galaxies, the central regions generally exhibit both enhanced star formation and higher dust attenuation. Such behaviour is expected when star formation occurs in dense, dust-rich molecular clouds, where a significant fraction of the UV radiation from young stars is absorbed by dust and re-emitted in the infrared. A similar trend is observed in more than 50% of the dwarf spiral galaxies in our sample.

In contrast, dwarf spiral galaxies with extended XUV disks, such as NGC 5474 and NGC 5832, exhibit an anti-correlation between sSFR and α, with higher sSFR values in the outer disk where the dust attenuation is lower. This behaviour is consistent with the resolved star-forming complex analysis presented in this work, which provides strong evidence for inside-out star formation. Dwarf irregular galaxies also show a positive correlation between sSFR and α, although the radius at which the peak sSFR and dust attenuation occur differs from galaxy to galaxy.

On the other hand, a negative correlation implies that regions with higher sSFR are relatively UV-bright and less dust-obscured. In our study, we see this behaviour in all BCD. A possible explanation is that stellar feedback from the central starburst has dispersed or cleared part of the surrounding dust, allowing a larger fraction of the UV photons to escape and thereby lowering the 24 μm-to-UV luminosity

ratio. In contrast, the outer regions, where star formation activity is weaker, exhibit relatively higher dust attenuation, resulting in larger values of α despite their lower sSFR.

Therefore, the presence of both positive and negative correlations reflects the diversity of dust content, metallicity, and local interstellar medium conditions among the galaxies, rather than indicating a universal relation between sSFR and dust attenuation.

6.6.6 The nature of star formation in SFDGs compared to massive galaxies

One of the main differences between massive star forming galaxies and SFDGs is their gravitational potential and metallicity. These are necessary for retaining the cold gas and supporting SF. Dwarf galaxies have shallower potentials and are metal-poor compared to massive galaxies. As a result, many of them lack prominent spiral arms and bars, which are the main global disk instabilities. These instabilities can make dense molecular clouds settle in either the spiral arms or bar ends. The lack of such instabilities makes SF spread all over the galaxies (Elmegreen et al. 1996). Hence, we expect different star forming properties in low-mass systems than in massive galaxies. The only dwarfs that have prominent spiral arms are the dwarf spirals, but they are at most Sd and Sm types. They lack grand spirals and instead have flocculent spiral arms.

In this subsection, We will compare our properties with previous studies of the massive galaxies studied using UVIT so that there should not be any instrumental bias. We are comparing with galaxies studied by Yadav et al. (2021), where massive XUV galaxies are analysed with a UVIT telescope. The SFCs are extracted to compare their properties in the inner and outer regions. However, to compare

the sizes of SFCs in the massive and dwarf galaxies, the galaxies should be at comparable distances. Hence, we compared the sizes of SFCs of NGC 5474 with NGC 628 and NGC 5457.

While comparing with NGC 628 and NGC 5457, we find that the smallest SFC detected in NGC 5474 is of the order of $10^{-2.5}$ kpc^2. And most of the SFCs are between $10^{-2.5}$ kpc^2 to 10^{-1} kpc^2. The larger SFCs that we find in NGC 5474 are of size $10^{-0.75}$ kpc^2, whereas in massive galaxies, there are SFCs with sizes larger than 10^{0} kpc^2. Hence, massive galaxies have SFCs with a larger range than dwarf galaxies such as NGC 5474. They are generally larger in the centre, and they become smaller as we go radially outwards. Some of our samples are farther than these massive galaxies; still, we see that they have SFCs with sizes less than 1 kpc^2. This result is consistent with previous studies. Elmegreen et al. (1996) that had shown that large galaxies form large star-forming complexes that form OB associations for a longer time, whereas dwarf galaxies form small complexes which, in turn, form dense, bright associations for short periods. The reason for the small SFC sizes in dwarfs could be low stellar density and shallower potential, which does not support the formation of larger complexes, although the shear is more for massive galaxies than dwarfs. The smallest complex detected in our sample is from the nearest galaxy, NGC 6822, with an area of around $10^{-4.5}$ kpc^2.

We can also compare the found Σ(SFR) in our galaxy with that of massive spiral galaxies. We see that dwarf spirals have a higher value of Σ(SFR) than massive spirals from Yadav et al. (2021). Hence, the dwarf spirals have much more compact SFCs. Another reason is that the SFR is not corrected for host galaxy extinction in massive galaxies. Hence, the range of Σ(SFR) is similar to dwarf irregulars where the environment for SF is completely different.

There are some studies, such as Elmegreen & Salzer (1999); Elmegreen et al. (2014), which discuss the hierarchical structure of these complexes. According to

them, large galaxies and LSB dwarfs have a tendency to form uniformly spread-out complexes. The hierarchical structure is seen within these complexes, whereas bright starburst dwarfs have very few large complexes with well-resolved hierarchical SF inside.

6.7 Conclusions

In this project, we used UVIT to study 16 star-forming dwarf galaxies and compare the SF properties of the three SFDG types. This is done by extracting UV-bright star-forming complexes and by analyzing their properties. Our main results are summarised below:

1. Most of the sample dwarf spirals have flocculent spiral arms and extended UV disks. Dwarf irregulars have clumpy SF and some ill-defined arms, whereas BCDs have very compact star forming inner disks and outer LSB disks. This result is consistent with the previous studies.

2. For most of the SFDGs in our sample, we have detected more FUV SFCs than NUV SFCs. This could be due to the recent SF in these galaxies. Some Extended UV galaxies (XUV) like NGC 5474 and NGC 2541 show high SF in sub-threshold environments, and they have more outer disk complexes (beyond optical radius) than inner disks where the stellar surface density is comparatively high.

3. Dwarf spirals have complexes with a higher area, Σ(SFR), and mass in the inner arms, rings, and at the ends of the bars compared to other SFCs. In some galaxies, it is higher even along the bar. The radial trends of these properties show that the SFR decreases as we go radially outwards. Irregulars and BCDs have no regular pattern in their radial trends. However, in general, outer complexes have smaller sizes, lower Σ(SFR), and mass.

4. We find that interacting galaxies such as NGC 4618, NGC 5474, and NGC 6822 show an overall high Σ(SFR); they also show SF in their outer regions that are triggered by interaction. These galaxies show radial trends different from non-interacting galaxies.

5. We see that the lower limit for Σ(SFR) for SFCs of each type is different. Dwarf spirals have a higher threshold or limit for Σ(SFR) (0.0078 $M_{\odot}yr^{-1}$), and dwarf irregulars have the least (0.0008 $M_{\odot}yr^{-1}$). But the mode of log(Σ(SFR)) for SFCs is higher for BCD with the value -1.50 $M_{\odot}yr^{-1}$. The mode of log(Σ(SFR)) for SFCs of dwarf irregulars is lower than dwarf spirals, which are -2.09 $M_{\odot}yr^{-1}$, and -1.84 $M_{\odot}yr^{-1}$ respectively.

6. SFDGs follow the SFMS with the slope and intercept as $\alpha = 0.899 \pm 0.087$ and $\beta = -8.59 \pm 0.75$. This fit is shallower than LSB dwarfs and steeper than massive galaxies, indicating recent high SF in them. The age of stellar disk formation is found to be around 2-4 Gyr.

7. We find that the SFCs of SFDGs also follow the SFMS, but the slope α is different for the different types. The mean slope of the SFMS for dwarf spirals is 0.74. In comparison, dwarf irregulars and BCD have slopes of 0.87 and 0.8, respectively. However, the age of SFCs approximately corresponds to 1 Gyr.

8. In the SFMS plots of mainly dwarf spirals, we find that the outer complexes have higher specific star formation rates compared to the inner ones. This is prominent in the interacting irregular galaxy NGC 6822. This implies that the SF mechanisms in the inner and outer regions of galaxies are different, which supports the inside-out evolution of galaxies. It is also different in different types of SFDGs.

9. Dwarf spirals have compact SFCs compared to massive galaxies. However, the SFCs of massive galaxies have a larger range of sizes and Σ(SFR).

Chapter 7

Ultraviolet Properties of the Ultra-Faint Dwarf Galaxy Leo T: Insights from UVIT Observations

7.1 Introduction

UFDGs are generally composed of older stellar populations and exhibit a CMD that is similar to that of globular clusters. Many of the satellite galaxies around our own Galaxy are UFDGs and do not show signs of recent SF. However, Leo T, which is a nearby satellite galaxy, is an exception as it shows signatures of intermediate and even recent SF. Hence, Leo T is located at the bright end of the MW UFDG galaxy distribution, with a brightness of $M_v = -8$. It is considered to be a transitional galaxy, having properties of both dwarf spheroidal galaxies (dSph) and UFDGs. Leo T is at a distance of 407^{+29}_{-27} kpc (Clementini et al. 2012),

and has a stellar mass of 2×10^5 $M_\odot$ (de Jong et al. 2008). However, deep HI observation has revealed that the galaxy is gas-dominated, with a gas mass that is twice that of the stellar mass, and is 4×10^5 $M_\odot$ (Adams & Oosterloo 2018). Hence, Leo T is one of the faintest star-forming, gas-rich galaxies. Such features are more commonly associated with dwarf irregular galaxies (Amrutha et al. 2024; Hunter et al. 2012).

Several studies have investigated the SFH of Leo T (Irwin et al. 2007; de Jong et al. 2008; Weisz et al. 2012; Clementini et al. 2012). Investigations using optical photometry from HST (Weisz et al. 2012; Clementini et al. 2012) have identified multiple episodes of SF in this galaxy. Overall, there is a marked absence of ongoing massive SF in Leo T. While 50% of the stellar population formed before 7 Gyr and forms a relatively old population, there is also a younger population that has an age of less than 500 Myr. Some SF activity at early epochs between 10 to 13 Gyr has also been detected, but with lesser SF rates than later episodes.

HI studies in Leo T have decomposed neutral gas as cold-neutral medium (CNM) and warm neutral medium (WNM) (Ryan-Weber et al. 2008; Adams & Oosterloo 2018). MUSE IFU studies show that the low velocity dispersion ($\sigma = 2.31^{+2.68}_{-1.65}\,\mathrm{kms}^{-1}$; Vaz, Daniel et al. 2023) of younger stars is in good agreement with a CNM. A recent study by Villanueva et al. (2025) revealed the presence of molecular hydrogen near the center of Leo T with $1.4 \pm 0.4 \times 10^4\,M_\odot$, which is 3% of the total gas mass of this galaxy.

The inner region exhibits very minimal Hα emission (Vaz, Daniel et al. 2023) and some UV emission (Donovan Meyer et al. 2015), both of which usually originate from massive stars. However, MUSE observations confirm that the Hα-emitting stars are associated with fast-rotating Be stars rather than massive stars, such as O or early B type stars (Vaz, Daniel et al. 2023). Thus, the mechanism of SF in Leo T is very different from that in typical disk galaxies. Given its exceptionally

low stellar surface density and correspondingly weak self-gravity, understanding the origin of the observed UV emission in such an extreme, faint system presents a compelling astrophysical puzzle.

In this study, we utilize UVIT FUV observations to extract UV SFCs and characterize them. We also utilize the MUSE IFU from (Vaz, Daniel et al. 2023) and the publicly available HST photometric catalog from (Weisz et al. 2012) to gain insights into the UV-emitting population in such extreme environments. We then compare our findings with those of previous studies.

7.2 Observations

Leo T is part of the MUSE Faint survey (Zoutendijk, Sebastiaan L. et al. 2020), a MUSE GTO survey of UFDGs galaxies (PI Brinchmann). The details of the MUSE observations and the data reduction of this galaxy are described in Vaz, Daniel et al. (2023).

We observed Leo T in the FUV band using the UVIT on board ASTROSAT (Kumar et al. 2012). This galaxy is observed in filter F148W $\lambda_{\rm mean}$=1481 Å, $\Delta\lambda$=500 Å). The exposure time of this data is around 13.8 ks. We downloaded the raw level 1 data from ISSDC and reduced it using the graphical user interface, CCDLAB (Postma & Leahy 2017, 2021). We also used archival FUV and NUV data from GALEX (Martin et al. 2005), which has a spatial resolution around 5″.

We use an archival Dark Energy Camera Legacy Survey (DECaLS) r-band image. The Dark Energy Camera (DECam; Flaugher et al. (2015)) is mounted on the Blanco 4-meter telescope, located at the Cerro Tololo Inter-American Observatory

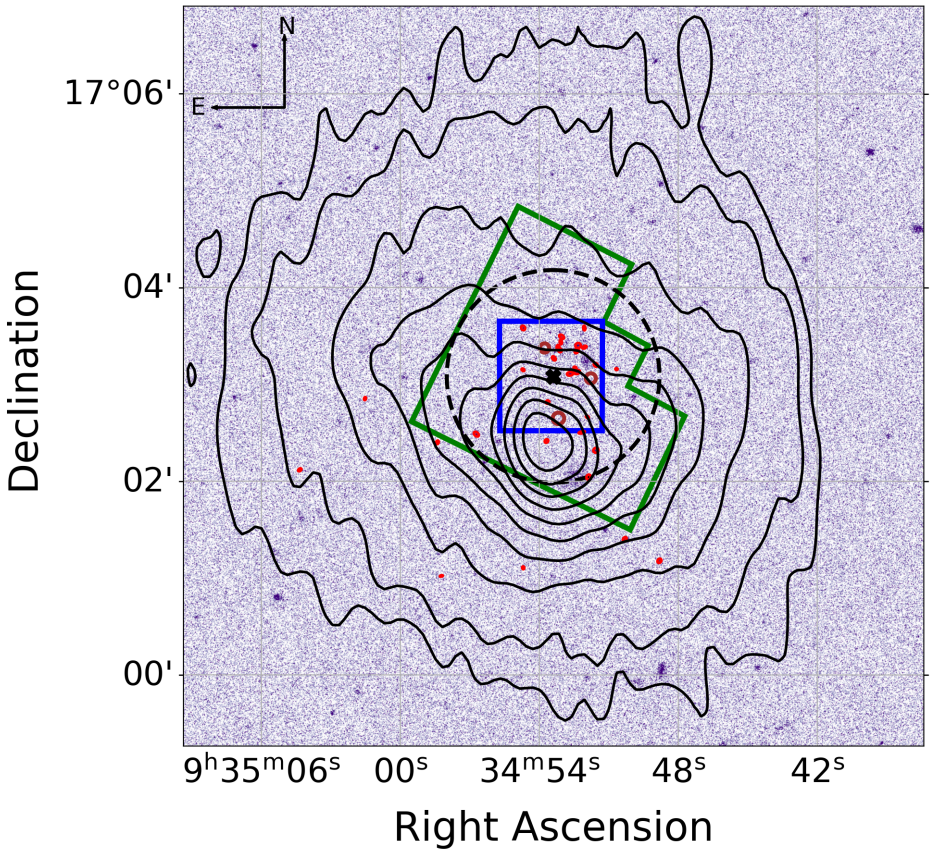


FIGURE A.1: The background image is the UVIT FUV image of Leo T. The optical center is marked as a black cross. The red ellipses are the extracted FUV SFCs. The black contours represent HI intensity contours from deep Westerbork Synthesis Radio Telescope observations (Adams & Oosterloo 2018), ranging from 5%, 10% to 90% of the peak flux with a step size of 10%. The peak HI column density is 4.2 $\times 10^{-20}$cm^{-2}. The green polygon is an HST FOV (Weisz et al. 2012), and the blue one is MUSE FOV (Vaz, Daniel et al. 2023). The black dashed circle is the FOV of Atacama Compact Array, and brown circles are the molecular cloud locations as mentioned in Villanueva et al. (2025).

(CTIO). It has a FOV of 3.2 square degrees and a median resolution of around 1.2 ″.

The HI emission extent and the confinement of UV clusters can be seen in Figure A.1. The plotted HI intensity contours are from deep Westerbork Synthesis Radio Telescope observations (Adams & Oosterloo 2018). This figure also compares the HST and MUSE FOV with the total HI and FUV extent of Leo T.

7.3 UV Star forming Clusters

We performed background subtraction of the science-ready UVIT-FUV image using IRAF (Tody 1993), as mentioned in Amrutha et al. (2024). We used SExtractor (Bertin & Arnouts 1996) to extract the UV Star-forming Clusters (SFCs) from the FUV image with a detection threshold of 2 σ, where σ is the estimated global background noise of the FUV image. We set a low threshold as there is no faint diffuse UV emission associated with this galaxy. We had set the minimum area to 10 pixels. We masked the foreground sources by comparing the extracted SFCs with the Gaia sources using TOPCAT (Taylor 2005). We also masked background extended sources by comparing the UVIT field with the optical SDSS field. We extracted 30 FUV SFCs in Leo T. Extracted SFCs are shown with red ellipses in Figure A.1. We get the position and the ellipse parameters of SFCs from the SExtractor.

7.3.1 Extent of UV SFCs in Leo T

We examined the distribution of UV SFCs with respect to HI extent. In Figure A.1, we can clearly see that most of the UV SFCs are clustered near the optical center (R.A. = 143.722500 deg, Dec. = 17.051389). 70% of SFCs are within the half light radius $R_{1/2}$=115 pc (Wolf et al. 2010). HI extent of the galaxy is around 400pc, which is nearly 4 times $R_{1/2}$ (Adams & Oosterloo 2018). The SFCs, which are far from the center, lie generally to the south or east of the optical and HI centers. The distribution can be seen in the Figure A.2.

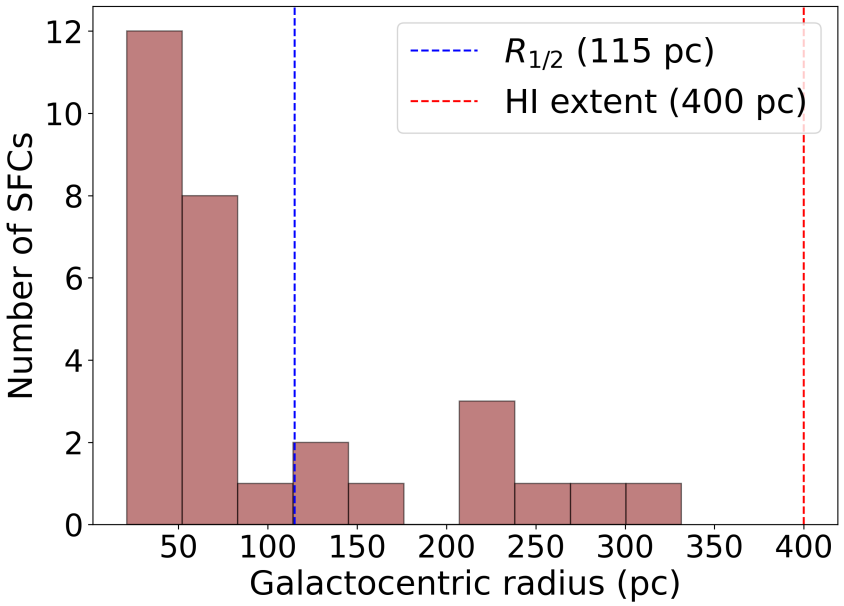


FIGURE A.2: Distribution of SFCs along the galactocentric radius. Vertical blue and red lines are half light radius $R_{1/2}$=115 pc (Wolf et al. 2010) and HI extent of the galaxy (400pc; Adams & Oosterloo (2018)).

7.3.2 Properties of UV Star forming Clusters

Radius: We can resolve star clusters above the size of 2.37 pc (blue dashed line in Figure A.3), which corresponds to UVIT resolution 1.2″ at the distance of 409 kpc. The radii of SFCs in Leo T are above this limit. This scale corresponds to the scale of bound star clusters (Elmegreen et al. 2014). Hence, the SFCs may have more than one star that emits in FUV. We see in Figure A.3 that the median radius of SFCs is approximately 4.4 pc (black solid line). There is not much difference in size as we go from the inner region to the outer region of the galaxy.

Luminosity: We found the total counts within the SFCs and corrected for Milky Way extinction (Schlafly & Finkbeiner 2011) for the FUV image. Based on detection in WISE imaging, the galaxy shows negligible dust (Donovan Meyer et al. 2015). Hence, we did not correct for internal extinction. We converted counts per second to flux using the conversion factor from Tandon et al. (2020). The FUV luminosity of these SFCs is distributed between 10^{34} ergs^{-1} to 10^{36} ergs^{-1}. By

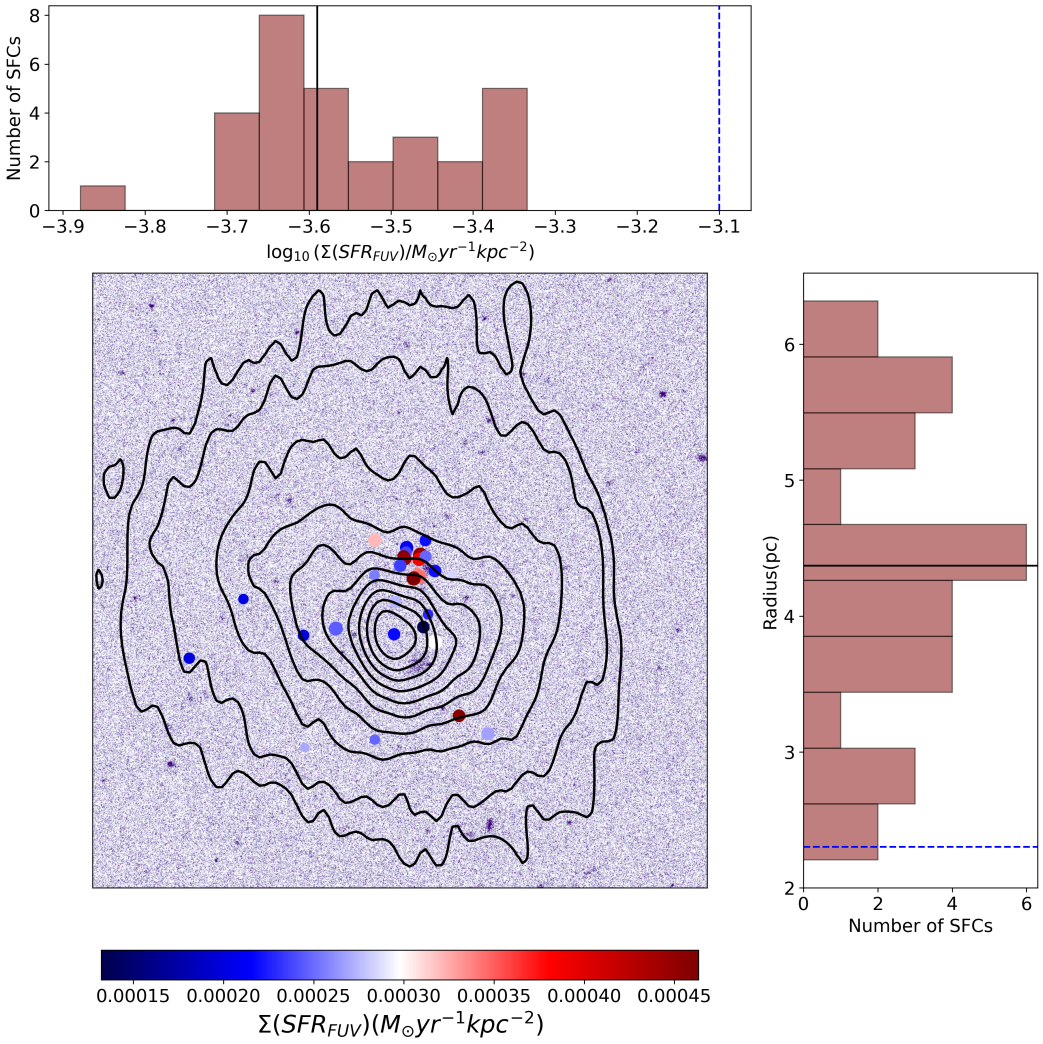


FIGURE A.3: The background image is the UVIT FUV image of Leo T. The black contours are the HI intensity contours (Adams & Oosterloo 2018). The image shows how Σ(SFR) and the radius of SFCs are distributed in the galaxy. The image also shows the SFC radii and Σ(SFR) histograms. The black solid lines are the median values. The dashed blue line in the SFC radii histogram is the resolution limit, and in the Σ(SFR) histogram, it is the lower Σ(SFR) limit for dwarf irregular galaxies in Amrutha et al. (2024).

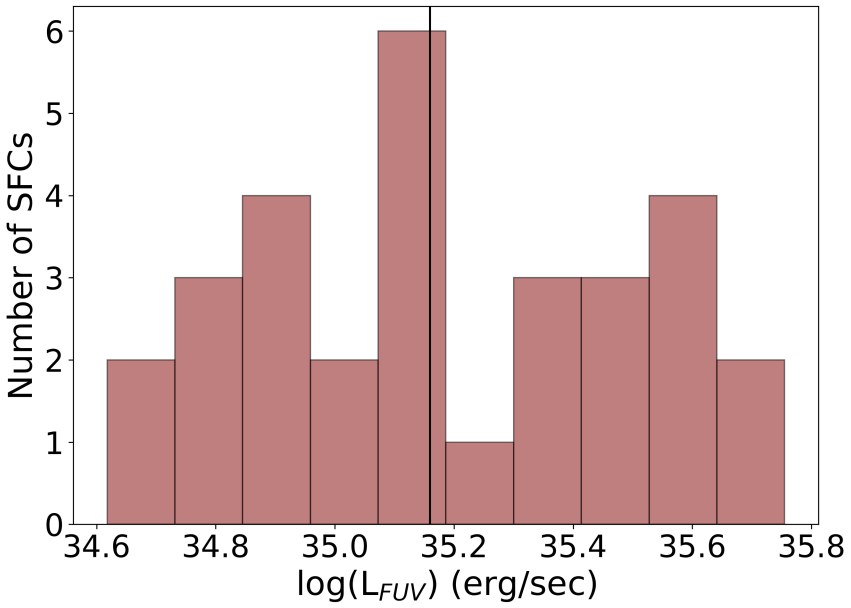


FIGURE A.4: Histogram of FUV luminosity of SFCs. The black solid line is the median value.

using Castelli & Kurucz (2004) model, Amrutha & Das (2025) found the FUV and NUV luminosities for massive O and B stars. UV luminosity corresponding to a massive B star is above 10^{36} ergs^{-1}. Hence, we can confirm that there are no massive OB stars in Leo T. The median luminosity corresponding to the SFCs is around $10^{35.16}$ ergs^{-1}. The distribution of FUV luminosity of SFCs is shown in Figure A.4.

Star formation rate density: We calculated the FUV star formation rate (SFR) for the SFCs using the relation,

$$\mathrm{SFR_{FUV}} = 0.68 \times 10^{-28} \times \mathrm{L_{FUV}} \tag{7.1}$$

where $\mathrm{L_{FUV}}$ is the extinction corrected FUV luminosity in ergs^{-1}Hz^{-1}. This relation is from Salim et al. (2007) for sub-solar metallicity and Chabrier IMF (Chabrier 2003).

The SFR density Σ(SFR) of these SFCs is between $10^{-3.9}$ to $10^{-3.3}\mathrm{M_{\odot}yr^{-1}kpc^{-2}}$.

We compare these values with the Σ(SFR) of SFCs in SFDGs, primarily dwarf irregulars. In Amrutha et al. (2024), it is shown that the Σ(SFR) of dwarf irregulars is very much lower than dwarf spirals and BCDs, with $10^{-3.09}\,M_{\odot}yr^{-1}kpc^{-2}$ as the lowest value of Σ(SFR). Even the highest Σ(SFR) measured for the Leo T SFCs falls below this value, highlighting the exceptionally inefficient star formation occurring in this low-mass satellite galaxy. Such low values are consistent with the stellar surface densities of Leo T compared to that of SFDGs.

7.4 Possible UV-emitting stars in Leo T

7.4.1 Cross-matching with HST catalog

Weisz et al. (2012) catalog provides the HST photometric properties of well-measured stars. The catalog provides information on the positions of stars, as well as their magnitudes in the F814W and F606W filters, along with their associated errors. We cross-matched our FUV clusters with the HST stars. The catalogue of UV clusters, associated HST stars, and their age is given in the Table 7.1. We had 22 out of 30 UV SFCs in the HST FOV, but we only identified possible UV stars for 19 SFCs. This is because of the few UV clusters located in the HST region, with incomplete HST coverage associated with the combination of the two HST fields used to construct the mosaic. One of three SFCs has a bright MUSE counterpart (UV source 15 in Table 7.1), but not HST.

We plotted all the associated HST stars in a CMD to find the possible FUV-emitting stars. We fitted isochrones of different ages from 10 Gyr to 150 Myr. We used Padova's set of stellar evolution models and took parameters from Weisz et al. (2012). However, we fixed the metallicity value as [M/H]=-1.6 (Vaz, Daniel et al. 2023). We removed all the stars with F814W > 25.5 and F606W-F814W >

0.5, as these are the faintest and reddest stars, which are the least likely to emit UV. The CMD with possible UV-emitting HST stars is shown in Figure A.5.

We compared the associated HST stars with Weisz et al. (2012) and Clementini et al. (2012) to classify them. We identified that the UV-emitting clusters contain Blue loop (BL) stars, Upper and lower Main sequence (MS) stars, and some Horizontal Branch (HB) stars. We find that 79% (15 out of 19) of FUV clusters have a single UV-emitting star. There are 5 BL stars and 9 SFCs that have upper-MS stars (including 3 emission line stars, discussed in the next section). Also, 7 SFCs have low-MS stars. However, 3 of them are accompanied by upper-MS stars. We find that 95% of the SFCs have ages less than 1 Gyr, out of which 11 SFCs have stars younger than 500 Myr, out of which only 2 SFCs have stars of age less than 200 Myr. The UV SFCs at the HI centre have 2 HB stars, which have an age of around 2 Gyr.

7.4.2 Cross-matching with MUSE sources

From MUSE IFU analysis, Vaz, Daniel et al. (2023) identified 58 stars. Out of which, 20 stars were identified with age $\leq$1 Gyr. We cross-matched UV SFCs with 58 stars and again with the HST catalog. Only 6 stars have the UV emission. Four out of 6 stars are classified as upper MS stars when compared with HST. Three of the FUV-emitting MUSE sources are Hα-emitting stars, also known as emission line stars (EL stars). These three stars are Be stars (Vaz, Daniel et al. 2023). There is one BL and one lower MS star that has an associated MUSE star. The upper age limit for 1 MUSE star is around a Gyr, and 4 stars have 500 Myr, and only one is younger than 150 Myr.

TABLE 7.1: Properties of UV Star-forming Complexes

Index	UV RA [deg]	UV Dec [deg]	Area [10^{-5}kpc^2]	$\Sigma(SFR_{FUV})$ [10^{-3} [$M_\odot yr^{-1}kpc^{-2}$]	HST RA [deg]	HST Dec [deg]	Color	F814W [mag]	Age [Gyr]	MUSE RA [deg]	MUSE Dec [deg]	Star Type
1	143.7170179	17.05982212	4.66	0.22 ± 0.003	143.7167917	17.05961111	-0.016	23.637	<0.5			Up MS
2	143.7280098	17.05983809	8.17	0.32 ± 0.003	143.72775	17.05963889	-0.01	22.965	<0.5	143.7279075	17.05968746	EL
3	143.7210927	17.05832311	8.38	0.21 ± 0.002	143.72125	17.05883333	-0.041	24.484	<0.5			Low MS
3					143.7207083	17.05805556	-0.008	23.587	<0.5			Up MS
4	143.7212312	17.05740724	4.39	0.24 ± 0.003	143.7210833	17.05727778	0.001	24.638	<1			Low MS
5	143.721749	17.05654516	5.59	0.46 ± 0.005	143.7214167	17.05633333	0.051	21.45	<0.5			BL
6	143.7213978	17.05599662	6.3	0.45 ± 0.004	143.721125	17.05572222	-0.047	22.7	<0.5	143.7212683	17.05580793	EL
7	143.7181246	17.05682249	12.53	0.45 ± 0.004								
8	143.7183826	17.05591634	8.75	0.38 ± 0.004	143.718125	17.05577778	0.048	25.257	<0.2			Low MS
8					143.7179167	17.05658333	-0.117	23.459	<0.2			Up MS
8					143.7182083	17.05547222	-0.058	23.994	<0.5			Up MS
9	143.7169908	17.05652612	5.24	0.25 ± 0.003								
10	143.7224884	17.05460462	6.47	0.23 ± 0.003	143.722875	17.05427778	0.076	23.97	<1			Up MS
11	143.714962	17.05349263	6.55	0.22 ± 0.002	143.7147917	17.05333333	-0.01	23.539	<0.5	143.7148875	17.05338229	Up MS
12	143.7112194	17.05275168	1.83	0.28 ± 0.005	143.7109167	17.05266667	0.008	23.93	<1			Up MS
13	143.728043	17.05263533	3.02	0.26 ± 0.003	143.727875	17.05233333	-0.004	24.699	<1			Low MS
13					143.7277917	17.0525	-0.096	23.47	<0.2	143.7280032	17.0524698	Up MS
14	143.7183057	17.05225203	10.21	0.34 ± 0.003	143.7180417	17.05219444	0.102	21.101	<0.5	143.7181491	17.05218401	BL
15	143.7195777	17.05195244	10.5	0.46 ± 0.004	143.7202083	17.05186111	0.037	25.288	<1			Low MS
15										143.719469	17.05177861	EL
16	143.7236156	17.04707352	5.26	0.27 ± 0.003	143.7235	17.04752778	0.092	25.517	<1			Low MS
17	143.716462	17.04451533	2.8	0.23 ± 0.003								
18	143.7174775	17.04187339	6.14	0.13 ± 0.002	143.717375	17.04166667	0.09	24.81	<1			Low MS
19	143.7364467	17.04155411	10.41	0.25 ± 0.002	143.7361667	17.04138889	0.037	21.506	<0.5			BL
20	143.7238222	17.04037914	5.85	0.22 ± 0.002	143.723625	17.04033333	0.12	23.562	<2			HB
20					143.723875	17.04022222	0.219	22.655	<2			HB
21	143.7149312	17.03878537	11.32	0.3 ± 0.003	143.7146667	17.03872222	0.024	20.901	<0.5			BL
22	143.7162566	17.03417653	9.86	0.41 ± 0.004	143.7159583	17.03405556	0.037	21.336	<0.5			BL
23	143.7280064	17.018557	2.79	0.25 ± 0.004								
24	143.7431595	17.01691507	1.53	0.27 ± 0.006								
25	143.7097425	17.0235024	6.52	0.46 ± 0.004								
26	143.7035042	17.01977132	7.68	0.27 ± 0.003								
27	143.7682088	17.03541104	4.12	0.20 ± 0.003								
28	143.7434459	17.04014448	4.37	0.20 ± 0.003								
29	143.7564737	17.04766672	2.76	0.20 ± 0.003								
30	143.7186868	17.05293903	4.15	0.34 ± 0.004								

Note: UV RA, UV Dec, and Area are SFC parameters obtained using SExtractor for the FUV SFCs. $\Sigma(\mathrm{SFR_{FUV}})$ is estimated FUV star formation rate density. HST RA, HST Dec, color (F606W-F814W), and magnitude F814W are the stellar parameters from the HST catalog Weisz et al. (2012) for cross-matched stars. Age is the age of HST stars. Age and Star types are inferred from the CMD (See Figure A.5). MUSE RA and MUSE dec are stellar parameters of cross-matched stars from Vaz, Daniel et al. (2023).

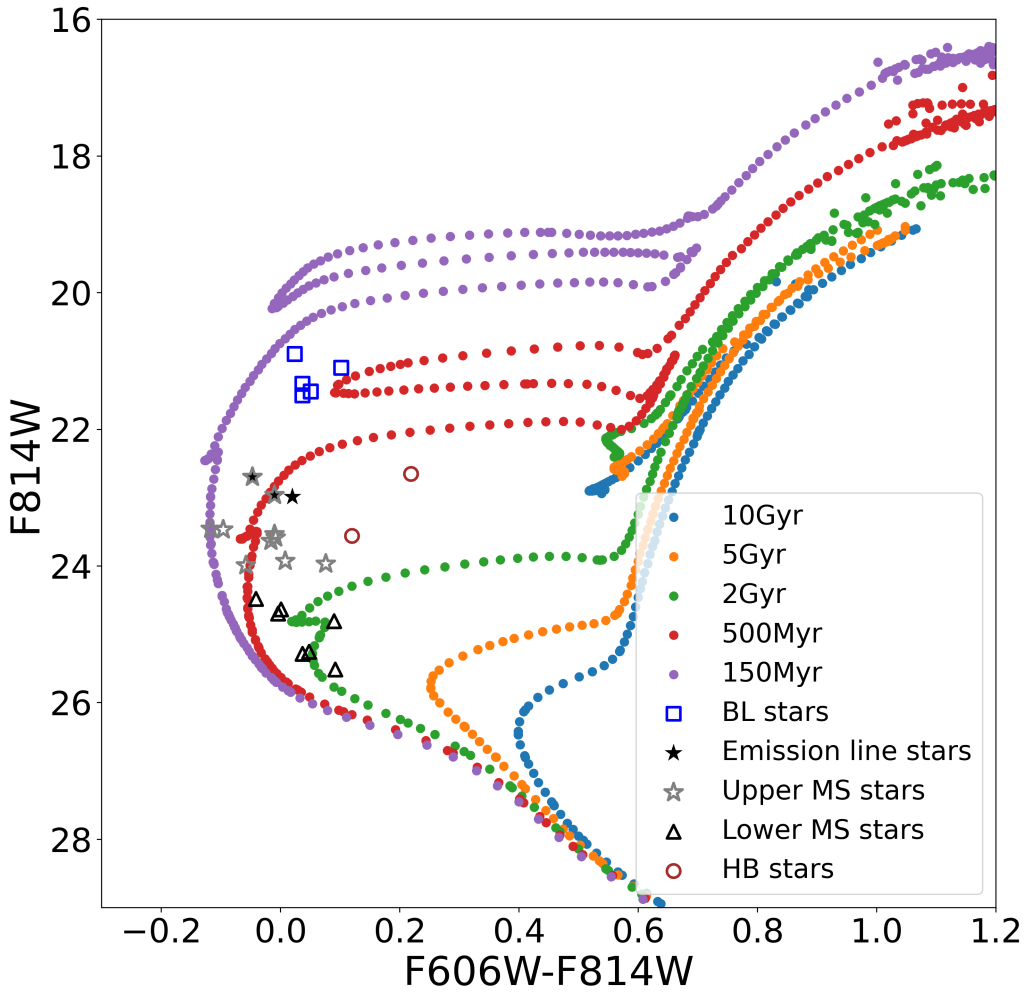


FIGURE A.5: The deep HST/WFPC2 CMD of Leo T with select Padova isochrones for UV sources. Isochrones of different colors represent different ages, and markers of different colors represent different populations.

7.4.3 Distribution of UV-emitting stars in Leo T

We can infer the propagation of SF by examining the distribution of stellar populations of different ages. We examined how different types of stars are distributed in Leo T with respect to the optical and HI centers. As seen in Figure A.2, most of the UV SFCs are present near the optical center. When we examined the type of stars we have identified, we found that all the upper-MS and EL stars lie near the optical center. There is one BL and a few lower-MS stars present in that region. However, as we move south, around the HI center, we find HB, BL, and a few

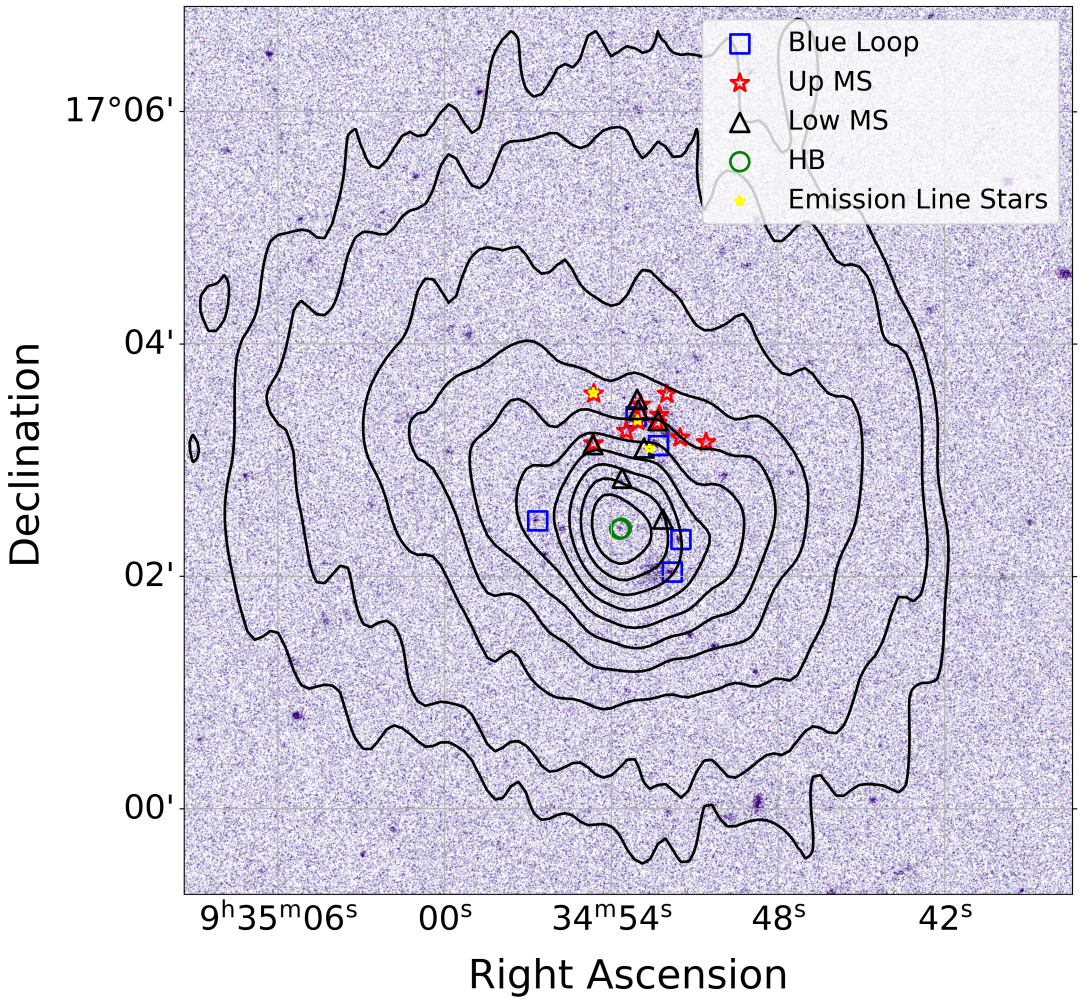


FIGURE A.6: Distribution of UV emitting stellar population of Leo T. Background image is UVIT FUV image of Leo T. Black contours are high-intensity contours (Adams & Oosterloo 2018). Different markers in the image represent different stellar populations emitting UV.

lower-MS stars. This indicates the recent episodes of SF are mainly localized to areas that lie towards the optical center. This distribution is shown in Figure A.6.

Next, we examined the physical properties of the UV-selected SFCs hosting different stellar populations. We find that the SFCs containing both EL stars and lower MS stars, as well as SFCs hosting BL stars, generally exhibit the largest areas and highest UV luminosities. The SFCs containing only EL stars show slightly lower luminosities and smaller areas compared to those with BL stars. Interestingly,

SFCs containing only lower-MS stars and those containing upper-MS stars display comparable areas and luminosities. Nevertheless, one SFC containing only upper-MS stars and another containing both upper- and lower-MS stars exhibit exceptionally low luminosities and small areas; this is puzzling and requires more attention. The SFCs containing two HB stars exhibit area and luminosity distributions similar to those of upper- and lower-MS SFCs. The distribution of these properties as a function of stellar content is shown in Figure A.7.

The larger sizes and higher UV luminosities of BL and EL containing SFCs are consistent with relatively recent or prolonged SF activity. The similarity in properties between upper- and lower-MS SFCs suggests that UV emission in these systems is not dominated by a single evolutionary phase. The mild UV excess observed within some UVIT apertures containing lower-MS stars may also arise from additional unresolved stellar populations, particularly in regions that fall within gaps in the HST mosaic coverage. Although we consider UV SFCs detected as the extended sources, as their radius is of the order of a few pc. When compared with HST or MUSE, we see that most of the UV SFCs have a single possible UV-emitting star. However, additional lower-mass or older stellar members may be present within the UVIT aperture but contribute little to the FUV emission or remain below the HST detection threshold for young UV-bright stars. This uncertainty of whether the UV source is a star or a cluster of stars may arise from instrumental and analysis-related effects, including UVIT–HST resolution mismatch, spatial variations in UV depth, astrometric uncertainties, and CMD-based stellar classification. In particular, unresolved UV blends and incompleteness in the resolved stellar catalog may lead to UV excess in SFCs classified as lower-MS dominated, while background subtraction and aperture definition can suppress UV luminosities in compact SFCs. This also creates a large scatter in the properties of UV SFCs containing a specific type of star, as shown in Fig. A.7.

This scatter in properties of UV SFCs makes it difficult to characterize the other

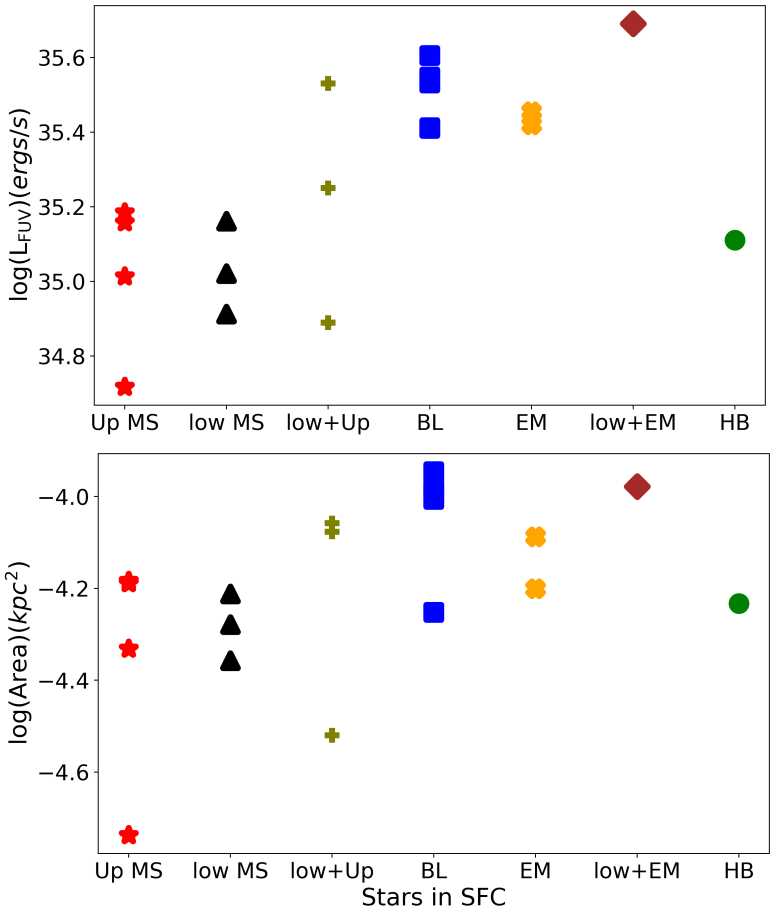


FIGURE A.7: FUV Luminosity (Top panel) and Area distribution of SFCs with respect to the type of star present in it. The star and triangular markers represent SFC with Upper MS and Lower MS, respectively. '+' marker represents SFC containing both lower and upper MS. BL and HB have square and circular markers, respectively. Whereas SFCs with cross and diamond markers have EL and both EL and lower MS stars.

outer SFCs. However, by comparing the properties of SFCs without UV Star information with those that are characterized, we can give an idea of what these sources might be. In the Table. 7.1, most of the outer SFCs have luminosities similar to those of MS or HB stars. Only two SFCs have high luminosity similar to BL and EL. This again indicates that most outer SFCs are likely low-mass stars.

7.5 Radial Profiles of Young and Old Stellar Population Tracers

We plotted the radial variation of GALEX FUV, NUV, and DECaLS r-band magnitudes to investigate the spatial distribution of the younger and older stellar populations in Leo T. This is shown in Fig. A.8. We used GALEX FUV and NUV data, as UVIT does not have NUV observations for Leo T. Both the FUV and NUV surface brightness profiles exhibit a strong decline with increasing galactocentric radius, fading by approximately 5 mag between 100 and 270 pc. The FUV profile shows larger fluctuations and a slightly steeper decline than the NUV profile, suggesting that the youngest stellar populations are more centrally concentrated and that the FUV emission is spatially patchier. The r-band profile follows a similar overall trend but declines by only $\sim$ 2 mag. This shallower gradient indicates that the older stellar population is more extended than the young UV-emitting component. The slight upturn is seen in the outermost radial bin of both the FUV and r bands is likely due to low signal-to-noise measurements at large radii.

FUV emission can come from both the younger and evolved populations. It is important to see what kind of population dominates the FUV emission, for a galaxy whose 50 % of stars formed 7 Gyr before. Therefore, we examined radial variation of NUV $-$ r over the galaxy. This is shown in the bottom panel of Fig. A.8. A NUV $-$ r $<$ 4 indicates that most of the FUV emission are generally dominated by stellar populations younger than $\sim$1 Gyr (Salim et al. 2005; Kaviraj et al. 2007; Renu et al. 2025). Our radial trend also falls within this value till 189 pc, indicating that FUV emission over Leo T is dominated by a younger population. (Kaviraj et al. 2007) also shows that for NUV $-$ r $>$ 5.5, the emission traces the UV upturn from older populations. Beyond a radius of 225 pc, we observed that NUV $-$ r $\geq$ 5.5, suggesting a transition to an older stellar population and a diminishing

contribution from recent star formation.

Although the NUV − r color has been extensively used to distinguish between young and old stellar populations in more massive galaxies, its interpretation in an extremely low-mass galaxy such as Leo T should be treated with caution owing to its low metallicity, stochastic star formation history, and low stellar mass. Consequently, the radii identified using these empirical NUV − r thresholds should be regarded as approximate indicators of changes in the dominant stellar population, rather than definitive boundaries.

7.6 Indications of Leo T infall into the MW from UV

Leo T is the lowest-mass galaxy known to have retained its gas. This may be explained if the galaxy is undergoing its first infall into the MW (Rocha et al. 2013), or if it is a wide-orbit backsplash dwarf that has experienced only minimal interaction with the MW in the past (Blaña et al. 2020, 2024). Leo T exhibits offsets between its gas and stellar components (Adams & Oosterloo 2018), as well as evidence of recent star formation in an extremely low-density and low-metallicity environment (de Jong et al. 2008; Weisz et al. 2012; Vaz, Daniel et al. 2023). In addition to possible environmental interactions, Blaña et al. (2024) showed that the observed offsets may also be influenced by the internal dynamical evolution of an initially displaced young stellar population oscillating within an extended cored dark-matter halo. This younger stellar population, which also includes evolved stars, emits in the UV, allowing us to constrain and characterise the UV-emitting stellar populations of Leo T.

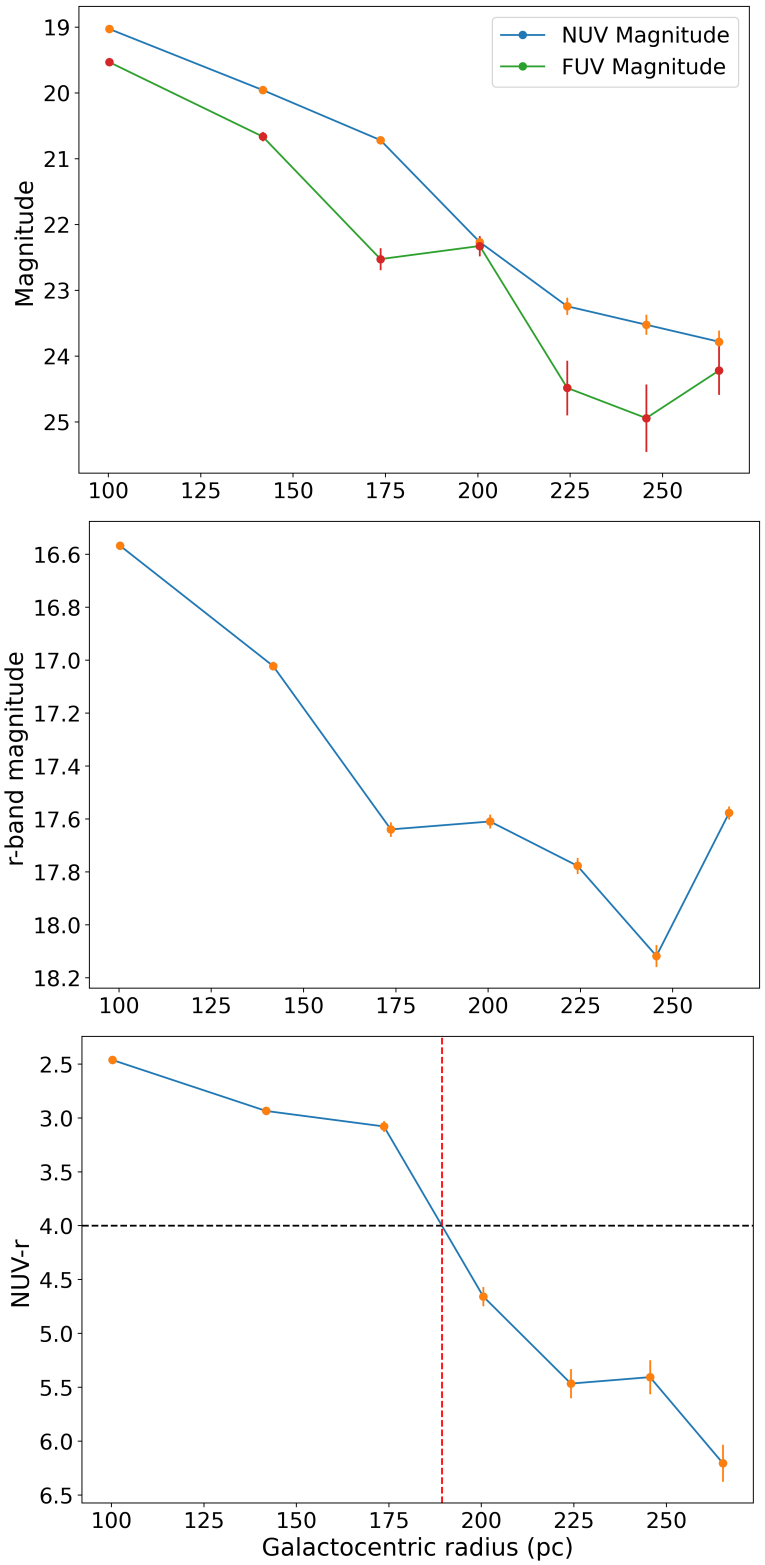


FIGURE A.8: Radial variation of GALEX FUV and NUV magnitudes (from Top panel), Decals r-band magnitude and NUV-r color.

The FUV observations cover the full extent of the galaxy's H I distribution, enabling us to examine the spatial relationship between FUV-bright stars or clusters and the neutral gas. The presence of an extended H I disk, together with a faint gaseous feature to the north, may be consistent with the effects of ram pressure, with the northern feature potentially representing trailing or displaced gas (Blaña et al. 2024). Although most SFCs are located close to the optical centre and slightly north of it, the southern distribution extends to larger galactocentric distances. Previous studies have also reported asymmetric H I morphology, with enhanced gas density towards the south and a compressed edge towards the west (Adams & Oosterloo 2018; Blaña et al. 2020). These complex gas and stellar morphologies may reflect a combination of environmental effects, such as ram pressure, and internal dynamical processes (Blaña et al. 2024). The faint northern H I extension may trace stripped or displaced material where the gas density is insufficient to sustain star formation. However, the absence of O- and B-type stars may indicate that recent star formation has been suppressed (Vaz, Daniel et al. 2023). Alternatively, the deficit of massive stars could reflect a truncated high-mass initial mass function (IMF) or stochastic sampling of the IMF (Weisz et al. 2012).

7.7 The Star Formation Rate and Star Formation Efficiency in Leo T

7.7.1 Leo T Star Formation Rate

Hα and UV emission trace star formation over different timescales. Hα primarily traces the instantaneous star formation rate over the past $\sim$10 Myr, whereas UV emission is sensitive to star formation over longer timescales of up to a few hundred Myr (Bell & Kennicutt 2001; Iglesias-Páramo et al. 2004; Salim et al.

2007). From the analysis presented in Section 7.4.1 and Table 7.1, we find that several UV-emitting stellar populations in Leo T have ages exceeding 500 Myr. Consequently, the UV luminosity may contain contributions from stars that are significantly older than those responsible for the Hα emission, leading to systematically higher UV-derived SFRs. This discrepancy is expected to be particularly pronounced in low-mass galaxies such as Leo T. At very low star formation rates, stochastic sampling of the upper end of the initial mass function can result in a deficit of massive O stars, suppressing the Hα luminosity while leaving the UV emission relatively unaffected. In addition, leakage of Lyman continuum photons can further reduce the observed Hα flux and lead to an underestimate of the Hα-derived SFR (Lee et al. 2009). Therefore, direct comparisons between UV- and Hα-based SFRs should be interpreted with caution, as the two tracers probe different stellar populations and timescales. In this section, we estimate the upper limit of UV-derived SFR of Leo T and compare it with previous measurements based on other star formation tracers. Any differences between these estimates provide insight into the recent star formation history and the stochastic nature of star formation in this extremely low-mass galaxy.

Leo T shows very minimal Hα emission. Using the small MUSE FOV, the upper limit of Hα Σ(SFR) is less than 10^{-5}M$_\odot$yr^{-1}kpc^{-2} (Vaz, Daniel et al. 2023). We derived Σ(SFR) within the effective radius (115 pc; Wolf et al. (2010)) and also until the radius of the last UV-detected SFC (at 325 pc). The values are 5×10^{-5}M$_\odot$yr^{-1}kpc^{-2} and 1.3×10^{-4}M$_\odot$yr^{-1}kpc^{-2} respectively. The Σ(SFR) within the effective radius is 5 times larger than the MUSE study (Vaz, Daniel et al. 2023). However, Σ(SFR) for the full extent is larger than the $\Sigma(SFR)$ within the effective radius, which indicates that there is significant SF in the outer disk, since the Σ(SFR) is larger. Still, this value is less than Σ(SFR) = 10^{-3}M$_\odot$yr^{-1}kpc^{-2}, which was derived using the SFHs obtained from stellar population models (Weisz et al. 2012). The observational Σ(SFR) for Leo T is at the lower end of Σ(SFR) of extremely metal-poor dwarfs (Filho et al. 2016). The UV SFCs have larger

Σ(SFR) compared to the integrated Σ(SFR); but this is due to the compact size of the SFCs.

Although there is no gradient in the sizes of the SFCs as we go from a high-density to lower-density regions, the Σ(SFR) is larger for the SFCs lying close to the optical center and generally lower towards the outer radius. This shows that to form stars efficiently (even if there is a SF trigger), both the stellar and gas surface densities must be high.

7.7.2 Correlation with molecular hydrogen and star formation efficiency

Villanueva et al. (2025) reported the first detection of CO(1–0) emission in Leo T and identified three regions with high signal-to-noise ratios. The locations of these regions are shown as brown circles in Figure A.1. No UV SFCs are detected within these CO-bright regions. However, diffuse UV emission arising from unresolved stellar populations can contribute to the UV emission within the aperture, but may not be associated with any compact SFCs. We measured the UV emission within the CO apertures and derived the corresponding upper limit of SFRs. The SFRs, molecular gas masses, and resulting SFEs are listed in Table 7.2. The mean values of $\log(\mathrm{SFR}/\mathrm{M}_\odot\ \mathrm{yr}^{-1})$ and $\log(\mathrm{SFE}/\mathrm{yr}^{-1})$ are -8.76 and -12.48, respectively, indicating extremely low SF activity and low efficiency in all three regions. Alternatively, the SF may have already faded below UV detectability. Another possibility is that the CO-bright region is expected to have significant internal extinction, rendering any UV emission invisible. Therefore, the absence of detected UV SFCs within the CO-bright regions should not be interpreted as evidence for the absence of recent star formation. These low SFRs and SFEs are also consistent with stochastic SF, where gas can remain molecular for long periods without forming stars in UFDGs. Hence, longer gas depletion times and

TABLE 7.2: Physical quantities of the CO clouds in Leo T.

Cloud position	r_{CO} [arcsec]	M_{mol} [10^3 $M_\odot$]	SFR_{FUV} [10^{-9} $M_\odot yr^{-1}$]	SFE [10^{-13}yr^{-1}]
N	5.7 ± 0.25	4.6 ± 1.4	0.96 ± 0.08	2.08 ± 0.66
W	6.2 ± 0.8	5.0 ± 1.6	1.53 ± 0.08	3.06 ± 0.99
S	7.1 ± 0.23	4.9 ± 1.5	2.74 ± 0.08	5.59 ± 1.71

Note: Parameters- cloud radius r_{CO}, mass of molecular gas M_{mol} are from Villanueva et al. (2025). SFR_{FUV} and SFE are estimated FUV star formation rate and star formation efficiency.

inefficient collapse of molecular clouds. Among the three clouds, the southern CO region exhibits a higher SFE compared to the other two regions. This region is also located farther from the UV SFCs and the optical centre of the galaxy. This region could be influenced by external processes, making it slightly distinct from the central regions.

7.8 Summary

In this work, we present UVIT FUV observations of the MW satellite galaxy Leo T, which is a gas-rich UFDG showing signs of recent SF. Utilizing high resolution and larger FOV of UVIT, we extracted and examined the properties of UV SFCs from this galaxy and compared them with HST and MUSE to know the possible UV emitting stellar populations. Our study offers new insights into the process of SF in extremely low-mass and low-metallicity environments. Our main results of this work are summarised below:

1. The UV-emitting SFCs in Leo T are distributed out to a radius of 300 pc. However, 70 % of the SFCs are within the half-light radius ($R_{1/2}$=115pc).

2. The UV luminosity of the UV-emitting SFCs is less than the UV luminosity of massive O and B stars. This confirms previous results in the literature that there are no massive O and B stars in Leo T. This constrains the recent SF to at least 30 Myr ago.

3. The Σ(SFR) of the SFCs of Leo T is less than the Σ(SFR) of the SFCs in SFDGs.

4. We cross-matched the FUV-emitting SFCs with the HST and MUSE stellar population catalogs and identified the possible UV-emitting stars. The UV-emitting stars in Leo T are Upper-MS, Lower-MS, BL, HB, and EL stars.

5. The Upper-MS and EL stars are concentrated within the optical radius. Whereas the lower-MS and BL stars have a larger distribution within the disk of Leo T.

6. We find that the SFCs with BL and EL stars are generally distributed, have larger radii, and have luminosities comparable to the other SFCs. Interestingly, the SFCs with upper and lower MS have similar properties, suggesting some uncertainty due to UVIT–HST resolution mismatch, spatial variations in UV depth, astrometric uncertainties, and CMD-based stellar classification.

7. Leo T has an (NUV − r) colour profile that indicates that the UV emission is dominated by stellar populations younger than 1 Gyr out to a radius of $\sim$ 189 pc, beyond which emission is dominated by older populations.

8. The UV SFCs are concentrated around the optical center and have extended south of the optical radius, suggesting a directional interaction with the MW's

halo.

9. Leo T has very low Σ(SFR), which is below $10^{-4} M_{\odot} yr^{-1} pc^{-2}$. When compared with CO clouds from Villanueva et al. (2025), we do not detect any FUV emission associated with it. Hence, the SFE is also very low. The southern CO region exhibits a higher SFE compared to the other regions, which indicates that it could be influenced by external processes.

Chapter 8

Conclusions & Future Work

8.1 Summary and Conclusions

This thesis is aimed at understanding how star formation varies across different galactic environments, which is a fundamental question in galaxy evolution. We investigated the physical processes that regulate extragalactic star formation and how local interstellar conditions, including the radiation field and gas properties, influence it. Additionally, we examined how star formation influences the ISM of the galaxy. This chapter summarises our main results from the thesis and presents conclusions. We also outline the future plans that require investigation.

Constraining the High-Mass End of the IMF in Star-forming Regions of a Massive Galaxy

Chapter 3 highlights a new observational approach to probe the high-mass end of the IMF at sub-kiloparsec resolution using UVIT-UV and MUSE-Hα observations in the inner disk of NGC 628. We classified the SFCs as arms, spur, and interarm SFCs and investigated whether there is any variation in their properties across the different regions of the galaxy. Assuming that the Hα emission primarily comes from O stars, whereas FUV emission arises from O ($M > 21M_{\odot}$) and massive B0 stars ($M > 10M_{\odot}$), and NUV emission arises from O, B0, and low mass B1 stars ($M \leq 10M_{\odot}$), we estimated the approximate numbers of O, B0 and B1 stars for each SFC. We obtained the high mass end of the IMF slopes or index, α_1 and α_2, from the ratios of O stars to B0 stars and B0 to B1 stars, respectively.

Our study shows that the IMF is top-light even in the inner regions of a massive galaxy. The high-mass IMF index α_2 has a mean slope of 2.64 ± 0.14, consistent across various combinations of O-type populations considered. Hence, α_2 is the reliable IMF index. We consider the IMF index of the arms and spurs SFCs shows minimal variation ($< \pm 0.2$). We also found evidence that the high-mass IMF index α_2 correlates with the local star-formation rate surface density, UV colour, and even gas density obtained from ALMA. This suggests that massive star formation is not strictly universal but may depend on the ambient conditions of the interstellar medium. This pilot method provides a foundation for applying consistent IMF diagnostics to a larger sample of galaxies that have multiwavelength data.

PAH Emission and Star Formation

Chapter 4 examines PAH molecules as tracers of star formation using PHANGS-JWST imaging of NGC 628. We analyzed the relationship between PAH emission features (F335M, F770W, F1130W) and classical star-formation indicators, such as FUV, NUV, and Hα. By calculating PAH ratios, we explored how PAH properties, such as size and charge, vary with the local IMF slope. Our findings indicate that smaller and ionized PAH fractions increase with a top-heavy IMF and younger stellar populations. We also investigated bubble regions, particularly the Phantom void, finding that NUV-only emissions are concentrated there. Two SFCs in this region displayed a top-heavy IMF due to gas accumulation from feedback mechanisms. At the same time, an SFC near an elongated bubble exhibited a top-light IMF, indicating a gas shear influence.

Quantifying Galaxy Structure Across Scales

Chapter 5 discusses the development of a methodology using ordinal pattern analysis to quantify multiscale complexity in galaxy morphology. Applied to a multi-wavelength data set, including UVIT, JWST, and ALMA images of NGC 628, this statistical framework establishes a new quantitative connection between the observed morphological structure and underlying physical processes, including turbulence and galactic dynamics. This technique offers a promising avenue for systematically comparing galactic environments using a statistical framework, complementing more traditional photometric or spectral diagnostics. Our results reveal a characteristic scale of approximately 196 parsecs, indicating the transition from small-scale structures influenced by turbulence to larger-scale morphology governed by the galaxy dynamics. This convergence suggests a universal

statistical behavior in large-scale galactic structure, despite the differing physical processes at each wavelength.

Star Formation in Dwarf Galaxies

Chapter 6 focuses on the study of star formation in 16 SFDGs using UVIT FUV imaging. In this project, we classified SFDGs morphologically - Dwarf spirals, Dwarf irregulars, and BCDs. We derived spatially resolved SFRs, stellar masses, and SFMS relations, revealing environmental and morphological dependencies in the low-mass regime. We found that the lower Σ(SFR) for each type is distinct, with dwarf irregulars exhibiting the lowest Σ(SFR). We find that although all SFDGs approximately follow the global SFMS relation, i.e. SFR $\propto$ ${M_*}^{\alpha}$, on the scale of SFCs, the α value for each type is different. Notably, the age of SFCs averaged around 1 Gyr, and outer SFCs in most galaxies had high sSFR, supporting the inside-out model of galaxy growth.

The UV Emission from an Ultra-faint Dwarf Galaxy: Leo T

In chapter 7, we study UV-emitting SFCs in a UFDG, the MW satellite galaxy Leo T (D=400 kpc). It shows recent star formation in a low-metallicity environment, similar to the early Universe. We extracted the UV SFCs and cross-matched them with resolved stellar populations from optical IFU and HST-based catalog, in order to characterize their young stellar populations and the physical conditions for star formation at low masses. This study showed that most of the recent and massive star formation is concentrated near the optical center, with UV-emitting populations like upper-MS and EL stars. In contrast, the southern region primarily contains BL and HB stars. However, the UV SFCs are extended mostly south of

the optical radius, suggesting a directional interaction with the MW's halo. There was also no UV association observed with molecular hydrogen, suggesting low star formation efficiency in those regions.

Each chapter of the thesis emphasizes the importance of studying star formation in various environments at different scales, spanning from parsec to kiloparsec scales. It demonstrates that both massive and ultra-faint galaxies adhere to the established laws of star formation at each of these scales. This thesis clearly captures the interplay between the star formation and the surrounding ISM. However, there is much more to explore with the amount of data we have. The methods utilized in this research can be enhanced and applied to larger datasets. Therefore, in the following section, I will discuss potential projects that can be undertaken in the future to gain a deeper understanding of extragalactic star formation.

8.2 Future work

The long-term objective is to develop a physically motivated, multiwavelength framework that links dust, gas, massive stars, feedback, and star formation across the diverse environments of nearby galaxies. For that, we plan to carry out a few projects such as,

- Building upon the framework developed in Amrutha & Das (2025), which links spatially resolved IMF slopes to local physical conditions using IFU and UV data—this project aims to expand that analysis to a diverse sample of nearby galaxies observed with VLT/MUSE, ALMA, and JWST, along with UVIT observations. Although Amrutha & Das (2025) presents a novel method for estimating the high-mass IMF, the method has limitations that need to be addressed. Some of them are considering contamination in the

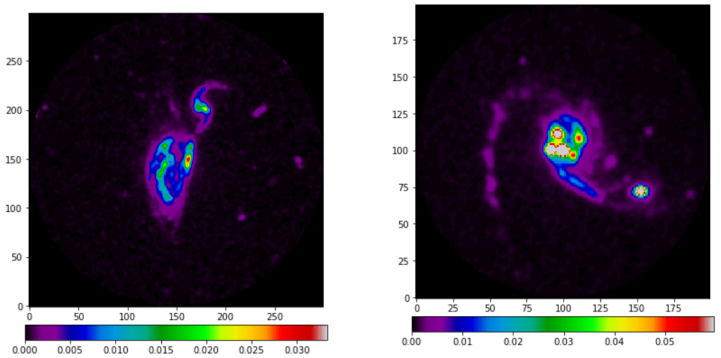


FIGURE A.1: The GALEX FUV image of the interacting galaxies -Mrk 1508 (Left) and Mrk 691. We see interaction features and associated star formation in both galaxies.

Hα and UV bands and correcting them to get an accurate estimate of the IMF. Another reason to extend the previous work is to validate the method with a large sample of galaxies.

- JWST imaging has revealed striking PAH-dominated bubbles and superbubbles, characterising the ISM conditions and massive-star populations associated with these features.

- **Understanding Star Formation in Closely Interacting Markarian Galaxies:** We have observed a few nearby, closely interacting Markarian galaxies, which are UV-bright both in their inner disks and tidal tails in UVIT. Two UV-bright interacting galaxies are shown in the Figure. A.1. Wet interactions or mergers typically lead to increased star formation. The gas that is driven into the central regions causes starburst and AGN activity. Additionally, these interactions result in the formation of tidal tails, leading to star formation in the outer disk and, in some cases, the creation of tidal dwarf galaxies. In this study, we will focus on the evolution of galaxies through both minor and major mergers.

- **Detecting star formation associated with gas accretion:** We plan to study star formation in accreting galaxies that have vertically extended neutral hydrogen (HI) gas filaments and diffuse HI gas in their halos lying above their stellar disks. Galaxies accrete gas, which can lead to star formation

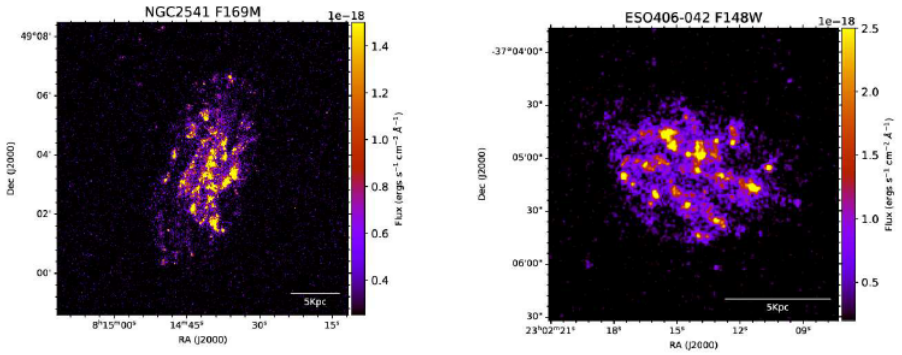


FIGURE A.2: The UVIT images of type II XUV disk galaxies from Das et al. (2021) - NGC 2541 (left), and ESO406-042. We can see resolved star-forming knots in these UVIT images of type two XUV galaxies.

in their outer disks, resulting in the inside-out growth of galaxies. Cold gas accretion is the cause of a large number of galaxies that have extended HI filaments and tails. We plan to correlate the SFCs with these filaments and put constraints on the SFRs and SFEs in these extraplanar regions. This study can enhance our understanding of star formation in low stellar density environments and contribute to research on galaxy evolution.

- **Understanding Star Formation in the Type II XUV Spiral Galaxies:** We have deep observations of Type II XUV spiral galaxies. Type II XUV disks exhibit filamentary star formation, typically associated with low-luminosity stellar disks, and are often truncated near the optical radius of the galaxy, as shown in the Figure. A.2. Hence, it is expected that they have different inner and outer disk properties. In this study, we aim to investigate the nature of star formation in the low-luminosity stellar disk regions of type II XUV disk galaxies and to determine the factors that lead to rapid star formation in these extreme environments. We will also image the diffuse UV emission, determine the extent of the XUV disks, and search for signatures of gas accretion by comparing it with HI data.

- **Exploring Star Formation in Dwarf Galaxies with MUSE Observations:** We have proposed a deep FUV study of nearby dwarf galaxies

with existing high-quality MUSE IFU data. Despite their shallow gravitational potential, which makes it difficult for them to form stars, a large population of dwarfs is still star-forming. LSB, diffuse stellar disks, and high dark matter fraction make detecting and studying them challenging in some optical and IR bands, which is why most studies of star-forming galaxies focus on more massive systems. The IFU, alongside UVIT data, can also help us understand metallicity, star formation history, and even shed light on kinematics, making it a more comprehensive study of dwarfs.

Bibliography

Ackermann, M., Ajello, M., Allafort, A., et al. 2012, *Astrophys. J.*, 755, 164, doi: 10.1088/0004-637X/755/2/164

Adamo, A., Ryon, J. E., Messa, M., et al. 2017, *Astrophys. J.*, 841, 131, doi: 10.3847/1538-4357/aa7132

Adamo, A., Östlin, G., Zackrisson, E., et al. 2010, MNRAS, 407, 870, doi: 10.1111/j.1365-2966.2010.16983.x

Adams, E. A. K., & Oosterloo, T. A. 2018, *Astron. Astrophys.*, 612, A26, doi: 10.1051/0004-6361/201732017

Aguerri, J. A. L. 2012, Advances in Astronomy, 2012, 382674, doi: https://doi.org/10.1155/2012/382674

Allamandola, L. J., Hudgins, D. M., & Sandford, S. A. 1999, *Astrophys. J.*, 511, L115, doi: 10.1086/311843

Allamandola, L. J., Tielens, A. G. G. M., & Barker, J. R. 1989, *Astrophys. J. Suppl.*, 71, 733, doi: 10.1086/191396

Amrutha, S., & Das, M. 2025, *Astrophys. J.*, 987, 11, doi: 10.3847/1538-4357/add68d

Amrutha, S., Das, M., & Yadav, J. 2024, *Mon. Not. Roy. Astron. Soc.*, 530, 2199, doi: 10.1093/mnras/stae907

Anand, G. S., Lee, J. C., Van Dyk, S. D., et al. 2020, MNRAS, 501, 3621, doi: 10.1093/mnras/staa3668

Argyriou, Ioannis, Glasse, Alistair, Law, David R., et al. 2023, A&A, 675, A111, doi: 10.1051/0004-6361/202346489

Armus, L., Lai, T., U, V., et al. 2023, *Astrophys. J. Lett.*, 942, L37, doi: 10.3847/2041-8213/acac66

Arnaboldi, M., Capaccioli, M., Cappellaro, E., Held, E. V., & Koribalski, B. 1995, *Astron. J.*, 110, 199, doi: 10.1086/117507

Aschwanden, M. 2011, Self-organized criticality in astrophysics: The statistics of nonlinear processes in the universe (Springer Science & Business Media)

Astropy Collaboration, Robitaille, T. P., Tollerud, E. J., et al. 2013, *Astron. Astrophys.*, 558, A33, doi: 10.1051/0004-6361/201322068

Astropy Collaboration, Price-Whelan, A. M., Sipőcz, B. M., et al. 2018, *Astron. J.*, 156, 123, doi: 10.3847/1538-3881/aabc4f

Bacon, R., Accardo, M., Adjali, L., et al. 2010, in Society of Photo-Optical Instrumentation Engineers (SPIE) Conference Series, Vol. 7735, Ground-based and Airborne Instrumentation for Astronomy III, ed. I. S. McLean, S. K. Ramsay, & H. Takami, 773508, doi: 10.1117/12.856027

Bak, P., Tang, C., & Wiesenfeld, K. 1988, Physical review A, 38, 364

Balasis, G., Donner, R. V., Potirakis, S. M., et al. 2013, Entropy, 15, 4844

Baldry, I. K., Glazebrook, K., Brinkmann, J., et al. 2004, *Astrophys. J.*, 600, 681, doi: 10.1086/380092

Bandt, C., & Pompe, B. 2002, Physical review letters, 88, 174102

Barabási, A.-L., & Albert, R. 1999, science, 286, 509

Barbary, K. 2016, The Journal of Open Source Software, 1, 58, doi: 10.21105/joss.00058

Barnes, A. T., Watkins, E. J., Meidt, S. E., et al. 2023, *Astrophys. J. Lett.*, 944, L22, doi: 10.3847/2041-8213/aca7b9

Bartlett, S., Li, J., Gu, L., et al. 2022, Nature Astronomy, 6, 387

Bastian, N., Covey, K. R., & Meyer, M. R. 2010, *Ann. Rev. Astron. Astrophys.*, 48, 339–389, doi: 10.1146/annurev-astro-082708-101642

Battisti, A. J., Calzetti, D., Johnson, B. D., & Elbaz, D. 2015, *Astrophys. J.*, 800, 143, doi: 10.1088/0004-637X/800/2/143

Bayo, A., Rodrigo, C., Barrado Y Navascués, D., et al. 2008, *Astron. Astrophys.*, 492, 277, doi: 10.1051/0004-6361:200810395

Begum, A., Chengalur, J. N., Karachentsev, I. D., Sharina, M. E., & Kaisin, S. S. 2008, MNRAS, 386, 1667, doi: 10.1111/j.1365-2966.2008.13150.x

Bekki, K. 1998, The Astrophysical Journal, 502, L133–L137, doi: 10.1086/311508

Belfiore, Francesco, Leroy, Adam K., Williams, Thomas G., et al. 2023, A&A, 678, A129, doi: 10.1051/0004-6361/202347175

Bell, E. F., & de Jong, R. S. 2000, *Mon. Not. Roy. Astron. Soc.*, 312, 497, doi: 10.1046/j.1365-8711.2000.03138.x

Bell, E. F., & Kennicutt, Jr., R. C. 2001, *Astrophys. J.*, 548, 681, doi: 10.1086/319025

Bellazzini, M., Annibali, F., Tosi, M., et al. 2020, *Astron. Astrophys.*, 634, A124, doi: 10.1051/0004-6361/201937284

Berg, D. A., Skillman, E. D., Marble, A. R., et al. 2012, ApJ, 754, 98, doi: 10.1088/0004-637x/754/2/98

Bergvall, N. 2011, in Astrophysics and Space Science Proceedings (Springer Berlin Heidelberg), 175–194, doi: 10.1007/978-3-642-22018-0_20

Bertin, E., & Arnouts, S. 1996, *Astron. Astrophys. Suppl.*, 117, 393, doi: 10.1051/aas:1996164

Besla, G., Kallivayalil, N., Hernquist, L., et al. 2010, ApJ, 721, L97, doi: 10.1088/2041-8205/721/2/l97

Bianchi, L. 2011, *Astrophys. Space Sci.*, 335, 51, doi: 10.1007/s10509-011-0612-2

Bigiel, F., Leroy, A., Walter, F., et al. 2008, The Astronomical Journal, 136, 2846–2871, doi: 10.1088/0004-6256/136/6/2846

Blaña, M., Burkert, A., Fellhauer, M., et al. 2024, Astronomy & Astrophysics, 692, A183, doi: 10.1051/0004-6361/202451649

Blaña, M., Burkert, A., Fellhauer, M., Schartmann, M., & Alig, C. 2020, Monthly Notices of the Royal Astronomical Society, 497, 3601, doi: 10.1093/mnras/staa2153

Blumenthal, G. R., Faber, S. M., Primack, J. R., & Rees, M. J. 1984, *Nature*, 311, 517, doi: 10.1038/311517a0

Boissier, S., de Paz, A. G., Boselli, A., et al. 2007, ApJS, 173, 524, doi: 10.1086/516642

Boselli, A., Boissier, S., Cortese, L., et al. 2009, *Astrophys. J.*, 706, 1527–1544, doi: 10.1088/0004-637x/706/2/1527

Bradley, L., Sipőcz, B., Robitaille, T., et al. 2022, Zenodo, doi: 10.5281/zenodo.6825092

Brinchmann, J., Charlot, S., White, S. D. M., et al. 2004, *Mon. Not. Roy. Astron. Soc.*, 351, 1151, doi: 10.1111/j.1365-2966.2004.07881.x

Bromm, V., Yoshida, N., Hernquist, L., & McKee, C. F. 2009, Nature, 459, 49–54, doi: 10.1038/nature07990

Brook, C. B., Kawata, D., Martel, H., Gibson, B. K., & Bailin, J. 2006, *Astrophys. J.*, 639, 126, doi: 10.1086/499154

Brooks, A. M., & Zolotov, A. 2014, *Astrophys. J.*, 786, 87, doi: 10.1088/0004-637X/786/2/87

Brown, T. M., Tumlinson, J., Geha, M., et al. 2014, *Astrophys. J.*, 796, 91, doi: 10.1088/0004-637X/796/2/91

Bruzzese, S. M., Thilker, D. A., Meurer, G. R., et al. 2019, *Mon. Not. Roy. Astron. Soc.*, 491, 2366, doi: 10.1093/mnras/stz3151

Bullock, J. S., & Boylan-Kolchin, M. 2017, Annual Review of Astronomy and Astrophysics, 55, 343–387, doi: 10.1146/annurev-astro-091916-055313

Bureau, M., & Carignan, C. 2002, *Astron. J.*, 123, 1316, doi: 10.1086/338899

Calzetti, D. 2013, in Secular Evolution of Galaxies, ed. J. Falcón-Barroso & J. H. Knapen (Cambridge University Press), 419, doi: 10.48550/arXiv.1208.2997

Calzetti, D., Armus, L., Bohlin, R. C., et al. 2000, *Astrophys. J.*, 533, 682, doi: 10.1086/308692

Calzetti, D., Chandar, R., Lee, J. C., et al. 2010, *Astrophys. J. Lett.*, 719, L158, doi: 10.1088/2041-8205/719/2/L158

Calzetti, D., Kinney, A. L., & Storchi-Bergmann, T. 1994, *Astrophys. J.*, 429, 582, doi: 10.1086/174346

Calzetti, D., Kennicutt, R. C., Engelbracht, C. W., et al. 2007, *Astrophys. J.*, 666, 870, doi: 10.1086/520082

Calzetti, D., Lee, J. C., Sabbi, E., et al. 2015, *Astron. J.*, 149, 51, doi: 10.1088/0004-6256/149/2/51

Cano-Díaz, M., Ávila-Reese, V., Sánchez, S. F., et al. 2019, *Mon. Not. Roy. Astron. Soc.*, 488, 3929, doi: 10.1093/mnras/stz1894

Carnall, A. C., Cullen, F., McLure, R. J., et al. 2024, Monthly Notices of the Royal Astronomical Society, 534, 325, doi: 10.1093/mnras/stae2092

Carvalho, A. S., Hillenbrand, L. A., France, K., & Herczeg, G. J. 2024, *Astrophys. J. Lett.*, 973, L40, doi: 10.3847/2041-8213/ad74eb

Castelli, F., & Kurucz, R. L. 2004, New Grids of ATLAS9 Model Atmospheres. https://arxiv.org/abs/astro-ph/0405087

Catinella, B., Schiminovich, D., Kauffmann, G., et al. 2010, *Mon. Not. Roy. Astron. Soc.*, 403, 683, doi: 10.1111/j.1365-2966.2009.16180.x

Chabrier, G. 2003, Publications of the Astronomical Society of the Pacific, 115, 763, doi: 10.1086/376392

Chabrier, G. 2003, *Pub. Astron. Soc. Pac.*, 115, 763, doi: 10.1086/376392

Chamba, N., Trujillo, I., & Knapen, J. H. 2022, Astronomy & Astrophysics, 667, A87, doi: 10.1051/0004-6361/202243612

Chanu, A. L., Park, Y., Cha, Y., et al. 2025, DOI arXiv:2503.19924

Chanu, A. L., Singh, R. B., & Jeon, J.-H. 2024, Chaos, Solitons & Fractals, 185, 115138

Chappell, D., & Scalo, J. 2001, Mon. Not. Roy. Astron. Soc., 325, 1, doi: 10.1046/j.1365-8711.2001.04196.x

Chastenet, J., Sutter, J., Sandstrom, K., et al. 2023, *Astrophys. J. Lett.*, 944, L12, doi: 10.3847/2041-8213/acac94

Chastenet, J., Sutter, J., Sandstrom, K., et al. 2023, *Astrophys. J. Lett.*, 944, L11, doi: 10.3847/2041-8213/acadd7

Chen, Y.-M., Wild, V., Kauffmann, G., et al. 2009, *Mon. Not. Roy. Astron. Soc.*, 393, 406, doi: 10.1111/j.1365-2966.2008.14247.x

Clementini, G., Cignoni, M., Contreras Ramos, R., et al. 2012, *Astrophys. J.*, 756, 108, doi: 10.1088/0004-637X/756/2/108

Condon, J. J. 1992, *Ann. Rev. Astron. Astrophys.*, 30, 575, doi: 10.1146/annurev.aa.30.090192.003043

Connolly, A. J., Szalay, A. S., Bershady, M. A., Kinney, A. L., & Calzetti, D. 1995, *Astron. J.*, 110, 1071, doi: 10.1086/117587

Conselice, C. J. 2006, MNRAS, 373, 1389, doi: 10.1111/j.1365-2966.2006.11114.x

Consolini, G., Tozzi, R., & De Michelis, P. 2009, A&A, 506, 1381

Cornett, R. H., O'Connell, R. W., Greason, M. R., et al. 1994, *Astrophys. J.*, 426, 553, doi: 10.1086/174092

Cover, T. M. 1999, Elements of information theory (John Wiley & Sons)

Daddi, E., Dickinson, M., Morrison, G., et al. 2007, The Astrophysical Journal, 670, 156, doi: 10.1086/521818

Dale, D. A., Anderson, K. R., Bran, L. M., et al. 2020, The Astronomical Journal, 159, 195, doi: 10.3847/1538-3881/ab7eb2

Dale, D. A., Boquien, M., Barnes, A. T., et al. 2023, *Astrophys. J. Lett.*, 944, L23, doi: 10.3847/2041-8213/aca769

Das, M., Ianjamasimanana, R., McGaugh, S. S., Schombert, J., & Dwarakanath, K. S. 2023, The Astrophysical Journal Letters, 946, L8, doi: 10.3847/2041-8213/acc10e

Das, M., McGaugh, S. S., Ianjamasimanana, R., Schombert, J., & Dwarakanath, K. S. 2020, *Astrophys. J.*, 889, 10, doi: 10.3847/1538-4357/ab5fcd

Das, M., O'Neil, K., Vogel, S. N., & McGaugh, S. 2006, *Astrophys. J.*, 651, 853, doi: 10.1086/507410

Das, M., Sengupta, C., & Honey, M. 2019, *Astrophys. J.*, 871, 197, doi: 10.3847/1538-4357/aaf864

Das, M., Yadav, J., Patra, N., et al. 2021, Journal of Astrophysics and Astronomy, 42, doi: 10.1007/s12036-021-09749-9

Das, M., Yadav, J., Patra, N., et al. 2021, Journal of Astrophysics and Astronomy, 42, 85, doi: 10.1007/s12036-021-09749-9

de Blok, W. J. G., & Walter, F. 2000, ApJ, 537, L95, doi: 10.1086/312777

De Blok, W. J. G., & Walter, F. 2003, MNRAS, 341, L39, doi: 10.1046/j.1365-8711.2003.06669.x

de Jong, J. T. A., Harris, J., Coleman, M. G., et al. 2008, The Astrophysical Journal, 680, 1112, doi: 10.1086/587835

De Lucia, G., Springel, V., White, S. D. M., Croton, D., & Kauffmann, G. 2006, *Mon. Not. Roy. Astron. Soc.*, 366, 499, doi: 10.1111/j.1365-2966.2005.09879.x

de Vaucouleurs, G. 1959, Handbuch der Physik, 53, 275, doi: 10.1007/978-3-642-45932-0_7

De Vaucouleurs, G. 1959, Classification and Morphology of External Galaxies (Berlin, Heidelberg: Springer Berlin Heidelberg), 275–310, doi: 10.1007/978-3-642-45932-0_7

de Vaucouleurs, G., de Vaucouleurs, A., Corwin, Herold G., J., et al. 1991, Third Reference Catalogue of Bright Galaxies (NADS)

Deason, A., Wetzel, A., & Garrison-Kimmel, S. 2014, *Astrophys. J.*, 794, 115, doi: 10.1088/0004-637X/794/2/115

Di Cintio, A., Brook, C. B., Macciò, A. V., et al. 2014, *Mon. Not. Roy. Astron. Soc.*, 437, 415, doi: 10.1093/mnras/stt1891

Díaz-García, S., Moyano, F. D., Comerón, S., et al. 2020, *Astron. Astrophys.*, 644, A38, doi: 10.1051/0004-6361/202039162

Dib, S. 2014, *Mon. Not. Roy. Astron. Soc.*, 444, 1957, doi: 10.1093/mnras/stu1521

Dieleman, S., Willett, K. W., & Dambre, J. 2015, Monthly Notices of the Royal Astronomical Society, 450, 1441–1459, doi: 10.1093/mnras/stv632

D'Onghia, E., & Fox, A. J. 2016, *Ann. Rev. Astron. Astrophys.*, 54, 363, doi: 10.1146/annurev-astro-081915-023251

Donnan, F. R., García-Bernete, I., Rigopoulou, D., et al. 2022, *Mon. Not. Roy. Astron. Soc.*, 519, 3691, doi: 10.1093/mnras/stac3729

Donovan Meyer, J., Peek, J. E. G., Putman, M., & Grcevich, J. 2015, *Astrophys. J.*, 808, 136, doi: 10.1088/0004-637X/808/2/136

Draine, B. T. 2003, *Ann. Rev. Astron. Astrophys.*, 41, 241, doi: 10.1146/annurev.astro.41.011802.094840

—. 2011, Physics of the Interstellar and Intergalactic Medium (Princeton University Press)

Draine, B. T., Li, A., Hensley, B. S., et al. 2021, *Astrophys. J.*, 917, 3, doi: 10.3847/1538-4357/abff51

Dressler, A. 1980, *Astrophys. J.*, 236, 351, doi: 10.1086/157753

Díaz-García, S., Salo, H., Knapen, J. H., & Herrera-Endoqui, M. 2019, A&A, 631, A94, doi: 10.1051/0004-6361/201936000

Eden, D. J., Moore, T. J. T., Morgan, L. K., Thompson, M. A., & Urquhart, J. S. 2013, *Mon. Not. Roy. Astron. Soc.*, 431, 1587, doi: 10.1093/mnras/stt279

Efremov, Y. N. 1995, *Astron. J.*, 110, 2757, doi: 10.1086/117728

Eggen, O. J., Lynden-Bell, D., & Sandage, A. R. 1962, *Astrophys. J.*, 136, 748, doi: 10.1086/147433

Egorov, O. V., Kreckel, K., Sandstrom, K. M., et al. 2023, *Astrophys. J. Lett.*, 944, L16, doi: 10.3847/2041-8213/acac92

Elbaz, D., Daddi, E., Le Borgne, D., et al. 2007, A&A, 468, 33, doi: 10.1051/0004-6361:20077525

Elia, D., Molinari, S., Schisano, E., et al. 2022, The Astrophysical Journal, 941, 162, doi: 10.3847/1538-4357/aca27d

Elmegreen, B. 2011, EAS Publications Series, 51, 19–30, doi: 10.1051/eas/1151002

Elmegreen, B. G. 2015, *Astrophys. J. Lett.*, 814, L30, doi: 10.1088/2041-8205/814/2/L30

Elmegreen, B. G., Elmegreen, D. M., Chandar, R., Whitmore, B., & Regan, M. 2006, *Astrophys. J.*, 644, 879, doi: 10.1086/503797

Elmegreen, B. G., Elmegreen, D. M., Salzer, J. J., & Mann, H. 1996, *Astrophys. J.*, 467, 579, doi: 10.1086/177634

Elmegreen, B. G., & Falgarone, E. 1996, *Astrophys. J.*, 471, 816, doi: 10.1086/178009

Elmegreen, B. G., & Scalo, J. 2004, *Ann. Rev. Astron. Astrophys.*, 42, 211, doi: 10.1146/annurev.astro.41.011802.094859

Elmegreen, D. M. 1981, *Astrophys. J. Suppl.*, 47, 229, doi: 10.1086/190757

Elmegreen, D. M., & Elmegreen, B. G. 1987, *Astrophys. J.*, 314, 3, doi: 10.1086/165034

Elmegreen, D. M., & Salzer, J. J. 1999, *Astron. J.*, 117, 764, doi: 10.1086/300739

Elmegreen, D. M., Elmegreen, B. G., Adamo, A., et al. 2014, *Astrophys. J. Lett.*, 787, L15, doi: 10.1088/2041-8205/787/1/L15

Elmegreen, D. M., Elmegreen, B. G., Adamo, A., et al. 2014, *Astrophys. J. Lett.*, 787, L15, doi: 10.1088/2041-8205/787/1/L15

Emsellem, Eric, Schinnerer, Eva, Santoro, Francesco, et al. 2022, A&A, 659, A191, doi: 10.1051/0004-6361/202141727

Epinat, B., Amram, P., Marcelin, M., et al. 2008, *Mon. Not. Roy. Astron. Soc.*, 388, 500, doi: 10.1111/j.1365-2966.2008.13422.x

Eskridge, P. B., Frogel, J. A., Pogge, R. W., et al. 2002, *Astrophys. J. Suppl.*, 143, 73, doi: 10.1086/342340

Fabbiano, G. 1989, *Ann. Rev. Astron. Astrophys.*, 27, 87, doi: 10.1146/annurev.aa.27.090189.000511

Fazio, G. G., Hora, J. L., Allen, L. E., et al. 2004, *Astrophys. J. Suppl.*, 154, 10, doi: 10.1086/422843

Ferrière, K. M. 2001, Reviews of Modern Physics, 73, 1031, doi: 10.1103/RevModPhys.73.1031

Filho, M. E., Sánchez Almeida, J., Amorín, R., et al. 2016, *Astrophys. J.*, 820, 109, doi: 10.3847/0004-637X/820/2/109

Finlator, K., & Davé, R. 2008, *Mon. Not. Roy. Astron. Soc.*, 385, 2181, doi: 10.1111/j.1365-2966.2008.12991.x

Fiore, F., Gaspari, M., Luminari, A., Tozzi, P., & De Arcangelis, L. 2024, A&A, 686, A36

Fitts, A., Boylan-Kolchin, M., Elbert, O. D., et al. 2017, *Mon. Not. Roy. Astron. Soc.*, 471, 3547, doi: 10.1093/mnras/stx1757

Flaugher, B., Diehl, H. T., Honscheid, K., et al. 2015, *Astron. J.*, 150, 150, doi: 10.1088/0004-6256/150/5/150

Foyle, K., Rix, H.-W., Walter, F., & Leroy, A. K. 2010, *Astrophys. J.*, 725, 534, doi: 10.1088/0004-637X/725/1/534

Freyer, T., Hensler, G., & Yorke, H. W. 2003, *Astrophys. J.*, 594, 888, doi: 10.1086/376937

Friedrich, R., Peinke, J., Sahimi, M., & Tabar, M. R. R. 2011, Physics Reports, 506, 87

Fritz, T. K., Battaglia, G., Pawlowski, M. S., et al. 2018, A&A, 619, A103, doi: 10.1051/0004-6361/201833343

García-Bernete, I., Rigopoulou, D., Alonso-Herrero, A., et al. 2022, A&A, 666, L5, doi: 10.1051/0004-6361/202244806

García-Bernete, I., Alonso-Herrero, A., Rigopoulou, D., et al. 2024, A&A, 681, L7, doi: 10.1051/0004-6361/202348266

Garn, T., & Best, P. N. 2010, *Mon. Not. Roy. Astron. Soc.*, 409, 421, doi: 10.1111/j.1365-2966.2010.17321.x

Gavazzi, G., Bonfanti, C., Sanvito, G., Boselli, A., & Scodeggio, M. 2002, *Astrophys. J.*, 576, 135, doi: 10.1086/341730

Geha. 2012, A&A, 757, 85, doi: 10.1088/0004-637X/757/1/85

Gekelman, W., Tang, S., DeHaas, T., et al. 2019, Proceedings of the National Academy of Sciences, 116, 18239

Gil de Paz, A., Boissier, S., Madore, B. F., et al. 2007, *Astrophys. J. Suppl.*, 173, 185, doi: 10.1086/516636

Gilbert, G. J., & Fabrycky, D. C. 2020, AJ, 159, 281

Gogarten, S. M., Dalcanton, J. J., Williams, B. F., et al. 2009, *Astrophys. J.*, 691, 115, doi: 10.1088/0004-637X/691/1/115

Gordon, K. D., Rieke, G. H., Engelbracht, C. W., et al. 2005, *Pub. Astron. Soc. Pac.*, 117, 503, doi: 10.1086/429309

Gott, III, J. R., & Thuan, T. X. 1976, *Astrophys. J.*, 204, 649, doi: 10.1086/154214

Graham, A. W., & Driver, S. P. 2005, , 22, 118, doi: 10.1071/AS05001

Grasha, K., Calzetti, D., Adamo, A., et al. 2017, *Astrophys. J.*, 840, 113, doi: 10.3847/1538-4357/aa6f15

Grasha, K., Calzetti, D., Adamo, A., et al. 2017, ApJ, 840, 113, doi: 10.3847/1538-4357/aa6f15

Guillet, V., Pineau Des Forêts, G., & Jones, A. P. 2011, *Astron. Astrophys.*, 527, A123, doi: 10.1051/0004-6361/201015973

Gunawardhana, M. L. P., Hopkins, A. M., Sharp, R. G., et al. 2011, *Mon. Not. Roy. Astron. Soc.*, 415, 1647, doi: 10.1111/j.1365-2966.2011.18800.x

Gusev, A. S. 2014, MNRAS, 442, 3711, doi: 10.1093/mnras/stu1095

Gusev, A. S., & Efremov, Y. N. 2013, *Mon. Not. Roy. Astron. Soc.*, 434, 313, doi: 10.1093/mnras/stt1019

Gusev, A. S., Egorov, O. V., & Sakhibov, F. 2013, *Mon. Not. Roy. Astron. Soc.*, 437, 1337, doi: 10.1093/mnras/stt1970

Hao, C.-N., Kennicutt, R. C., Johnson, B. D., et al. 2011, *Astrophys. J.*, 741, 124, doi: 10.1088/0004-637X/741/2/124

Harris, C. R., Millman, K. J., van der Walt, S. J., et al. 2020, Nature, 585, 357, doi: 10.1038/s41586-020-2649-2

Hogg, D. W., Blanton, M. R., Brinchmann, J., et al. 2004, ApJ, 601, L29, doi: 10.1086/381749

Holmberg, E. 1958, Meddelanden fran Lunds Astronomiska Observatorium Serie II, 136, 1

Honey, M., van Driel, W., Das, M., & Martin, J. M. 2018, *Mon. Not. Roy. Astron. Soc.*, 476, 4488, doi: 10.1093/mnras/sty530

Hoversten, E. A., & Glazebrook, K. 2008, *Astrophys. J.*, 675, 163, doi: 10.1086/524095

Hubble, E. P. 1926, *Astrophys. J.*, 64, 321, doi: 10.1086/143018

—. 1936, Realm of the Nebulae (New Haven: Yale University Press)

Huertas-Company, M., Aguerri, J. A. L., Bernardi, M., Mei, S., & Sánchez Almeida, J. 2011, *Astron. Astrophys.*, 525, A157, doi: 10.1051/0004-6361/201015735

Hunter, D. A., Elmegreen, B. G., & Ludka, B. C. 2010, *Astron. J.*, 139, 447, doi: 10.1088/0004-6256/139/2/447

Hunter, D. A., Elmegreen, B. G., & Ludka, B. C. 2010, *Astron. J.*, 139, 447, doi: 10.1088/0004-6256/139/2/447

Hunter, D. A., Ficut-Vicas, D., Ashley, T., et al. 2012, The Astronomical Journal, 144, 134, doi: 10.1088/0004-6256/144/5/134

Hunter, J. D. 2007, Computing in Science and Engineering, 9, 90, doi: 10.1109/MCSE.2007.55

Hyman, S. Ó., Daniel, K. J., & Schaffner, D. A. 2025, The Astrophysical Journal, 987, 195

Iglesias-Páramo, J., Boselli, A., Gavazzi, G., & Zaccardo, A. 2004, *Astron. Astrophys.*, 421, 887, doi: 10.1051/0004-6361:20034572

Irwin, M. J., Belokurov, V., Evans, N. W., et al. 2007, The Astrophysical Journal, 656, L13, doi: 10.1086/512183

Jain, R., & Wadadekar, Y. 2025, *Astron. Astrophys.*, 703, A96, doi: 10.1051/0004-6361/202451689

Jang, In Sung, de Jong, Roelof S., Holwerda, Benne W., et al. 2020, A&A, 637, A8, doi: 10.1051/0004-6361/201936994

Jarrett, T. H., Chester, T., Cutri, R., Schneider, S. E., & Huchra, J. P. 2003, *Astron. J.*, 125, 525, doi: 10.1086/345794

Jeans, J. H. 1902, Philosophical Transactions of the Royal Society of London Series A, 199, 1, doi: 10.1098/rsta.1902.0012

—. 1929, The Observatory, 52, 172

Jeřábková, T., Zonoozi, A. H., Kroupa, P., et al. 2018, *Astron. Astrophys.*, 620, A39, doi: 10.1051/0004-6361/201833055

Jones, A. P., Tielens, A. G. G. M., & Hollenbach, D. J. 1996, *Astrophys. J.*, 469, 740, doi: 10.1086/177823

Kalari, V. M., Horch, E. P., Salinas, R., et al. 2022, The Astrophysical Journal, 935, 162, doi: 10.3847/1538-4357/ac8424

Kamphuis, J., & Briggs, F. 1992, *Astron. Astrophys.*, 253, 335

Kaneda, H., Onaka, T., Sakon, I., et al. 2008, *Astrophys. J.*, 684, 270, doi: 10.1086/590243

Karachentsev, I. D., & Kaisina, E. I. 2013, *Astron. J.*, 146, 46, doi: 10.1088/0004-6256/146/3/46

Karachentsev, I. D., Karachentseva, V. E., Huchtmeier, W. K., & Makarov, D. I. 2004, *Astron. J.*, 127, 2031, doi: 10.1086/382905

Karbashewski, S., Sydora, R., Van Compernolle, B., Simala-Grant, T., & Poulos, M. 2022, Physics of Plasmas, 29

Kathiravan, S., Tandon, S. N., Raghavendra Prasad, B., et al. 2021, Journal of Astrophysics and Astronomy, 42, 41, doi: 10.1007/s12036-020-09681-4

Kauffman, S. A., et al. 1993, The origins of order: Self-organization and selection in evolution (Oxford University Press, USA)

Kaviraj, S., Schawinski, K., Devriendt, J. E. G., et al. 2007, *Astrophys. J. Suppl.*, 173, 619, doi: 10.1086/516633

Kennicutt, R. C., J. 1983, *Astrophys. J.*, 272, 54, doi: 10.1086/161261

Kennicutt, Robert C., J. 1992, *Astrophys. J.*, 388, 310, doi: 10.1086/171154

Kennicutt, Robert C., J., Hao, C.-N., Calzetti, D., et al. 2009, *Astrophys. J.*, 703, 1672, doi: 10.1088/0004-637X/703/2/1672

Kennicutt, R. C. 1998, *Ann. Rev. Astron. Astrophys.*, 36, 189–231, doi: 10.1146/annurev.astro.36.1.189

Kennicutt, R. C., & Evans, N. J. 2012, Annual Review of Astronomy and Astrophysics, 50, 531–608, doi: 10.1146/annurev-astro-081811-125610

Kennicutt, Jr., R. C. 1998, *Astrophys. J.*, 498, 541, doi: 10.1086/305588

Kim, S., & Park, C. 2007, ApJ, 663, 244

Kim, W.-T., & Ostriker, E. C. 2002, *Astrophys. J.*, 570, 132, doi: 10.1086/339352

Kimble, R. A., MacKenty, J. W., O'Connell, R. W., & Townsend, J. A. 2008, in Society of Photo-Optical Instrumentation Engineers (SPIE) Conference Series, Vol. 7010, Space Telescopes and Instrumentation 2008: Optical, Infrared, and Millimeter, ed. J. M. Oschmann, Jr., M. W. M. de Graauw, & H. A. MacEwen, 70101E, doi: 10.1117/12.789581

Klessen, R. S., Spaans, M., & Jappsen, A.-K. 2007, Monthly Notices of the Royal Astronomical Society: Letters, 374, L29, doi: 10.1111/j.1745-3933.2006.00258.x

Koda, J., Yagi, M., Boissier, S., et al. 2012, *Astrophys. J.*, 749, 20, doi: 10.1088/0004-637X/749/1/20

Koda, J., Yagi, M., Yamanoi, H., & Komiyama, Y. 2015, *Astrophys. J. Lett.*, 807, L2, doi: 10.1088/2041-8205/807/1/L2

Koleva, M., De Rijcke, S., Zeilinger, W. W., et al. 2014, MNRAS, 441, 452, doi: 10.1093/mnras/stu556

Komiyama, Y., Okamura, S., Yagi, M., et al. 2003, *Astrophys. J. Lett.*, 590, L17, doi: 10.1086/376551

Kreckel, K., Blanc, G. A., Schinnerer, E., et al. 2016, *Astrophys. J.*, 827, 103, doi: 10.3847/0004-637X/827/2/103

Kreckel, K., Faesi, C., Kruijssen, J. M. D., et al. 2018, ApJL, 863, L21, doi: 10.3847/2041-8213/aad77d

Kreckel, K., Faesi, C., Kruijssen, J. M. D., et al. 2018, *Astrophys. J. Lett.*, 863, L21, doi: 10.3847/2041-8213/aad77d

Kroupa, P. 2001, *Mon. Not. Roy. Astron. Soc.*, 322, 231, doi: 10.1046/j.1365-8711.2001.04022.x

—. 2002, Science, 295, 82, doi: 10.1126/science.1067524

Kroupa, P., Gjergo, E., Jerabkova, T., & Yan, Z. 2024, The initial mass function of stars. https://arxiv.org/abs/2410.07311

Krumholz, M. R. 2014, Physics Reports, 539, 49, doi: https://doi.org/10.1016/j.physrep.2014.02.001

Kumar, A., Ghosh, S. K., Hutchings, J., et al. 2012, in Society of Photo-Optical Instrumentation Engineers (SPIE) Conference Series, Vol. 8443, Space Telescopes and Instrumentation 2012: Ultraviolet to Gamma Ray, ed. T. Takahashi, S. S. Murray, & J.-W. A. den Herder, 84431N, doi: 10.1117/12.924507

Kunth, D., & Östlin, G. 2000, Astronomy and Astrophysics Review, 10, 1, doi: 10.1007/s001590000005

Lai, T. S.-Y., Smith, J. D. T., Baba, S., Spoon, H. W. W., & Imanishi, M. 2020, *Astrophys. J.*, 905, 55, doi: 10.3847/1538-4357/abc002

Lai, T. S.-Y., Armus, L., Bianchin, M., et al. 2023, *Astrophys. J. Lett.*, 957, L26, doi: 10.3847/2041-8213/ad0387

Lang, P., Meidt, S. E., Rosolowsky, E., et al. 2020, ApJ, 897, 122, doi: 10.3847/1538-4357/ab9953

Larson, R. B. 1975, Monthly Notices of the Royal Astronomical Society, 173, 671, doi: 10.1093/mnras/173.3.671

Larson, R. B. 1981, *Mon. Not. Roy. Astron. Soc.*, 194, 809, doi: 10.1093/mnras/194.4.809

—. 2003, Reports on Progress in Physics, 66, 1651, doi: 10.1088/0034-4885/66/10/R03

Larson, R. B. 2006, Understanding the Stellar Initial Mass Function. https://arxiv.org/abs/astro-ph/0602469

Lee, J. C., Kennicutt, Robert C., J., Funes, S. J. J. G., Sakai, S., & Akiyama, S. 2009, *Astrophys. J.*, 692, 1305, doi: 10.1088/0004-637X/692/2/1305

Lee, J. C., de Paz, A. G., Tremonti, C., et al. 2009, *Astrophys. J.*, 706, 599, doi: 10.1088/0004-637X/706/1/599

Lee, J. C., Gil de Paz, A., Tremonti, C., et al. 2009a, *Astrophys. J.*, 706, 599, doi: 10.1088/0004-637X/706/1/599

—. 2009b, *Astrophys. J.*, 706, 599, doi: 10.1088/0004-637X/706/1/599

Lee, J. C., Sandstrom, K. M., Leroy, A. K., et al. 2023, ApJL, 944, L17, doi: 10.3847/2041-8213/acaaae

Leger, A., & Puget, J. L. 1984, *Astron. Astrophys.*, 137, L5

Leitherer, C., Ortiz Otálvaro, P. A., Bresolin, F., et al. 2010, *Astrophys. J. Suppl.*, 189, 309, doi: 10.1088/0067-0049/189/2/309

Leitherer, C., Schaerer, D., Goldader, J. D., et al. 1999, *Astrophys. J. Suppl.*, 123, 3, doi: 10.1086/313233

Lelli, F. 2022, Nature Astronomy, 6, 35, doi: 10.1038/s41550-021-01562-2

Leroy, A., Bolatto, A. D., Simon, J. D., & Blitz, L. 2005, The Astrophysical Journal, 625, 763, doi: 10.1086/429578

Leroy, A. K., Walter, F., Brinks, E., et al. 2008, *Astron. J.*, 136, 2782, doi: 10.1088/0004-6256/136/6/2782

Leroy, A. K., Walter, F., Bigiel, F., et al. 2009, *Astron. J.*, 137, 4670, doi: 10.1088/0004-6256/137/6/4670

Leroy, A. K., Sandstrom, K. M., Lang, D., et al. 2019, The Astrophysical Journal Supplement Series, 244, 24, doi: 10.3847/1538-4365/ab3925

Leroy, A. K., Sandstrom, K. M., Lang, D., et al. 2019, *Astrophys. J. Suppl.*, 244, 24, doi: 10.3847/1538-4365/ab3925

Leroy, A. K., Schinnerer, E., Hughes, A., et al. 2021, *Astrophys. J. Suppl.*, 257, 43, doi: 10.3847/1538-4365/ac17f3

Leroy, A. K., Hughes, A., Liu, D., et al. 2021a, The Astrophysical Journal Supplement Series, 255, 19, doi: 10.3847/1538-4365/abec80

Leroy, A. K., Schinnerer, E., Hughes, A., et al. 2021b, The Astrophysical Journal Supplement Series, 257, 43, doi: 10.3847/1538-4365/ac17f3

Leroy, A. K., Sandstrom, K., Rosolowsky, E., et al. 2023, The Astrophysical Journal Letters, 944, L9, doi: 10.3847/2041-8213/acaf85

Li, A. 2020, Nature Astronomy, 4, 339, doi: 10.1038/s41550-020-1051-1

Lin, C. C., & Shu, F. H. 1964, *Astrophys. J.*, 140, 646, doi: 10.1086/147955

Lin, C. C., & Shu, F. H. 1966, Proceedings of the National Academy of Sciences, 55, 229, doi: 10.1073/pnas.55.2.229

Lindblad, B. 1959, Galactic Dynamics (Berlin, Heidelberg: Springer Berlin Heidelberg), 21–99, doi: 10.1007/978-3-642-45932-0_2

Lintott, C., Schawinski, K., Bamford, S., et al. 2011, *Mon. Not. Roy. Astron. Soc.*, 410, 166, doi: 10.1111/j.1365-2966.2010.17432.x

Lloyd, S. 2001, IEEE Control Systems Magazine, 21, 7

Lomaeva, M., De Looze, I., Saintonge, A., & Decleir, M. 2022, Monthly Notices of the Royal Astronomical Society, 517, 3763, doi: 10.1093/mnras/stac2940

Lopez-Ruiz, R., Mancini, H. L., & Calbet, X. 1995, Physics letters A, 209, 321

López-Sánchez, Á . R. 2010, Astronomy and Astrophysics, 521, A63, doi: 10.1051/0004-6361/201014295

Lotz, J. M., Primack, J., & Madau, P. 2004, *Astron. J.*, 128, 163, doi: 10.1086/421849

Lovallo, M., & Telesca, L. 2011, Journal of Statistical Mechanics: Theory and Experiment, 2011, P03029

Loveday, J. 1997, *Astrophys. J.*, 489, 29, doi: 10.1086/304778

Mac Low, M.-M., & Ferrara, A. 1999, *Astrophys. J.*, 513, 142, doi: 10.1086/306832

Mac Low, M.-M., & Klessen, R. S. 2004, Reviews of Modern Physics, 76, 125, doi: 10.1103/RevModPhys.76.125

Madden, S. C., Galliano, F., Jones, A. P., & Sauvage, M. 2006, A&A, 446, 877, doi: 10.1051/0004-6361:20053890

Maeder, A., & Conti, P. S. 1994, *Ann. Rev. Astron. Astrophys.*, 32, 227, doi: 10.1146/annurev.astro.32.1.227

Mandelbrot, B. B. 1985, Physica scripta, 32, 257

Mao, X., Shang, P., & Li, Q. 2019, Nonlinear Dynamics, 96, 2449

Maragkoudakis, A., Boersma, C., Temi, P., Bregman, J. D., & Allamandola, L. J. 2022, *Astrophys. J.*, 931, 38, doi: 10.3847/1538-4357/ac666f

Maraston, C. 2005, *Mon. Not. Roy. Astron. Soc.*, 362, 799, doi: 10.1111/j.1365-2966.2005.09270.x

Marquez-Lugo, R. A., Kemp, S. N., Ramos-Larios, G., et al. 2025, Research Notes of the AAS, 9, 339, doi: 10.3847/2515-5172/ae2bf8

Martin, D. C., Fanson, J., Schiminovich, D., et al. 2005, *Astrophys. J. Lett.*, 619, L1, doi: 10.1086/426387

Martin, G., Jackson, R. A., Kaviraj, S., et al. 2020, MNRAS, 500, 4937, doi: 10.1093/mnras/staa3443

Martin, M., Plastino, A., & Rosso, O. 2003, Physics Letters A, 311, 126

Mayya, Y. D., Alzate, J. A., Lomelí-Núez, L., et al. 2023, *Mon. Not. Roy. Astron. Soc.*, 521, 5492, doi: 10.1093/mnras/stad636

McCullough, M., Small, M., Iu, H., & Stemler, T. 2017, Philosophical Transactions of the Royal Society A: Mathematical, Physical and Engineering Sciences, 375, 20160292

McGaugh, S. S., Schombert, J. M., & Lelli, F. 2017, ApJ, 851, 22, doi: 10.3847/1538-4357/aa9790

McKee, C. F., & Ostriker, E. C. 2007, Annual Review of Astronomy and Astrophysics, 45, 565–687, doi: 10.1146/annurev.astro.45.051806.110602

McKinney, J., Armus, L., Pope, A., et al. 2021, *Astrophys. J.*, 908, 238, doi: 10.3847/1538-4357/abd6f2

McQuinn, K. B. W., Skillman, E. D., Cannon, J. M., et al. 2010, *Astrophys. J.*, 721, 297, doi: 10.1088/0004-637X/721/1/297

Melena, N. W., Elmegreen, B. G., Hunter, D. A., & Zernow, L. 2009, AJ, 138, 1203, doi: 10.1088/0004-6256/138/5/1203

Menon, S. H., Grasha, K., Elmegreen, B. G., et al. 2021, *Mon. Not. Roy. Astron. Soc.*, 507, 5542, doi: 10.1093/mnras/stab2413

Menon, S. H., Grasha, K., Elmegreen, B. G., et al. 2021, MNRAS, 507, 5542, doi: 10.1093/mnras/stab2413

Meurer, G. R., Heckman, T. M., Leitherer, C., et al. 1995, *Astron. J.*, 110, 2665, doi: 10.1086/117721

Meurer, G. R., Wong, O. I., Kim, J. H., et al. 2009, *Astrophys. J.*, 695, 765, doi: 10.1088/0004-637X/695/1/765

Micelotta, E. R., Jones, A. P., & Tielens, A. G. G. M. 2010, *Astron. Astrophys.*, 510, A37, doi: 10.1051/0004-6361/200911683

Mihos, J. C., Harding, P., Spengler, C. E., Rudick, C. S., & Feldmeier, J. J. 2013, *Astrophys. J.*, 762, 82, doi: 10.1088/0004-637X/762/2/82

Miller, G. E., & Scalo, J. M. 1979, *Astrophys. J. Suppl.*, 41, 513, doi: 10.1086/190629

Mo, H., van den Bosch, F. C., & White, S. 2010, Galaxy Formation and Evolution (UK: Cambridge University Press), doi: 10.1017/CBO9780511807244

Mondal, C., Subramaniam, A., & George, K. 2021, Journal of Astrophysics and Astronomy, 42, 50, doi: 10.1007/s12036-021-09761-z

Mondal, C., Subramaniam, A., George, K., et al. 2021, The Astrophysical Journal, 909, 203, doi: 10.3847/1538-4357/abe0b4

Morel, C., & Humeau-Heurtier, A. 2021, Pattern Recognition Letters, 150, 139

Morrissey, P., Conrow, T., Barlow, T. A., et al. 2007, The Astrophysical Journal Supplement Series, 173, 682, doi: 10.1086/520512

Moustakas, J., Robert C. Kennicutt, J., & Tremonti, C. A. 2006, *Astrophys. J.*, 642, 775, doi: 10.1086/500964

Navarro, J. F., Frenk, C. S., & White, S. D. M. 1996, *Astrophys. J.*, 462, 563, doi: 10.1086/177173

Nidever, D. L., Olsen, K., Walker, A. R., et al. 2017, *Astron. J.*, 154, 199, doi: 10.3847/1538-3881/aa8d1c

Oemler, A., Abramson, L. E., Gladders, M. D., et al. 2017, ApJ, 844, 45, doi: 10.3847/1538-4357/aa789e

Osterbrock, D. E. 1989, Astrophysics of gaseous nebulae and active galactic nuclei (University Science Books)

Pasquali, A., Gallazzi, A., Fontanot, F., et al. 2010, *Mon. Not. Roy. Astron. Soc.*, 407, 937, doi: 10.1111/j.1365-2966.2010.17074.x

Pattle, K., Fissel, L., Tahani, M., Liu, T., & Ntormousi, E. 2022, Magnetic fields in star formation: from clouds to cores. https://arxiv.org/abs/2203.11179

Pedrini, A., Adamo, A., Calzetti, D., et al. 2024, *Astrophys. J.*, 971, 32, doi: 10.3847/1538-4357/ad534d

Peeters, E., Spoon, H. W. W., & Tielens, A. G. G. M. 2004, *Astrophys. J.*, 613, 986, doi: 10.1086/423237

Pessa, A. A., & Ribeiro, H. V. 2019, Physical Review E, 100, 042304

—. 2020, Physical Review E, 102, 052312

—. 2021, Chaos: An Interdisciplinary Journal of Nonlinear Science, 31

Peñarrubia, J., Ma, Y.-Z., Walker, M. G., & McConnachie, A. 2014, Monthly Notices of the Royal Astronomical Society, 443, 2204–2222, doi: 10.1093/mnras/stu879

Pflamm-Altenburg, J., & Kroupa, P. 2008, *Nature*, 455, 641, doi: 10.1038/nature07266

Poggianti, B. M., Fasano, G., Bettoni, D., et al. 2009, ApJ, 697, L137, doi: 10.1088/0004-637X/697/2/L137

Postma, J. E., & Leahy, D. 2017, *Pub. Astron. Soc. Pac.*, 129, 115002, doi: 10.1088/1538-3873/aa8800

—. 2021, Journal of Astrophysics and Astronomy, 42, 30, doi: 10.1007/s12036-020-09689-w

Pustilnik, S. A., Kniazev, A. Y., Lipovetsky, V. A., & Ugryumov, A. V. 2001, A&A, 373, 24, doi: 10.1051/0004-6361:20010555

Putman, M. E., Zheng, Y., Price-Whelan, A. M., et al. 2021, *Astrophys. J.*, 913, 53, doi: 10.3847/1538-4357/abe391

Rahna, P. T., Das, M., Murthy, J., Gudennavar, S. B., & Bubbly, S. G. 2018, *Mon. Not. Roy. Astron. Soc.*, 481, 1212, doi: 10.1093/mnras/sty2250

Reddy, N. A., Oesch, P. A., Bouwens, R. J., et al. 2018, *Astrophys. J.*, 853, 56, doi: 10.3847/1538-4357/aaa3e7

Regan, M. W., Thornley, M. D., Vogel, S. N., et al. 2006, *Astrophys. J.*, 652, 1112, doi: 10.1086/505382

Regev, O. 2006, Chaos and complexity in astrophysics (Cambridge University Press)

Renu, D., Subramanian, S., Rao, S., & George, K. 2025, *Astron. Astrophys.*, 696, A118, doi: 10.1051/0004-6361/202452701

Ribeiro, H. V., Zunino, L., Lenzi, E. K., Santoro, P. A., & Mendes, R. S. 2012, PLoS ONE

Richer, M. G., & McCall, M. L. 1995, *Astrophys. J.*, 445, 642, doi: 10.1086/175727

Rieke, G. H., Young, E. T., Engelbracht, C. W., et al. 2004, *Astrophys. J. Suppl.*, 154, 25, doi: 10.1086/422717

Rieke, M. J., Kelly, D. M., Misselt, K., et al. 2023, *Pub. Astron. Soc. Pac.*, 135, 028001, doi: 10.1088/1538-3873/acac53

Rigopoulou, D., Spoon, H. W. W., Genzel, R., et al. 1999, *Astron. J.*, 118, 2625, doi: 10.1086/301146

Rigopoulou, D., Barale, M., Clary, D. C., et al. 2021, *Mon. Not. Roy. Astron. Soc.*, 504, 5287, doi: 10.1093/mnras/stab959

Rigopoulou, D., Donnan, F. R., García-Bernete, I., et al. 2024, *Mon. Not. Roy. Astron. Soc.*, 532, 1598, doi: 10.1093/mnras/stae1535

Robertson, B. E., Tacchella, S., Johnson, B. D., et al. 2023, *Astrophys. J. Lett.*, 942, L42, doi: 10.3847/2041-8213/aca086

Rocha, M., Peter, A. H. G., Bullock, J. S., et al. 2013, Monthly Notices of the Royal Astronomical Society, 430, 81–104, doi: 10.1093/mnras/sts514

Rodrigo, C., Solano, E., & Bayo, A. 2012, SVO Filter Profile Service Version 1.0, IVOA Working Draft 15 October 2012, doi: 10.5479/ADS/bib/2012ivoa.rept.1015R

Rodríguez, M. J., Lee, J. C., Indebetouw, R., et al. 2025, *Astrophys. J.*, 983, 137, doi: 10.3847/1538-4357/adbb69

Rodriguez Wimberly, M. K., Cooper, M. C., Fillingham, S. P., et al. 2018, Monthly Notices of the Royal Astronomical Society, 483, 4031–4039, doi: 10.1093/mnras/sty3357

Roli, A., Ligot, A., & Birattari, M. 2019, Frontiers in Robotics and AI, 6, 130

Rosso, O. A., Larrondo, H., Martin, M. T., Plastino, A., & Fuentes, M. A. 2007, Physical review letters, 99, 154102

Ryan-Weber, E. V., Begum, A., Oosterloo, T., et al. 2008, Monthly Notices of the Royal Astronomical Society, 384, 535, doi: 10.1111/j.1365-2966.2007.12734.x

Ryon, J. E., Bastian, N., Adamo, A., et al. 2015, *Mon. Not. Roy. Astron. Soc.*, 452, 525, doi: 10.1093/mnras/stv1282

Salim, S., Charlot, S., Rich, R. M., et al. 2005, The Astrophysical Journal, 619, L39, doi: 10.1086/424800

Salim, S., Rich, R. M., Charlot, S., et al. 2007, The Astrophysical Journal Supplement Series, 173, 267, doi: 10.1086/519218

Salpeter, E. E. 1955, *Astrophys. J.*, 121, 161, doi: 10.1086/145971

Sandage, A. 1961, The Hubble Atlas of Galaxies (Washington: Carnegie Institution)

Sandstrom, K. M., Leroy, A. K., Walter, F., et al. 2013, *Astrophys. J.*, 777, 5, doi: 10.1088/0004-637X/777/1/5

Sandstrom, K. M., Koch, E. W., Leroy, A. K., et al. 2023, *Astrophys. J. Lett.*, 944, L8, doi: 10.3847/2041-8213/aca972

Sandstrom, K. M., Chastenet, J., Sutter, J., et al. 2023, *Astrophys. J. Lett.*, 944, L7, doi: 10.3847/2041-8213/acb0cf

Scalo, J. 1990, in Windows on Galaxies, ed. G. Fabbiano, J. S. Gallagher, & A. Renzini (Dordrecht: Springer Netherlands), 125–140

Scalo, J. M. 1986a, , 11, 1

Scalo, J. M. 1986b, in IAU Symposium, Vol. 116, Luminous Stars and Associations in Galaxies, ed. C. W. H. De Loore, A. J. Willis, & P. Laskarides, 451–466

Schawinski, K., Urry, C. M., Simmons, B. D., et al. 2014, *Mon. Not. Roy. Astron. Soc.*, 440, 889, doi: 10.1093/mnras/stu327

Schinnerer, E., Meidt, S. E., Colombo, D., et al. 2017, *Astrophys. J.*, 836, 62, doi: 10.3847/1538-4357/836/1/62

Schlafly, E. F., & Finkbeiner, D. P. 2011, *Astrophys. J.*, 737, 103, doi: 10.1088/0004-637X/737/2/103

Schmidt, M. 1959, *Astrophys. J.*, 129, 243, doi: 10.1086/146614

Schombert, J., McGaugh, S., & Lelli, F. 2022, The Astronomical Journal, 163, 154, doi: 10.3847/1538-3881/ac5249

Schombert, J. M., McGaugh, S. S., & Eder, J. A. 2001, AJ, 121, 2420, doi: 10.1086/320398

Schruba, A., Leroy, A. K., Walter, F., et al. 2012, *Astron. J.*, 143, 138, doi: 10.1088/0004-6256/143/6/138

Searle, L., & Zinn, R. 1978, *Astrophys. J.*, 225, 357, doi: 10.1086/156499

Segal, G., Parkinson, D., Norris, R. P., & Swan, J. 2019, Publications of the Astronomical Society of the Pacific, 131, 108007

Shannon, C. E. 1948, The Bell system technical journal, 27, 379

Shen, L., Papovich, C., Yang, G., et al. 2023, *Astrophys. J.*, 950, 7, doi: 10.3847/1538-4357/acc944

Shetty, R., & Ostriker, E. C. 2006, *Astrophys. J.*, 647, 997, doi: 10.1086/505594

Shipley, H. V., Papovich, C., Rieke, G. H., Brown, M. J. I., & Moustakas, J. 2016, *Astrophys. J.*, 818, 60, doi: 10.3847/0004-637X/818/1/60

Shivaei, I., & Boogaard, L. A. 2024, *Astron. Astrophys.*, 691, L2, doi: 10.1051/0004-6361/202451826

Shivaei, I., Alberts, S., Florian, M., et al. 2024, *Astron. Astrophys.*, 690, A89, doi: 10.1051/0004-6361/202449579

Shore, S. N., & Galli, D. 2003, Astrophysics and space science, 284, 809

Shu, F. H., Adams, F. C., & Lizano, S. 1987, *Ann. Rev. Astron. Astrophys.*, 25, 23, doi: 10.1146/annurev.aa.25.090187.000323

Sigaki, H. Y., De Souza, R., De Souza, R., Zola, R., & Ribeiro, H. 2019, Physical Review E, 99, 013311

Sigaki, H. Y., Perc, M., & Ribeiro, H. V. 2018, Proceedings of the National Academy of Sciences, 115, E8585

Simard, L., Mendel, J. T., Patton, D. R., Ellison, S. L., & McConnachie, A. W. 2011, *Astrophys. J. Suppl.*, 196, 11, doi: 10.1088/0067-0049/196/1/11

Simon, J. D. 2018, The Astrophysical Journal, 863, 89, doi: 10.3847/1538-4357/aacdfb

Simon, J. D. 2019, *Ann. Rev. Astron. Astrophys.*, 57, 375, doi: 10.1146/annurev-astro-091918-104453

Sirianni, M., Jee, M. J., Benítez, N., et al. 2005, *Pub. Astron. Soc. Pac.*, 117, 1049, doi: 10.1086/444553

Skillman, E. D., Côté, S., & Miller, B. W. 2003, *Astron. J.*, 125, 610, doi: 10.1086/345965

Small, M., McCullough, M., & Sakellariou, K. 2018, in 2018 IEEE International Symposium on Circuits and Systems (ISCAS), IEEE, 1–5

Smith, J. D. T., Draine, B. T., Dale, D. A., et al. 2007, *Astrophys. J.*, 656, 770, doi: 10.1086/510549

Smith, M. V., van Zee, L., Salim, S., et al. 2021, *Mon. Not. Roy. Astron. Soc.*, 505, 3998, doi: 10.1093/mnras/stab1530

Smith, M. V., van Zee, L., Dale, D. A., et al. 2022, Monthly Notices of the Royal Astronomical Society, 515, 3270, doi: 10.1093/mnras/stac1974

Soria, R., & Kong, A. K. H. 2002, *Astrophys. J. Lett.*, 572, L33, doi: 10.1086/341445

Speagle, J. S., Steinhardt, C. L., Capak, P. L., & Silverman, J. D. 2014, *Astrophys. J. Suppl.*, 214, 15, doi: 10.1088/0067-0049/214/2/15

Stedman, S., & Knapen, J. H. 2001, *Astrophys. Space Sci.*, 276, 517, doi: 10.1023/A:1017576608042

Sternberg, A., Hoffmann, T. L., & Pauldrach, A. W. A. 2003, The Astrophysical Journal, 599, 1333, doi: 10.1086/379506

Stierwalt, S., Besla, G., Patton, D., et al. 2015, *Astrophys. J.*, 805, 2, doi: 10.1088/0004-637X/805/1/2

Strateva, I., Ivezić, Ž., Knapp, G. R., et al. 2001, *Astron. J.*, 122, 1861, doi: 10.1086/323301

Sun, J., Leroy, A. K., Schruba, A., et al. 2018, *Astrophys. J.*, 860, 172, doi: 10.3847/1538-4357/aac326

Sutter, J., Sandstrom, K., Chastenet, J., et al. 2024, *Astrophys. J.*, 971, 178, doi: 10.3847/1538-4357/ad54bd

Tandon, S. N., Hutchings, J. B., Ghosh, S. K., et al. 2017, Journal of Astrophysics and Astronomy, 38, 28, doi: 10.1007/s12036-017-9445-x

Tandon, S. N., Postma, J., Joseph, P., et al. 2020, *Astron. J.*, 159, 158, doi: 10.3847/1538-3881/ab72a3

Tanvir, T. S., Krumholz, M. R., & Federrath, C. 2022, *Mon. Not. Roy. Astron. Soc.*, 516, 5712, doi: 10.1093/mnras/stac2642

Taylor, M. B. 2005, in Astronomical Society of the Pacific Conference Series, Vol. 347, Astronomical Data Analysis Software and Systems XIV, ed. P. Shopbell, M. Britton, & R. Ebert, 29

Thilker, D. A., Bianchi, L., Boissier, S., et al. 2005, *Astrophys. J. Lett.*, 619, L79, doi: 10.1086/425251

Thilker, D. A., Bianchi, L., Meurer, G., et al. 2007, *Astrophys. J. Suppl.*, 173, 538, doi: 10.1086/523853

Thilker, D. A., Lee, J. C., Deger, S., et al. 2023, *Astrophys. J. Lett.*, 944, L13, doi: 10.3847/2041-8213/acaeac

Tielens, A. G. G. M. 2008, *Ann. Rev. Astron. Astrophys.*, 46, 289, doi: 10.1146/annurev.astro.46.060407.145211

Tielens, A. G. G. M., Meixner, M. M., van der Werf, P. P., et al. 1993, Science, 262, 86. http://www.jstor.org/stable/2885669

Tody, D. 1993, in Astronomical Society of the Pacific Conference Series, Vol. 52, Astronomical Data Analysis Software and Systems II, ed. R. J. Hanisch, R. J. V. Brissenden, & J. Barnes, 173

Toomre, A. 1964, *Astrophys. J.*, 139, 1217, doi: 10.1086/147861

Ujjwal, K., Kartha, S. S., Subramanian, S., et al. 2022, Monthly Notices of the Royal Astronomical Society, 516, 2171–2180, doi: 10.1093/mnras/stac2285

Ujjwal, Krishnan, Kartha, Sreeja S., Akhil, Krishna R., et al. 2024, A&A, 684, A71, doi: 10.1051/0004-6361/202347620

Vacca, W. D., Garmany, C. D., & Shull, J. M. 1996, *Astrophys. J.*, 460, 914, doi: 10.1086/177020

van den Bergh, S. 1976, *Astrophys. J.*, 206, 883, doi: 10.1086/154452

Vaz, Daniel, Brinchmann, Jarle, Zoutendijk, Sebastiaan L., et al. 2023, A&A, 678, A59, doi: 10.1051/0004-6361/202346453

Vega, O., Bressan, A., Panuzzo, P., et al. 2010, *Astrophys. J.*, 721, 1090, doi: 10.1088/0004-637X/721/2/1090

Villanueva, V., Blaña, M., Bolatto, A. D., et al. 2025, *Astron. Astrophys.*, 699, L11, doi: 10.1051/0004-6361/202555635

Wainer, T. M., Williams, B. F., Johnson, L. C., et al. 2024, The Astronomical Journal, 168, 86, doi: 10.3847/1538-3881/ad5a6e

Walter, F., Brinks, E., de Blok, W. J. G., et al. 2008, *Astron. J.*, 136, 2563, doi: 10.1088/0004-6256/136/6/2563

Watkins, E. J., Barnes, A. T., Henny, K., et al. 2023, ApJL, 944, L24, doi: 10.3847/2041-8213/aca6e4

Weck, P. J., Schaffner, D. A., Brown, M. R., & Wicks, R. T. 2015, Physical Review E, 91, 023101

Weidner, C., Kroupa, P., & Pflamm-Altenburg, J. 2011, *Mon. Not. Roy. Astron. Soc.*, 412, 979, doi: 10.1111/j.1365-2966.2010.17959.x

Weisz, D. R., Dolphin, A. E., Skillman, E. D., et al. 2014, *Astrophys. J.*, 789, 147, doi: 10.1088/0004-637X/789/2/147

Weisz, D. R., Skillman, E. D., Cannon, J. M., et al. 2009, ApJ, 704, 1538, doi: 10.1088/0004-637X/704/2/1538

Weisz, D. R., Zucker, D. B., Dolphin, A. E., et al. 2012, The Astrophysical Journal, 748, 88, doi: 10.1088/0004-637X/748/2/88

Weisz, D. R., Johnson, L. C., Foreman-Mackey, D., et al. 2015, *Astrophys. J.*, 806, 198, doi: 10.1088/0004-637X/806/2/198

Weygand, J. M., & Kivelson, M. G. 2019, ApJ, 872, 59

Wheeler, C., Hopkins, P. F., Pace, A. B., et al. 2019, *Mon. Not. Roy. Astron. Soc.*, 490, 4447, doi: 10.1093/mnras/stz2887

Whitcomb, C. M., Sandstrom, K., & Smith, J.-D. T. 2023, Research Notes of the AAS, 7, 38, doi: 10.3847/2515-5172/acc073

White, S. D. M., & Frenk, C. S. 1991, *Astrophys. J.*, 379, 52, doi: 10.1086/170483

White, S. D. M., & Rees, M. J. 1978, *Mon. Not. Roy. Astron. Soc.*, 183, 341, doi: 10.1093/mnras/183.3.341

Williams, T. G., Sun, J., Barnes, A. T., et al. 2022, *Astrophys. J. Lett.*, 941, L27, doi: 10.3847/2041-8213/aca674

Willman, B., Geha, M., Strader, J., et al. 2011, *Astron. J.*, 142, 128, doi: 10.1088/0004-6256/142/4/128

Willman, B., Dalcanton, J. J., Martinez-Delgado, D., et al. 2005, *Astrophys. J. Lett.*, 626, L85, doi: 10.1086/431760

Wolf, A., Swift, J. B., Swinney, H. L., & Vastano, J. A. 1985, Physica D: nonlinear phenomena, 16, 285

Wolf, J., Martinez, G. D., Bullock, J. S., et al. 2010, Monthly Notices of the Royal Astronomical Society, 406, 1220, doi: 10.1111/j.1365-2966.2010.16753.x

Wootten, A., & Thompson, A. R. 2009, Proceedings of the IEEE, 97, 1463, doi: 10.1109/JPROC.2009.2020572

Xiao, M., Oesch, P. A., Elbaz, D., et al. 2024, *Nature*, 635, 311, doi: 10.1038/s41586-024-08094-5

Xiao, M., Williams, C. C., Oesch, P. A., et al. 2025, *Astron. Astrophys.*, 696, A156, doi: 10.1051/0004-6361/202453487

Yadav, J., Das, M., Barway, S., & Combes, F. 2023, Monthly Notices of the Royal Astronomical Society, 526, 198, doi: 10.1093/mnras/stad2672

Yadav, J., Das, M., Patra, N. N., et al. 2021, ApJ, 914, 54, doi: 10.3847/1538-4357/abf8c1

Yamagishi, M., Kaneda, H., Ishihara, D., et al. 2012, *Astron. Astrophys.*, 541, A10, doi: 10.1051/0004-6361/201218904

Yip, C. W., Connolly, A. J., Szalay, A. S., et al. 2004, *Astron. J.*, 128, 585, doi: 10.1086/422429

Yu, S.-Y., & Ho, L. C. 2020, The Astrophysical Journal, 900, 150, doi: 10.3847/1538-4357/abac5b

Zaragoza-Cardiel, J., Fritz, J., Aretxaga, I., et al. 2019, MNRASL, 487, L61, doi: 10.1093/mnrasl/slz093

Zaritsky, D., & Christlein, D. 2007, *Astron. J.*, 134, 135, doi: 10.1086/518238

Zhang, H.-X., Hunter, D. A., Elmegreen, B. G., Gao, Y., & Schruba, A. 2012, The Astronomical Journal, 143, 47, doi: 10.1088/0004-6256/143/2/47

Zhang, S., Mackey, D., & Costa, G. S. D. 2021, MNRAS, 508, 2098, doi: 10.1093/mnras/stab2642

Zhu, X.-P., Dai, J.-M., Bian, C.-J., et al. 2019, *Astrophys. Space Sci.*, 364, 55, doi: 10.1007/s10509-019-3540-1

Zoutendijk, Sebastiaan L., Brinchmann, Jarle, Boogaard, Leindert A., et al. 2020, A&A, 635, A107, doi: 10.1051/0004-6361/201936155

Zunino, L., & Ribeiro, H. V. 2016, Chaos, Solitons & Fractals, 91, 679